Active Cloaking and Waves in Structured Media

Thesis submitted in accordance with the requirements of
the University of Liverpool for the degree of Doctor in Philosophy
by
Jane O'Neill

November 18, 2016

Abstract

This thesis presents a novel method for active cloaking problems involving finite defects embedded in thin elastic plates. We demonstrate the approach by considering several geometries and boundary conditions, which include circular geometries with clamped boundaries, circular shaped coated inclusions and a finite cluster of rigid pins. We use results from plate theory, including problems on scattering of flexural waves from canonical geometries and platonic crystals. Such systems are governed by the fourth-order biharmonic plate equation.

The method employed involves surrounding an object with a configuration of active sources whose complex amplitudes are chosen such that the main contribution to the scattered wave is cancelled in the far field. The active sources are represented by the Green's function for the biharmonic operator, describing the response to a point force. This Green's function has the beneficial property of being non-singular at the origin and the approximate cloak leads to an analytical system of linear algebraic equations for calculating the amplitudes of the active sources, required for effective cloaking.

We demonstrate that the method described is applicable to arbitrarily shaped scatterers; effective cloaking is presented for a scatterer with a smooth, clamped boundary. Cloaking is also demonstrated for a circular clamped inclusion subject to flexural waves generated by a remote point source. Studying this problem enables us to find a Green's function for the cloaking problem which can be used to cloak a discretely distributed time-harmonic load.

The cloaking is shown to work well at lower frequency regimes, however, at higher frequency resonant regimes, rapid changes in scattering from the inclusion are observed in narrow frequency intervals. This makes the cloak vulnerable to detection using frequency swept probe beams; time lags can arise as the sources adapt to the alterations in frequency. We extend the approach to the case of a resonant inclusion, combining active and passive techniques to tame regions of rapid variation in scattering properties. We then apply the active cloaking method approach to the coated inclusion.

Finally, we modify the method for cloaking finite clusters of pins, where the geometry of the cluster causes interactions between the evanescent terms of solutions to the biharmonic equation, leading to interesting scattering patterns. Our method of active cloaking in thin elastic plates is shown to work for scattering phenomena such as localisation, wave-trapping and neutrality. We analyse band diagrams and dispersion surfaces from the infinite structure to estimate frequencies at which these phenomena occur in the finite cluster, and demonstrate effective cloaking using a finite number of sources.

Contents

Abstract **i**

Contents **ii**

List of Figures **v**

List of Tables **xv**

List of Publications **xv**

Conference Presentations **xvii**

Acknowledgement **xviii**

Introduction **1**

1 Multipole method and fundamental solution for Kirchhoff plates **9**

1.1 Scattering of flexural waves by a circular clamped edge cavity 11

1.1.1 Obtaining the scattering matrix 12

1.1.2 Multipole representation of the scattered field 13

1.1.3 Illustrative examples of scattering from a clamped cavity 14

1.1.4 Free edge boundary conditions 15

1.2 Scattering of flexural waves by a circular inclusion 17

1.2.1 Obtaining the scattered field from conditions of perfect bonding . . . 18

1.2.2 Illustrative examples of scattering from a circular inclusion 19

1.3 Active sources and the fundamental solution for the biharmonic operator . . 21

1.3.1 Graf's addition theorem 23

1.4 Scattering of flexural waves by a doubly periodic array 24

1.4.1 Problem setting for an array of circular clamped cavities 25

1.4.2 Band diagram for a doubly-periodic array of pins 32

2 Active cloaking of flexural waves for clamped cavities in thin elastic plates **35**

2.1 Method of solution for a general forcing term 36

2.2 Achieving scattering reduction with active sources 38

2.3 Active cloaking with two control sources . . . 40
2.4 Active cloaking with additional control sources . . . 43
2.5 The fundamental solution for cloaking a circular clamped cavity . . . 50
2.6 Active cloaking of an arbitrarily shaped cavity with a smooth clamped boundary 54
2.7 Remarks and discussions . . . 58

3 Active cloaking at resonant regimes 60
3.1 Scattering of membrane waves by a coated inclusion . . . 62
3.1.1 Governing equations . . . 62
3.1.2 Derivation of the scattering relation . . . 64
3.1.3 Resonant regimes for an uncoated inclusion . . . 66
3.1.4 Design of the coating targeting resonant frequencies . . . 69
3.1.5 Active cloaking of a coated inclusion . . . 70
3.2 Scattering of flexural waves by a coated inclusion in a Kirchhoff plate . . . 78
3.2.1 Relationship between flexural waves in thin plates and membranes . . 78
3.2.2 Governing equations . . . 81
3.2.3 Derivation of the scattering matrix . . . 82
3.2.4 Resonant regimes for an uncoated inclusion . . . 84
3.2.5 Design of the coating targeting resonant frequencies . . . 88
3.2.6 Active cloaking of a coated inclusion . . . 90
3.3 Remarks and discussions . . . 97

4 Active cloaking of finite clusters of pins 99
4.1 Formulation of the problem and governing equations . . . 100
4.1.1 Problem setting . . . 100
4.1.2 Calculating active source amplitudes $\mathcal{B}_m$ . . . 101
4.1.3 Selecting the spectral parameter to demonstrate broadband cloaking . 103
4.2 Active cloaking results . . . 105
4.2.1 Cloaking in the zero-frequency stop band . . . 106
4.2.2 Cloaking at higher spectral values in the pass band . . . 107
4.3 Remarks and discussions . . . 114

5 Conclusions and future work 116

Bibliography 119

Appendix A 127
A.1 Kirchhoff plates: The representations for the matrices $\mathcal{A}^{(ci)}$, $\mathcal{B}^{(ci)}$, $\mathcal{A}^{(ec)}$, $\mathcal{B}^{(ec)}$ and their reduced forms $\mathcal{A}^{(ci,*)}$, $\mathcal{B}^{(ci,*)}$, $\mathcal{A}^{(ec,*)}$, $\mathcal{B}^{(ec,*)}$ . . . 127
A.1.1 Transmission conditions at the interior interface of the coating . . . 127

A.1.2 Reduction of the system of transmission conditions on $r = a_i$ to block diagonal form 128
A.1.3 Transmission conditions at the exterior interface of the coating 131
A.1.4 Reduction of the system of transmission conditions on $r = a_c$ to block diagonal form 132
A.1.5 Further algebraic simplification 134
A.2 Kirchhoff plate: explicit representations for the entries of the scattering matrix $\mathcal{S}$ and the coefficients $A_n^{(i)}$, $B_n^{(i)}$, $A_n^{(c)}$, $E_n^{(c)}$, $B_n^{(c)}$, $F_n^{(c)}$, $E_n^{(e)}$ and $F_n^{(e)}$ 135

Appendix B **137**

B.1 Supplementary cloaking results for a 5×5 cluster 137

List of Figures

1.1 Schematic view of a clamped edge cavity of radius a_i embedded in a Kirchhoff plate subject to an incident field denoted by $w_{inc}(\mathbf{x})$. In part (a) $w_{inc}(\mathbf{x})$ is an incident plane wave such that $\theta_{inc} = 0$, and in part (b) $w_{inc}(\mathbf{x})$ is a remote point source. 11

1.2 In both figures $\beta = 0.3$, $a_i = 1.0$, $N = 2$. In either plot, there are no control sources and the large black disk depicts the position of the clamped cavity. Part (a) shows the flexural wave amplitude outside a clamped circular inclusion subject to an incident plane wave, and part (b) shows the flexural wave amplitude oustide a clamped circular inclusion subject to a remote point force depicted by the small black disk, which is located at a distance of 2.5 units from the origin, at an angle of $2\pi/3$ radians to the x_1-axis. 15

1.3 In all figures there are no control sources, the large black dot depicts the location of the free-edge cavity of raduis $a_i = 1.0$, and $N = 2$. In all parts, we show the total flexural wave amplitude due to (a) an incident plane wave such that $\beta = 0.3$, (b) a remote point source such that $\beta = 0.3$, (c) an incident plane wave such that $\beta = 0.5$, (d) an incident plane wave such that $\beta = 0.7$. . 17

1.4 Schematic view of an inclusion of radius a_i embedded in a Kirchhoff plate subject to an incident field denoted by $w_{inc}(\mathbf{x})$. In part (a) $w_{inc}(\mathbf{x})$ is an incident plane wave such that $\theta_{inc} = 0$, and in part (b) $w_{inc}(\mathbf{x})$ is a remote point source. 18

1.5 Flexural wave amplitude of the total field in a plate containing an inclusion of radius $a_i = 0.5$ whose boundary is depicted by the black circle. The material parameters in all figures are $\rho_i = 0.05$, $\rho_e = 1.0$, $\nu_i = \nu_e = 0.3$, $D_i = 2.5 \times 10^{-4}$, $D_e = 1.0$, $a_i = 0.50$. In either plot, there are no control sources. In parts (a) and (b) $\omega = 0.3$, whilst in parts (c)-(g) $\omega = 11.30$. Part (c) depicts amplitudes exterior to the inclusion, whilst parts (d) and (e) detail the amplitudes both inside the inclusion and the exterior medium. Parts (f) and (g) detail the amplitudes due to a remote point force depicted by the small black disk, which is located at a distance of 2.5 units from the origin, at an angle of $2\pi/3$ radians to the x_1-axis. Part (f) depicts amplitudes in the exterior medium only whilst part (g) depicts wave amplitudes throughout the inclusion and exterior medium. 20

1.6 Schematic diagram showing locations of an active source at $\mathbf{x}^{(s,l)} = ({x_1}^{(s,l)}, {x_2}^{(s,l)})^\top$, and a general point $\overline{\mathbf{X}} = (\overline{X_1}, \overline{X_2})^\top$. The vectors $\mathbf{r}$ and $\mathbf{r}_l$ denote the position vectors of the general point $\overline{\mathbf{X}}$ relative the origins O and O_l, respectively. The arguments of $\mathbf{r}$ and $\mathbf{r}_l$ to their respective origins are θ and θ_l. The vector $\mathbf{b} = -\mathbf{x}^{(s,l)}$ joins O_l to O, and has an argument of $(\phi - \pi)$ with respect to O_l. 23

1.7 In part (a) we show a schematic view of a doubly periodic array of clamped edge cavities throughout a Kirchhoff plate. Each cavity has radius a and the unit cell is denoted by $\Omega_{0,0}$. In part (b) we show a close-up view of the unit cell $\Omega_{0,0}$. 26

1.8 Part (a) depicts the irreducible Brillouin zone shown as the vertices of the solid triangle Γ, X and M. The first Brillouin zone is depicted by square with vertices Γ, X, M and Y. Part (b) depicts the nodes of the reciprocal lattice detailing the vector $\mathbf{K_h}$ from the first Brillouin zone the h-th node of the reciprocal lattice. 28

1.9 Band diagram for square array of rigid pins with $d = 1$, using square Brillouin zone $(k_x, k_y) = [0, \pi] \times [0, \pi]$. The solid lines represent solutions of the dispersion relation (1.50), and the dashed lines represent both dispersion curves and segments of the singularity lines (1.51). 32

1.10 In both figures, the real part of the amplitude of flexural displacement for the total field is shown, with its range, indicated by the colourbar, determined by the degree of localisation within the system. In addition, the pins are depicted by black discs and the horizontal and vertical axes are the x_1- and x_2-axes, respectively. Part (a) depicts a plane wave normally incident on an uncloaked 8×8 ($N = 8$) cluster of pins. Part (b) depicts a plane wave incident at $\theta_{inc} = \pi/4$ on 2000 gratings with $d = 1$ for $\beta = 4.44$, $\kappa_y = 3.1396$ corresponding to M in the reciprocal lattice. 33

2.1 Both figures depict the total flexural wave amplitude exterior to a circular clamped cavity depicted by the larger black dot. In either plot: $\beta = 0.3$, $a_i = 1.0$, $N = 2$, and $\Phi = \pi$. In part (a) there are no control sources, and in part (b) two control sources are located exterior to the cavity, depicted by the two smaller black dots positioned at $a^{(s,l)} = 2.5$ for $l = 1, 2$, with respective amplitudes $Q_{1,2} = -3.075 \mp 1.728\, i$. 41

2.2 In all figures we plot the flexural wave amplitude as a function of θ, on a circle of radius 20. The scatterer is a circular clamped cavity with radius $a_i = 1.0$. In all figures $\beta = 0.3$, $N = 2$, dashed (blue): real part, dotted (red): imaginary part. Parts (a) and (b) depict the the respective amplitudes of the total and scattered fields with no control sources. Parts (c) and (d) are as (a) and (b), respectively, with the addition of two control sources positioned at $a^{(s,l)} = 2.5$ for $l = 1, 2$ whose respective amplitudes are $Q_{1,2} = -3.075 \mp 1.728\, i$. 42

2.3 The amplitude of the outgoing Hankel function term from a circular rigid inclusion with angular dependence $\exp(2i\theta)$ in the flexural wave expansion, plotted as a function of $a^{(s,2)}$ and $a^{(s,1)}$. Note the almost constant amplitude levels, apparent in the legend. 42

2.4 Part (a) shows a possible configuration four sources, detailing how ξ is measured. In parts (b)-(f) scattering is due a circular clamped cavity of radius $a_i = 1.0$, $\beta = 0.3$, $N = 2$, and $\Phi = \pi$. Contour plots (b)-(d) detail the total flexural wave amplitude due to the cavity and four control sources, which are depicted by the large and small black dots, respectively. The sources are located on a circle of radius $a^{(s,l)} = 2.5$, $l = 1, 2, 3$. In parts (b) $\xi = \pi/4$, and source amplitudes are $Q_1 = 2.628 - 1.728\,i$, $Q_2 = -2.096 + 1.728\,i$, and $Q_3 = -3.341$, (c) $\xi = \pi/3$ with $Q_1 = 0.266 - 1.728\,i$, $Q_2 = -1.961 + 1.728\,i$, $Q_3 = -2.227$, and in (d) $\xi = \pi/2$ with $Q_{1,2} = -1.404 \mp 1.728\,i$, $Q_3 = -1.670$. Parts (e) and (f) depict the the respective amplitudes of the total and scattered fields with four control sources when $\xi = \pi/2$. The dashed (blue) curve is the real part, whilst the dotted (red) is the imaginary part of the field. 45

2.5 Total flexural wave amplitude exterior to a circular clamped cavity, depicted by the larger black dot of radius $a_i = 1.0$, where $\beta = 0.3$, $N = 2$, and $\Phi = \pi$. Six control sources are located exterior to the cavity such that $\xi = \pi/3$, $\eta = 2\pi/3$, and $a^{(s,l)} = 2.5$ for $l = 1, 2, 3, 4$. The respective amplitudes are $Q_{1,2} = -0.848 \mp 1.146\,i$, $Q_{3,4} = -1.114 \mp 0.582\,i$. Note that $Q_{3,4}$ are the amplitudes of both sources off the x_1-axis in the Ist, IVth and IInd, IIIrd quadrants, respectively. 46

2.6 Flexural wave amplitude as a function of θ, on a circle of radius 40. The scatterer is a circular clamped cavity with radius $a_i = 1.0$. In both figures the dashed (blue) curve is the real part, whilst the dotted (red) curve is the imaginary part, also $\beta = 0.3$, and $N = 2$. Parts (a) and (b) depict the the respective amplitudes of the total and scattered fields with six control sources, such that $a^{(s,l)} = 2.5$ for $l = 1, 2, 3, 4$, $\xi = \pi/3$, $\eta = 2\pi/3$, and $Q_{1,2} = -0.848 \pm 1.146$, $Q_{3,4} = -1.114 \mp 0.582\,i$. 48

2.7 Total flexural wave amplitude exterior to a circular clamped cavity, depicted by the larger black dot of radius $a_i = 1.0$, where $\beta = 0.3$, $N = 2$, and $\Phi = \pi$. The configuration of six control sources as in Fig. 2.5, is rotated by an angle of (a) 5 degrees, (b) 10 degrees, (c) 15 degrees, (d) 20 degrees, respectively. . 48

2.8 Both figures depict the total flexural wave amplitude exterior to a circular clamped cavity depicted by the larger black dot. In both plots, the incident wave is due to a remote point source depicted by a small black dot at $(-40, 0)$. Other parameters in the figures are $\beta = 0.3$, $a_i = 1.0$, $N = 2$, and $\Phi = \pi$. In part (a) there are no control sources, and in part (b) two control sources are located exterior to the cavity, depicted by the two smaller black dots positioned at $a^{(s,l)} = 2.5$ for $l = 1, 2$, with amplitudes $Q_1 = 0.825 + 0.740i$ and $Q_2 = 1.099 - 0.333i$. 52

2.9 Total flexural wave amplitude exterior to a circular clamped cavity of radius $a_i = 1.0$, depicted by the large black dot. In all figures $\beta = 0.3$, $N = 2$, and $\Phi = \pi$. The incident wave is due to a remote point source depicted by a small black dot at $(-40, 0)$. Four control sources surround the cavity and are depicted by the small black dots located on a circle of radius $a^{(s,l)} = 2.5$, $l = 1, 2, 3$. In parts (a) $\xi = \pi/4$, and source amplitudes are $Q_1 = -0.953 + 0.339i$, $Q_2 = 0.794 - 0.402i$, $Q_3 = 1.042 + 0.235i$, (b) $\xi = \pi/3$ with $Q_1 = -0.217 + 0.505i$, $Q_2 = 0.752 - 0.411i$, $Q_3 = 0.694 + 0.157i$, and in (c) $\xi = \pi/2$ with $Q_1 = -0.304 + 0.623i$, $Q_2 = 0.578 - 0.450i$, $Q_3 = 0.521 + 0.118i$. 53

2.10 Total flexural wave amplitude exterior to a circular clamped cavity, depicted by the larger black dot of radius $a_i = 1.0$, where $\beta = 0.3$, $N = 2$, and $\Phi = \pi$. The incident wave is due to a remote point source depicted by a small black dot at $(-40, 0)$. Six control sources are depicted by the small black dots located exterior to the cavity such that $\xi = \pi/3$, $\eta = 2\pi/3$, and $a^{(s,l)} = 2.5$ for $l = 1, 2, 3, 4$. The respective amplitudes are $Q_1 = -0.253 + 0.386i$, $Q_2 = 0.282 - 0.292i$, $Q_3 = 0.224 + 0.275$, $Q_4 = 0.470 - 0.119i$. 53

2.11 Model problems for flexural wave scattering by an arbitrarily shaped scatterer. The incident field is due to (a) a plane wave where $\theta_{inc} = 0$, and (b) a remote point source at the position of the l-th active source $\mathbf{x}^{(s,l)}$. 55

2.12 (a) Plane wave generated by displacing the boundary of the PML region on the left by 1 unit. (b) Flexural wave amplitude for an arbitrarily shaped cavity with no control sources. (c) Enlarged view of the cavity and the locations of the control sources. (d) Cloaking achieved by the use of seven control sources. 57

2.13 Resulting total flexural amplitude plotted along the x_1-axis ((a) real, (b) imaginary) for plane wave propagation in a plate with no scatterer (corresponding to Fig. 2.12(a)) in red (numbered as 1), with an arbitrarily shaped scatterer (corresponding to Fig. 2.12(b)) in green (numbered as 2) and with the added active control sources (corresponding to Fig. 2.12(d)) in blue (numbered as 3). 58

3.1 The geometry is shown for a coated inclusion embedded in a membrane. The material properties of the inclusion, its coating and the exterior medium are associated with the subscripts i, c, e, respectively. The respective interior and exterior radii of the coating are denoted by a_i, a_c. 63

3.2 Membrane wave scattering by an uncoated inclusion with the parameters $\rho_i = 1.5$, $\rho_e = 1.0$, $\mu_i = 0.1$, $\mu_e = 1.0$, $a_i = 0.50$. The graph of $|E_0^{(e)}|$ as a function of ω displays spikes corresponding to some resonant regimes. 67

3.3 Membrane wave scattering by an uncoated inclusion for the parameters $\rho_i = 1.5$, $\rho_e = 1.0$, $\mu_i = 0.1$, $\mu_e = 1.0$, $a_i = 0.50$. (a) Total field for $\omega = 0.3$, (b) Total field for $\omega = 2.62$ where $E_0^{(e)}$ vanishes, (c) Total field for $\omega = 3.0$ where $|E_0^{(e)}|$ has nearly a maximum. In the last frame of each row, we present a zoomed-in version of the displacement inside and in the close vicinity of the inclusion. The first two frames in the inset (b) represent the same field outside the inclusion, but with different colour maps, where the first frame excludes the internal field, whereas the second frame includes it. The same comment applies to the first two frames of the inset (c). 68

3.4 (a) Monopole $|E_0^{(e)}|$ (dot-dashed/orange) and dipole $|E_1^{(e)}|$ (dotted/red) amplitudes for membrane wave scattering by a coated inclusion with parameter values $\rho_i = 1.5$, $\rho_e = 1.0$, $\rho_c \approx 0.635$ (see (3.29)), $\mu_i = 0.1$, $\mu_c \approx 2.257$ (see (3.30)), $\mu_e = 1.0$, $a_i = 0.50$, $a_c = 0.77$ as a function of ω. The empirical fit $0.15\omega^4$ (solid/grey) for the monopole term is also included. (b) Monopole amplitude over a wider range of frequencies. 70

3.5 (a) Monopole amplitude for membrane wave scattering by (i) an uncoated inclusion (dashed/green) with parameter values $\rho_i = 1.5$, $\rho_e = 1.0$, $\mu_i = 0.1$, $\mu_e = 1.0$, $a_i = 0.50$, (ii) a coated inclusion (dot-dashed/orange) with parameter values as in (i) together with $\rho_c \approx 0.635$, $\mu_c \approx 2.257$ and $a_c = 0.77$, and (iii) a coated inclusion (solid/blue) with parameter values as in (i) together with $\rho_c = 0.81$, $\mu_c = 0.11$ and $a_c = 0.77$. Note, the red box highlights where the blue/solid curve flattens approximately for $\omega \in [2.4, 2.9]$. (b) Monopole amplitude for membrane wave scattering for the parameters of (i)-(iii) in (a), but for a range of ω highlighted by the red box in (a). We see strong variation in $|E_0^{(e)}|$ for an uncoated inclusion in this frequency range, but it is clear that with an appropriate choice of parameter values for the coating, we can create a region where $|E_0^{(e)}|$ remains fairly flat. 71

3.6 (a) Total field for membrane wave scattering by a coated inclusion with parameter values: $\rho_i = 1.5$, $\rho_e = 1.0$, $\rho_c \approx 0.635$, $\mu_i = 0.1$, $\mu_c \approx 2.257$, $\mu_e = 1.0$, $a_i = 0.50$, $a_c = 0.77$ and $\omega = 0.3$. (b) A zoomed in version of the total field inside the inclusion, coating and in close vicinity of the coating. 71

3.7 Membrane wave scattering: absolute value of the component n, $E_n^{(e)} H_n^{(1)}(\beta_e a_s)$, of the displacement field, where a_s is the radius of circle on which the control sources are placed, as a function of n for $\omega = 2.62$. Parameter values as for (blue/solid) curve in Fig. 3.5: $\rho_i = 1.5$, $\rho_c = 0.81$, $\rho_e = 1.0$, $\mu_i = 0.1$, $\mu_c = 0.11$, $\mu_e = 1.0$, $a_i = 0.5$, $a_c = 0.77$, $a_s = 1.57$. 72

3.8 Membrane wave scattering: (a) Total displacement field exterior to a coated inclusion with parameter values $\omega = 2.62$, $\rho_i = 1.5$, $\rho_c = 0.81$, $\rho_e = 1.0$, $\mu_i = 0.1$, $\mu_c = 0.11$, $\mu_e = 1.0$, $a_c = 0.77$, $a_i = 0.5$ over a square region of side length 20. (b) Total displacement field exterior to a coated inclusion in the presence of 4 active sources located on the axes (black dots), all $a_s = 1.57$ units away from the origin. Parameter values as in (a). (c) Total displacement field exterior to a coated inclusion in the presence of 8 active sources (black dots), all $a_s = 1.57$ units away from the origin; sources off the x_1- and x_2-axes lie on $x_2 = \pm x_1$. Parameter values as in (a). 75

3.9 Total displacement field for membrane wave scattering in the presence of 12 active sources (small black dots surrounding the inclusion) all $a_s = 1.57$ units away from the origin: (a) exterior to the coated inclusion, (b) the entire plate including the inclusion and the coating, (c) as in (b) but a detailed view. The material properties and frequency value are the same as in Fig. 3.8. 75

3.10 Membrane wave scattering: total displacement field exterior to a coated inclusion, where material properties are as in Fig. 3.8, for (a) $\omega = 0.7$, (b) $\omega = 0.8$, (c) $\omega = 1.2$. Left: uncloaked coated inclusion; centre: coated inclusion cloaked using four active control sources (small black dots surrounding the coated inclusion); right: same as the central images but over a wider range of x_1, x_2 values. 76

3.11 The geometry is shown for a coated inclusion embedded in a Kirchhoff plate. The material properties of the inclusion, its coating and the exterior medium are associated with the subscripts i, c, e, respectively. The respective interior and exterior radii of the coating are denoted by a_i, a_c. 82

3.12 Flexural wave scattering by an uncoated inclusion with the parameters $\rho_i = 0.05$, $\rho_e = 1.0$, $\nu_i = \nu_e = 0.3$, $D_i = 2.5 \times 10^{-4}$, $D_e = 1.0$, $a_i = 0.50$: (a) In the low-frequency regime, $|E_0^{(e)}|$ (dashed/green) and $|E_2^{(e)}|$ (dotted/red) are shown as functions of β_e (lower horizontal axis); for convenience ω is also shown (upper horizontal axis). The empirical fits are also presented: $|E_0^{(e)}| \approx 0.086\,\beta_e^2$, $|E_2^{(e)}| \approx 0.02\,\beta_e^2$ (both solid/grey), (b) the graph of $|E_0^{(e)}|$ as a function of β_e over a larger range. 85

3.13 Flexural wave scattering by an uncoated inclusion for the parameters as in Fig. 3.12: (a) Total field for $\omega = 0.3$, (b) Total field for $\omega = 11.15$ where $E_0^{(e)}$ vanishes, (c) Total field for $\omega = 11.30$ where $|E_0^{(e)}|$ has a relatively large value. On the right, in each image we present a zoomed-in version of the displacement inside and in the close vicinity of the inclusion. The first two frames in the inset (b) and (c) represent the same field outside the inclusion, but with different colour maps, where the first frame excludes the internal field, whereas the second frame includes it. In all contour plots horizontal and vertical axes are the x_1- and x_2-axes, respectively. 86

3.14 (a), (b) Flexural wave scattering by (i) an uncoated inclusion with parameter values $\rho_i = 0.05$, $\rho_e = 1.0$, $\nu_i = \nu_e = 0.3$, $D_i = 2.5 \times 10^{-4}$, $D_e = 1.0$, $a_i = 0.50$ (dashed/green); (a) (ii) a coated inclusion with parameter values as in (i) but with material properties of the coating reading $\rho_c = 0.005$, $\nu_c = 0.3$, $D_c = 2.5 \times 10^{-2}$ and $a_c = 0.77$ (solid/blue), (b) Flexural wave scattering for the parameters of (i) and (ii) in (a), but for a range of β_e highlighted by the (red) rectangular box in (a); (c) (iii) a coated inclusion with parameter values as in (i) but with material properties of the (heavier) coating reading $\rho_c = 0.05$, $\nu_c = 0.3$, $D_c = 3 \times 10^{-2}$ and $a_c = 1.5$ (solid/blue); (b) Flexural wave scattering for the parameters of (i) and (iii) in (a), but for a range of β_e highlighted by the (red) rectangular box in (c). 87

3.15 Flexural wave scattering in the low-frequency regime by a coated inclusion with parameter values $\rho_i = 0.05$, $\rho_c = 0.005$, $\rho_e = 1.0$, $\nu_i = \nu_c = \nu_e = 0.3$, $D_i = 2.5 \times 10^{-4}$, $D_c = 2.5 \times 10^{-2}$, $D_e = 1.0$, $a_i = 0.50$, $a_c = 0.77$. The absolute values of the monopole $|E_0^{(e)}|$ (dashed/dark blue) and the quadrupole $|E_2^{(e)}|$ (dot-dashed/light blue) coefficients are quadratic in spectral parameter β_e. The empirical fits are $|E_0^{(e)}| \approx 0.185{\beta_e}^2, |E_2^{(e)}| \approx 0.05{\beta_e}^2$ (both solid/grey). 89

3.16 Flexural wave scattering: (a) Total displacement field exterior to a coated inclusion with parameter values as in Fig. 3.15 and $\omega = 11.15$. (b) Total displacement field of a coated inclusion with parameter values as in (a) plotted for the whole plate, including the coating and inclusion. Note that the displacements inside the coating and inclusion dominate in this case and thus the detail in the exterior is more difficult to observe. (c) A zoomed-in version of the displacement inside the inclusion, coating and in close vicinity of the coating. 89

3.17 Model problems: (a) plane wave $w_{inc}(\mathbf{x})$ incident on a coated elastic inclusion; (b) a point source near the coated inclusion. 90

3.18 A configuration of twelve sources positioned symmetrically around the coated inclusion with complex amplitudes $Q_1, Q_2, \ldots, Q_7$. 92

3.19 Flexural wave scattering: (a) Total displacement field exterior to a coated inclusion with material properties as in Fig. 3.15 but at the smaller frequency of $\omega = 1.50$. (b) Total displacement field for the parameter values as in (a) but in the presence of 4 active sources located on the axes (black dots), all $a_s = 1.57$ units away from the centre of the inclusion. 93
3.20 Flexural wave scattering: absolute value of the normalised outgoing wave components $E_n^{(e)} H_n^{(1)}(\beta_e a_s)$ against the multipole order n for $\omega = 11.15$. Parameter values as in Fig. 3.15 with $a_s = 1.57$. 94
3.21 Flexural wave scattering: (a) Total displacement field exterior to a coated inclusion with parameter values as in Fig. 3.15 and $\omega = 11.15$. (b), (c) Total displacement field in the presence of 4 and 8, respectively active sources located on the axes (black dots), $a_s = 1.57$ units away from the origin. 94
3.22 Flexural wave scattering: (a) Total displacement field exterior to a coated inclusion with parameter values as in Fig. 3.15 and $\omega = 11.15$ in the presence of 12 active sources positioned $a_s = 1.57$ units away from the origin. (b) Same as (a) but the total displacement field plotted in all three regions. (c) Same as (b) but over a smaller range of the plate detailing localised fields in the inclusion. 95
3.23 Angular plot of the scattered field along the circular contour of radius 7.85 (five times the radius of the circle on which the active sources are located) centred at the origin, for the simulations in Fig. 3.21(a) with no sources present and in Fig. 3.22 with 12 sources present. No active sources present: Solid/green curve represents the real and dot-dashed/purple curve the imaginary part of the scattered field; active cloaking with 12 sources present: Dashed/red curve represents the real and dotted/blue curve the imaginary part of the scattered field, which show a significant reduction in the amplitude of the scattered field. 95

4.1 Grid for a 4×4 ($N = 4$) cluster of pins (larger black discs) surrounded by $m = 4N = 16$ active sources (smaller grey discs). A plane wave at an angle θ_{inc} to the x_1-axis, $w_{inc}(\mathbf{x})$, is incident upon the array. The spacings between the pins in the x_1 and x_2-directions are denoted by d. The spacings between the sources and the pins in the x_1 and x_2-directions are denoted by S. . . . 101
4.2 Band diagram for square array of rigid pins with $d = 1$, using square Brillouin zone $(k_x, k_y) = [0, \pi] \times [0, \pi]$. The solid lines represent solutions of the dispersion relation (4.12), (4.13), and the dashed lines represent both dispersion curves and segments of the singularity lines (1.51) from chapter 1. 104
4.3 (a) The first three dispersion surfaces shown together with the Dirac-like point highlighted. In (b) we display the first dispersion surface with the β-values of interest. 104

4.4 In all figures here and in what follows, the real part of the amplitude of flexural displacement for the total field is shown, with its range, indicated by the colourbar, determined by the degree of localisation within the system. In addition, the pins are depicted by black discs and the horizontal and vertical axes are the x_1 and x_2-axes, respectively. (a) Plane wave normally incident on an uncloaked 8×8 ($N = 8$) cluster of pins. (b) Plane wave incident at $\theta_{inc} = \pi/4$ on 2000 gratings with $d = 1$ for $\beta = 4.44$, $\kappa_y = 3.1396$ corresponding to M in the reciprocal lattice. (c) Localisation of flexural waves in a stack of 4 gratings with $d = 1$ for a plane wave incident at $\theta_{inc} = \pi/6$ for $\beta = 3.60$. . 105

4.5 Flexural wave scattering by (a) a 4×4 ($N = 4$) and (b) a 5×5 ($N = 5$) cluster of pins, depicted by large black discs. Plane wave is incident at $\theta_{inc} = 0$ with $\beta = 2.0$. Left: scattering with no active sources; middle: cloaking with $m = 4N$ active sources; right: cloaking with $m = 4(N + 1)$ active sources. We note here and in what follows that the active source are illustrated by small black discs surrounding the cluster. 106

4.6 Flexural wave scattering by a (a) 4×4 ($N = 4$) and (b) 5×5 ($N = 5$) cluster of pins with an incident plane wave at an angle of $\theta_{inc} = 0$. From left to right: (left) no active sources, (middle) $m = 4N$ active sources, (right) $m = 4N + 4$ active sources, all for $\beta = \pi$. 108

4.7 Same as in Fig. 4.6 but (a) shows the case of $N = 4$ for $\beta = 3.60$ and (b) shows the case of $N = 5$ for $\beta = 3.565$. 109

4.8 For a 4×4 ($N = 4$) cluster of pins with an incident plane wave at an angle of $\theta_{inc} = 0$: (a) Flexural wave amplitudes for a cloaked cluster with $m = 20$ evenly spaced sources on a circle of radius $a_s = (3\sqrt{2}+2)/2$, (b) absolute value of the coefficient premultiplying the Hankel function in the total field $|w^{(p)}|$ on the circle a_s versus multipole order n, (c) flexural displacement amplitudes for a cloaked cluster with $m = 26$, all for $\beta = 3.60$. 110

4.9 Difference in total wave amplitude and the incident plane wave evaluated on a circle of radius 15 versus the polar angle. 4×4 cluster of pins for $\theta_{inc} = 0$ and $\beta = 3.60$. (a) $m = 20$ (solid curve), $m = 26$ (dashed curve) which is magnified in part (b) to clearly display its order. 110

4.10 4×4 ($N = 4$) cluster of pins with a plane wave incident at $\theta_{inc} = \pi/6$ for $\beta = 3.60$. Flexural wave amplitudes for (a) an uncloaked, (b) a cloaked cluster with $m = 26$, (c) absolute value of the coefficient premultiplying the Hankel function in the total field $|w^{(p)}|$ on the circle, of radius $a_s = (3\sqrt{2}+2)/2$, versus multipole order n, (d) absolute error evaluated on a circle of radius 15 versus the polar angle. 111

4.11 4×4 ($N = 4$) cluster of pins with a plane wave incident at $\theta_{inc} = 0$ for $\beta = 3.90$. Flexural wave amplitudes for (a) an uncloaked , (b) a cloaked cluster with $m = 26$, (c) $|w^{(p)}|$ versus multipole order n for a circle of radius $a_s = (3\sqrt{2}+2)/2$, (d) absolute error evaluated on a circle of radius 15 versus the polar angle. 112
4.12 4×4 ($N = 4$) cluster of pins with a plane wave incident at $\theta_{inc} = \pi/4$ for $\beta = 3.90$. Flexural wave amplitudes for (a) an uncloaked, (b) a cloaked cluster with $m = 26$, (c) absolute error evaluated on a circle of radius 15 versus the polar angle. 113
4.13 4×4 ($N = 4$) cluster of pins with a plane wave incident at $\theta_{inc} = \pi/4$ for $\beta = 4.44$. Flexural wave amplitudes for (a) an uncloaked, (b) a cloaked cluster with $m = 30$, (c) $|w^{(p)}|$ versus multipole order n for a circle of radius $a_s = (3\sqrt{2}+2)/2$, (d) absolute error evaluated on a circle of radius 15 versus the polar angle. 114

B.1 Cloaking results for a 5×5 cluster for comparison with the corresponding Figure 4.8 for the 4×4 cluster. Here, $\theta_{inc} = 0$, $\beta = 3.565$ and in (a) $m = 24$ and in (b) $m = 36$. 137
B.2 Absolute error evaluated on a circle of radius 15 versus the polar angle. 5×5 cluster of pins for $\theta_{inc} = 0$ and $inc = 3.565$. (a) $m = 24$ (solid curve), $m = 36$ (dashed curve) which is magnified in part (b). 138
B.3 Cloaking results for a 5×5 cluster for comparison with the corresponding Figure 4.10 for the 4×4 cluster. Here, $\theta_{inc} = \pi/6$, $\beta = 3.565$ and $m = 36$. . . 138
B.4 Cloaking results for a 5×5 cluster for comparison with the corresponding Figure 4.11 for the 4×4 cluster. Here, $\theta_{inc} = 0$, $\beta = 3.90$ and $m = 38$. 139
B.5 Cloaking results for a 5×5 cluster for comparison with the corresponding Figure 4.12 for the 4×4 cluster. Here, $\theta_{inc} = \pi/4$, $\beta = 3.90$ and $m = 38$. . . . 140
B.6 Cloaking results for a 5×5 cluster for comparison with the corresponding Figure 4.13 for the 4×4 cluster. Here, $\theta_{inc} = \pi/4$, $\beta = 4.44$ and $m = 40$. . . . 141

List of Tables

2.1 $\tilde{E}_n$ and $\tilde{F}_n$ denote the coefficients of $H_n^{(1)}(\beta r)$ and $K_n(\beta r)$ terms, respectively (referring to equations (2.6) and (2.7) for a configuration of two control sources located on the x_1-axis). Shaded entries correspond to the values of $n\,(= 0, \pm 1, \ldots, \pm 4)$ for which we have eliminated the coefficients multiplying $H_n^{(1)}(\beta r)$ terms. 49

3.1 The coefficients $\tilde{E}_n^{(e)}$ of $H_n^{(1)}(\beta_e r)$ terms, for a configuration with zero, four, eight and twelve control sources positioned symmetrically on a circle of radius of 1.57 units from the origin. The frequency of the incident wave is $\omega = 2.62$. 77

3.2 The coefficients $\tilde{E}_n^{(e)}$ of $H_n^{(1)}(\beta_e r)$ terms for a configuration with zero, four, eight and twelve control sources positioned symmetrically on a circle of radius of 1.57 units from the origin. The frequency of the incident plane wave is $\omega = 11.15$. 96

List of Publications

1. J. O'Neill, Ö. Selsil, R.C. McPhedran, A.B. Movchan and N.V. Movchan, Active cloaking of inclusions for flexural waves in thin elastic plates, *Quart. J. Mech. Appl. Math.*, **68** (3), (2015), 263.

2. J. O'Neill, Ö. Selsil, R.C. McPhedran, A.B. Movchan, N.V. Movchan and C. Henderson Moggach, Active cloaking of resonant coated inclusions for waves in membranes and Kirchhoff plates, *Quart. J. Mech. Appl. Math.*, **69** (2), (2016), 115.

3. J. O'Neill, Ö. Selsil, S. G. Haslinger, N.V. Movchan and R. V. Craster, Active cloaking for finite clusters of pins in thin plates, *http://arxiv.org/pdf/1608.08512.pdf*, (2016), (submitted to *SIAM J. Appl. Math.*).

Conference Presentations

(2014)

1. Active cloaking of finite defects for flexural waves in elastic plates, *BAMC, Cardiff.*
2. Active cloaking for flexural waves, *Waves in Acoustics, Elasticity and Structured Media, Imperial College London.*
3. Active cloaking of finite defects for flexural waves in elastic plates, *Metamaterials'2014, DTU, Copenhagen, Denmark.*
4. Active cloaking of inclusions for flexural waves in Kirchhoff plates, (Seminar), *Tel Aviv University, Israel.*

(2015)

1. Active cloaking of elastic coated inclusions in resonant regimes, *Research day on modelling metamaterials and waves in multiscale systems, Liverpool.*
2. Active cloaking of inclusions for membrane and elastic flexural waves in resonant regimes, 8^{th} *international symposium on mechanics of materials and structures, Augustów, Poland.*
3. Active cloaking of clamped voids and coated inclusions in membranes and Kirchhoff plates, (Poster) *ETOPIM10, Israel.*
4. Active cloaking of an inclusion at resonant frequencies for membrane and elastic flexural waves, 8^{th} *Polish congress of mechanics, Gdańsk, Poland.*
5. Resonant regimes and active cloaking of inclusions for membrane and elastic flexural waves, *IMECE, Texas, USA.*
6. Active cloaking of rigid inclusions in Kirchhoff plates, *KOZWaves 2015, Adelaide, Australia.*

Acknowledgement

Throughout the course of my PhD, there have been several key figures who have always been willing to share their knowledge and insight. They have always provided a rich plethora of exciting ideas whilst providing guidance, encouragement and support - especially when I needed it most. For these reasons I would like to thank both my supervisors Dr. Özgür Selsil and Prof. Natalia Movchan. I cannot express the immense gratitude that I feel towards you both; you have given me the confidence and patience to pursue a career in academia, and I appreciate all the time you have spent working with me. I would also like to thank both Prof. Alexander Movchan and Prof. Ross McPhedran; you have always been willing to offer guidance and wisdom making it an absolute pleasure to work with you both. I would like to thank Prof. Richard Craster for his help and advice on the work presented in chapter 4. I would also like to thank Dr. Stewart Haslinger; you have always offered kind words of support throughout my PhD and I am particularly grateful for access to your exemplary thesis!

I would like to acknowledge the support from the EPSRC through the grant EP/L50518/1, without which, my PhD would not have been possible. Thank you to Prof. Natalia Movchan for giving me the rare opportunity to travel to amazing destinations and gain invaluable experience. I have been able to attend a variety of conferences across the globe with the European Commission's Seventh Framework Programme under the contract number PIAPP-GA-284544-PARM-2.

It is important to give special thanks to my examiners: Dr. Daniel Colquitt and Prof. Chris Poulton. I not only appreciate your valuable input, but I am grateful for the time you spent reading the thesis and travelling great distances for my viva.

I would like to thank my Mum and Dad for all your kind words, hugs and cups of tea - you have always been able to motivate and reassure me. I would like to thank my sister Beverley for her sage advice - you have understood and articulated the trials and tribulations of a PhD throughout, and have been a source of great inspiration to me. I would like to thank my sister Katherine for her motivational speeches and endless support - you always know how to make me smile. The dynamic trio that is Pechenzo have always helped me never to lose sight of what is important - and for that I thank you for keeping me grounded. Finally, I would like to thank Chris - I cannot even begin to express the gratitude I have for your limitless patience and caring nature.

Introduction

Studying wave scattering from various objects can provide valuable insight into the physics behind wave propagation in a given structure. More importantly, seeking to control or cancel wave scattering from such structures may be highly desirable. In this thesis we present a method for the active cloaking of flexural waves in Kirchhoff plates, considering wave scattering for a number of different configurations and boundary conditions. There are many engineering and physical problems for which mathematical modelling of thin plates is particularly useful. Applications include construction of large structures or design within the aviation and motor industries. Active cloaking of defects in thin plates can provide a method of protecting systems vulnerable to damage from waves propagating through them.

In this thesis, cloaking is understood to mean that scattered fields are cancelled in such a way that an observer exterior to the system of object and cloak, receives no information about the object's presence. This is a slightly different approach to that of shielding problems, for which a quiet region is created around an object at a specific frequency. The idea being that scattering by the object is reduced because no waves reach it. However, the shield itself may leave a scattering signature exterior to the quiet region surrounding the object, which may be detectable by an outside observer.

We distinguish between two approaches for achieving invisibility, the first being passive cloaking. Passive cloaks surround a scatterer, usually taking the form of a coating specifically designed to redirect waves around the object, reduce scattering from the object within, or cancel incident fields altogether. Passive cloaks are designed in such a way that they are unique to a particular scenario, making them narrowband in nature. Monticone and Alú [65] demonstrated that passive techniques designed to cancel wave scattering in a small frequency window, actually increased scattering globally, making them particularly visible in transient regimes. It was discussed that passive cloaks could fail when subjected to a broadband frequency pulse, which included frequencies outside of the range for which the cloak was designed to work. The broadband frequency pulse could therefore cause the cloaked object to scatter more than the corresponding uncloaked counterpart. The work was done in the context of electromagnetic waves and the authors highlighted that the method was applicable to "acoustic, mechanical and matter waves".

The paper by Chen *et al.* [14] highlighted the bandwidth limitations associated with realising metamaterials encompassing the extreme properties required for passive cloaking.

The cloaking method investigated was an example of mantle cloaking, a passive technique that involved coating an object with a "meta-surface" (in this paper, an array of metallic patches whose periodicity was smaller than the wavelength of the incident field), that was designed to radiate fields in "anti-phase" to the scattering from the uncloaked object. The narrowband nature of such a cloak was discussed, and a new design involving "active elements" was proposed. The authors achieved broadband cloaking of an infinite dielectric cylinder from transverse magnetic waves with a mantle cloak consisting of an array of square metal patches that were loaded with negative impedance converter elements within the gaps. The negative impedance converter elements were based on a cross coupled pair of transistors. Such active elements ensured that the cloak had the required frequency dispersion for minimising the total scattering from the cylinder for wavelengths much larger than the array spacing. The cloak was shown not only to work for broad frequency regimes, but also for short Gaussian pulses in the transient regime.

The introduction of active elements in the work of Chen *et al.* [14], was an example of controlling scattered fields with active devices. The ideas presented in this paper are an example of active cloaking, which is the second approach to achieving invisibility, and the technique we use in this thesis. Active cloaking serves a desirable alternative to passive techniques due to its broadband nature and ability to adapt to changes in incident frequency and type of wave. The approach employs devices which can be tuned to cancel wave scattering for a wide range of problems. This is not the case for passive cloaks, whose design is only effective for a narrow frequency range and specific type of incident wave.

The paper by Miller [61] was aimed at answering the question of whether it was possible to achieve a perfect cloak. Miller [61] proposed a design which measured waves near the surface of a volume to be cloaked and excited active sources positioned along the volume surface. The amplitude of the active sources were tuned to cancel incident fields as well contributions from the sources themselves. As a result, the amplitude of each source depended on all the other sources in the configuration. Miller [61] chose an active approach to avoid the narrow band nature of passive techniques, which are vulnerable to discovery when subjected to a pulse. Causal simulations for the approximate cloaking of a pulse from a spherical volume using 3,264 source pairs were presented. It was discussed however, that near perfect cloaking could be observed if prior information about the incident field were given so that the sources could reconstruct the unperturbed field exterior to the cloak accordingly.

Active techniques have long been established in acoustics since the 1980s, Ffowcs Williams [26] wrote a comprehensive summary of the early work into active acoustic cloaking, and the book by Nelson and Elliot [72] also covered early techniques and ideas in the field of "anti-sound". We note that the field of active cloaking for systems governed by the Helmholtz equation is exhaustive, however, there are very few publications which investigate the problem of active cloaking in thin elastic plates, making it relatively understudied.

The governing equation describing the flexural vibrations of Kirchhoff plates involves

solutions which are either propagating or evanescent. The latter yields interesting features and interactions which have contributed to the vast field of platonics. Chapter 1 of this thesis introduces background theory and some of the mathematical techniques that are used to solve various scattering problems in thin elastic plates. This includes an outline of the main assumptions of Kirchhoff plate theory leading to the governing equation that describes pure bending in thin elastic plates. We also discuss the multipole method, Green's function for the biharmonic operator and the useful Graf's addition theorem.

In chapter 2, we present a method for cloaking a clamped circular scatterer in a Kirchhoff plate. This method was motivated by the work presented by Guevara-Vasquez *et al.* [33]-[37] where a shielding problem for the two-dimensional Laplace and Helmholtz equations was developed. The shield itself consisted of a finite number of active devices, which were represented mathematically by multipole expansions of point sources located exterior to the object. These expansions were found by applying Green's theorem to the Helmholtz equation, and also by utilising addition theorems for the Hankel function. The devices created a quiet region around the object, and cancelled wave scattering in the far field (including any contributions from the devices themselves). It was shown that three active devices were necessary to successfully shield the object from incident fields. Solutions to the variational formulation for the Helmholtz equations were solved numerically and a variational problem was also developed for the quasi-static case. Our active cloaking approach is similar in that we aim to cloak an object with a finite number of active sources. Since we cloak objects in Kirchhoff plates, the system is governed by the biharmonic plate equation and our active sources radiate fields that cancel wave scattering from the object as well as any propagating terms from the sources themselves.

The shielding method employed by Guevara-Vasquez *et al.* [33]-[37], was also employed by Norris *et al.* [82], [83] for describing acoustic systems governed by the Helmholtz equation, where active source amplitudes were represented by infinite multipole expansions. Amplitudes of the sources were found by solving a derived system of linear integral equations numerically. The problem formulated by Norris *et al.* [82], [83], required the devices to cancel fields within a targeted region interior to the configuration of sources whilst simultaneously ensuring fields exterior to the configuration were indistinguishable from the unperturbed, incident field. In order to achieve this, the resulting multipole expansions representing each device were only valid in the region outside a disc surrounding the source. Norris *et al.* [82], [83] commented on the disadvantage that using Graf's addition theorem in this way caused fields to diverge in the circular region within which the active device was located. The shielding problem presented by Norris *et al.* [82], [83] was deemed perfect if the multipole expansions were summed over $(-\infty, \infty)$, but in order to realise the problem, multipole expansions were truncated to an order large enough to ensure accuracy and finite fields within the devices. The authors presented an example of an approximate shield involving active devices represented by dipoles in an attempt to avoid potentially large fields in the region containing the active device.

In our active cloaking method, the active sources are represented by the non-singular Green's function for the biharmonic operator. We formulate a cloaking problem in which the incident field is reconstructed everywhere outside the configuration of sources and scatterer. As discussed earlier in this chapter, the objectives of cloaking and shielding problems differ. In our cloaking method, Graf's addition theorem is used only to find the contributions to the total field propagating away from the scatterer due to the active sources. A system of algebraic equations is then solved to calculate the amplitudes of the sources necessary for effective cloaking. By using Graf's addition theorem in this way, there are no finite-sized regions enclosing our sources, within which fields are divergent.

The method of cloaking we employ is detailed in chapter 2, and is based on the first of our papers [86]. We demonstrate active cloaking of clamped voids and study the canonical case of a circular shaped scatterer. We derive a linear algebraic system of equations which cancel out selected orders of the scattered field and show near-perfect cloaking with as little as six active sources. These sources are located symmetrically on a circle, surrounding the clamped void. We present several illustrative examples showing the improvement in cloaking as the number of sources is increased and more orders of the scattered field are successfully eliminated. In section 2.5 of chapter 2 we demonstrate that by employing our approach, it is possible to cloak any incident wave given its Fourier expansion. We present efficient cloaking for an incident point source, which exemplifies the generic nature of our cloaking method. Finally, section 2.6 describes how the cloaking scheme can be applied to cloak an arbitrarily shaped scatterer with a smooth, clamped boundary. In an illustrative example, we successfully reconstruct the incident field around an arbitrarily shaped scatterer using seven active sources.

In chapter 3, we focus our attention on cloaking inclusions in a Kirchhoff plate. The material parameters of the inclusion are chosen to be in high contrast with those of the exterior medium. A high contrast in material parameters can often induce interesting scattering properties, namely resonances within the inclusion. At resonant regimes, the scattering properties of the inclusion vary significantly in a small frequency range. The active cloaking method described in chapter 2 may prove challenging at resonant regimes, as the active source amplitudes must adapt to the sudden changes in the scattered field. We instead combine passive and active techniques, proposing a cloak comprised of a coating surrounding the inclusion as well as active sources located exterior to the coated inclusion. The coating is designed to work at frequencies outside the quasi-static regime, and is aimed at "taming" regions of rapid change associated with resonant regimes, instead of annulling leading order contributions to the scattered field. The active sources are then employed to cancel out selected orders of the scattered wave, but since we are cloaking at higher frequencies, more sources are necessary. We present a useful check that enables us to see the number of sources required for effective cloaking. We also derive the leading order behaviour of the scattered field for the general case of an inclusion in a thin elastic plate. In chapter 3, we study

flexural waves in membranes which are governed by the Helmholtz equation. By considering membranes, we see the role of the evanescent terms in the biharmonic pate equation. In section 3.2.1 of chapter 3, we discuss under what circumstances solutions to the biharmonic problem can be approximated by flexural waves in membranes.

Many passive techniques involve introducing a coating around the object specifically designed to ensure invisibility. There exists a vast catalogue of work using coordinate transformations as the cloaking mechanism for passive approaches. Often, the coating in transformational cloaking has specific material properties which guide waves around the object. In order to achieve a transformed space with the desired properties, transformational cloaking relies on the fact that the form of the governing equations remains invariant under coordinate transformations. In 1961, Dolin [21] published a paper which demonstrated that Maxwell's equations were form-invariant under a transformation of the space metric and the medium permeability and permittivity. In 1975, Kerker [44] published a paper which showed that for particular combinations of dielectric constant, scattering was zero from compound ellipsoids comprised of an inner ellipsoid surrounded by a confocal ellipsoidal shell.

In 2006, the important paper presented by Milton and Nicorovici [63], used anomalous resonance to cloak a coated cylinder from an infinite line of polarisable dipoles. The material properties of the cylinder were chosen in such a way that in the quasistatic regime, resonance was induced in the cylinder when subjected to a remote polarisable line or point dipole. The field produced by the resonance cancelled out the incident field cloaking the cylinder as a result. This paper built on previous ideas introduced in the early 1990s by Nicorovici *et al.* [78], [79]. The work in [63], was later extended to discrete systems of hollow shells by Nicorovici *et al.* [81]. A related form of passive cloaking was described in the work of Chen *et al.* [47]. The paper combined ideas behind complementary media and transformation optics to develop an electromagnetic cloak for objects exterior to the cloak itself. Cloaking in this way requires full information about the object to be cloaked as an "anti-image" of the external object was imbedded into the coating, cancelling detectable scattering effects.

In 2006, the work of Dolin [21] together with ideas published by Greenleaf *et al.* [31], were combined in the work of Leonhardt [49] for geometrical optics, and Pendry *et al.* [88] for electromagnetism. Examples of publications employing transformational cloaking later followed in the context of surface plasmons by Kadic *et al.* [42] and surface waves by Farhat *et al.* [24]. Milton *et al.* [62] provided a comprehensive summary of the work into optics and acoustics for transformational cloaking, however, the main aim of [62], was to determine under what conditions was it possible to achieve a transformation in elasticity that was invariant. The paper provided several examples of physical equations which have the desired form. Later, Brun *et al.* [10] used the ideas presented in [62] to provide a coordinate transformation that was invariant for the case of in-plane coupled shear and pressure waves.

Much of the early literature on passive techniques involves problems which are governed by the full Maxwell equations or the Helmholtz equation. However, in 2014, Farhat *et al.*

[23] published a paper which achieved leading order scattering reduction in the quasi-static limit of flexural waves in thin plates. This was done for a particular case when the cylinder, coating and ambient matrix had the same flexural rigidities, Young's moduli and Poisson's ratios. Under these strict assumptions, the plates problem was described using the Helmholtz equation and the subsequent analysis used the classical result of mass compensation by Voigt [102]. The work presented by Farhat *et al.* [23] was only applicable in the quasi-static regime, and we show in chapter 1 (and later in chapter 3) that scattering is low in this regime. in chapter 3, we therefore present an approach involving a combination of passive and active techniques, which is applicable to higher frequency regimes where scattering is significant.

We note that the work of Farhat *et al.* [23] has some similarities to the ideas published in 2005 by Alú and Engheta [2]. It was demonstrated in [2], that the scattering cross section of a cylinder (or sphere), could be reduced by a metamaterial coating with a specific permittivity and/or permeability. The coating was designed to work at frequencies near the metamaterial's plasmonic resonance. "Transparency" was achieved for a dielectric sphere in the quasi-static regime, by eliminating the leading order dipolar term of the scattered field through a particular choice of material parameters. Eliminating only the leading order behaviour meant that an observer exterior to the sphere received a signal of an incident field that appeared to "pass through the sphere", but was noticeably distorted by the object's presence.

For the cloaking method presented in this thesis, we select the number of terms to eliminate from the scattered field, which enables us to cancel higher order contributions and achieve effective cloaking to a desired accuracy. The work we present is a novel approach to the active cloaking of flexural waves from finite defects in thin elastic plates, and serves a comprehensive summary of our recent publications by O'Neill *et al.* [86], [87] and [85]. We apply an active source approach to the case of a thin elastic plate, and formulate a method for cloaking (that is, a reduction in scattering) as opposed to shielding - the active sources reconstruct the incident field in a region exterior to the cloaking configuration, however, a quiet region is not created around the object. Our active sources are represented by the Green's function for the biharmonic operator and the method we present does not introduce finite regions around the active sources within which fields are divergent.

In chapter 4, we answer the question of whether it is possible to cloak objects with a discrete structure. Problems involving discrete structures in Kirchhoff plates, are more involved than single continuous defects, and we adapt the method of cloaking described in chapter 2, to the case of a finite cluster of pins. Effective cloaking is demonstrated for frequencies at which interesting scattering patterns occur due to evanescent waves interacting within the microstructure of the cluster. This creates a different shadow region to the case of a single scatterer making it a worthwhile problem to investigate.

Over the decades, there has been great interest in problems that model flexural vibrations in thin elastic plates perforated with a periodic array of scatterers. The simplest type of scat-

terer is a rigid pin. Mace [52] was one of the first to study wave propagation in infinite doubly periodic structures for plates. The paper [52], provided an in depth study into calculating the response of a plate laid on a doubly periodic array of point supports, invoking translational and rotational constraints, which was done using Fourier transform methods.

Mead [59] provided an extensive overview of early contributions to the field of wave propagation in periodic structures from the University of Southampton. The paper included a review of the method of "space-harmonics", which was used to describe the effect on the forced harmonic response of sound waves travelling along the surface of periodic structures subject to fluid damping. The method involved writing a space harmonic series modelling such surface waves. The author derived a series for a harmonic pressure field propagating through a periodic beam, and summarised work published for two-dimensional plates requiring Fourier transform methods.

Recently, Antonakakis *et al.* in the papers [3]-[6] published several papers on high frequency homogenisation theory to describe wave propagation in discrete structures for the fourth-order plate equation, but examples considered also included wave propagation in transverse magnetic electromagnetism, anti-plane shear waves in an isotropic elastic material with a periodic array of inclusions, and transverse electric polarisation in a medium containing either a periodic array of split ring resonators or perfectly conducting cylindrical holes. The method of high frequency homogenisation described in [3]-[6], used a two-scale asymptotic approach with Fourier transform techniques to derive an effective medium equation whose coefficients could be used to capture the anisotropy of the system in the long-scale around a given frequency. A key result was that high frequency homogenisation was shown to predict the frequencies at which interesting features such as stop-bands and Dirac-like cones occurred. The authors discuss that scattering reduction could be achieved at frequencies corresponding to Dirac-like points, which has applications in passive cloaking techniques.

McPhedran *et al.* [57], found that for finite clusters of pins, unidirectionally localised vibration modes could occur in the vicinity of Dirac cones. It was demonstrated by McPhedran *et al.* [57], that the direction of propagation was related to the dispersion surface being locally parabolic in the vicinity of the Dirac cone. Interesting scattering patterns related to dynamic neutrality were generated in [57], which we touch upon in chapter 4.

The structure of the thesis is as follows. In chapter 1, we summarise an approach applying multipole methods for modelling flexural waves in a Kirchhoff plate perforated by a square array of holes, which was developed by Movchan *et al.* in the papers [67], [57] and [71]. The authors obtained a dispersion relation for the analytical solution of the spectral problem formulated for the biharmonic operator. It was highlighted that solutions to the biharmonic equation were the superposition of solutions to the Helmholtz and modified Helmholtz equations. In the plate exterior to the circular holes, two types of wave solution were found to propagate independently and were either oscillatory or exponential, depending on whether they solved the Helmholtz or modified Helmholtz equation, respectively. Rayleigh identities

(the consistency relations for the system) were substituted into the appropriate boundary conditions and a matrix equation was written for the unknown complex coefficients introduced via the series solution to the biharmonic equation. The dispersion relation was derived by finding zeroes of the determinant of the matrix premultiplying the unknown coefficients. For a given Bloch vector (namely, the edges of the irreducible Brillouin zone) and specified number of solutions for the spectral parameter, solutions to the dispersion relation were found numerically.

The method of solution discussed in by Movchan *et al.* [67] was shown to converge rapidly requiring only a small number of terms in the Rayleigh identities. For the limiting case of clamped holes with zero radius, truncated Rayleigh identities were used to obtain a band diagram for a Kirchhoff plate containing a square array of pins. It was also shown that the free-edge case of zero-radius holes produced wave propagation comparable to a homogeneous plate.

We use the results from the paper by Movchan *et al.* [67] to reproduce the band diagram for an infinite doubly-periodic array of pins that relates Bloch vector to frequency. Band diagrams are used to predict effects such as waveguiding, lensing, focusing, shielding and scattering reduction in periodic arrays or finite discrete structures. For an infinite array of circular holes, the key features of the band diagram were discussed by Movchan *et al.* [67], but the paper by McPhedran *et al.* [56] discussed in more detail the properties of a doubly-periodic array of pins subject to flexural waves in Kirchhoff plates. It was shown that this geometry led to a non-trivial band diagram, with a complete band gap and whose key properties could be calculated analytically. For example, the boundaries of stop bands, locations of saddle points and of dynamic neutrality were discussed in [56] for the first three pass bands of the system. McPhedran *et al.* [56] also defined dynamic neutrality as the resulting response when group and phase velocities of the system are equivalent to those of an unperforated elastic plate, for a particular frequency and direction of wave propagation. A "stop-band" Green's function was also derived, which satisfied Dirichlet conditions at the boundaries of the circular holes for the limiting case of zero-radius. The relationship between infinite arrays and finite clusters was discussed in [56] when finding frequencies causing strong localisation, as well as locating resonant defect modes.

An example of cloaking of a discrete structure (such as a finite cluster of pins in a Kirchhoff plate), is presented in chapter 4. We show that cloaking is possible over a broad range of frequencies in platonics. In particular, we make use of previous results by selecting several key frequencies from band diagrams and dispersion surfaces for which waves interact within the cluster to produce distinct scattering patterns. We estimate the frequencies for which the distinct scattering patterns arise in the finite cluster by using information from the infinite structure.

Chapter 1

Multipole method and fundamental solution for Kirchhoff plates

In this chapter, we outline the mathematical techniques implemented in our method for active cloaking of finite defects in thin elastic plates. Throughout this thesis, the governing equation is the fourth-order biharmonic equation. In 1850, Kirchhoff [45] published the classical work that described the dynamics of thin elastic plates. A derivation of the plate theory can also be found in the books by Graff [30] and Timoshenko and Woinowsky-Krieger [100].

Kirchhoff plate theory is considered to be the two-dimensional extension of Bernoulli-Euler theory for beams, and the kinematics for either theory are analogous to each other. Several assumptions are made when formulating the problem describing pure bending in thin elastic plates subject to a laterally applied load, which read as follows:

1. The thickness of the plate remains unchanged for pure bending.

2. During bending, straight lines initially perpendicular to the mid-plane remain both straight and perpendicular to the mid-plane.

Deflections in the plate are assumed to be small and in the transverse direction. As a result, the transverse out-of-plane displacement $W(x_1, x_2, t)$, can be written as an expression of time and two, rather than three, spatial variables (the transverse direction being parallel to x_3-axis). The theory's applicability is restricted to lower frequency regimes to ensure that rotary inertial effects can be neglected. The above assumptions simplify the equations of motion making it possible to obtain the biharmonic equation by considering moments and forces acting on a differential element in the plate. The governing equation describing the out-of-plane displacement $W(\mathbf{x}; t)$, is as follows

$$\Delta^2 W(\mathbf{x}; t) + \frac{\rho h}{D} \ddot{W}(\mathbf{x}; t) = 0, \quad \mathbf{x} = (x_1, x_2) \in \mathbb{R}^2, \tag{1.1}$$

where dot on the variable denotes the derivative with respect to time t, ρ is the mass density, Δ^2 is the biharmonic operator, $D = Eh^3/12(1-\nu)$, represents the flexural rigidity of the plate, E is the Young's modulus, and ν is the Poisson's ratio.

Assuming time-harmonic wave propagation, that is, $W(\mathbf{x};t) = w(\mathbf{x})\exp(\mathrm{i}\omega\mathrm{t})$, the governing equation (1.1) can be reduced to

$$\left(\Delta^2 - \frac{\rho h\omega^2}{D}\right) w(\mathbf{x}) = (\Delta + \beta^2)(\Delta - \beta^2)w(\mathbf{x}) = 0, \quad \mathbf{x} \in \mathbb{R}^2. \tag{1.2}$$

Here, $\beta^2 = \omega\sqrt{\rho h/D}$ is the spectral parameter, with ω denoting frequency of vibrations within the plate. Equation (1.2) is the product of the Helmholtz and modified Helmholtz equations. The solution to this equation therefore takes the following form

$$w(\mathbf{x}) = w_H(\mathbf{x}) + w_M(\mathbf{x}), \tag{1.3}$$

where

$$(\Delta + \beta^2)w_H(\mathbf{x}) = 0, \qquad (\Delta - \beta^2)w_M(\mathbf{x}) = 0. \tag{1.4}$$

Hence, $w_H(\mathbf{x})$ and $w_M(\mathbf{x})$, denote solutions to the Helmholtz and modified Helmholtz equations, respectively. Solutions represented by the those of the Helmholtz equation can be either propagating or evanescent, whilst those of the modified Helmholtz equation only represent evanescent waves. The Helmholtz and modified Helmholtz solutions to equation (1.2) propagate independently, but are coupled by the boundary conditions.

Alternative plate theories do exist for describing wave propagation in plates, for example, Mindlin plate theory takes into account the effects due to transverse shear and rotary inertia. Here, we restrict ourselves to Kirchhoff plate theory since it provides an accurate model for thin plates at lower frequency regimes, and the Green's function for the biharmonic operator is non-singular at the origin.

Both Kirchhoff and Mindlin theory were discussed in the paper by Movchan *et al.* [70], and it was found that each model predicted different behaviours for low frequency wave propagation in a periodic array of circular clamped holes. The difference in the models was accredited to the different Green's functions for each theory. In Kirchhoff plate theory, the Green's function is non-singular, which is not the case in Mindlin theory.

In what follows, we consider flexural wave scattering in a Kirchhoff plate, from a circular defect of radius a_i. The circular geometry of the problem means that a general solution can be written analytically using the multipole method generalised for the fourth-order equation. We consider the types of boundary conditions that are imposed on the defect throughout this thesis. First, we derive the scattering matrix for a circular clamped cavity, and highlight the difference in scattering properties compared to a free-edge cavity of identical size. We then consider wave scattering from an inclusion subject to conditions of perfect bonding, and compare results of scattering between the cavity and inclusion. We state Green's function for the biharmonic operator and highlight that the function is non-singular at the origin. We make use of this fact in our cloaking method when choosing a representation for the active sources. We also state Graf's addition theorem, which is used to re-expand multipole representations centred at a location different to the origin. Finally, we discuss Bloch-Floquet

waves in discrete structured media, detailing how to obtain band diagrams and dispersion curves which are used in chapter 4 of the thesis.

1.1 Scattering of flexural waves by a circular clamped edge cavity

In this section, we consider flexural wave scattering from a circular clamped cavity of radius a_i, subject to a time-harmonic wave denoted by $W(\mathbf{x};t) = w(\mathbf{x})\exp(\mathrm{i}\omega\mathrm{t})$. A schematic view of the configuration is presented in Fig. 1.1, for the cases when the incident field is a plane wave and a remote point source.

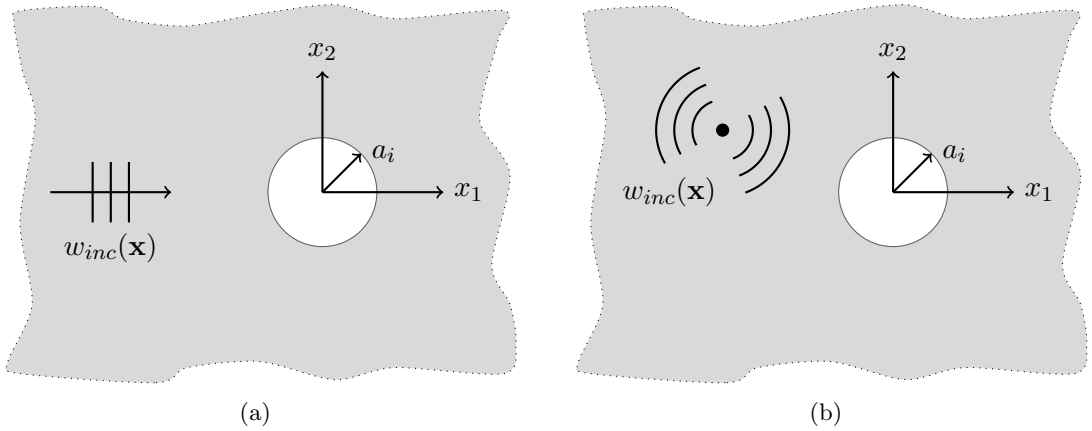

(a) (b)

Figure 1.1: Schematic view of a clamped edge cavity of radius a_i embedded in a Kirchhoff plate subject to an incident field denoted by $w_{inc}(\mathbf{x})$. In part (a) $w_{inc}(\mathbf{x})$ is an incident plane wave such that $\theta_{inc} = 0$, and in part (b) $w_{inc}(\mathbf{x})$ is a remote point source.

Everywhere outside the scatterer, the out-of-plane displacement for a time-harmonic wave satisfies the following equation

$$\left(\Delta^2 - \frac{\rho h\omega^2}{D}\right) w(\mathbf{x}) = (\Delta + \beta^2)(\Delta - \beta^2)w(\mathbf{x}) = 0, \quad \mathbf{x} \in \mathbb{R}^2 \setminus \bar{\mathcal{D}}, \tag{1.5}$$

where $\mathcal{D}$ denotes the region occupied by the circular clamped cavity of radius a_i. Due to the circular geometry of the problem, we use the multipole method to write an analytical solution of equation (1.5). We begin by assuming that solutions to (1.5) can be expressed as a product of two functions that depend on r and θ separately. As previously discussed, the solution to equation (1.5) is the superposition of solutions to the Helmholtz equation ($w_H(r,\theta)$) and modified Helmholtz equation ($w_M(r,\theta)$), which satisfy the respective equations in (1.4). We obtain Bessel's equation and modified Bessel's equation by considering the equations of (1.4) individually. Solutions to Bessel's equation and modified Bessel's equation are written as a combination of the Bessel functions $J_n(\beta r)$ and $H_n^{(1)}(\beta r)$ (relating to $w_H(r,\theta)$) and modified Bessel functions $K_n(\beta r)$ and $I_n(\beta r)$ (relating to $w_M(r,\theta)$), respectively.

According to equation (1.3), the general solution of equation (1.5) can therefore be expressed in polar coordinates as the following multipole expansion

$$w(r,\theta) = \sum_{n=-\infty}^{\infty} \left[A_n J_n(\beta r) + E_n H_n^{(1)}(\beta r) + B_n I_n(\beta r) + F_n K_n(\beta r)\right] e^{in\theta}, \tag{1.6}$$

where A_n and B_n denote the incoming wave coefficients, and E_n and F_n denote the outgoing wave coefficients.

In this thesis, we employ a technique involving multipoles that was first introduced in 1892, in the classical paper by Rayleigh [91]. However, much of the early theory involving doubly periodic arrays of scatterers was developed in several works, notably McPhedran and Dawes [54], Nicorovici and McPhedran [73], Nicorovici *et al.* [80], [77], [74], [75], McPhedran and Movchan [55] and Movchan *et al.* [69]. The work in these papers was summarised in the book by McPhedran *et al.* [58], and the method of multipoles was later generalised to case of plates by Movhcan *et al.* [67], [71], McPhedran *et al.* [56], and Poulton *et al.* [89]. Related publications using the multipole method for plates include Smith *et al.* [98], [96]. We also highlight notable contributions employing multipole methods in optics by Chen *et al.* [15] and Kan *et al.* [43].

Multipole expansions are series representations of fields produced by a given system, and are constructed in such a way that terms in the expansion decrease exponentially as multipole order becomes significantly large. The convergence of multipole expansions means that often a small number of terms can accurately describe the fields in the system. The method of Rayleigh [91] enables a system involving multiple scatterers or sources to be expressed explicitly. This is achieved by re-writing multipole expansions centred at a particular location in coordinate space, in terms of a different position in the coordinate space.

1.1.1 Obtaining the scattering matrix

In what follows, we outline how to obtain the scattering matrix for a circular scatterer with a clamped boundary. The scattering matrix enables one to find the outgoing wave coefficients from those of the incoming wave, and represents how the solutions to the Helmholtz and modified Helmholtz equations are coupled via the boundary conditions.

In a system involving clamped boundary conditions, the function $w(\mathbf{x})$, and its normal derivative are set to zero. The conditions take the following form,

$$w(\mathbf{x}) = \frac{\partial w(\mathbf{x})}{\partial n} = 0, \quad \mathbf{x} \in \partial\mathcal{D}, \tag{1.7}$$

where $\partial\mathcal{D}$ is the boundary of the inclusion, and $\mathbf{n}$ is the unit outward normal on $\partial\mathcal{D}$. After substituting equation (1.6) into the conditions (1.7), we obtain the following equation

$$\begin{pmatrix} H_n^{(1)}(\beta a_i) & K_n(\beta a_i) \\ H_n^{(1)'}(\beta a_i) & K_n'(\beta a_i) \end{pmatrix} \begin{pmatrix} E_n \\ F_n \end{pmatrix} = - \begin{pmatrix} J_n(\beta a_i) & I_n(\beta a_i) \\ J_n'(\beta a_i) & I_n'(\beta a_i) \end{pmatrix} \begin{pmatrix} A_n \\ B_n \end{pmatrix}, \tag{1.8}$$

which relates outgoing wave coefficients in terms of incident wave coefficients. The solution of equation (1.8) may be written in terms of Wronskians, which we denote by $\mathcal{W}[\mathcal{U}_1(\beta a_i),\mathcal{U}_2(\beta a_i)]$, where $\mathcal{U}_1(\beta a_i)$ and $\mathcal{U}_2(\beta a_i)$ are either $J_n(\beta a_i)$, $H_n^{(1)}(\beta a_i)$, $K_n(\beta a_i)$ or $I_n(\beta a_i)$. The Wronskians are written as follows

$$\begin{aligned}
\mathcal{W}[H_n^{(1)}(\beta a_i), K_n(\beta a_i)] &= H_n^{(1)}(\beta a_i)K_n'(\beta a_i) - H_n^{(1)'}(\beta a_i)K_n(\beta a_i),\\
\mathcal{W}[K_n(\beta a_i), J_n(\beta a_i)] &= K_n(\beta a_i)J_n'(\beta a_i) - K_n'(\beta a_i)J_n(\beta a_i),\\
\mathcal{W}[K_n(\beta a_i), I_n(\beta a_i)] &= K_n(\beta a_i)I_n'(\beta a_i) - K_n'(\beta a_i)I_n(\beta a_i) = \frac{1}{\beta a_i},\\
\mathcal{W}[J_n(\beta a_i), H_n^{(1)}(\beta a_i)] &= J_n(\beta a_i)H_n^{(1)'}(\beta a_i) - J_n'(\beta a_i)H_n^{(1)}(\beta a_i) = \frac{2i}{\pi\beta a_i},\\
\mathcal{W}[I_n(\beta a_i), H_n^{(1)}(\beta a_i)] &= I_n(\beta a_i)H_n^{(1)'}(\beta a_i) - I_n'(\beta a_i)H_n^{(1)}(\beta a_i).
\end{aligned}$$

The Wronksians $\mathcal{W}[K_n(\beta a_i), I_n(\beta a_i)]$ and $\mathcal{W}[J_n(\beta a_i), H_n^{(1)}(\beta a_i)]$ can be found using the respective formulae (9.6.15) and (9.1.16) in Chapter 9 of [1].

Rearranging equation (1.8), enables us to write the outgoing wave coefficients in terms of the incident wave coefficients in the following equation

$$\begin{pmatrix} E_n \\ F_n \end{pmatrix} = \frac{1}{\mathcal{W}[H_n^{(1)}(\beta a_i), K_n(\beta a_i)]}\times \\ \times \begin{pmatrix} \mathcal{W}[K_n(\beta a_i), J_n(\beta a_i)] & 1/(\beta a_i) \\ 2i/(\pi\beta a_i) & \mathcal{W}[I_n(\beta a_i), H_n^{(1)}(\beta a_i)] \end{pmatrix} \begin{pmatrix} A_n \\ B_n \end{pmatrix}. \tag{1.9}$$

We denote by $\mathcal{S}^{(n)}$, the entries of the n-th order scattering matrix premultiplying $(A_n, B_n)^\top$ in (1.9). Note that for any $n \neq 0$, the scattering matrix elements obey the following symmetry relations:

$$\begin{aligned}
\mathcal{S}_{-n}^{11}(\beta a_i) = \mathcal{S}_n^{11}(\beta a_i), \qquad \mathcal{S}_{-n}^{12}(\beta a_i) = (-1)^n\mathcal{S}_n^{12}(\beta a_i),\\
\mathcal{S}_{-n}^{21}(\beta a_i) = (-1)^n\mathcal{S}_n^{21}(\beta a_i), \qquad \mathcal{S}_{-n}^{22}(\beta a_i) = \mathcal{S}_n^{22}(\beta a_i).
\end{aligned} \tag{1.10}$$

1.1.2 Multipole representation of the scattered field

The theory of wave scattering from circular boundaries is well established in the literature, for example, the book by Leissa [48] provides a comprehensive study of free vibrations of plates for a number of different configurations with regard to frequency and geometry. The work of Konenkov [46] and Norris and Vermula [84] present results of wave scattering from a circular-shaped inhomogeneity in a Kirchhoff plate. Both papers study the case of a clamped and free boundary at the defect's edge. In this section, we write the field scattered by a circular clamped inclusion.

We consider flexural plane waves travelling at an angle θ_{inc} to the x_1-axis and interacting with a clamped circular inclusion whose centre coincides with the origin as in Fig. 1.1(a). The incident field takes the form

$$w_{inc}(x_1, x_2) = \exp\{i\beta(x_1\cos\theta_{inc} + x_2\sin\theta_{inc})\}, \tag{1.11}$$

and can also be written in polar form using the Jacobi-Anger expansion, that is,

$$w_{inc}(r,\theta) = \exp\{i\beta r\cos(\theta-\theta_{inc})\} = \sum_{n=-\infty}^{\infty} i^n J_n(\beta r)e^{in(\theta-\theta_{inc})}, \tag{1.12}$$

From equation (1.12), we can deduce that $A_n = i^n$ and $B_n = 0$ for the incoming wave coefficients. Once A_n and B_n are known, they can be substituted into equation (1.9) to obtain the outgoing wave coefficients E_n and F_n. We write a general expression for the scattered field, recalling that terms $E_nH_n^{(1)}(\beta r)$ and $F_nK_n(\beta r)$ denote the n-th multipole order of the scattered wave. Using the symmetry relations (1.10), the general expression for the scattered field is

$$\begin{aligned} w_{sc}(r,\theta) &= \mathcal{S}_0^{11}(\beta a_i)H_0^{(1)}(\beta r) + \mathcal{S}_0^{21}(\beta a_i)K_0(\beta r) \\ &\quad + \sum_{n=1}^{\infty}[\mathcal{S}_n^{11}(\beta a_i)H_n^{(1)}(\beta r) + \mathcal{S}_n^{21}(\beta a_i)K_n(\beta r)]i^n e^{in(\theta-\theta_{inc})} \\ &\quad + \sum_{n=1}^{\infty}[\mathcal{S}_n^{11}(\beta a_i)(-1)^n H_n^{(1)}(\beta r) + (-1)^n\mathcal{S}_n^{21}(\beta a_i)K_n(\beta r)](-i)^n e^{-in(\theta-\theta_{inc})}, \end{aligned}$$

which may be reduced to the more concise representation

$$\begin{aligned} w_{sc}(r,\theta) &= \mathcal{S}_0^{11}(\beta a_i)H_0^{(1)}(\beta r) + \mathcal{S}_0^{21}(\beta a_i)K_0(\beta r) \\ &\quad + \sum_{n=1}^{\infty} 2i^n[\mathcal{S}_n^{11}(\beta a_i)H_n^{(1)}(\beta r) + \mathcal{S}_n^{21}(\beta a_i)K_n(\beta r)]\cos\left(n(\theta-\theta_{inc})\right). \end{aligned} \tag{1.13}$$

Writing only the monopole and dipole terms of the scattered flexural wave, we obtain the following

$$\begin{aligned} w_{sc}(r,\theta) &\approx \mathcal{S}_0^{11}(\beta a_i)H_0^{(1)}(\beta r) + \mathcal{S}_0^{21}(\beta a_i)K_0(\beta r) \\ &\quad + 2i\cos(\theta-\theta_{inc})\left[\mathcal{S}_1^{11}(\beta a_i)H_1^{(1)}(\beta r) + \mathcal{S}_1^{21}(\beta a_i)K_1(\beta r)\right]. \end{aligned} \tag{1.14}$$

We find the small argument expansions, that is $\beta a_i \ll 1$, for the entries of the scattering matrix in equation (1.9), and reduce equation (1.14) to the following representation

$$w_{sc}(r,\theta) \approx i\left[iH_0^{(1)}(\beta r) - \frac{2}{\pi}K_0(\beta r)\right] - \frac{2\pi\cos(\theta-\theta_{inc})}{4i\gamma + \pi + 4i\log(\beta a_i/2)}\left[iH_1^{(1)}(\beta r) - \frac{2}{\pi}K_1(\beta r)\right],$$

where $\beta a_i < \beta r$. The first group of terms in square brackets of the above correspond to the normalised Green's function for the biharmonic operator, and the second group is the dipole contribution. This tells us that the scattered wave has leading order behaviour analogous to a point source in the far field.

1.1.3 Illustrative examples of scattering from a clamped cavity

We plot the total flexural amplitude everywhere outside the cavity, to see the effect on scattering by a clamped boundary at $r = a_i$. Throughout this thesis, we will assume that

the plane wave is incident along the x_1-axis (hence $\theta_{inc} = 0$). This is easy to impose since the circular boundary of the scatterer means that the configuration can always be rotated to ensure that $\theta_{inc} = 0$. In Figs. 1.2, we see that the clamped circular boundary produces a strong scattered field that contributes significantly to the total field everywhere outside the scatterer for both an incident plane wave (Fig. 1.2(a)), and a remote point source (Fig. 1.2(b)). In both plots of Fig. 1.2, we see large shadow regions which are the biggest indicator of the defect's presence.

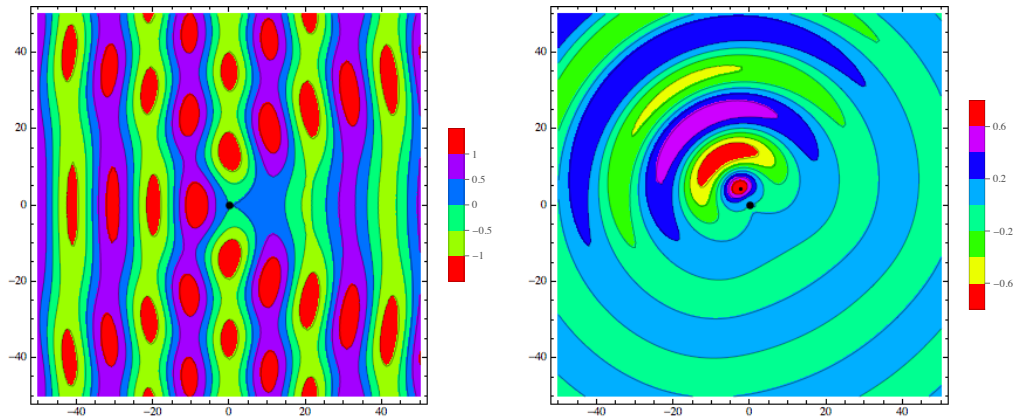

(a) (b)

Figure 1.2: In both figures $\beta = 0.3$, $a_i = 1.0$, $N = 2$. In either plot, there are no control sources and the large black disk depicts the position of the clamped cavity. Part (a) shows the flexural wave amplitude outside a clamped circular inclusion subject to an incident plane wave, and part (b) shows the flexural wave amplitude oustide a clamped circular inclusion subject to a remote point force depicted by the small black disk, which is located at a distance of 2.5 units from the origin, at an angle of $2\pi/3$ radians to the x_1-axis.

1.1.4 Free edge boundary conditions

In this section we compare wave scattering from a circular free-edge cavity of radius a_i, to that from the clamped cavity studied above. The geometry of this problem is as in Fig. 1.1 however, the boundary of the cavity is now free, meaning bending and twisting moments as well as the vertical shearing force are zero. Kirchhoff [45] showed that the conditions for the vertical shearing force and twisting moment could be replaced by a single condition ensuring that the transverse force is equal to zero. The resulting equations for free-edge boundary conditions on a circular cavity of radius a_i read as follows

$$-D\left\{\frac{\partial^2 w(r,\theta)}{\partial r^2}+\nu\left(\frac{1}{r}\frac{\partial w(r,\theta)}{\partial r}+\frac{1}{r^2}\frac{\partial^2 w(r,\theta)}{\partial \theta^2}\right)\right\}\Bigg|_{r=a_i}=0, \tag{1.15}$$

for the bending moment in the vertical direction, and

$$-D\frac{\partial}{\partial r}\left\{\frac{\partial w(r,\theta)}{\partial r^2}+\frac{1}{r}\frac{\partial w(r,\theta)}{\partial r}+\frac{1}{r^2}\frac{\partial^2 w(r,\theta)}{\partial \theta^2}\right\}\Bigg|_{r=a_i} - \frac{D(1-\nu)}{r}\frac{\partial}{\partial\theta}\left\{\frac{1}{r}\frac{\partial^2 w(r,\theta)}{\partial r\partial\theta}-\frac{1}{r^2}\frac{\partial w(r,\theta)}{\partial\theta}\right\}\Bigg|_{r=a_i}=0, \tag{1.16}$$

for the transverse force.

It is possible to obtain a scattering matrix that enables us to write the outgoing wave coefficients in terms of the incident wave coefficients for the solution given in equation (1.6). This is done by following a method analogous to section 1.1.1, that is, we substitute the multipole expansion of $w(r,\theta)$ into the boundary conditions (1.15), (1.16), which will lead to the following matrix equation

$$\begin{pmatrix} E_n \\ F_n \end{pmatrix} = \mathcal{S}_n \begin{pmatrix} A_n \\ B_n \end{pmatrix},$$

where the matrix $\mathcal{S}_n$ encapsulates free-edge boundary conditions on a circular cavity. The scattered field is therefore written

$$w_{sc}(r,\theta) = \mathcal{S}_0^{11}H_0^{(1)}(\beta r)+\mathcal{S}_0^{21}K_0(\beta r)+\sum_{n=1}^{\infty}2i^n[\mathcal{S}_n^{11}H_n^{(1)}(\beta r)+\mathcal{S}_n^{21}K_n(\beta r)]\cos(n\theta),$$

where $\mathcal{S}_n^{ij}$, $i,j=1,2$, denote the entries of the scattering matrix appearing in the previous equation. We also note that the direction of the incident field coincides with the x_1-axis, meaning $\theta_{inc}=0$. The entries of this matrix are more involved than the clamped boundary case and since we do not cloak free-edge boundaries in this thesis the resulting matrix is not presented here.

In Fig. 1.3, we present the total flexural wave amplitude outside a circular free-edge cavity. We see that when $\beta=0.3$, there is little perturbation to the incident field from the cavity for both an incident plane wave (Fig. 1.3(a)), and a remote point source (1.3(b)). We consider scattering of a plane wave from the cavity for the spectral parameters $\beta=0.5$ (Fig. 1.3(c)) and $\beta=0.7$ (Fig. 1.3(d)); it is clear from Fig. 1.3(c) and (d) that even when the wavelength is comparable to the size of the cavity, there is little effect on wave scattering.

The lack of a prominent shadow region in any of the amplitude plots of Fig. 1.3, is because the monopole coefficient of the propagating outgoing wave (pre-multiplying $H_0^{(1)}$) is small. This term of the outgoing wave forms part of the scattering cross-section, and its coefficient is small as derivatives of the solution $w(r,\theta)$ are introduced to the scattered field from the free-edge boundary conditions. Therefore, we do not wish to cloak a free-edge cavity since scattered fields from the defect are small compared to the corresponding clamped cavity case.

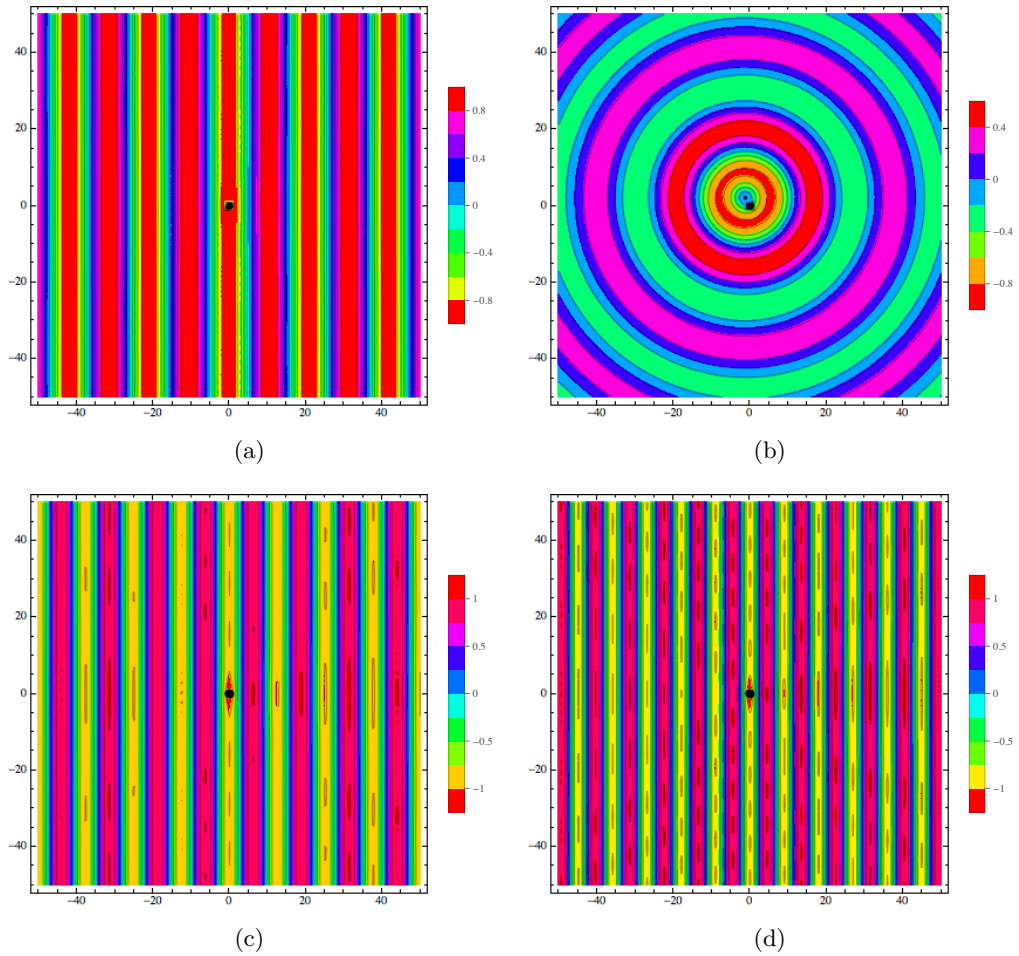

Figure 1.3: In all figures there are no control sources, the large black dot depicts the location of the free-edge cavity of raduis $a_i = 1.0$, and $N = 2$. In all parts, we show the total flexural wave amplitude due to (a) an incident plane wave such that $\beta = 0.3$, (b) a remote point source such that $\beta = 0.3$, (c) an incident plane wave such that $\beta = 0.5$, (d) an incident plane wave such that $\beta = 0.7$.

1.2 Scattering of flexural waves by a circular inclusion

In this section, we consider flexural wave scattering from a circular inclusion of radius a_i, subject to a time-harmonic wave denoted by $W(\mathbf{x};t) = w(\mathbf{x})\exp(\mathrm{i}\omega t)$. A schematic view of the configuration is presented in Fig. 1.4, for the cases when the incident field is a plane wave and a remote point source.

For the case of a circular inclusion subject to time-harmonic vibrations, that is $W^{(q)}(\mathbf{x};t) = w^{(q)}(\mathbf{x})\exp(\mathrm{i}\omega t)$, the equation for the out-of-plane displacement reads

$$\left(\Delta^2 - \frac{\rho_q h\,\omega^2}{D_q}\right) w^{(q)}(\mathbf{x}) = \left(\Delta + \beta_q^2\right)\left(\Delta - \beta_q^2\right) w^{(q)}(\mathbf{x}) = 0, \quad \mathbf{x} \in \Omega_q, \quad q = i, e, \tag{1.17}$$

where $\beta_q^2 = \omega\sqrt{\rho_q h/D_q}$ is the spectral parameter, Ω_q denotes the region corresponding to the inclusion or exterior medium, and the super/sub-script (q) is either (i) or (e), denoting

the inclusion and exterior medium, respectively. For the geometry of Fig. 1.4, the inclusion and exterior regions are defined as follows:

$$\Omega_i = \{\mathbf{x} : x_1^2 + x_2^2 < a_i^2\}, \quad \Omega_e = \mathbb{R}^2 \setminus \overline{\Omega_i}. \tag{1.18}$$

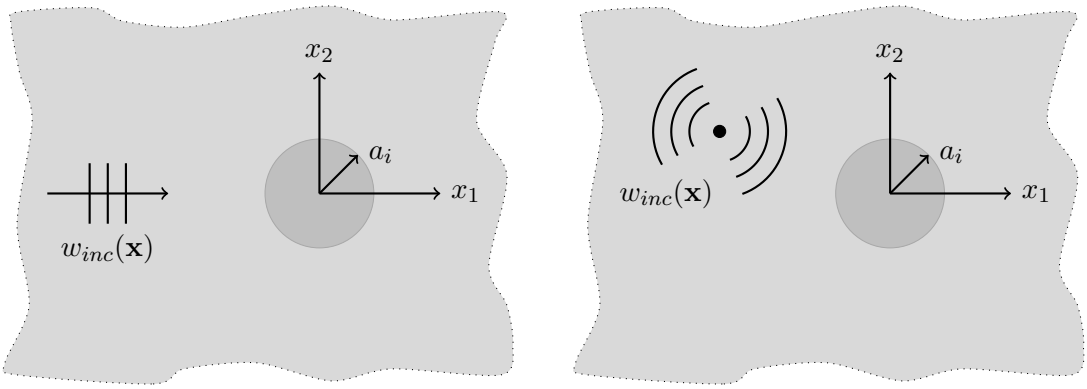

(a) (b)

Figure 1.4: Schematic view of an inclusion of radius a_i embedded in a Kirchhoff plate subject to an incident field denoted by $w_{inc}(\mathbf{x})$. In part (a) $w_{inc}(\mathbf{x})$ is an incident plane wave such that $\theta_{inc} = 0$, and in part (b) $w_{inc}(\mathbf{x})$ is a remote point source.

It has been discussed that the solution $w^{(q)}(\mathbf{x})$ to equation (1.17), is the superposition of solutions to the Helmholtz and modified Helmholtz equations. In polar coordinates, the fields $w^{(q)}(r,\theta)$, are therefore written as follows

$$w^{(q)}(r,\theta) = \sum_{n=-\infty}^{\infty} \left[A_n^{(q)} J_n(\beta_q r) + E_n^{(q)} H_n^{(1)}(\beta_q r) + B_n^{(q)} I_n(\beta_q r) + F_n^{(q)} K_n(\beta_q r) \right] e^{in\theta}, \tag{1.19}$$

where again, the super(/sub)-script (q) is either (i) or (e), denoting fields in the inclusion and exterior matrix, respectively. Note that, inside the inclusion, we set $E_n^{(i)}$ and $F_n^{(i)}$ equal to zero to ensure finite displacements at the origin.

1.2.1 Obtaining the scattered field from conditions of perfect bonding

In chapter 3, we consider the resonant regimes of a circular inclusion embedded within Kirchhoff plate. Here, we present the conditions of perfect bonding imposed on the interface of a circular inclusion of radius a_i. This interface describes where the inclusion and exterior medium meet. Perfect bonding implies continuity of the displacement, its normal derivative, the moment and the transverse force, which leads to

$$w^{(i)}(r,\theta) = w^{(e)}(r,\theta), \quad \frac{\partial w^{(i)}(r,\theta)}{\partial r} = \frac{\partial w^{(e)}(r,\theta)}{\partial r}, \qquad \text{on } r = a_i, \tag{1.20}$$

and

$$D_i\left[\frac{\partial^2 w^{(i)}(r,\theta)}{\partial r^2}+\frac{\nu_i}{r}\left(\frac{\partial w^{(i)}(r,\theta)}{\partial r}+\frac{1}{r}\frac{\partial^2 w^{(i)}(r,\theta)}{\partial \theta^2}\right)\right] = D_e\left[\frac{\partial^2 w^{(e)}(r,\theta)}{\partial r^2}+\frac{\nu_e}{r}\left(\frac{\partial w^{(e)}(r,\theta)}{\partial r}+\frac{1}{r}\frac{\partial^2 w^{(e)}(r,\theta)}{\partial \theta^2}\right)\right], \quad \text{on } r=a_i, \tag{1.21}$$

$$D_i\left[\frac{\partial}{\partial r}\Delta_{r\theta} w^{(i)}(r,\theta)+\frac{1-\nu_i}{r^2}\frac{\partial^2}{\partial \theta^2}\left(\frac{\partial w^{(i)}(r,\theta)}{\partial r}-\frac{w^{(i)}(r,\theta)}{r}\right)\right] = D_e\left[\frac{\partial}{\partial r}\Delta_{r\theta} w^{(e)}(r,\theta)+\frac{1-\nu_e}{r^2}\frac{\partial^2}{\partial \theta^2}\left(\frac{\partial w^{(e)}(r,\theta)}{\partial r}-\frac{w^{(e)}(r,\theta)}{r}\right)\right], \quad \text{on } r=a_i. \tag{1.22}$$

In the above conditions, the super(/sub)-scripts (i) and (e) denote fields and material parameters for the inclusion and exterior medium, respectively. It is possible to obtain a scattering matrix for these boundary conditions, by following a method analogous to that outlined in the clamped boundary case of section 1.1.1. The appropriate field representations given in equation (1.19) are substituted into the corresponding conditions (1.20) - (1.22). Eventually one obtains a matrix equation relating the outgoing wave coefficients in terms of those of the incident wave, that is,

$$\begin{pmatrix} E_n^{(e)} \\ F_n^{(e)} \end{pmatrix} = \mathcal{S}_n \begin{pmatrix} A_n^{(e)} \\ B_n^{(e)} \end{pmatrix},$$

where the matrix $\mathcal{S}_n$ encapsulates the conditions of perfect bonding for a circular inclusion. The scattered field is therefore written

$$w_{sc}(r,\theta) = \mathcal{S}_0^{11} H_0^{(1)}(\beta_e r) + \mathcal{S}_0^{21} K_0(\beta_e r) + \sum_{n=1}^{\infty} 2i^n [\mathcal{S}_n^{11} H_n^{(1)}(\beta_e r) + \mathcal{S}_n^{21} K_n(\beta_e r)] \cos(n\theta),$$

where $\mathcal{S}_n^{ij}$, $i,j=1,2$, denote the entries of the scattering matrix appearing in the previous equation. For the case of perfect bonding, the entries of the scattering matrix are more involved. In chapter 3, we combine passive and active techniques by introducing a specifically designed coating to aid cloaking with our active sources at higher frequency resonant regimes. Thus, we do not write the entries of $\mathcal{S}_n$ here, but give detail in chapter 3 for obtaining the scattering matrix for a coated inclusion.

1.2.2 Illustrative examples of scattering from a circular inclusion

We plot the total flexural amplitude everywhere outside the inclusion in order to observe the effect on scattering from a perfectly bonded inclusion of radius $r=a_i$. In the following illustrative examples, we consider a high contrast inclusion whose elastic properties vary significantly from the exterior medium. Scattering from a high contrast inclusion often brings interesting results compared to an inclusion with comparable elastic properties to the exterior medium.

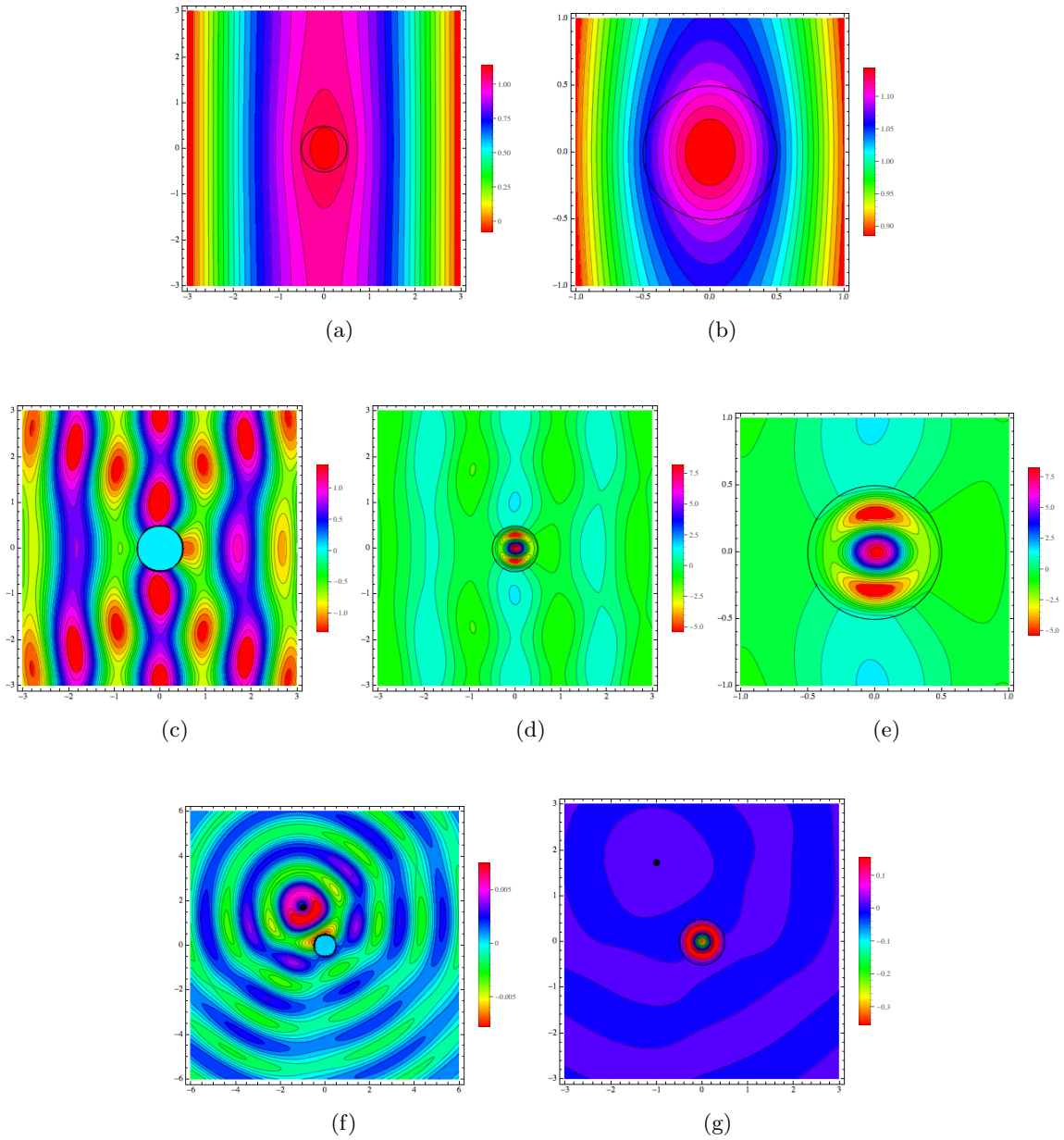

Figure 1.5: Flexural wave amplitude of the total field in a plate containing an inclusion of radius $a_i = 0.5$ whose boundary is depicted by the black circle. The material parameters in all figures are $\rho_i = 0.05$, $\rho_e = 1.0$, $\nu_i = \nu_e = 0.3$, $D_i = 2.5 \times 10^{-4}$, $D_e = 1.0$, $a_i = 0.50$. In either plot, there are no control sources. In parts (a) and (b) $\omega = 0.3$, whilst in parts (c)-(g) $\omega = 11.30$. Part (c) depicts amplitudes exterior to the inclusion, whilst parts (d) and (e) detail the amplitudes both inside the inclusion and the exterior medium. Parts (f) and (g) detail the amplitudes due to a remote point force depicted by the small black disk, which is located at a distance of 2.5 units from the origin, at an angle of $2\pi/3$ radians to the x_1-axis. Part (f) depicts amplitudes in the exterior medium only whilst part (g) depicts wave amplitudes throughout the inclusion and exterior medium.

In Fig. 1.5, we see the effect on the total field everywhere outside the scatterer for a incident plane wave of frequency $\omega = 0.3$ (Fig. 1.5(a),(b)), and $\omega = 11.30$ (Fig. 1.5(c)-(g)).

It is clear in that even with a high contrast inclusion, scattering is weak at the lower frequency regime (note that Fig. 1.5(b) depicts a more detailed view of the fields inside the inclusion). For this reason, we do not seek to cloak an inclusion at low frequencies where the scatterer is small compared to the wavelength of the incident wave.

Instead, we consider higher frequencies, focusing our attention to resonant regimes. Scattering properties of the inclusion change significantly within a small frequency range at resonant regimes. If the incident wave frequency changes slightly at a resonant regime, then our active sources have to adapt to considerable changes in scattering, which can prove challenging. In chapter 3, we update our cloaking method to combine active and passive techniques ensuring that active cloaking is possible at resonant regimes. We introduce a coating around the inclusion which "tames" the rapid variation in scattering from the inclusion. We also present an approach for predicting at what frequencies the inclusion resonates within the plate.

The scattering pattern at a higher frequency is shown in the total wave amplitude plots of Figs. 1.5(c)-(e) for $\omega = 11.30$. It can be seen in Fig. 1.5(c) that scattering in the exterior medium is significant compared to the lower frequency case, and in Figs. 1.5(d), (e), localised fields inside the inclusion are visible, which indicates that we are at a resonant regime. Scattering from a remote point source is also presented in Figs. 1.5(f) and 1.5(g), detailing fields exterior and inside the inclusion, respectively. For the case of an incident point source, the scattering is weak however, a shadow region region is clearly visible in Fig. 1.5(f).

1.3 Active sources and the fundamental solution for the bi-harmonic operator

In this thesis, our active cloaking method was motivated by the work presented by Guevara-Vasquez *et al.* [33]-[37]. In these papers, a shielding problem was developed for systems governed by the Helmholtz equation, namely transverse electric or magnetic waves. Active devices shielded an object by creating a quiet region, whilst simultaneously cancelling fields from the devices themselves in a region exterior to the shielding configuration. As a result of the shielding method, the incident field appeared unperturbed at a finite distance outside the devices and object. In [33], Guevara-Vasquez initially demonstrated the shielding method for a two-dimensional quasi-static problem, before considering systems governed by the Helmholtz equation.

In the work by Guevara-Vasquez *et al.* [33]-[37], active devices were modelled by a finite number of multipolar point-like sources. The field emitted from the devices, which had the required properties necessary for the shielding and scattering reduction problem, was obtained using Green's formula together with the Green's function for the two-dimensional wave equation. The field was written as an integral equation whose terms corresponded to potentials due to a distribution of monopoles and dipoles aligned with, and normal to

the boundary of the quiet region, respectively. The double distribution of sources was then replaced with a finite number of multipolar active devices. The argument given for replacing the double distribution was that the quiet region was no longer entirely surrounded by a surface. The sources were represented by a series expansion dependent on the Hankel function of the first kind, which were chosen to be radiating solutions to the Helmholtz equation, satisfying the Sommerfeld radiation condition. The field generated by the sources with the required properties for the problem was written as a series representation with unknown coefficients whose amplitudes were computed numerically in [33] and [34]. The amplitudes necessary for shielding problem were then given explicitly in the paper by Guevara-Vasquez *et al.* [35].

Analogous to Guevara-Vasquez *et al.* [33]-[37], we develop a cloaking method (as opposed to shielding) where a finite number of active sources reduce scattering exterior to the configuration, without creating a quiet region around the object. The amplitudes of the sources are chosen such that the incident field is reconstructed exterior to the cloaking configuration making the scatterer essentially undetectable. In this thesis, the active sources are point sources represented by the Green's function for the biharmonic operator, which we show is non-singular at the origin. The function $G(\mathbf{x};\mathbf{X})$ representing the Green's function for the biharmonic operator, is a model solution to the following problem

$$\left(\Delta^2 - \frac{\rho h \omega^2}{D}\right) G(\mathbf{x};\mathbf{X}) - \delta(|\mathbf{x}-\mathbf{X}|) = 0, \qquad \mathbf{x} = (x_1, x_2),\ \mathbf{X} = (X_1, X_2) \in \mathbb{R}^2, \tag{1.23}$$

where $\delta(|\mathbf{x}-\mathbf{X}|)$ is the Dirac delta function centred at $\mathbf{X}$. We assume that $G(\mathbf{x};\mathbf{X})$ satisfies the radiation condition at infinity. The Green's function for the biharmonic operator is given by Norris and Vermula [84] in the following form

$$G(\mathbf{x};\mathbf{X}) = -\frac{1}{8\beta^2}\left[iH_0^{(1)}(\beta|\mathbf{x}-\mathbf{X}|) - \frac{2}{\pi}K_0(\beta|\mathbf{x}-\mathbf{X}|)\right], \tag{1.24}$$

We show that $G(\mathbf{x};\mathbf{X})$ is non-singular and bounded at the origin by considering terms from the ascending series expansions of the Helmholtz and modified Helmholtz functions. For arguments z, the functions $H_0^{(1)}(z)$ and $K_0(z)$ have the following ascending series expansions according to chapter 9 of the book by Abramowitz and Stegun [1]

$$\begin{aligned} H_0^{(1)}(z) =& 1 + \frac{2i}{\pi}\gamma + \frac{2i}{\pi}\ln(z/2) - \frac{i}{2\pi}\left(\gamma + \ln(z/2)\right)z^2 - \frac{1}{4}z^2 + \frac{i}{2\pi}z^2 + \ldots, \\ K_0(z) =& -\ln(z/2) - \gamma - \frac{1}{4}(\gamma + \ln(z/2))z^2 + z^2/4 + \ldots. \end{aligned} \tag{1.25}$$

Thus, by setting $z = \beta|\mathbf{x}-\mathbf{X}|$, substituting the equations of (1.25) into equation (1.24) leads to

$$G(\mathbf{x};\mathbf{X}) = -\frac{1}{8\beta^2}\left[i - \frac{i(\beta|\mathbf{x}-\mathbf{X}|)^2}{4} + \ldots\right]. \tag{1.26}$$

The linear combination of Bessel and modified Bessel functions in $G(\mathbf{x};\mathbf{X})$ cancels terms that would be singular at the origin and $G(\mathbf{x};\mathbf{X}) \to -i/8\beta^2$ as $|\mathbf{x}-\mathbf{X}| \to 0$.

1.3.1 Graf's addition theorem

As previously mentioned, throughout this thesis, our active sources will be represented by the Green's function for the biharmonic operator. The form of Green's function given in equation (1.24), is centred at the point $\mathbf{X}$, which will correspond to the position of the active source $\mathbf{x}^{(s,l)}$ in our cloaking configuration. To cancel the scattered field, we find the contribution to the incoming and outgoing waves from each active source, relative to the origin of the coordinate axes, which requires the re-expansion of each Green's function centred at a source position relative to the origin. This is done using Graf's addition theorem, which can be found in the book by Abramowitz and Stegun [1]. Here, we outline the theorem as presented by Martin [53], in the setting relevant to our cloaking problem.

We aim to find the contribution of a point source positioned at $\mathbf{x}^{(s,l)} = ({x_1}^{(s,l)}, {x_2}^{(s,l)})^\top$, relative to the origin at a general point in $\mathbb{R}^2$ space $\overline{\mathbf{X}} = (\overline{X_1}, \overline{X_2})^\top$, we let O and O_l denote two origins, where O coincides with that of the coordinate axes, and O_l coincides with $\mathbf{x}^{(s,l)}$. We introduce three position vectors to the configuration: Let $\mathbf{b} = -\mathbf{x}^{(s,l)}$ denote the vector joining O_l to the origin O, $\mathbf{r}$ denotes the vector joining O to the general point $\overline{\mathbf{X}}$ and $\mathbf{r}_l$ joins the origin at O_l to $\overline{\mathbf{X}}$. The geometry of this configuration is shown in Fig. 1.6. Finally, the angles $\arg(\mathbf{x}^{(s,l)}) = \phi$, $\arg(\mathbf{r}) = \theta$ are the arguments about the origin O, and $\arg(\mathbf{b}) = (\phi - \pi)$, $\arg(\mathbf{r}_l) = \theta_l$ are the arguments about O_l, which are also highlighted in Fig. 1.6.

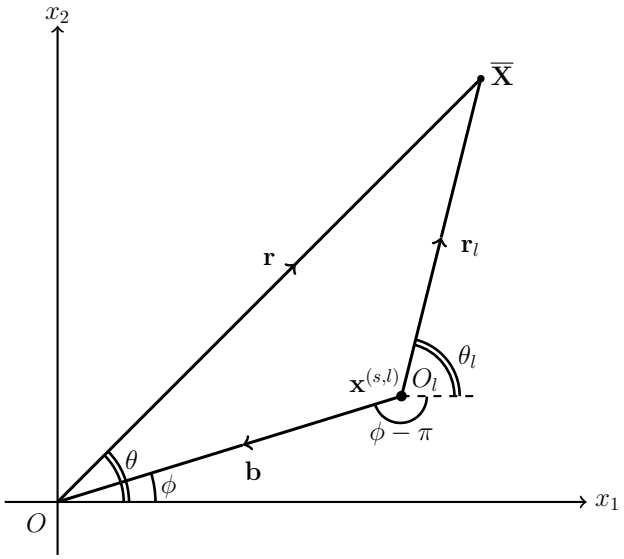

Figure 1.6: Schematic diagram showing locations of an active source at $\mathbf{x}^{(s,l)} = ({x_1}^{(s,l)}, {x_2}^{(s,l)})^\top$, and a general point $\overline{\mathbf{X}} = (\overline{X_1}, \overline{X_2})^\top$. The vectors $\mathbf{r}$ and $\mathbf{r}_l$ denote the position vectors of the general point $\overline{\mathbf{X}}$ relative the origins O and O_l, respectively. The arguments of $\mathbf{r}$ and $\mathbf{r}_l$ to their respective origins are θ and θ_l. The vector $\mathbf{b} = -\mathbf{x}^{(s,l)}$ joins O_l to O, and has an argument of $(\phi - \pi)$ with respect to O_l.

For the Hankel function $H_n^{(1)}$, and for $|\mathbf{r}| > |\mathbf{b}|$, Graf's addition theorem reads

$$H_n^{(1)}(\beta|\mathbf{r}_l|)e^{in\theta_l} = H_n^{(1)}(\beta|\mathbf{r}+\mathbf{b}|)e^{in\theta_l} = \sum_{k=-\infty}^{\infty} H_{n-k}^{(1)}(\beta|\mathbf{r}|)e^{i(n-k)\theta}J_k(\beta|\mathbf{b}|)e^{ik(\phi-\pi)}, \quad (1.27)$$

and for $|\mathbf{r}| < |\mathbf{b}|$ we have

$$H_n^{(1)}(\beta|\mathbf{r}_l|)e^{in\theta_l} = H_n^{(1)}(\beta|\mathbf{r}+\mathbf{b}|)e^{in\theta_l} = \sum_{k=-\infty}^{\infty} H_{n-k}^{(1)}(\beta|\mathbf{b}|)e^{i(n-k)(\phi-\pi)}J_k(\beta|\mathbf{r}|)e^{ik\theta}. \quad (1.28)$$

Likewise for the Macdonald function K_n, for $|\mathbf{r}| > |\mathbf{b}|$, Graf's addition theorem reads

$$K_n(\beta|\mathbf{r}_l|)e^{in\theta_l} = K_n(\beta|\mathbf{r}+\mathbf{b}|)e^{in\theta_l} = \sum_{k=-\infty}^{\infty} (-1)^k K_{n-k}(\beta|\mathbf{r}|)e^{i(n-k)\theta}I_k(\beta|\mathbf{b}|)e^{ik(\phi-\pi)}, \quad (1.29)$$

and for $|\mathbf{r}| < |\mathbf{b}|$ we have

$$K_n^{(1)}(\beta|\mathbf{r}_l|)e^{in\theta_l} = K_n^{(1)}(\beta|\mathbf{r}+\mathbf{b}|)e^{in\theta_l} = \sum_{k=-\infty}^{\infty} (-1)^k K_{n-k}(\beta|\mathbf{b}|)e^{i(n-k)(\phi-\pi)}I_k(\beta|\mathbf{r}|)e^{ik\theta}. \quad (1.30)$$

By substituting $n = 0$ in equations (1.27) - (1.30), we obtain the following representation for the Green's function $G(|\overline{\mathbf{X}};\mathbf{x}^{(s,l)}|) = G(|\mathbf{r};\mathbf{b}|)$ for the case when $|\mathbf{r}| > |\mathbf{b}|$

$$G(\overline{\mathbf{X}};\mathbf{x}^{(s,l)}) = -\frac{1}{8\beta^2}\sum_{k=-\infty}^{\infty}\left[iH_k^{(1)}(\beta|\mathbf{r}|)J_k(\beta|\mathbf{b}|) - \frac{2}{\pi}K_k(\beta|\mathbf{r}|)I_k(\beta|\mathbf{b}|)\right]e^{ik(\theta-\phi)}, \quad (1.31)$$

and for the case $|\mathbf{r}| < |\mathbf{b}|$ we obtain

$$G(\overline{\mathbf{X}};\mathbf{x}^{(s,l)}) = -\frac{1}{8\beta^2}\sum_{k=-\infty}^{\infty}\left[iH_k^{(1)}(\beta|\mathbf{b}|)J_k(\beta|\mathbf{r}|) - \frac{2}{\pi}K_k(\beta|\mathbf{b}|)I_k(\beta|\mathbf{r}|)\right]e^{ik(\theta-\phi)}. \quad (1.32)$$

1.4 Scattering of flexural waves by a doubly periodic array

In chapter 4, we adapt our method of cloaking to reduce scattered fields from a finite cluster of pins. We show that properties of the infinite array can be used to predict those of the finite cluster. We aim to cloak at frequencies where the cluster displays interesting scattering properties. Finite clusters of pins are considered to be a subset of an infinite doubly periodic array. As a result, frequencies at which interesting scattering effects are observed in the infinite structure, are used as estimates for the frequencies at which they occur in the finite cluster. These interesting effects arise from the interaction of both propagating and evanescent wave solutions within the microstructure of the array (and hence the finite cluster). We show that the cloaking can be achieved at these frequencies, exemplifying the broadband nature of our active cloaking method.

In this section we consider an infinite doubly periodic array, and discuss the frequencies at which interesting effects are observed. The regimes we investigate are selected using dispersion surfaces and band diagrams, which are obtained by plotting solutions to the dispersion

relation for Bloch-Floquet waves in an infinite array. In what follows, we detail the method of obtaining band diagrams and dispersion surfaces according to that presented by Movchan *et al.* [67], which was later employed by McPhedran *et al.* [56] and Poulton *et al.* [89]. In the paper by Movchan *et al.* [67], the problem was formulated for a doubly periodic array of circular holes of radius a, with clamped or free boundaries. We also summarise important results of the theory presented in chapter 3 of the book by Movchan *et al.* [68], which described multipole methods for obtaining field representations in doubly periodic arrays when systems are governed by the Helmholtz equation. The multipole method was summarised for the static and dynamic cases, the latter involving a spectral problem. The properties for an infinite array of pins can be obtained by imposing clamped boundaries on the edge of each void, and considering the limiting case when the radius of the cavities a, tends to zero. Since we only cloak a finite array of pins, we summarise the results of [67] for the case of a doubly periodic array of circular holes with clamped boundaries.

1.4.1 Problem setting for an array of circular clamped cavities

We consider an infinite array of circular cavities with clamped boundaries. In order to derive the solution describing the out-of-plane displacement of the perforated plate, we consider a unit cell, which is centred about the origin of the axes. The solution is formulated for this unit cell and is then related to the entire array constructing the solution across the plate. The unit cell is defined is as follows

$$\Omega_{0,0} = (-d/2, d/2) \times (-d/2, d/2) \setminus \overline{\mathcal{D}_{0,0}^{(a)}}, \tag{1.33}$$

where $\mathcal{D}_{0,0}^{(a)} = (x_1, x_2) : x_1^2 + x_2^2 < a^2$, denotes the cavity in the unit cell of radius a. In Fig. 1.7, we show the details of the doubly periodic array in the plate as well as the unit cell.

We consider time-harmonic flexural vibrations, such that $W(\mathbf{x}; t) = w(\mathbf{x}) \exp(\mathrm{i}\omega \mathrm{t})$. The amplitude $w(\mathbf{x})$ of the out-of-plane displacement in the unit cell satisfies the biharmonic equation given in equation (1.2). Note that for now, we only consider the central unit cell, that is $\mathbf{x} \in \Omega_{0,0}$. It has been discussed that solutions to the biharmonic equation are the superposition of solutions to the Helmholtz and modified Helmholtz equations. As shown in section 1.1, everywhere outside the cavity in $\Omega_{(0,0)}$, the solution to the governing equation can be expressed as the multipole expansion (1.6), which we write again as

$$w(r, \theta) = \sum_{n=-\infty}^{\infty} \left[A_n J_n(\beta r) + E_n H_n^{(1)}(\beta r) + B_n I_n(\beta r) + F_n K_n(\beta r) \right] e^{in\theta}.$$

Recall from equation (1.6) that the coefficients A_n and E_n are related to solutions to the Helmholtz equation, whilst B_n and F_n are related to solutions of the modified Helmholtz equation (with both equations presented in (1.4)). If we consider the multipole expansion given above about the central cavity; the expansion will only converge in the region between the cavity of the unit cell and the four nearest cavities of the adjoining cells that is, for

distances r such that $a < r < d - a$. If we want to ensure that the entire unit cell is covered by a convergent multipole expansion, the radius of the cavities must satisfy $a \leq d(1 - 1/\sqrt{2})$. Movchan *et al.* [67] highlight that for cavity radii exceeding the previous condition, band diagrams are calculated using the Rayleigh identity, which is derived under the assumption that there is a circle between the boundaries of the unit cell and the cavity. Movchan *et al.* also mention that the properties of such a solution can found using the Wijngaard expansion which is a convergent multiple origin expansion written as a combination of the Bessel functions $H_n^{(1)}$ and K_n. Such an expansion was first introduced by Wijngaard [103] when solving the boundary value problem of two parallel, circular and lossless dielectric rods in electromagnetism.

By obtaining a representation for the solution in the unit cell, we can relate this to the entire array and construct the solution for the out-of-plane displacement in the plate. To find these relations, we set Bloch-Floquet quasi-periodicity conditions within the array which are described in what follows.

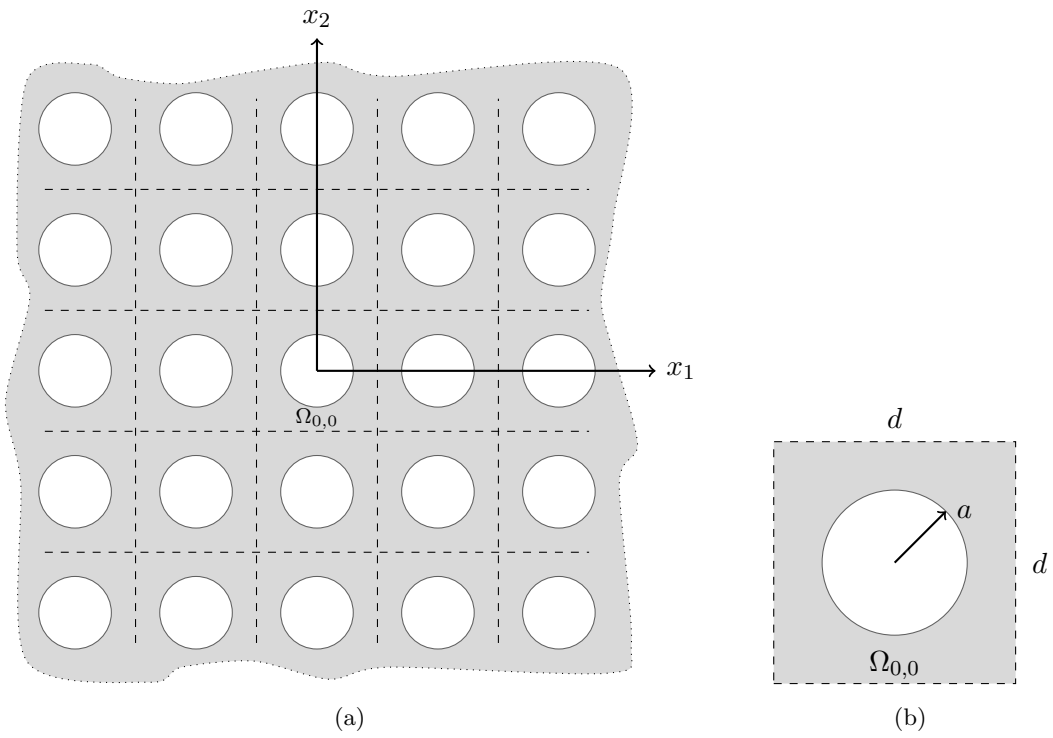

Figure 1.7: In part (a) we show a schematic view of a doubly periodic array of clamped edge cavities throughout a Kirchhoff plate. Each cavity has radius a and the unit cell is denoted by $\Omega_{0,0}$. In part (b) we show a close-up view of the unit cell $\Omega_{0,0}$.

Bloch-Floquet quasi-periodicity conditions

We have made use of the fact that the array is doubly-periodic by initially focusing our attention to the solution inside the unit cell. In order to find the solution across the entire structure, we impose specific boundary conditions on the edges of the unit cell. These

conditions relate the solution for the out-of-plane displacement in a general cell, whose domain we denote by Ω_{q_1,q_2}, to that of the central unit cell denoted by $\Omega_{0,0}$. These conditions are called the Bloch-Floquet quasi-periodicity conditions and they take into account the periodic nature of the array (and hence the periodic nature of the solution for the out-of-plane displacement), as well as any changes in phase across each cell in the array. The quasi-periodicity conditions take the following form

$$w(\mathbf{r} + \mathbf{R_q}) = w(\mathbf{r})e^{i\mathbf{R_q}\cdot\mathbf{k}_0}, \tag{1.34}$$

where $\mathbf{k}_0$ is the Bloch vector which encapsulates all information about the wave propagating through the plate, and $\mathbf{R_q}$ denotes the real-space lattice vector describing the doubly-periodic array of cavities. As a result of the configurational geometry, the lattice vector takes the following form $\mathbf{R_q} = q_1 d\mathbf{e}^{(1)} + q_2 d\mathbf{e}^{(2)}$, where $\mathbf{q} = (q_1, q_2)$ for integers q_1, q_2, and $\mathbf{e}^{(1)}, \mathbf{e}^{(2)}$ denote the unit vectors in the x_1-, x_2-directions, respectively.

Fourier lattices and the irreducible Brillouin zone

For the spectral problem, much of the analysis relies on Fourier transforms between the direct lattice, which describes the geometry of the array of cavities, and the reciprocal lattice, which describes the geometry of the array in Fourier space. The unit cell from the direct lattice, is often referred to as the Wigner-Seitz cell, whilst the corresponding cell in the reciprocal lattice is known as the first Brillouin zone. The book by Brillouin [9] includes a detailed summary of the relationship between direct and reciprocal lattices.

Analogous to the direct lattice, we can describe any point in the reciprocal lattice via the following relation

$$\mathbf{K_h} = \frac{2\pi}{d}\left(h_1\mathbf{e}'^{(1)}, h_2\mathbf{e}'^{(2)}\right), \qquad \text{for } \mathbf{h} = (h_1, h_2),\ h_1, h_2 \in \mathbb{Z}, \tag{1.35}$$

where $\mathbf{K_h}$ denotes the vector from the node in the first Brillouin zone to that of the h-th node of the reciprocal lattice, and $\mathbf{e}'^{(1)}, \mathbf{e}'^{(2)}$ denote the unit vectors of the reciprocal lattice coordinate axes. For the doubly-periodic square array, the first Brillouin zone in the reciprocal space is a square, and the period of the array is $2\pi/d$. The Brillouin zones of the reciprocal lattice are constructed in a similar way to that in the direct lattice; it is the smallest area surrounding the node centred at the origin, composed from the perpendicular bisectors of the vectors connecting the central node to those nearest. Details of the reciprocal lattice are presented in Fig. 1.8(b).

It is possible to utilise any symmetry of the Brillouin zone and find the "irreducible Brillouin zone", which corresponds to the smallest area necessary in order to obtain band surfaces for the first Brillouin zone. These band surfaces will encompass the information about wave propagation in the doubly-periodic array.

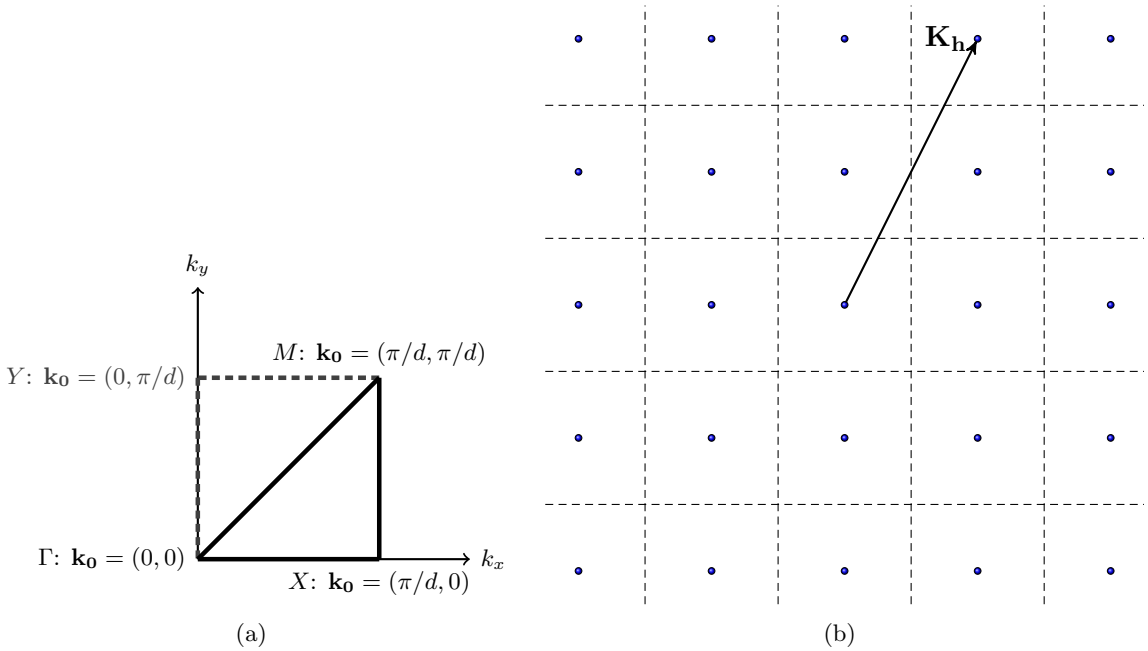

Figure 1.8: Part (a) depicts the irreducible Brillouin zone shown as the vertices of the solid triangle Γ, X and M. The first Brillouin zone is depicted by square with vertices Γ, X, M and Y. Part (b) depicts the nodes of the reciprocal lattice detailing the vector $\mathbf{K_h}$ from the first Brillouin zone the h-th node of the reciprocal lattice.

For the doubly-periodic square array considered in this section, the irreducible Brillouin zone is the triangle depicted in Fig. 1.8(a). The vertices of the irreducible Brillouin zone are denoted by Γ at (0,0), X at $(\pi/d, 0)$ and M at $(\pi/d, \pi/d)$. Having information about the direct and reciprocal lattices, we aim to find the dispersion relation in order to solve the spectral problem of wave propagation in the doubly-periodic array.

Rayleigh identities and lattice sums

Since the Helmholtz and modified Helmholtz solutions propagate independently within the perforated plate, each type of solution has their own consistency relations. These relations are found using Rayleigh identities and ensure that the multipole expansions about each cavity in the array are made consistent with the quasi-periodicity conditions given in equation (1.34). That is, in the direct lattice, the multipole expansion for the central unit cell is made consistent with the multipole expansion for a general cell in the array. The method of obtaining Rayleigh identities employs both Green's theorem and Graf's addition theorem, and is summarised in the book by Botten *et al.* [8].

For the Helmholtz equation, the Rayleigh identity reads

$$A_n = \sum_{l=-\infty}^{\infty} (-1)^{l-n} S^H_{l-n}(\beta, \mathbf{k}_0) E_l, \tag{1.36}$$

where $\mathbf{k}_0 = (k_x, k_y)$ is the Bloch vector and $S^H_l(\beta, \mathbf{k}_0)$ denotes the lattice sum of order l for

the Hankel function such that

$$S_l^H(\beta,\mathbf{k}_0)=\sum_{\mathbf{q}\neq 0,0} H_l^{(1)}(\beta R_{\mathbf{q}})e^{il\theta_{\mathbf{q}}}e^{i\mathbf{k}_0\cdot\mathbf{R}_{\mathbf{q}}}, \tag{1.37}$$

where the real-space lattice vector $\mathbf{R}_{\mathbf{q}}$ has the polar representation $\mathbf{R}_{\mathbf{q}}=R_{\mathbf{q}}\exp(i\theta_{\mathbf{q}})$. Whilst this form of the lattice sum is an insightful representation analytically, it converges slowly. For numerical computations, the following accelerated convergent sum may be used as an alternative

$$\begin{aligned} S_l^Y(\beta,\mathbf{k}_0)J_{l+p}(\beta\zeta)=-\left\{Y_p(\beta\zeta)+\frac{1}{\pi}\sum_{n=1}^{p}\frac{(p-n)!}{(n-1)!}\left(\frac{2}{\beta\zeta}\right)^{p-2n+2}\right\}\delta_{l,0} \\ -\frac{4i^l}{d^2}\sum_{\mathbf{h}}\left(\frac{\beta}{Q_{\mathbf{h}}}\right)^p\frac{J_{l+p}(Q_{\mathbf{h}}\zeta)}{Q_{\mathbf{h}}^2-\beta^2}e^{i\theta_{\mathbf{h}}}, \end{aligned} \tag{1.38}$$

which is written in terms of the reciprocal lattice and can be found in the paper by Chin *et al.* [17]. In the above, $\mathbf{h}=(h_1,h_2)$ are pairs of integers that are summed over an order large enough to guarantee accuracy of the above representation. In equation (1.38), $\mathbf{Q}_{\mathbf{h}}=\mathbf{K}_{\mathbf{h}}+\mathbf{k}_0$ are vectors that ensure quasi-periodicity runs over the Bloch vector $\mathbf{k}_0$. The vectors $\mathbf{Q}_{\mathbf{h}}$ have the polar representation $\mathbf{Q}_{\mathbf{h}}=Q_{\mathbf{h}}\exp(i\theta_{\mathbf{h}})$. We note that ζ is arbitrary and can be set to d, (the width of the unit cell), and p denotes the acceleration parameter.

We draw attention to the fact that the accelerated lattice sum in equation (1.38) is only valid for orders $l>0$. Therefore, when calculating negative orders, we make use of the following symmetry relations

$$S_l^Y(\beta,-\mathbf{k}_0)=(-1)^lS_l^Y(\beta,\mathbf{k}_0),\qquad S_{-l}^Y(\beta,\mathbf{k}_0)=(S_l^Y(\beta,\mathbf{k}_0))^*,$$

where $(\cdot)^*$ denotes complex conjugation.

Similar to equation (1.36), the Rayleigh identity satisfying the modified Helmholtz equation reads

$$B_n=\sum_{l=-\infty}^{\infty}(-1)^lS_{l-n}^K(\beta,\mathbf{k}_0)F_l, \tag{1.39}$$

where $S_l^K(\beta,\mathbf{k}_0)$ has the following form

$$S_l^K(\beta,\mathbf{k}_0)=\sum_{\mathbf{q}\neq 0,0}K_l(\beta R_{\mathbf{q}})e^{il\theta_{\mathbf{q}}}e^{i\mathbf{k}_0\cdot\mathbf{R}_{\mathbf{q}}}. \tag{1.40}$$

The lattice sum for $S_l^K(\beta,\mathbf{k}_0)$ is exponentially convergent, and can be evaluated directly. The above can be written in terms of the reciprocal lattice, and is given by

$$S_l^K(\beta,\mathbf{k}_0)I_l(\beta\zeta)=-K_0(\beta\zeta)\delta_{l,0}+2\pi i^l\sum_{\mathbf{h}}\frac{J_l(Q_{\mathbf{h}}\zeta)e^{i\theta_{\mathbf{h}}}}{Q_{\mathbf{h}}^2+\beta^2}. \tag{1.41}$$

Solution to the spectral problem using the dispersion relation

We now have enough information from previous sections to obtain the dispersion relation which is used to find solutions of the spectral problem. In what follows, we show that the dispersion relation is used for plotting band diagrams and dispersion surfaces. The first step in obtaining the dispersion relation is to find the matrix equation for the eigenmodes of elastic vibrations. This is done by substituting the solution $w(r,\theta)$ from equation (1.6), into the equations for clamped boundaries, which were given in equation (1.7). As a result, we obtain the following,

$$\begin{aligned}\sum_{n=-\infty}^{\infty}\left[A_nJ_n(\beta a)+E_nH_n^{(1)}(\beta a)+B_nI_n(\beta a)+F_nK_n(\beta a)\right]=0,\\ \sum_{n=-\infty}^{\infty}\left[A_nJ_n'(\beta a)+E_nH_n^{(1)'}(\beta a)+B_nI_n'(\beta a)+F_nK_n'(\beta a)\right]=0,\end{aligned}\tag{1.42}$$

where prime denotes the derivative with respect to the argument βr.

We then substitute the Rayleigh identities (1.36) and (1.39) into equations of (1.42), which leads to the following two equations

$$\sum_{n=-\infty}^{\infty}\Bigg[\sum_{l=-\infty}^{\infty}\left\{(-1)^{l-n}S_{l-n}^{H}(\beta,\mathbf{k}_0)J_n(\beta a)+\delta_{l,n}H_n^{(1)}(\beta a)\right\}El + \sum_{l=-\infty}^{\infty}\left\{(-1)^{l}S_{l-n}^{K}(\beta,\mathbf{k}_0)I_n(\beta a)+\delta_{l,n}K_n(\beta a)\right\}Fl=0\Bigg],\tag{1.43}$$

$$\sum_{n=-\infty}^{\infty}\Bigg[\sum_{l=-\infty}^{\infty}\left\{(-1)^{l-n}S_{l-n}^{H}(\beta,\mathbf{k}_0)J_n'(\beta a)+\delta_{l,n}H_n^{(1)'}(\beta a)\right\}El + \sum_{l=-\infty}^{\infty}\left\{(-1)^{l}S_{l-n}^{K}(\beta,\mathbf{k}_0)I_n'(\beta a)+\delta_{l,n}K_n'(\beta a)\right\}Fl=0\Bigg],\tag{1.44}$$

For computational purposes, we truncate the series representations (1.43) and (1.44) to an order L. Truncating to this order results in the order of summation running from $-L$ to L in the above, which leads to the orders of summation in the lattice sums running from $-2L$ to $2L$. Using the truncated forms of (1.43) and (1.44) we write the following matrix equation for the column vectors $\mathbf{E}$, and $\mathbf{F}$ whose entries are E_l and F_l, respectively

$$\begin{pmatrix}\mathcal{A}^{(11)}(\beta,\mathbf{k}_0) & \mathcal{A}^{(12)}(\beta,\mathbf{k}_0)\\ \mathcal{A}^{(21)}(\beta,\mathbf{k}_0) & \mathcal{A}^{(22)}(\beta,\mathbf{k}_0)\end{pmatrix}\begin{pmatrix}\mathbf{E}\\ \mathbf{F}\end{pmatrix}=\mathbf{0},\tag{1.45}$$

where $\mathcal{A}^{(mn)}(\beta,\mathbf{k}_0)$ for $m,n=1,2$ are $(2L+1)\times(2L+1)$ sub-blocks of the matrix $\mathcal{A}(\beta,\mathbf{k}_0)$. Thus the dispersion relation for a double-periodic array with circular clamped cavities reads

$$\det(\mathcal{A}(\beta,\mathbf{k}_0))=0,\tag{1.46}$$

which is solved numerically for a given Bloch vector $\mathbf{k}_0$. A band diagram for the case of finite sized cylinders ($a = 0.2$) was presented in the in the paper by Movchan *et al.* [67], and it was highlighted that the rate of convergence for the multipole method was rapid when boundaries of the cavities were clamped. Due to the fast rates of convergence, Movchan *et al.* [67] accurately estimated the dispersion relation (1.46) by considering only the monopole terms of the entries in the matrix $\mathcal{A}(\beta, \mathbf{k_0})$ from (1.45). By setting $l = n = 0$ in equations (1.43) and (1.44), the determinant of matrix $\mathcal{A}(\beta, \mathbf{k_0})$ reduces to the following

$$\begin{aligned} H_1^{(1)}(\beta a)K_0(\beta a) + H_0^{(1)}(\beta a)K_1(\beta a) + S_0^H(\beta, \mathbf{k}_0)S_0^K(\beta, \mathbf{k}_0)[J_0(\beta a)I_1(\beta a) + J_1(\beta a)I_0(\beta a)] \\ + S_0^H(\beta, \mathbf{k}_0)[-J_0(\beta a)K_1(\beta a) + J_1(\beta a)K_0(\beta a)] \\ + S_0^K(\beta, \mathbf{k}_0)[H_0^{(1)}(\beta a)I_1(\beta a) + H_1^{(1)}(\beta a)I_0(\beta a)] \\ = \det(\mathcal{A}(\beta, \mathbf{k}_0)). \end{aligned} \tag{1.47}$$

Formula (1.47) can be found in the paper by Movchan *et al.* [67]. Since we cloak a finite cluster of pins, we consider the limiting case when the radius of the clamped cavities tends to zero ($a \to 0$). The following ascending series expansions for arguments z, can be found in chapter 9 of the book by Abramowitz and Stegun [1]

$$\begin{aligned} J_0(z) = 1 - \frac{z^2}{4} + \ldots, \qquad I_0(z) = 1 + \frac{z^2}{4} + \ldots, \\ H_0^{(1)}(z) = 1 + \frac{2i}{\pi}\gamma + \frac{2i}{\pi}\ln(z/2) - \frac{i}{2\pi}\left(\gamma + \ln(z/2)\right)z^2 - \frac{1}{4}z^2 + \frac{i}{2\pi}z^2 + \ldots, \\ K_0(z) = -\ln(z/2) - \gamma - \frac{1}{4}(\gamma + \ln(z/2))z^2 + z^2/4 + \ldots. \end{aligned} \tag{1.48}$$

Using the series expansions of (1.48) together with the following identities (also found in [1])

$$J_1(z) = -J_0'(z), \qquad I_1(z) = I_0'(z), \qquad H_1^{(1)}(z) = -H_0^{(1)'}(z), \qquad K_1(z) = -K_0'(z),$$

it is possible to write the leading order behaviour of the determinant given in equation (1.47). Note that in the above identities, prime denotes the derivative of the function with respect to the argument z. For small arguments (βa) in equation (1.47), we obtain the following leading order behaviour for the determinant of $\mathcal{A}(\beta, \mathbf{k}_0)$

$$\det(\mathcal{A}(\beta, \mathbf{k}_0)) \sim -\left[S_0^H(\beta, \mathbf{k}_0) + \frac{2i}{\pi}S_0^K(\beta, \mathbf{k}_0) + 1\right]\left(\frac{1}{\beta a}\right). \tag{1.49}$$

Hence, we obtain the following for the dispersion relation (1.46) in the case of rigid pins

$$S_0^H(\beta, \mathbf{k}_0) + 1 + \frac{2i}{\pi}S_0^K(\beta, \mathbf{k}_0) = 0.$$

Note that for the dispersion relation $\det(\mathcal{A}(\beta, \mathbf{k}_0)) = 0$, we can normalise by (βa) in equation (1.49). It should also be noted that for the doubly periodic array considered here, it is sufficient to compute band diagrams for Bloch vectors from the first Brillouin zone depicted in Fig. 1.8(a).

1.4.2 Band diagram for a doubly-periodic array of pins

As previously discussed, in the case of rigid pins, the dispersion relation can be written as the following equation

$$S_0^H(\beta, \mathbf{k}_0) + 1 + \frac{2i}{\pi} S_0^K(\beta, \mathbf{k}_0) = 0, \tag{1.50}$$

expressed in terms of the lattice sums S_0^H and S_0^K given in equations (1.37) and (1.40) for $l = 0$.

As first mentioned by McPhedran *et al.* [56], the dispersion bands for platonic crystals may be sandwiched between "light lines" in reciprocal space (the dashed lines in Fig. 4.2 represent segments of these light lines) which, for the square array, are defined by the equation

$$\left(k_x + \frac{2\pi h_1}{d}\right)^2 + \left(k_y + \frac{2\pi h_2}{d}\right)^2 = \beta^2, \quad h_1, h_2 \in \mathbb{Z}. \tag{1.51}$$

These singularity relations correspond to Bloch modes for the homogeneous plate, which for some frequency regimes, also satisfy the dispersion relation (1.50). Thus, the dashed lines in Fig. 4.2 represent both dispersion curves and segments of the singularity lines.

Figure 1.9 is the band diagram showing the first five dispersion curves for an infinite square array of rigid pins with $d = 1$, first investigated by Movchan *et al.* [67].

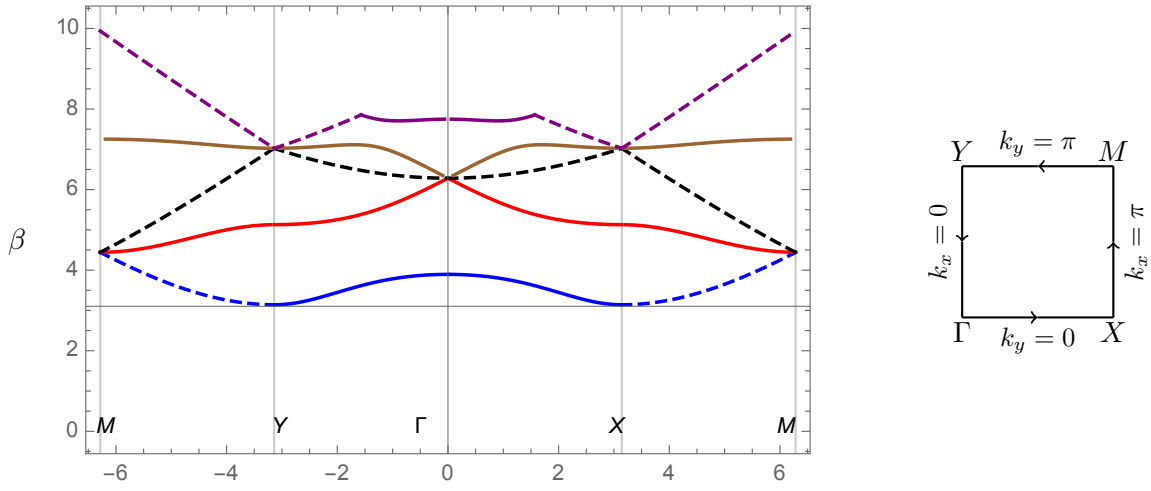

Figure 1.9: Band diagram for square array of rigid pins with $d = 1$, using square Brillouin zone $(k_x, k_y) = [0, \pi] \times [0, \pi]$. The solid lines represent solutions of the dispersion relation (1.50), and the dashed lines represent both dispersion curves and segments of the singularity lines (1.51).

The stop band (defined by $\beta < \pi$ for this square array, as shown in Fig. 1.9) corresponds to frequency regimes for which waves do not propagate through the infinite periodic array of pins. For a finite cluster of pins at frequencies that fall within these ranges, the uncloaked cluster scatters the waves, producing a shadow region. For frequencies in the pass bands ($\beta > \pi$ in this case as shown in Fig. 1.9), with a large enough cluster of pins, one would

expect to see evidence of propagation through the pinned array. An example of such a cluster is shown in Fig. 1.10(a) for the case of an 8×8 cluster. In Fig. 1.10(a), we see both propagation and scattering, which arises from an effective impedance mis-match between the array and the homogeneous plate exterior to the array. We use active sources to cloak the cluster and reconstruct the incident plane wave in the region exterior to the finite cluster and sources, thereby resembling the propagation properties of the infinite periodic system for pass band frequencies. In chapter 4, when cloaking the finite cluster at lower frequency regimes such as those in the stop band, and the beginning of the pass band, we show that square configuration of sources positioned on the grid is adequate for reducing scattered fields.

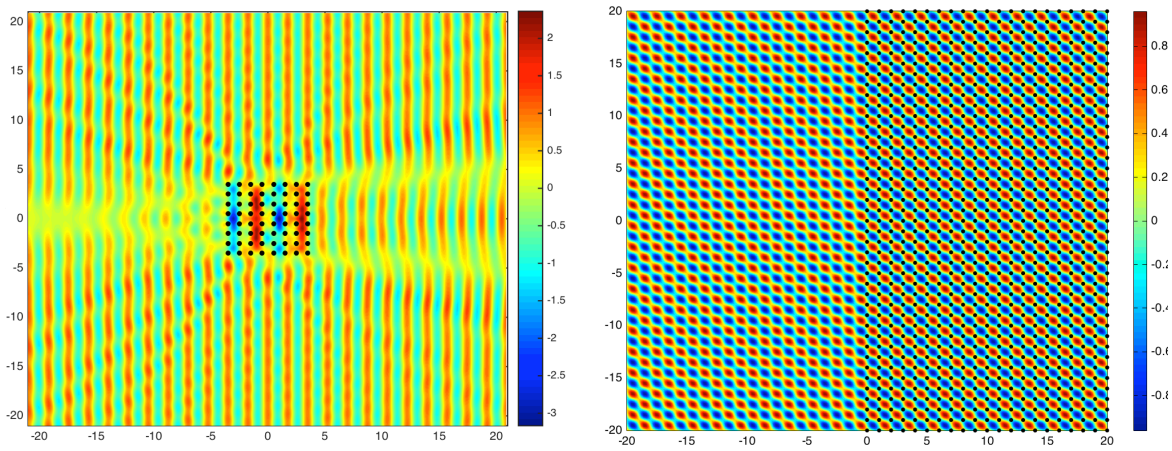

(a) (b)

Figure 1.10: In both figures, the real part of the amplitude of flexural displacement for the total field is shown, with its range, indicated by the colourbar, determined by the degree of localisation within the system. In addition, the pins are depicted by black discs and the horizontal and vertical axes are the x_1- and x_2-axes, respectively. Part (a) depicts a plane wave normally incident on an uncloaked 8×8 ($N = 8$) cluster of pins. Part (b) depicts a plane wave incident at $\theta_{inc} = \pi/4$ on 2000 gratings with $d = 1$ for $\beta = 4.44$, $\kappa_y = 3.1396$ corresponding to M in the reciprocal lattice.

Flat bands (see the vicinities of Γ for the first and fifth bands, and X and Y for the first and second, in Fig. 1.9) possess low group velocities $\partial\omega/\partial k \approx 0$, and are therefore associated with standing wave frequencies. Standing wave frequencies and "slow" waves are also synonymous with trapped modes and localisation, which are well known to arise from clamped boundary conditions, discussed in the paper by Poulton *et al.* [89].

As is typical for platonic crystals, the infinite square array of pins exhibits Dirac-like points, where a triple degeneracy arises from a flat surface passing through the intersection of two Dirac-like cones. An example of a Dirac-like point at Γ is evident for $\beta = 2\pi$ in Fig. 1.9, where the third band (dashed curve) is the additional flat surface typical of pinned platonic crystal dispersion pictures. We also observe Dirac-like points on the edge of the Brillouin zone at M, X and Y in Fig. 1.9. Similar to the free propagation of electrons in the vicinity of Dirac points, there are directions of neutral propagation around a Dirac-like point in a

platonic crystal, where the wave propagates with its direction unaffected by interaction with the microstructure. This effect of dynamic neutrality (which was considered as a form of cloaking by McPhedran *et al.* [57]) is also observed for subsets of the infinite periodic array. In Fig. 1.10(b), we show an example of a semi-infinite platonic crystal with a square array of pins similar to examples given by Haslinger *et al.* [38].

We also select some β-values from known scattering and eigenvalue problems for other subsets of the infinite doubly periodic array. For arrays of infinite gratings, an elegant methodology for exploring Rayleigh-Bloch modes can be employed to identify localisation regimes and wave-trapping behaviour for scattering problems. The work of Movchan *et al.* [71], Poulton *et al.* [89], Haslinger *et al.* [39] provide key results within this topic.

In chapter 4 we select frequencies at which the phenomena discussed above occur, in particular localisation, wave-trapping and neutrality. These scattering effects are typically observed at higher frequency regimes which require an increased number of active sources. In chapter 4, we present a way of checking how many sources are required for effective cloaking, and we discuss that the simplest way to increase the number of sources, is to locate them on a circle of set radius, exterior to the cluster. We present several illustrative examples and show that effective active cloaking is possible over a broad range of frequencies.

Chapter 2

Active cloaking of flexural waves for clamped cavities in thin elastic plates

In this chapter, we describe the method of active cloaking of flexural waves in Kirchhoff plates from scatterers with clamped boundaries. In order to implement the active cloaking method in thin elastic plates, we need to use techniques presented in the background theory of chapter 1.

We summarise the work published in the paper by O'Neill *et al.* [86], which was, to the best of our knowledge, one of the first investigations into active cloaking in Kirchhoff plates. A paper by Futhazar *et al.* [29] proposed a variational active shielding problem in elastic plates, based on the approach of Norris *et al.* [82], [83]. Similar to the works of Norris *et al.* [82], [83], Futhazar *et al.* [29] noted that a disadvantage of their approach was that "the active field may become uncontrollably large in the vicinity of the (point) source positions." This was due to how Graf's addition theorem was employed by the authors; the expressions for the fields produced by the active sources as well as the integral equations calculating source amplitudes, were only valid in a region that excluded the active source positions. As a result, the authors truncated the source multipole representations to "ensure a finite, (but large) field inside the source regions."

We recall that cloaking in this thesis is the cancellation of the scattered field, and is distinct in the approach from shielding problems that create a silent region around the object. Both methods achieve analogous results in the far field, yet the analysis for the cloaking problem described here is purely analytical and does not involve any integral representations such as those presented by Futhazar *et al.* [29]. Since we do not present a shielding problem, Graf's addition theorem can by employed to find the contributions to the total field propagating away from the scatterer due to the active sources. We can then obtain a system of algebraic equations for the unknown active source amplitudes, which can be solved analytically. It is important to note that by using Graf's addition theorem in this way, there are no divergent fields in a finite-sized region enclosing each source.

In section 2.1, we formulate the problem for scatterers that have an arbitrary shape, with a smooth, clamped boundary. We study in detail the canonical case of a rigid circular cavity with a clamped boundary in sections 2.2-2.5. The case of a circular scatterer is considered initially, to present the main ideas behind the cloaking method within the setting of a simpler geometry. The method described in this chapter produces closed form analytical solutions using the multipole method for circular scatterers. One can also appreciate how parameters of the configuration can be chosen in order to deliver effective cloaking.

In chapter 1, it was stated that solutions to problems governed by the fourth order biharmonic equation, describing pure bending in plates, were the superposition of solutions to the Helmholtz and modified Helmholtz equations. All waves solving the modified Helmholtz equation are evanescent and thus we annul only propagating components of the scattered field in order to deliver an effective approximate cloak at significant distances from the object.

A finite number of active sources are located exterior to the scatterer and each source is represented by a fundamental solution centred at the source position. The complex amplitudes of the active sources are tuned in order to cancel out selected multipole orders of the scattered field. The analytical method provides an approximate cloak that yields effective cloaking with only a few sources. We derive closed form analytical equations for calculating the unknown active source amplitudes that cancel selected orders of the scattered wave as well as propagating contributions to the outgoing wave from the active sources themselves.

We show results of cloaking with two active sources in section 2.3, and increase this number incrementally, and compare the effect on cloaking efficiency due to two, four and six active sources in section 2.4. It is shown that with the configuration of active sources described, as little as six sources cloaks a circular clamped scatterer.

The method of cloaking described in section 2.1 is generic and not limited to plane waves. In section 2.5 we show that the same method of cloaking can be applied to an incident field produced by a remote point source emitting a cylindrical wave. We show that six sources also produces effective cloaking from the remote point source.

We conclude the chapter by presenting results for cloaking an arbitrarily shaped scatterer with a clamped boundary in section 2.6. The same method is employed, but in this section, seven sources are required to deliver efficient cloaking of flexural waves.

2.1 Method of solution for a general forcing term

In this section, we state the method of solution for cloaking a single cavity of arbitrary shape subject to a general time-harmonic distributed load. In chapter 1, equation (1.5) described flexural waves in a Kirchhoff plate containing a circular clamped cavity. For an arbitrarily shaped scatterer, the governing equation (1.5) applies, but here, $\mathcal{D}$ is the region occupied by the arbitrarily shaped scatterer. Note that for this geometry, the coordinate axes are centred at a location inside $\mathcal{D}$. It was discussed in chapter 1 that solutions to the governing equation were the superposition of those to the Helmholtz and modified Helmholtz equations.

These solutions propagate independently, but are coupled by the boundary conditions.

The boundary of the arbitrarily shaped scatterer is denoted by $\partial\mathcal{D}$ as before, and clamped boundary conditions are imposed on $\partial\mathcal{D}$ as stated by equations (1.7). Clamped boundary conditions mean that the scatterer is immovable and no fields propagate inside.

To cloak an arbitrarily shaped clamped scatterer, subject to a time-harmonic distributed load, we place m active sources exterior to the scatterer at the points $\mathbf{x}^{(s,l)}$, where $l = 1, 2, \ldots, m$, and solve the following boundary value problem

$$\begin{aligned} (\Delta^2 - \beta^4)w(\mathbf{x}) + \mathcal{F}(\mathbf{x}) + \sum_{l=1}^{m} \mathcal{Q}_l\, \delta(\mathbf{x} - \mathbf{x}^{(s,l)}) = 0, \quad \mathbf{x} \in \mathbb{R}^2 \setminus \bar{\mathcal{D}}, \\ w(\mathbf{x}) = \frac{\partial w(\mathbf{x})}{\partial n} = 0, \quad \mathbf{x} \in \partial\mathcal{D}, \end{aligned} \tag{2.1}$$

where $w(\mathbf{x})$ denotes the flexural displacement, $\mathcal{F}(\mathbf{x})$ denotes the amplitude of the load and $\mathcal{Q}_l$ are the amplitudes of the active sources required to cloak the scatterer.

We write $w(\mathbf{x})$ as a sum of the incoming incident field $w_{inc}(\mathbf{x})$ and of the scattered field $w_{sc}(\mathbf{x})$:

$$w(\mathbf{x}) = w_{inc}(\mathbf{x}) + w_{sc}(\mathbf{x}).$$

The main objective behind our method of active cloaking is to reduce the scattered field so that the resulting total field satisfies the following

$$w(\mathbf{x}) \approx w_{inc}(\mathbf{x}). \tag{2.2}$$

To achieve (2.2), terms from the scattered field are cancelled using the active sources. We choose the active source amplitudes to cancel out both the scattered field and any propagating contributions to the outgoing wave due to the introduction of the sources.

The main outcome of our cloaking approach is to reduce $w_{sc}(\mathbf{x})$, satisfying condition (2.2). For incident plane waves and circular scatterers, we use the multipole method which leads to analytical solutions to the cloaking problem. The required number of the multipole terms in the representation of the scattered field are cancelled at some distance away from the scatterer. In the next section, we explain the algorithm for evaluating $\mathcal{Q}_l$ in the case of an incident plane wave.

Finally, we note that in general, solutions to boundary value problems can be written as integrals involving fundamental solutions. This technique can be used for obtaining solutions to equation (2.1). The fundamental solution $\overline{g}(\mathbf{x}; \mathbf{x}')$, is found by solving the boundary value problem corresponding to scattering reduction of a remote point source and m point sources positioned at $\mathbf{x}'$ and $\mathbf{x}^{(s,l)}$ (where $l = 1, 2, \ldots, m$), respectively. The boundary value problem reads as follows

$$\begin{aligned} (\Delta^2 - \beta^4)g(\mathbf{x}; \mathbf{x}') + \delta(\mathbf{x} - \mathbf{x}') + \sum_{l=1}^{m} \overline{\mathcal{Q}}_l(\mathbf{x}')\, \delta(\mathbf{x} - \mathbf{x}^{(s,l)}) = 0, \quad \mathbf{x} \in \mathbb{R}^2 \setminus \bar{\mathcal{D}}, \\ g(\mathbf{x}; \mathbf{x}') = \frac{\partial g(\mathbf{x}; \mathbf{x}')}{\partial n} = 0, \quad \mathbf{x} \in \partial\mathcal{D}, \end{aligned} \tag{2.3}$$

where $\delta(\mathbf{x}-\mathbf{X})$ denotes the Dirac delta function centred at the point $\mathbf{X}$ and $\overline{\mathcal{Q}}_l(\mathbf{x}')$ denotes the complex amplitudes of the remote point sources located at the positions $\mathbf{x}^{(s,l)}$, where $l = 1, 2, \ldots, m$. We assume that the fundamental solution $g(\mathbf{x};\mathbf{x}')$, satisfies the radiation condition at infinity to ensure that fields propagate away from the scatterer. In this case, the amplitudes $\mathcal{Q}_l$ required for cloaking the scatterer subject to the general forcing term will be written as integral representations dependant on $\overline{\mathcal{Q}}_l(\mathbf{x}')$.

2.2 Achieving scattering reduction with active sources

In section 2.1, we stated that complex amplitudes of the active sources were chosen to eliminate selected orders of the scattered field ensuring effective cloaking. We consider the case of plane waves incident on a rigid circular scatterer, since the geometry of the problem lends itself to the multipole method and an analytical solution of the problem can be obtained. For this case, the method outlined in section 2.1, leads to a system of linear algebraic equations for the active source amplitudes.

In section 1.1.2 of chapter 1, we derived a formula for a plane wave scattered from a circular clamped inclusion. In this section, we introduce two active sources, each located on the x_1-axis exterior to the clamped inclusion. The active sources are point sources of flexural waves located at $\mathbf{x}^{(s,1)} = (a^{(s,1)}, 0)$ and $\mathbf{x}^{(s,2)} = (-a^{(s,2)}, 0)$, with amplitudes Q_1 and Q_2, respectively. Here, we derive a system of equations for calculating the unknown source amplitudes such that terms from the scattered field are cancelled as well as any contributions to the far-field from the sources themselves. The amplitudes are complex to account for the phase of the incident wave. Since the function describing displacement is harmonic, throughout this chapter, we present snapshots of $\Re[\exp(-i\Phi)w(r,\theta)]$ for a particular value of the phase Φ between 0 and 2π. In all the contour plots within the text, we present results with a value of Φ that corresponds to a maximum displacement that coincides with the x_2-axis.

With the addition of active sources, the field incident on the cylinder now consists of the plane wave (referring to equation (1.12)) as well as contributions from the control sources. The multipole expansions are:

$$Q_1 G(x_1 - a^{(s,1)}, x_2) = -\frac{Q_1}{8\beta^2}\left[iH_0^{(1)}(\beta\sqrt{(x_1-a^{(s,1)})^2+x_2^2}) - \frac{2}{\pi}K_0(\beta\sqrt{(x_1-a^{(s,1)})^2+x_2^2})\right],$$

$$Q_2 G(x_1 + a^{(s,2)}, x_2) = -\frac{Q_2}{8\beta^2}\left[iH_0^{(1)}(\beta\sqrt{(x_1+a^{(s,2)})^2+x_2^2}) - \frac{2}{\pi}K_0(\beta\sqrt{(x_1+a^{(s,2)})^2+x_2^2})\right],$$

which, after using Graf's addition theorem outlined in section 1.3.1 of chapter 1, can be written as

$$Q_1 G(x_1 - a^{(s,1)}, x_2) = -\frac{Q_1}{8\beta^2}\sum_{k=-\infty}^{\infty} e^{ik\theta}\left[iH_k^{(1)}(\beta a^{(s,1)})J_k(\beta r) - \frac{2}{\pi}K_k(\beta a^{(s,1)})I_k(\beta r)\right],$$

$$Q_2 G(x_1 + a^{(s,2)}, x_2) = -\frac{Q_2}{8\beta^2} \sum_{k=-\infty}^{\infty} e^{ik(\theta-\pi)} \left[iH_k^{(1)}(\beta a^{(s,2)}) J_k(\beta r) - \frac{2}{\pi} K_k(\beta a^{(s,2)}) I_k(\beta r) \right],$$

In the above formulae, $G(x_1 - x_1^{(s,l)}, x_2 - x_2^{(s,l)})$ corresponds to the Green's function for the biharmonic operator centred at the position of the l-th point source (that is, $G(\mathbf{x}; \mathbf{x}^{(s,l)})$). The n-th order coefficients for the total wave incident on the rigid inclusion now read

$$\begin{aligned} A_n &= i^n \exp[-in\theta_{inc}] - \frac{i}{8\beta^2} \left[Q_1 H_n^{(1)}(\beta a^{(s,1)}) + (-1)^n Q_2 H_n^{(1)}(\beta a^{(s,2)}) \right], \\ B_n &= \frac{1}{4\pi\beta^2} \left[Q_1 K_n(\beta a^{(s,1)}) + (-1)^n Q_2 K_n(\beta a^{(s,2)}) \right], \end{aligned} \tag{2.4}$$

recalling that A_n and B_n premultiply $J_n(\beta r)$ and $I_n(\beta r)$ in equation (1.6) from chapter 1. From the scattering relation (1.9) in chapter 1, the n-th order coefficients for the scattered field are written as follows

$$E_n = \mathcal{S}_n^{11} A_n + \mathcal{S}_n^{12} B_n, \quad F_n = \mathcal{S}_n^{21} A_n + \mathcal{S}_n^{22} B_n. \tag{2.5}$$

We write the n-th order coefficient for the $H_n^{(1)}(\beta r)$ term in the field for $r > \max(a^{(s,l)})$ for $l = 1, 2$ that takes into account the field scattered from the clamped inclusion as well any propagating contributions to the far field from the active sources themselves, which are not part of the total scattered field. That is,

$$\mathcal{S}_n^{11} A_n + \mathcal{S}_n^{12} B_n - \frac{i}{8\beta^2} [Q_1 J_n(\beta a^{(s,1)}) + (-1)^n Q_2 J_n(\beta a^{(s,2)})], \tag{2.6}$$

while that for $K_n(\beta r)$ is

$$\mathcal{S}_n^{21} A_n + \mathcal{S}_n^{22} B_n + \frac{1}{4\pi\beta^2} [Q_1 I_n(\beta a^{(s,1)}) + (-1)^n Q_2 I_n(\beta a^{(s,2)})]. \tag{2.7}$$

We now have enough information satisfy the cloaking condition of equation (2.2) in section 2.1. This involves writing a system of equations for the source amplitudes, annulling multipole orders of the scattered wave and any propagating contributions from the sources themselves. For two sources, we can only eliminate up to the dipole term in order to obtain a consistent set of algebraic equations for Q_1, Q_2. The equations to be satisfied therefore read

$$\mathcal{S}_0^{11} A_0 + \mathcal{S}_0^{12} B_0 - \frac{i}{8\beta^2} [Q_1 J_0(\beta a^{(s,1)}) + Q_2 J_0(\beta a^{(s,2)})] = 0,$$

$$\mathcal{S}_1^{11} A_1 + \mathcal{S}_1^{12} B_1 - \frac{i}{8\beta^2} [Q_1 J_1(\beta a^{(s,1)}) - Q_2 J_1(\beta a^{(s,2)})] = 0,$$

and

$$\mathcal{S}_1^{11} A_{-1} - \mathcal{S}_1^{12} B_{-1} + \frac{i}{8\beta^2} [Q_1 J_1(\beta a^{(s,1)}) - Q_2 J_1(\beta a^{(s,2)})] = 0.$$

Using equation (2.4), we find for the monopole and dipole terms

$$S_0^{11} = \mathcal{L}_0, \quad ie^{-i\theta_{inc}} S_1^{11} = \mathcal{L}_1, \quad ie^{i\theta_{inc}} S_1^{11} = \mathcal{L}_1, \tag{2.8}$$

where

$$\begin{aligned}\mathcal{L}_j =& \frac{iQ_1}{8\beta^2}\left[\mathcal{S}_j^{11}H_j^{(1)}(\beta a^{(s,1)}) + \frac{2i}{\pi}\mathcal{S}_j^{12}K_j(\beta a^{(s,1)}) + J_j(\beta a^{(s,1)})\right] \\ &+ (-1)^j\,\frac{iQ_2}{8\beta^2}\left[\mathcal{S}_j^{11}H_j^{(1)}(\beta a^{(s,1)}) + \frac{2i}{\pi}\mathcal{S}_j^{12}K_j(\beta a^{(s,2)}) + J_j(\beta a^{(s,2)})\right], \quad j = 0, 1.\end{aligned} \tag{2.9}$$

We note that for a incident plane wave normal to the clamped inclusion, that is $\theta_{inc} = 0$, the last two equations in (2.8) are equivalent. It is also important to note that $\mathcal{L}_j = \mathcal{L}_{-j}$ for $j \in \mathbb{N}$ in equation (2.9). This property is due to the symmetry relations of the scattering matrix, and the Bessel and modified Bessel functions. As a result, the system of three equations in (2.8), reduces to a consistent set of equations for the unknown amplitudes Q_1 and Q_2.

Hence, for a circular geometry, we fix the angle of incidence so that $\theta_{inc} = 0$, and locate the active sources such that up-down symmetry is preserved. This leads to a system of consistent equations and if we wish to eliminate up to the general order L in the scattered field, we will require $2L$ active sources.

2.3 Active cloaking with two control sources

We consider examples illustrating the effect on scattering by a clamped circular inclusion due to the presence of active control sources. For given β, a_i, $a^{(s,1)}$ and $a^{(s,2)}$, and with $\theta_{inc} = 0$, the linear equations (2.8) are solved for Q_1 and Q_2. The n-th order scattered wave coefficients E_n and F_n follow from equations (2.4) and (2.5). Everywhere outside the scatterer, the flexural wave is given by

$$\begin{aligned}w(r,\theta) \;\approx\; & w_{inc}(r,\theta) + Q_1 G(r\cos\theta - a^{(s,1)}, r\sin\theta) + Q_2 G(r\cos\theta + a^{(s,2)}, r\sin\theta) \\ & + \sum_{n=-N}^{N}\left[E_n H_n^{(1)}(\beta r) + F_n K_n(\beta r)\right] e^{in\theta},\end{aligned} \tag{2.10}$$

where the summation limit N is chosen to be sufficiently large to ensure accuracy of the wave amplitude. The expression (2.10) of course gives a complex value, its real part representing the wave amplitude.

Fig. 2.1(a) shows flexural wave amplitude of the the total field outside a clamped circular inclusion with no control sources present. In the plot of Fig. 2.1(a), the region of small amplitude behind the cylinder is the most prominent indicator of the clamped inclusion's presence. Throughout this thesis, we refer to regions of small amplitude behind the scatterer as the shadow region.

Fig. 2.1(b) shows the flexural amplitude of the total field when two control sources with complex amplitudes $Q_{1,2} = -3.075 \mp 1.728\,i$ at $(a^{(s,1)}, 0)$, $(-a^{(s,2)}, 0)$, respectively, (with $a^{(s,1)} = a^{(s,2)} = 2.5$), annul the monopole and dipole components from both the scattered wave and the propagating contributions from the active sources. One can see that the shadow region has been suppressed and the wavefronts are straighter.

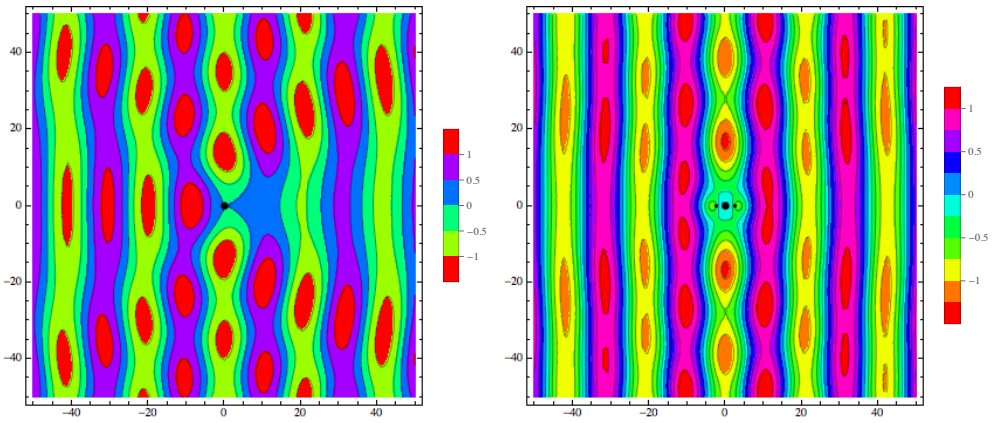

(a) (b)

Figure 2.1: Both figures depict the total flexural wave amplitude exterior to a circular clamped cavity depicted by the larger black dot. In either plot: $\beta = 0.3$, $a_i = 1.0$, $N = 2$, and $\Phi = \pi$. In part (a) there are no control sources, and in part (b) two control sources are located exterior to the cavity, depicted by the two smaller black dots positioned at $a^{(s,l)} = 2.5$ for $l = 1, 2$, with respective amplitudes $Q_{1,2} = -3.075 \mp 1.728\, i$.

The required strengths of the control sources increase strongly as $a^{(s,1)}, a^{(s,2)}$ tend towards a_i. (For example, with $a^{(s,1)}, a^{(s,2)} = 1.5$, they are $Q_{1,2} = -19.4 \mp 10.5\, i$.) The fact that the control amplitudes $Q_{1,2}$ are complex indicates that they depend on the phase Φ.

We plot the results the flexural wave amplitude of the total and scattered fields evalutated around a circle, whose radius is sufficiently large for the evanescent terms to have decayed. In Fig. 2.2, we compare the angular variations with no control sources to those with two control sources. The series solution for the scattered field was given in equation (1.13) which involved a $\cos(n(\theta - \theta_{inc}))$ term for each multipole order n. It is immediately clear from the scattered field amplitude plots in Figs. 2.2(b) and 2.2(d), that the control sources have successfully eliminated the monopole and dipole terms from the scattered wave, leaving the $\cos(2\theta)$-like term as the leading contributor to the wave amplitude.

A natural query relates to the optimal choice of the positions of the control sources. Given that for any $a^{(s,1)}, a^{(s,2)}$ one can annul monopole and dipole terms from the scattered wave and propagating field from the active sources, one might hope to minimise the amplitude of the quadrupole term by varying $a^{(s,1)}, a^{(s,2)}$. In Fig. 2.3, we plot the amplitude of the Hankel function quadrupole term as a function of $a^{(s,2)}$ and $a^{(s,1)}$. A line of symmetry exists along the line $a^{(s,1)}$=$a^{(s,2)}$, which implies that placing the sources at different distances from the inclusion will have little effect. This is also highlighted by the fact that there exists little variation in the numbers of the legend for the value of the quadrupole term. For these reasons, in all remaining illustrative plots, we position all active sources on a circle of equal radius.

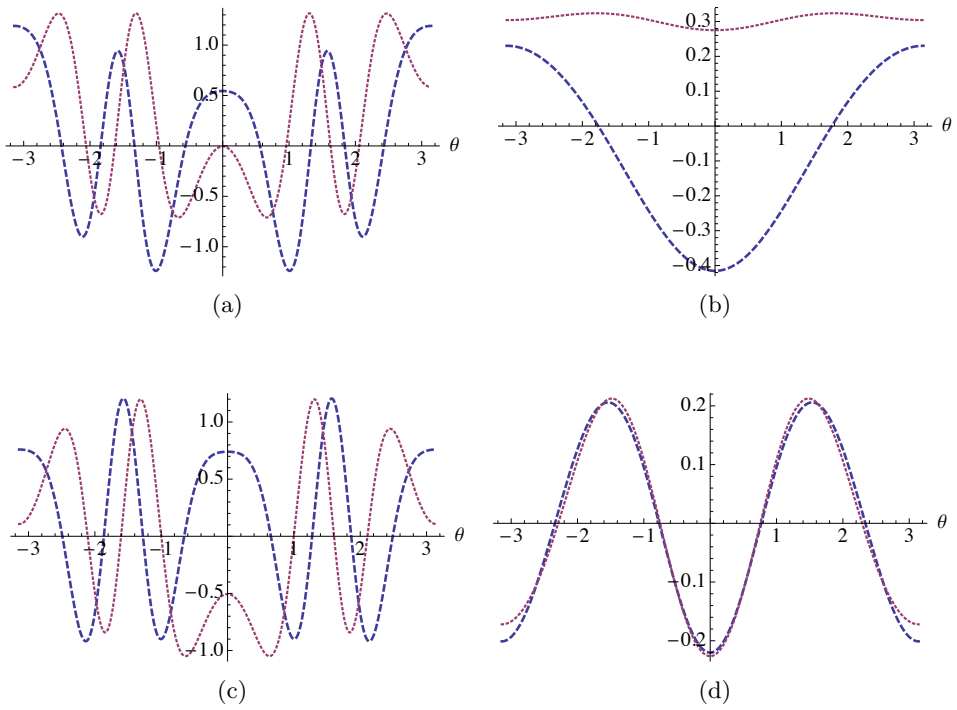

Figure 2.2: In all figures we plot the flexural wave amplitude as a function of θ, on a circle of radius 20. The scatterer is a circular clamped cavity with radius $a_i = 1.0$. In all figures $\beta = 0.3$, $N = 2$, dashed (blue): real part, dotted (red): imaginary part. Parts (a) and (b) depict the the respective amplitudes of the total and scattered fields with no control sources. Parts (c) and (d) are as (a) and (b), respectively, with the addition of two control sources positioned at $a^{(s,l)} = 2.5$ for $l = 1, 2$ whose respective amplitudes are $Q_{1,2} = -3.075 \mp 1.728\, i$.

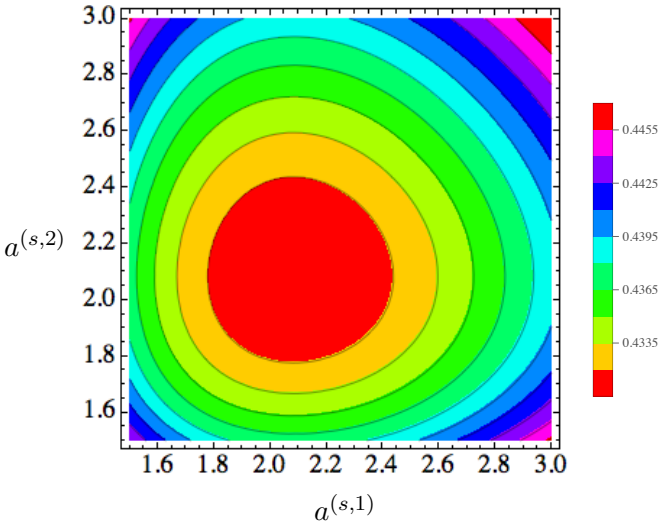

Figure 2.3: The amplitude of the outgoing Hankel function term from a circular rigid inclusion with angular dependence $\exp(2i\theta)$ in the flexural wave expansion, plotted as a function of $a^{(s,2)}$ and $a^{(s,1)}$. Note the almost constant amplitude levels, apparent in the legend.

2.4 Active cloaking with additional control sources

In what follows, we investigate how the number of active sources affects cloaking efficiency. We expect the cloaking results to improve when the number of control sources is increased. For a circular rigid inclusion, it is possible to ensure that $\theta_{inc} = 0$, by aligning the x_1-axis to coincide with the direction of the incident plane wave. We position additional active sources off the x_1-axis such that up-down symmetry is preserved, which also restricts the amplitudes of the active sources. Sources located opposite each other about the x_1-axis will have the same amplitude. By enforcing symmetry in the problem, we obtain a consistent set of algebraic equations analogous to equation (2.8), which calculate the active source amplitudes. If symmetry is broken by the positioning of additional active sources, or by a scatterer which does not have a symmetric profile, then the number of unknown amplitudes to be calculated is equal to the number of active sources, with this being the case for an arbitrarily shaped scatterer.

The multipole expansions for two additional control sources, located off the x_1-axis at $(a^{(s,3)}\cos\xi, \pm a^{(s,3)}\sin\xi)$, $0 < \xi < \pi/2$ (depicted in Fig. 2.4(a)), are

$$\begin{aligned} Q_3\, G(x_1 - a^{(s,3)}\cos\xi, x_2 \mp a^{(s,3)}\sin\xi) = \\ -\frac{Q_3}{8\beta^2}\left[iH_0^{(1)}\left(\beta\sqrt{(x_1 - a^{(s,3)}\cos\xi)^2 + (x_2 \mp a^{(s,3)}\sin\xi)^2}\right)\right. \\ \left. -\frac{2}{\pi}K_0\left(\beta\sqrt{(x_1 - a^{(s,3)}\cos\xi)^2 + (x_2 \mp a^{(s,3)}\sin\xi)^2}\right)\right], \end{aligned}$$

where Q_3 denotes the amplitude of the pair. Graf's addition theorem then gives the following for the multipole expansions of the additional sources

$$\begin{aligned} &Q_3\, G(x_1 - a^{(s,3)}\cos\xi, x_2 \mp a^{(s,3)}\sin\xi) = \\ &-\frac{Q_3}{8\beta^2}\sum_{k=-\infty}^{\infty} e^{ik(\theta\mp\xi)}\left[iH_k^{(1)}(\beta a^{(s,3)})J_k(\beta r) - \frac{2}{\pi}K_k(\beta a^{(s,3)})I_k(\beta r)\right]. \end{aligned} \tag{2.11}$$

We now have enough information to write the n-th order coefficients for the total wave incident on the clamped inclusion as

$$\begin{aligned} A_n &= i^n - \frac{i}{8\beta^2}\left[Q_1 H_n^{(1)}(\beta a^{(s,1)}) + (-1)^n Q_2 H_n^{(1)}(\beta a^{(s,2)}) - 2Q_3 H_n^{(1)}(\beta a^{(s,3)})\cos(n\xi)\right], \\ B_n &= \frac{1}{4\pi\beta^2}\left[Q_1 K_n(\beta a^{(s,1)}) + (-1)^n Q_2 K_n(\beta a^{(s,2)}) + 2Q_3 K_n(\beta a^{(s,3)})\cos(n\xi)\right]. \end{aligned} \tag{2.12}$$

Analogous to section 2.2, we set the n-th order coefficient for the $H_n^{(1)}$ term equal to zero, but this time for $r > \max(a^{(s,l)})$ for $l = 1, 2, 3$. We obtain the following constraints (when compared with equation (2.8))

$$\mathcal{S}_0^{11} = \mathcal{M}_0, \quad i\mathcal{S}_1^{11} = \mathcal{M}_1, \quad -\mathcal{S}_2^{11} = \mathcal{M}_2, \tag{2.13}$$

where

$$\mathcal{M}_j = \mathcal{L}_j + \frac{iQ_3}{4\beta^2}\Big[\mathcal{S}_j^{11} H_j^{(1)}(\beta a^{(s,3)}) + \frac{2i}{\pi}\mathcal{S}_j^{12} K_j(\beta a^{(s,3)}) + J_j(\beta a^{(s,3)})\Big]\cos(j\xi), \quad j = 0, 1, 2. \tag{2.14}$$

Note that $\mathcal{L}_2$ is defined by the formula (2.9) with $j = 2$. Again, for given $\beta, a_i, a^{(s,l)}$ $(l = 1, 2, 3)$ and ξ, we solve equations (2.13) for the unknown wave amplitudes Q_1, Q_2, and Q_3. The representation for the flexural wave outside the scatterer is now written as

$$\begin{aligned} w(r,\theta) \approx\ & w_{inc}(r,\theta) + \sum_{n=-N}^{N} \left[E_n H_n^{(1)}(\beta r) + F_n K_n(\beta r)\right] e^{in\theta} \\ & + Q_1 G(r\cos\theta - a^{(s,1)}, r\sin\theta) + Q_2 G(r\cos\theta + a^{(s,2)}, r\sin\theta) \\ & + Q_3 \big\{G(r\cos\theta - a^{(s,3)}\cos\xi, r\sin\theta - a^{(s,3)}\sin\xi) \\ & \qquad + G(r\cos\theta - a^{(s,3)}\cos\xi, r\sin\theta + a^{(s,3)}\sin\xi)\big\}. \end{aligned} \tag{2.15}$$

We note that the remark for the choice of N from section 2.3 still holds here (see equation (2.10)).

In Fig. 2.4, we present the total flexural wave amplitude pattern for four control sources, two on the x_1-axis as in section 2.3, positioned at $\mathbf{x}^{(s,1)} = (a^{(s,1)}, 0)$, $\mathbf{x}^{(s,2)} = (-a^{(s,2)}, 0)$ with amplitudes Q_1 and Q_2, respectively, and two additional sources symmetrically located off the x_1-axis at $\mathbf{x}^{(s,3)} = (a^{(s,3)}\cos\xi, a^{(s,3)}\sin\xi)$ and $\mathbf{x}^{(s,4)} = (a^{(s,3)}\cos\xi, -a^{(s,3)}\sin\xi)$ with the same intensity Q_3 (here, $a^{(s,l)} = 2.5$ for $l = 1, 2, 3$ and $\xi = \pi/4$, $\pi/3$, and $\pi/2$ in Figs. 2.4(b), 2.4(c) and 2.4(d), respectively) thus annulling quadrupole, as well as monopole and dipole outgoing wave amplitudes.

A marked improvement of Fig. 2.1(b) is clearly visible. In Figs. 2.4(b) and 2.4(c), the plane wave is almost reconstructed behind the rigid inclusion, and there is very little to distinguish between the amplitude fields. A visible improvement can be obtained by locating the two additional control sources on the x_2-axis ($\xi = \pi/2$), as shown in Fig. 2.4(d), where we see almost straight wave-fronts.

The efficiency of the method can be once again illustrated by the presence of the $\cos(3\theta)$ like term as the leading contributor to the wave amplitude in Fig. 2.4(f) (compare with Fig. 2.2(d) where $\cos(2\theta)$ is the leading contributor). Note, we only include the total and scattered wave amplitudes for the case of $\xi = \pi/2$. This is because the maximum of the scattered wave amplitude is in the region of 0.03, which was much larger that that for the $\xi = \pi/4$ and $\xi = \pi/3$ cases. The maximum of the scattered wave amplitude was in the region of 0.06 and 0.04 for $\xi = \pi/4$ and $\pi/3$, respectively. In all three cases, $\cos(3\theta)$-like behaviour was observed in the scattered wave plot. The analysis presented in Fig. 2.4 informs us that sources positioned on the same circle are most effective when they are equispaced.

If any further improvement to Fig. 2.4(d) is required, it is straightforward to add two more control sources to achieve effectively perfect cloaking. The new two control sources,

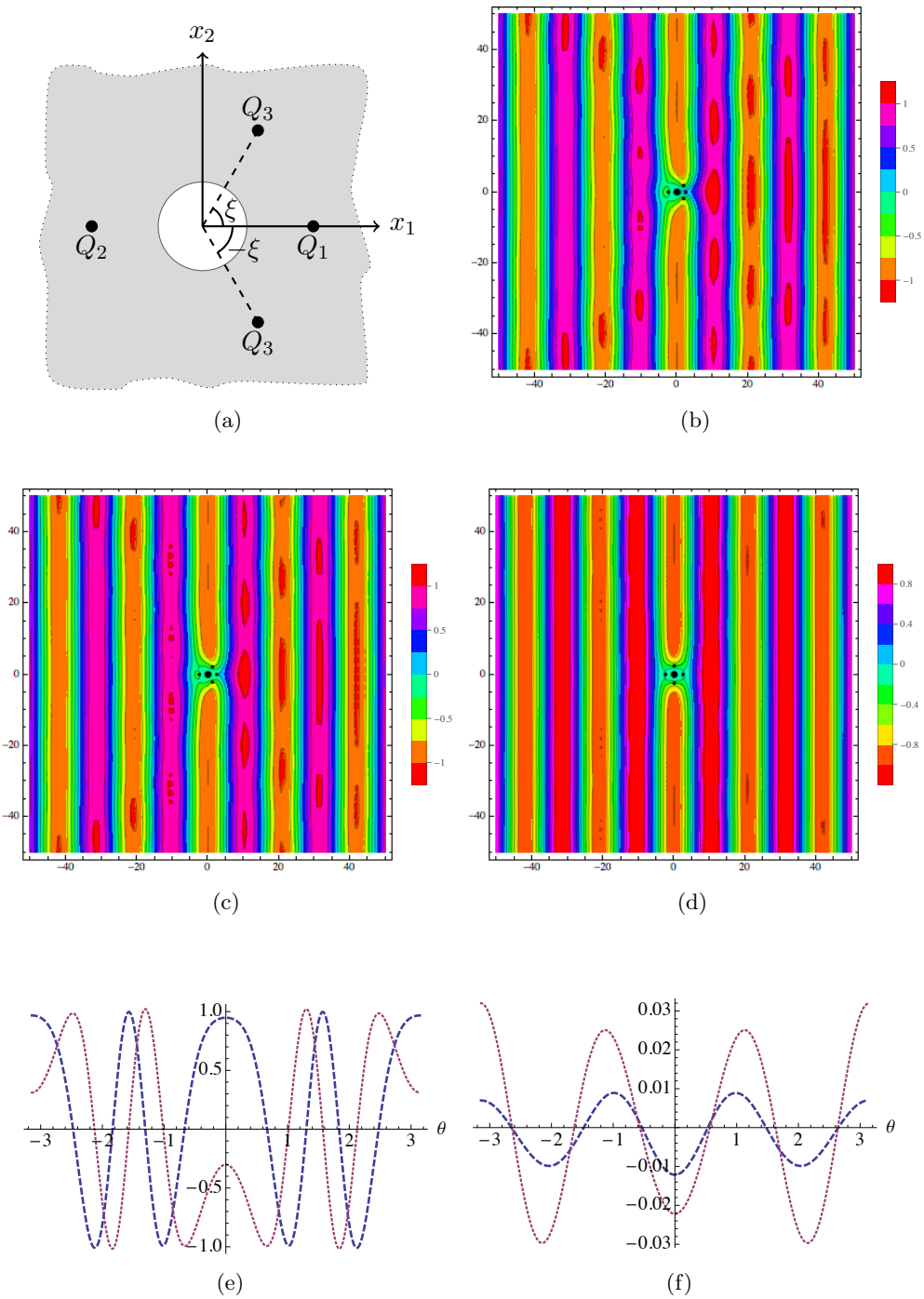

Figure 2.4: Part (a) shows a possible configuration four sources, detailing how ξ is measured. In parts (b)-(f) scattering is due a circular clamped cavity of radius $a_i = 1.0$, $\beta = 0.3$, $N = 2$, and $\Phi = \pi$. Contour plots (b)-(d) detail the total flexural wave amplitude due to the cavity and four control sources, which are depicted by the large and small black dots, respectively. The sources are located on a circle of radius $a^{(s,l)} = 2.5$, $l = 1, 2, 3$. In parts (b) $\xi = \pi/4$, and source amplitudes are $Q_1 = 2.628 - 1.728\,i$, $Q_2 = -2.096 + 1.728\,i$, and $Q_3 = -3.341$, (c) $\xi = \pi/3$ with $Q_1 = 0.266 - 1.728\,i$, $Q_2 = -1.961 + 1.728\,i$, $Q_3 = -2.227$, and in (d) $\xi = \pi/2$ with $Q_{1,2} = -1.404 \mp 1.728\,i$, $Q_3 = -1.670$. Parts (e) and (f) depict the the respective amplitudes of the total and scattered fields with four control sources when $\xi = \pi/2$. The dashed (blue) curve is the real part, whilst the dotted (red) is the imaginary part of the field.

symmetrically located about the x_1-axis at $\mathbf{x}^{(s,5)} = (a^{(s,4)}\cos\eta, a^{(s,4)}\sin\eta)$ and $\mathbf{x}^{(s,6)} = (a^{(s,4)}\cos\eta, -a^{(s,4)}\sin\eta)$, for $\pi/2 < \eta < \pi$, are both assumed to have unknown amplitude Q_4. Then similar to equation (2.11), we can write

$$Q_4\, G(x_1 - a^{(s,4)}\cos\eta, x_2 \mp a^{(s,4)}\sin\eta) = \\ -\frac{Q_4}{8\beta^2}\sum_{k=-\infty}^{\infty} e^{ik(\theta\mp\eta)}[iH_k^{(1)}(\beta a^{(s,4)})J_k(\beta r) - \frac{2}{\pi}K_k(\beta a^{(s,4)})I_k(\beta r)]. \tag{2.16}$$

Thus the n-th order coefficients A_n, B_n for the total wave incident on the cylinder (see equation (2.12)) will have the respective additional terms $-iQ_4H_n^{(1)}(\beta a^{(s,4)})\cos(n\eta)/(4\beta^2)$ and $Q_4K_n(\beta a^{(s,4)})\cos(n\eta)/(2\pi\beta^2)$. Just as before, for $r > \max(a^{(s,l)})$ for $l = 1,2,3,4$, we obtain the equations

$$\mathcal{S}_0^{11} = \mathcal{N}_0, \quad i\mathcal{S}_1^{11} = \mathcal{N}_1, \quad -\mathcal{S}_2^{11} = \mathcal{N}_2, \quad -i\mathcal{S}_3^{11} = \mathcal{N}_3, \tag{2.17}$$

$$\mathcal{N}_j = \mathcal{M}_j + \frac{iQ_3}{4\beta^2}\Big[\mathcal{S}_j^{11}H_j^{(1)}(\beta a^{(s,4)}) \\ + \frac{2i}{\pi}\mathcal{S}_j^{12}K_j(\beta a^{(s,4)}) + J_j(\beta a^{(s,4)})\Big]\cos(j\eta), \quad j = 0,1,2,3.$$

Here $\mathcal{M}_3$ is defined by formula (2.14) with $j = 3$.

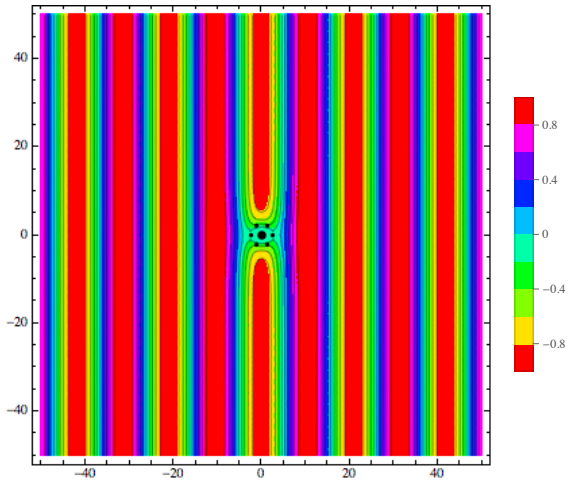

Figure 2.5: Total flexural wave amplitude exterior to a circular clamped cavity, depicted by the larger black dot of radius $a_i = 1.0$, where $\beta = 0.3$, $N = 2$, and $\Phi = \pi$. Six control sources are located exterior to the cavity such that $\xi = \pi/3$, $\eta = 2\pi/3$, and $a^{(s,l)} = 2.5$ for $l = 1,2,3,4$. The respective amplitudes are $Q_{1,2} = -0.848 \mp 1.146\,i$, $Q_{3,4} = -1.114 \mp 0.582\,i$. Note that $Q_{3,4}$ are the amplitudes of both sources off the x_1-axis in the Ist, IVth and IInd, IIIrd quadrants, respectively.

The intensities Q_1, Q_2, Q_3 and Q_4 are found by solving the system (2.17). The representation for the flexural wave outside the scatterer can then be modified accordingly (with the addition of two terms to formula (2.15)).

Fig. 2.5 presents the scattered wave amplitudes for a cylinder with six control sources, two on the x_1-axis as before, and four off the x_1-axis with $a^{(s,3)} = a^{(s,4)} = 2.5$ and $\xi = \pi/3$, $\eta = 2\pi/3$. Here, $Q_{1,2} = -0.848 \mp 1.146\,i$, $Q_{3,4} = -1.114 \mp 0.582\,i$ ($Q_{3,4}$ are the amplitudes of both sources off the x_1-axis in the Ist, IVth and IInd, IIIrd quadrants, respectively). It is clear that the presence of six control sources improves cloaking when compared with the already effective cloaking in Fig. 2.4(d).

Another demonstration of improved cloaking is clearly visible in Fig. 2.6(b) where the leading contribution to the wave amplitude shows $\cos(4\theta)$-like behaviour. Note that the scattered amplitude now peaks close to 0.0003, to be compared with 0.03 in the case of four control sources in Fig. 2.4(f).

To compare the cloaking achieved using two, four or six control sources, we present the coefficients of $H_n^{(1)}(\beta r)$ and $K_n(\beta r)$ terms in table 2.1. Note here that for four sources, we give coefficients for the configuration shown in Fig. 2.4(d). We can clearly see from the table that the shaded entries are satisfactorily small for $\tilde{E}_n$ compared to those in the no sources column, meaning the coefficients of $H_n^{(1)}(\beta r)$ for the targeted multipole orders n, have been successfully eliminated. As a result, the incident field is reconstructed in a region outside the sources and scatterer.

As trade-off for these eliminations, we expect to see an increase in the $\tilde{F}_n$ values. This is true for higher order coefficients ($|n| = 2, 3, 4$) when we first introduce two sources, however, comparing the four and six source configurations to that with two sources, the coefficients remain fairly constant for orders of n that have not been eliminated in $\tilde{E}_n$. The fact that there is little change is due to the circular geometry of the inclusion; we do not see any coupling between different orders of the multipole coefficients (which can be seen in equations (2.8), (2.13), and (2.17)) for sources placed in a way that does not break the symmetry of the problem.

Finally, we investigate the robustness of the cloak to small rotations. This is done by rotating the configuration of six control sources (with complex amplitudes as stated in Fig. 2.5) and rotating the entire configuration by an angle in the anti-clockwise direction. The results are presented in Fig. 2.7, which indicate that small rotations does not disrupt the cloaking drastically.

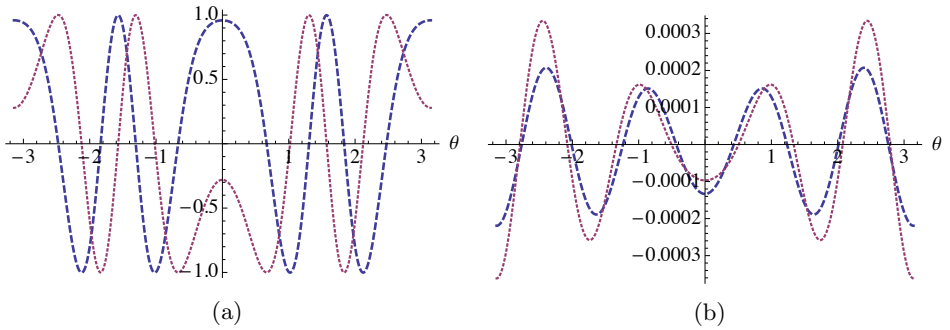

Figure 2.6: Flexural wave amplitude as a function of θ, on a circle of radius 40. The scatterer is a circular clamped cavity with radius $a_i = 1.0$. In both figures the dashed (blue) curve is the real part, whilst the dotted (red) curve is the imaginary part, also $\beta = 0.3$, and $N = 2$. Parts (a) and (b) depict the the respective amplitudes of the total and scattered fields with six control sources, such that $a^{(s,l)} = 2.5$ for $l = 1, 2, 3, 4$, $\xi = \pi/3$, $\eta = 2\pi/3$, and $Q_{1,2} = -0.848 \pm 1.146\,, Q_{3,4} = -1.114 \mp 0.582\,i$.

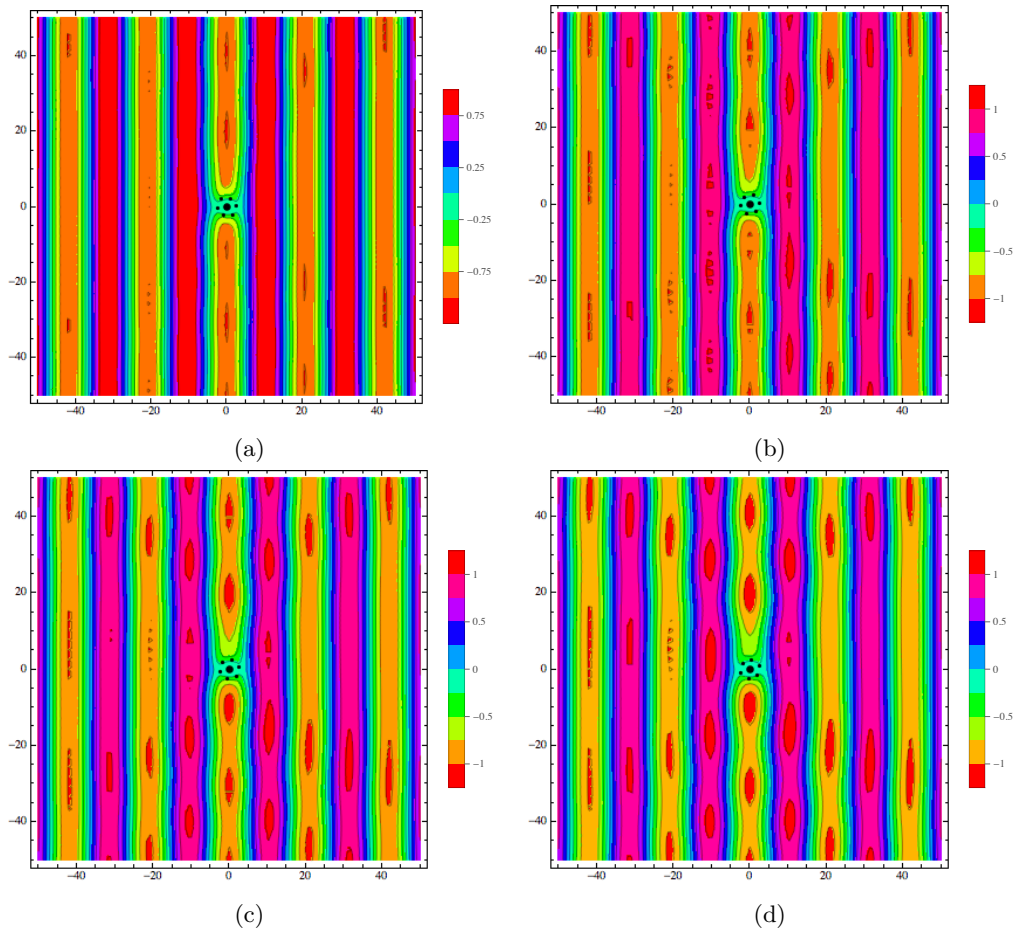

Figure 2.7: Total flexural wave amplitude exterior to a circular clamped cavity, depicted by the larger black dot of radius $a_i = 1.0$, where $\beta = 0.3$, $N = 2$, and $\Phi = \pi$. The configuration of six control sources as in Fig. 2.5, is rotated by an angle of (a) 5 degrees, (b) 10 degrees, (c) 15 degrees, (d) 20 degrees, respectively.

	n	no sources	2 sources	4 sources ($\pi/2$)	6 sources
$\tilde{E}_n$	-4	$-2.17\times10^{-12}-1.47\times10^{-6}\,i$	$9.94\times10^{-9}+0.007\,i$	$9.94\times10^{-9}+0.007\,i$	$-8.62\times10^{-10}-0.0006\,i$
	-3	$0.0004-1.53\times10^{-7}\,i$	$0.04-0.00001\,i$	$0.04-0.00001\,i$	$-1.20\times10^{-17}-1.64\times10^{-17}\,i$
	-2	$0.001+0.03\,i$	$0.02+0.43\,i$	$1.18\times10^{-16}-4.16\times10^{-17}\,i$	$-5.36\times10^{-17}+1.39\times10^{-17}\,i$
	-1	$-0.43+0.24\,i$	$-7.47\times10^{-7}+4.24\times10^{-7}\,i$	$-2.22\times10^{-16}-1.85\times10^{-17}\,i$	$2.22\times10^{-16}-1.88\times10^{-16}\,i$
	0	$-0.94+0.23\,i$	$-4.72\times10^{-7}+1.15\times10^{-7}\,i$	-5.50×10^{-16}	$-1.36\times10^{-16}+1.78\times10^{-15}\,i$
	1	$0.43-0.24\,i$	$7.47\times10^{-7}-4.24\times10^{-7}\,i$	$2.22\times10^{-16}+1.85\times10^{-17}\,i$	$-6.66\times10^{-16}-1.63\times10^{-16}\,i$
	2	$0.001+0.03\,i$	$0.02+0.43\,i$	$1.18\times10^{-16}-4.16\times10^{-17}\,i$	$6.05\times10^{-18}-2.78\times10^{-17}\,i$
	3	$-0.0004+1.53\times10^{-7}\,i$	$-0.04+0.00001\,i$	$-0.04+0.00001\,i$	$1.20\times10^{-17}+1.64\times10^{-17}\,i$
	4	$-2.17\times10^{-12}-1.47\times10^{-6}\,i$	$9.94\times10^{-9}+0.007\,i$	$9.94\times10^{-9}+0.007\,i$	$-8.62\times10^{-10}-0.0006\,i$
$\tilde{F}_n$	-4	$9.49\times10^{-7}-1.40\times10^{-12}\,i$	$-0.005+6.40\times10^{-9}\,i$	$-0.005+6.40\times10^{-9}\,i$	$0.0004-5.55\times10^{-10}\,i$
	-3	$-9.90\times10^{-8}-0.0003\,i$	$-9.67\times10^{-6}-0.03\,i$	$-9.67\times10^{-6}-0.03\,i$	$-1.28\times10^{-17}+1.55\times10^{-5}\,i$
	-2	$-0.02+0.0008\,i$	$-0.31+0.01\,i$	$0.002+8.52\times10^{-17}i$	$0.002-3.49\times10^{-17}\,i$
	-1	$0.16+0.29\,i$	$2.82\times10^{-7}-0.12\,i$	$3.86\times10^{-17}-0.12\,i$	$-1.54\times10^{-16}-0.12\,i$
	0	$-0.18-0.72\,i$	$-0.96-3.60\times10^{-7}\,i$	$-0.96-1.16\times10^{-16}\,i$	$-0.96-6.92\times10^{-16}\,i$
	1	$0.16+0.29\,i$	$2.82\times10^{-7}-0.12\,i$	$3.86\times10^{-17}-0.12\,i$	$3.93\times10^{-16}-0.12\,i$
	2	$-0.02+0.0008\,i$	$-0.31+0.01\,i$	$0.002+8.52\times10^{-17}i$	$0.002-8.67\times10^{-18}\,i$
	3	$-9.90\times10^{-8}-0.0003\,i$	$-9.67\times10^{-6}-0.03\,i$	$-9.67\times10^{-6}-0.03\,i$	$-1.28\times10^{-17}+1.55\times10^{-5}\,i$
	4	$9.49\times10^{-7}-1.40\times10^{-12}\,i$	$-0.005+6.40\times10^{-9}\,i$	$-0.005+6.40\times10^{-9}\,i$	$0.0004-5.55\times10^{-10}\,i$

Table 2.1: $\tilde{E}_n$ and $\tilde{F}_n$ denote the coefficients of $H_n^{(1)}(\beta r)$ and $K_n(\beta r)$ terms, respectively (referring to equations (2.6) and (2.7) for a configuration of two control sources located on the x_1-axis). Shaded entries correspond to the values of $n\,(=0,\pm1,\ldots,\pm4)$ for which we have eliminated the coefficients multiplying $H_n^{(1)}(\beta r)$ terms.

2.5 The fundamental solution for cloaking a circular clamped cavity

The method of cloaking presented in sections 2.2-2.4, is not limited to incident fields created by plane waves. In this section we consider the problem where the incident wave is generated by a remote point source, which corresponds to the Green's function for the biharmonic equation. We denote this Green's function by $G(\mathbf{x};\mathbf{x}')$ and in an infinite plate containing a circular rigid inclusion, it satisfies the following boundary value problem

$$\begin{aligned}(\Delta^2-\beta^4)G(\mathbf{x};\mathbf{x}')+\delta(\mathbf{x}-\mathbf{x}')=0, \quad \mathbf{x}\in\mathbb{R}^2\setminus\bar{\mathcal{D}}\\ G(\mathbf{x};\mathbf{x}')=\frac{\partial G(\mathbf{x};\mathbf{x}')}{\partial n}=0, \quad \mathbf{x}\in\partial\mathcal{D},\end{aligned} \tag{2.18}$$

where $\delta(\mathbf{x}-\mathbf{x}')$ denotes the Dirac delta function centred at the point $\mathbf{x}'$. In addition, $G(\mathbf{x};\mathbf{x}')$ satisfies the radiation condition at infinity. Our m active sources are described by the same Green's function, but for $\mathbf{x}'$ coinciding with the source location $\mathbf{x}^{(s,l)}$, for $l=1,2,\ldots,m$. We can write the fundamental solution $g(\mathbf{x};\mathbf{x}')$ for cloaking a circular rigid inclusion from a remote point source as the following

$$g(\mathbf{x};\mathbf{X})=G(\mathbf{x};\mathbf{x}')+\sum_{l=1}^{m}\mathcal{B}_l G(\mathbf{x};\mathbf{x}^{(s,l)}), \tag{2.19}$$

where $\mathbf{x}'$ denotes the position of the remote point source of the incident cylindrical wave and $\mathbf{x}^{(s,l)}$ the position of the l-th active source.

In the text below we find a representation for the fundamental solution $g(\mathbf{x};\mathbf{x}')$, in a plate containing a rigid circular inclusion of radius a_i, when the incident field is produced by a remote point source positioned on the x_1-axis. The origin of the coordinate axes coincides with the centre of the rigid inclusion as in previous sections, meaning $\mathcal{D}$ is a circle of radius a_i in formulae (2.18). We also impose up-down symmetry throughout, which restricts the positions $\mathbf{x}'$ and $\mathbf{x}^{(s,l)}$ to maintain the symmetry.

We place the remote point source sufficiently far away from the clamped inclusion at $\mathbf{x}'=(-c,0)$ to ensure that modified Helmholtz terms have decayed sufficiently. The incident wave is therefore represented by

$$w_{inc}(r,\theta)=-\frac{1}{8\beta^2}\sum_{k=-\infty}^{\infty}(-1)^k\left[iH_k^{(1)}(\beta c)J_k(\beta r)-\frac{2}{\pi}K_k(\beta c)I_k(\beta r)\right]e^{ik\theta},$$

where we assume that the amplitude of the incident wave is unity.

In this particular case, the coefficients of the n-th order total wave incident on the cylinder

now read

$$
\begin{aligned}
A_n = -\frac{i}{8\beta^2}\Bigg[&(-1)^n H_n^{(1)}(\beta c) + Q_1 H_n^{(1)}(\beta a^{(s,1)}) + (-1)^n Q_2 H_n^{(1)}(\beta a^{(s,2)}) \\
&+ 2[Q_3 H_n^{(1)}(\beta a^{(s,3)})\,\cos(n\xi) + Q_4 H_n^{(1)}(\beta a^{(s,4)})\cos(n\eta)]\Bigg], \\
B_n = \frac{1}{4\beta^2\pi}\Bigg[&(-1)^n K_n(\beta c) + Q_1 K_n(\beta a^{(s,1)}) + (-1)^n Q_2 K_n(\beta a^{(s,2)}) \\
&+ 2[Q_3 K_n(\beta a^{(s,3)})\,\cos(n\xi) + Q_4 K_n(\beta a^{(s,4)})\cos(n\eta)]\Bigg].
\end{aligned}
\tag{2.20}
$$

We note that formulae (2.20) are given for six control sources around the inclusion (targeting multipole orders between $-3 \le n \le 3$ in the scattered field); if there are only two control sources in the configuration (targeting multipole orders $-1 \le n \le 1$ in the scattered field) then $Q_3 = Q_4 = 0$, and if there are four control sources (targeting multipole orders $-2 \le n \le 2$ in the scattered field), then $Q_4 = 0$.

For $\max(a^{(s,l)}) < r < c$ where $l = 1, 2, 3, 4$, we obtain the following equations to find the amplitudes of the control sources Q_1,Q_2, Q_3 and Q_4

$$
-\frac{i}{8\beta^2}(-1)^j H_j^{(1)}(\beta c)\mathcal{S}_j^{11} + \frac{1}{4\beta^2\pi}(-1)^j K_j(\beta c)\mathcal{S}_j^{12} = \mathcal{N}_j, \tag{2.21}
$$

where

$$
\begin{aligned}
\mathcal{N}_j = \ \mathcal{M}_j + \frac{iQ_4}{4\beta^2}\Bigg[&\mathcal{S}_j^{11} H_j^{(1)}(\beta a^{(s,4)}) \\
&+ \frac{2i}{\pi}\mathcal{S}_j^{12} K_j(\beta a^{(s,4)}) + J_j(\beta a^{(s,4)})\Bigg]\cos(j\eta), \quad j = 0, 1, 2, 3.
\end{aligned}
$$

Here $\mathcal{M}_3$ is defined by formula (2.14) with $j = 3$. We note that the system of four linear algebraic equations in (2.21) can be written in matrix form as

$$
\begin{bmatrix}
\mathcal{C}_0^{(1)}(\beta a^{s,1}) & \mathcal{C}_0^{(1)}(\beta a^{(s,2)}) & 2\mathcal{C}_0^{(1)}(\beta a^{(s,3)})\cos(\xi) & 2\mathcal{C}_0^{(1)}(\beta a^{(s,4)})\cos(\eta) \\
\mathcal{C}_1^{(1)}(\beta a^{(s,1)}) & -\mathcal{C}_1^{(1)}(\beta a^{(s,2)}) & 2\mathcal{C}_1^{(1)}(\beta a^{(s,3)})\cos(2\xi) & 2\mathcal{C}_1^{(1)}(\beta a^{(s,4)})\cos(2\eta) \\
\mathcal{C}_2^{(1)}(\beta a^{(s,1)}) & \mathcal{C}_2^{(1)}(\beta a^{(s,2)}) & 2\mathcal{C}_2^{(1)}(\beta a^{(s,3)})\cos(3\xi) & 2\mathcal{C}_2^{(1)}(\beta a^{(s,4)})\cos(3\eta) \\
\mathcal{C}_3^{(1)}(\beta a^{(s,1)}) & -\mathcal{C}_3^{(1)}(\beta a^{(s,2)}) & 2\mathcal{C}_3^{(1)}(\beta a^{(s,3)})\cos(4\xi) & 2\mathcal{C}_3^{(1)}(\beta a^{(s,4)})\cos(4\eta)
\end{bmatrix}
\begin{bmatrix} Q_1 \\ Q_2 \\ Q_3 \\ Q_4 \end{bmatrix}
=
\begin{bmatrix}
-\mathcal{C}_0^{(2)}(\beta c) \\ \mathcal{C}_1^{(2)}(\beta c) \\ -\mathcal{C}_2^{(2)}(\beta c) \\ \mathcal{C}_3^{(2)}(\beta c)
\end{bmatrix},
$$

where

$$
\begin{aligned}
\mathcal{C}_p^{(2)}(\beta z) &= S_p^{11} H_p^{(1)}(\beta z) + \frac{2i}{\pi} S_p^{12} K_p(\beta z), \\
\mathcal{C}_p^{(1)}(\beta z) &= \mathcal{C}_p^{(2)}(\beta z) + J_p(\beta z), \qquad\qquad p = 0, 1, 2, 3,
\end{aligned}
$$

with z equal to c or $a^{(s,l)}$ $(l = 1, 2, 3, 4)$. The amplitudes Q_1, Q_2, Q_3 and Q_4 correspond to the coefficients $\mathcal{B}_l$ in equation (2.19) for the particular case of a circular inclusion with a remote point source placed on the x-axis at $\mathbf{x}' = (-c, 0)$ and up-down symmetry imposed.

Moreover, the Green's function for cloaking in this case is the total flexural wave everywhere outside the scatterer, which reads as follows for the case of six active sources

$$\begin{aligned} g(\mathbf{x};\mathbf{x}') \approx\ & G(r\cos\theta + c, r\sin\theta) + Q_1 G(r\cos\theta - a^{(s,1)}, r\sin\theta) + Q_2 G(r\cos\theta + a^{(s,2)}, r\sin\theta) \\ & + Q_3\{G(r\cos\theta - a^{(s,3)}\cos\xi, r\sin\theta - a^{(s,3)}\sin\xi) \\ & \qquad + G(r\cos\theta - a^{(s,3)}\cos\xi, r\sin\theta + a^{(s,3)}\sin\xi)\} \\ & + Q_4\{G(r\cos\theta - a^{(s,4)}\cos\eta, r\sin\theta - a^{(s,4)}\sin\eta) \\ & \qquad + G(r\cos\theta - a^{(s,4)}\cos\eta, r\sin\theta + a^{(s,4)}\sin\eta)\} \\ & + \sum_{n=-N}^{N} [E_n H_n^{(1)}(\beta r) + F_n K_n(\beta r)]\, e^{in\theta}. \end{aligned}$$

Referring back to the problem formulation of section 2.1, we have now obtained the Green's function that enables us to cloak a time-harmonic forcing term with amplitude $\mathcal{F}(\mathbf{x})$.

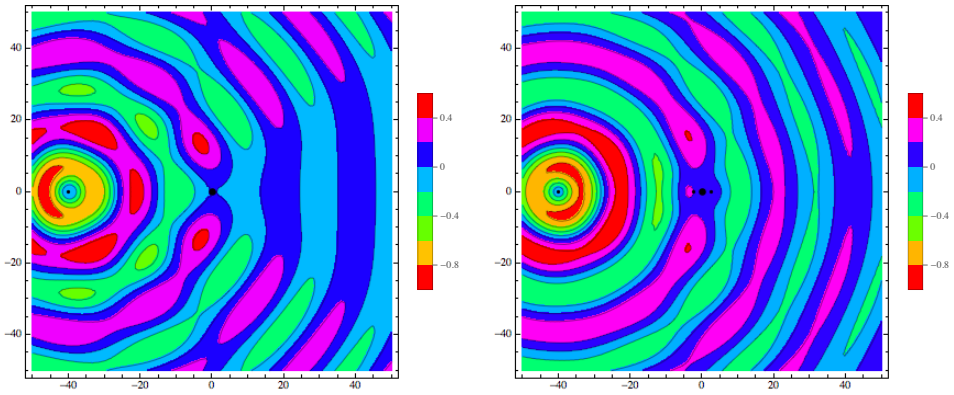

(a) (b)

Figure 2.8: Both figures depict the total flexural wave amplitude exterior to a circular clamped cavity depicted by the larger black dot. In both plots, the incident wave is due to a remote point source depicted by a small black dot at $(-40, 0)$. Other parameters in the figures are $\beta = 0.3$, $a_i = 1.0$, $N = 2$, and $\Phi = \pi$. In part (a) there are no control sources, and in part (b) two control sources are located exterior to the cavity, depicted by the two smaller black dots positioned at $a^{(s,l)} = 2.5$ for $l = 1, 2$, with amplitudes $Q_1 = 0.825 + 0.740i$ and $Q_2 = 1.099 - 0.333i$.

Figs. 2.8(a) and 2.8(b) depict the total wave amplitudes for a cylinder with no control sources present, and two control sources positioned on the x_1-axis as in section 2.3, respectively. The control sources in Fig. 2.8(b) have intensities $Q_1 = 0.825 + 0.740i$ and $Q_2 = 1.099 - 0.333i$. When there are no control sources present, we see a large shadow region behind the cylinder, but a clear improvement is made when two sources are added; we begin to reconstruct the cylindrical wave in this region.

Amplitude plots for four control sources surrounding the inclusion with the same configuration as in section 2.4 are presented in Fig. 2.9. The progression of the efficiency of cloaking from $\xi = \pi/4$ or $\xi = \pi/3$ to $\xi = \pi/2$ is clearly visible.

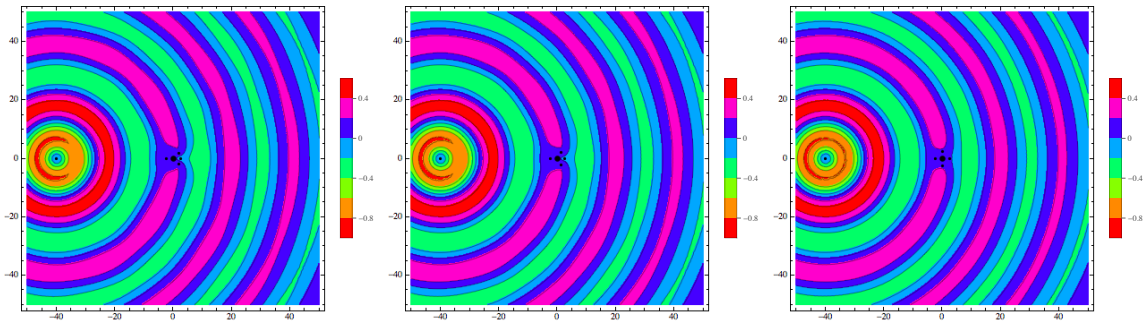

(a) (b) (c)

Figure 2.9: Total flexural wave amplitude exterior to a circular clamped cavity of radius $a_i = 1.0$, depicted by the large black dot. In all figures $\beta = 0.3$, $N = 2$, and $\Phi = \pi$. The incident wave is due to a remote point source depicted by a small black dot at $(-40, 0)$. Four control sources surround the cavity and are depicted by the small black dots located on a circle of radius $a^{(s,l)} = 2.5$, $l = 1, 2, 3$. In parts (a) $\xi = \pi/4$, and source amplitudes are $Q_1 = -0.953 + 0.339i$, $Q_2 = 0.794 - 0.402i$, $Q_3 = 1.042 + 0.235i$, (b) $\xi = \pi/3$ with $Q_1 = -0.217 + 0.505i$, $Q_2 = 0.752 - 0.411i$, $Q_3 = 0.694 + 0.157i$, and in (c) $\xi = \pi/2$ with $Q_1 = -0.304 + 0.623i$, $Q_2 = 0.578 - 0.450i$, $Q_3 = 0.521 + 0.118i$.

Finally in Fig. 2.10, we illustrate the cloaking of the inclusion using six control sources. It is clear from Fig. 2.10, that the scattered field has been significantly suppressed, and effective cloaking of a remote point source has been achieved.

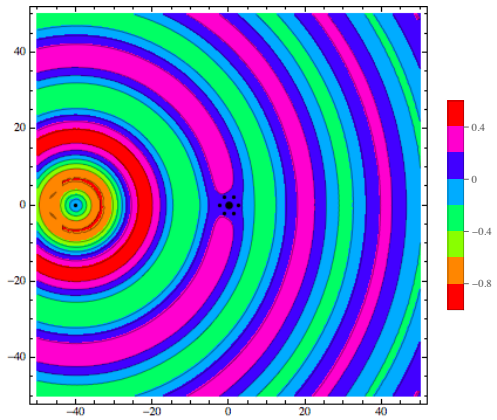

Figure 2.10: Total flexural wave amplitude exterior to a circular clamped cavity, depicted by the larger black dot of radius $a_i = 1.0$, where $\beta = 0.3$, $N = 2$, and $\Phi = \pi$. The incident wave is due to a remote point source depicted by a small black dot at $(-40, 0)$. Six control sources are depicted by the small black dots located exterior to the cavity such that $\xi = \pi/3$, $\eta = 2\pi/3$, and $a^{(s,l)} = 2.5$ for $l = 1, 2, 3, 4$. The respective amplitudes are $Q_1 = -0.253 + 0.386i$, $Q_2 = 0.282 - 0.292i$, $Q_3 = 0.224 + 0.275$, $Q_4 = 0.470 - 0.119i$.

2.6 Active cloaking of an arbitrarily shaped cavity with a smooth clamped boundary

In what follows, we generalise the algorithm of the previous sections to cloaking an arbitrarily shaped cavity (rigid inclusion) with a smooth boundary. In this section, we show that the main idea of annulling selected terms of the total scattered field everywhere outside the scatterer, by an appropriate tuning of the active source intensities, can be combined with numerics to obtain effective cloaking.

For an arbitrarily shaped cavity, we can still implement the same cloaking method as before. The method now uses Fourier series expansions that are obtained numerically by solving two model problems illustrated in Fig. 2.11. (Note, these series can only be obtained for sufficiently large arguments βr.) These problems deal with scattering from the cavity by an incident plane wave, and a remote point source. The Fourier series expansions are used to obtain an algebraic system of equations for the active source amplitudes which ensures that a targeted number of terms from the total wave scattered from the cavity are successfully annulled. We note that the origin of our coordinate axes resides inside the arbitrarily shaped cavity. For the first model problem of plane wave scattering, we write the following boundary value problem for the displacement field $w(\mathbf{x})$

$$\begin{aligned} \Delta^2 w(\mathbf{x}) - \beta^4 w(\mathbf{x}) = 0 \quad &\text{in } \mathbb{R}^2 \setminus \bar{\mathcal{D}}, \\ w(\mathbf{x}) = \frac{\partial w(\mathbf{x})}{\partial n} = 0 \quad &\text{on } \partial\mathcal{D}, \end{aligned}$$

where $\mathcal{D}$ is the region occupied by the arbitrarily shaped scatterer. Note that $w(\mathbf{x})$ can be written as the sum of the incident field $w_{inc}(\mathbf{x})$ and the scattered field $w_{sc}(\mathbf{x})$, that is

$$w(\mathbf{x}) = w_{inc}(\mathbf{x}) + w_{sc}(\mathbf{x}),$$

where $w_{inc}(\mathbf{x})$ is the same as $w_{inc}(\mathbf{x})$ defined in equations (1.11) and (1.12) and the scattered wave $w_{sc}(\mathbf{x})$ has the asymptotic representation

$$\begin{aligned} w_{sc}(\mathbf{x}) &= \sum_{n=-\infty}^{\infty} \left[E_n H_n^{(1)}(\beta r) + F_n K_n(\beta r) \right] e^{in(\theta - \theta_{inc})} \\ &\sim \sum_{n=-\infty}^{\infty} E_n H_n^{(1)}(\beta r) e^{in(\theta - \theta_{inc})}, \end{aligned} \tag{2.22}$$

where E_n are constant coefficients. We note that the evanescent term in the scattered field is neglected since $K_n(\beta r) = O(\exp(-\beta r)/(\beta r))$ as $\beta r \gg 1$. (Note, this can be found in [1] as formula 9.7.2.)

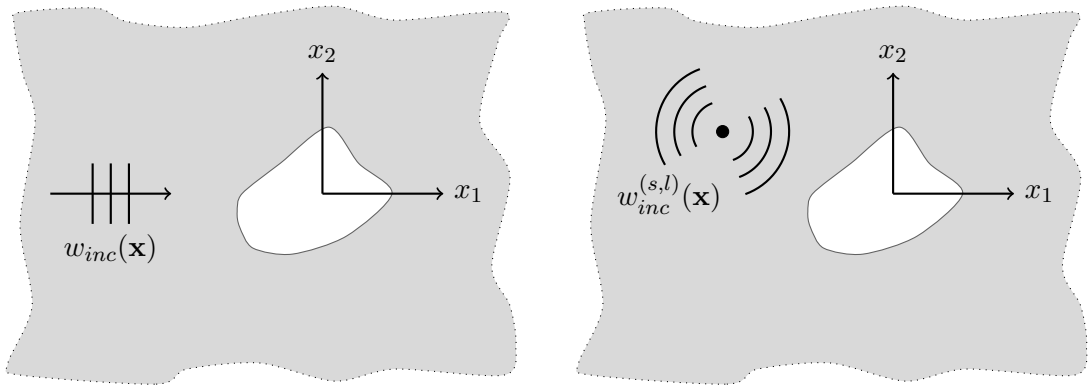

(a) (b)

Figure 2.11: Model problems for flexural wave scattering by an arbitrarily shaped scatterer. The incident field is due to (a) a plane wave where $\theta_{inc} = 0$, and (b) a remote point source at the position of the l-th active source $\mathbf{x}^{(s,l)}$.

The second model problem involves scattering of a point source from the arbitrarily shaped cavity. We note that a model problem of this type is solved separately for each source position in the configuration. That is, for a configuration of m active sources, there are m model problems of the second type considering a single source; in each problem the position of the remote source changes to coincide with that of the active source in question. This enables us to find the contribution to the total scattered wave from the active sources, everywhere outside the scatterer. We denote the displacement field due to the l-th point source by $w^{(s,l)}(\mathbf{x})$, and write the following boundary value problem

$$\begin{aligned} \Delta^2 w^{(s,l)}(\mathbf{x}) - \beta^4 w^{(s,l)}(\mathbf{x}) + \delta(\mathbf{x} - \mathbf{x}^{(s,l)}) = 0 \quad &\text{in } \mathbb{R}^2 \setminus \bar{\mathcal{D}}, \\ w^{(s,l)}(\mathbf{x}) = \frac{\partial w^{(s,l)}(\mathbf{x})}{\partial n} = 0 \quad &\text{on } \partial\mathcal{D}, \end{aligned}$$

where $\delta(\mathbf{x}-\mathbf{x}^{(s,l)})$ denotes the Dirac delta function, centred at $\mathbf{x}^{(s,l)}$. In fact, $w^{(s,l)}(\mathbf{x})$ admits the solution

$$\begin{aligned} w^{(s,l)}(\mathbf{x}) &= w_{inc}^{(s,l)}(\mathbf{x}) + w_{sc}^{(s,l)}(\mathbf{x}) = G(\mathbf{x};\mathbf{x}^{(s,l)}) + w_{sc}^{(s,l)}(\mathbf{x}), \\ &\sim \sum_{n=-\infty}^{\infty} A_n^{(s,l)} H_n^{(1)}(\beta r) e^{in\theta}, \quad l = 1, \ldots, m, \end{aligned} \tag{2.23}$$

where once again, exponentially small terms, that satisfy the modified Helmholtz equation, are not shown. Here $G(\mathbf{x};\mathbf{x}^{(s,l)})$ denotes the Green's function for the biharmonic operator, $w_{sc}^{(s,l)}(\mathbf{x})$ is the scattered field due to the unit source at $\mathbf{x}^{(s,l)}$, and $A_n^{(s,l)}$ are complex coefficients.

For sufficiently large arguments βr, the coefficients E_n and $A_n^{(s,l)}$ can be taken from the Fourier series expansions found by numerically solving the model problems discussed above. That is, we a obtain a number of Fourier series expansions which approximate the total field exterior to the scatterer. One of these expansions approximates the solution to the first model

problem and takes the form of (2.22), whilst the remaining expansions approximate solutions to the second model problem at each of the active source positions in the configuration and each take the form of (2.23).

Active cloaking is therefore achieved by introducing a set of m control sources, with complex intensities Q_l, placed exterior to the scatterer $\mathcal{D}$ at the points $\mathbf{x}^{(s,l)}$. After truncation to order L in the expansions (2.22), (2.23), we choose $m = 2L+1$, so that the total displacement field $w_{tot}(\mathbf{x})$ is approximately equal to the incident field $w_{inc}(\mathbf{x})$, that is

$$w_{tot}(\mathbf{x}) = w(\mathbf{x}) + \sum_{l=1}^{m} Q_l w^{(s,l)}(\mathbf{x}) \approx w_{inc}(\mathbf{x}). \tag{2.24}$$

To find Q_l, we substitute (2.22) and (2.23) into (2.24), and obtain the following system of linear algebraic equations

$$E_k e^{-ik\theta_{inc}} + \sum_{l=1}^{m=2L+1} Q_l A_k^{(s,l)} = 0, \quad k = -L, \ldots, L. \tag{2.25}$$

The evaluation of Q_l relies on the solution of the model problems discussed above. Note that for convenience, we assume that $\theta_{inc} = 0$. We only require that the first $m = 2L + 1$ coefficients be calculated in the Fourier series expansions of (2.22) and (2.23). This can be done, for example, numerically using a FEM package such as COMSOL. Once we know the necessary coefficients E_k and $A_k^{(s,l)}$ for $k = -L, \ldots, L$, we solve the system (2.25) for the intensities Q_l of the control sources. Note here, that the number of sources determines the value of L in equation (2.25).

We illustrate the results of cloaking depicting an unperturbed plane wave propagating horizontally against the plane wave interacting with a clamped scatterer are shown in Figs. 2.12(a) and 2.12(b), respectively. We note that perfectly matched layers (PML) are used on the exterior boundary of the computational domain to provide non-reflective boundary conditions. A shadow region is clearly visible behind the scatterer in Fig. 2.12(b).

To set up an active cloak, seven control sources are positioned around the scatterer, as displayed in Fig. 2.12(c). This means we have seven Fourier coefficients, which is enough to sufficiently approximate series (2.22) and (2.23). These coefficients are calculated on the circle shown in Fig. 2.12(b). The resulting computation in Fig. 2.12(d) indicates that the unperturbed plane wave has emerged behind the scatterer, meaning the cloak successfully reconstructs the incident field as required.

The efficiency of cloaking can be also shown by plotting the total displacement field along the x_1-axis of the plate (see Fig. 2.13). Data set 2 (green) shows the real (Fig. 2.13(a)) and imaginary (Fig. 2.13(b)) parts of the field in a plate where there is an arbitrarily shaped scatterer with no control sources surrounding it. The presence of the shadow region is prominent in Fig. 2.13(a) as the real part of the displacement field decreases dramatically behind the scatterer. We also see no sinusoidal features of the imaginary part of the field from Fig. 2.13(b). Data set 1 (in red), shows the real (Fig. 2.13(a)) and imaginary (Fig.

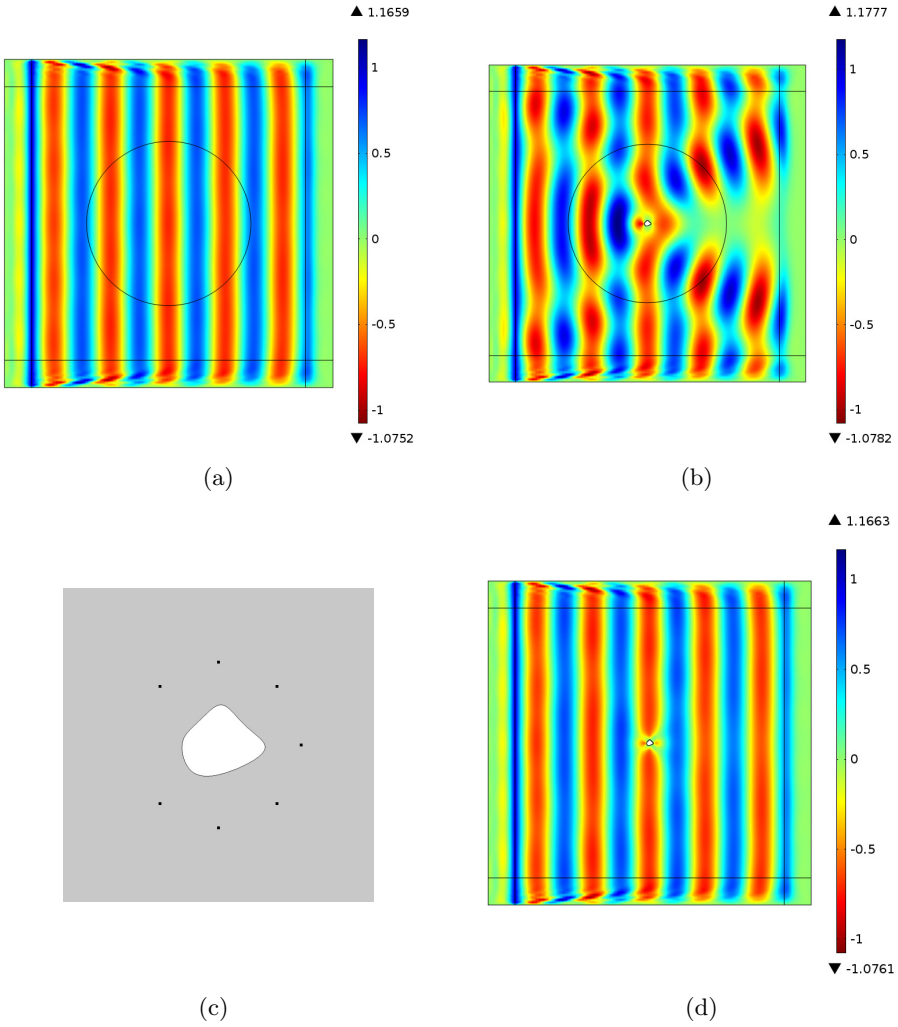

Figure 2.12: (a) Plane wave generated by displacing the boundary of the PML region on the left by 1 unit. (b) Flexural wave amplitude for an arbitrarily shaped cavity with no control sources. (c) Enlarged view of the cavity and the locations of the control sources. (d) Cloaking achieved by the use of seven control sources.

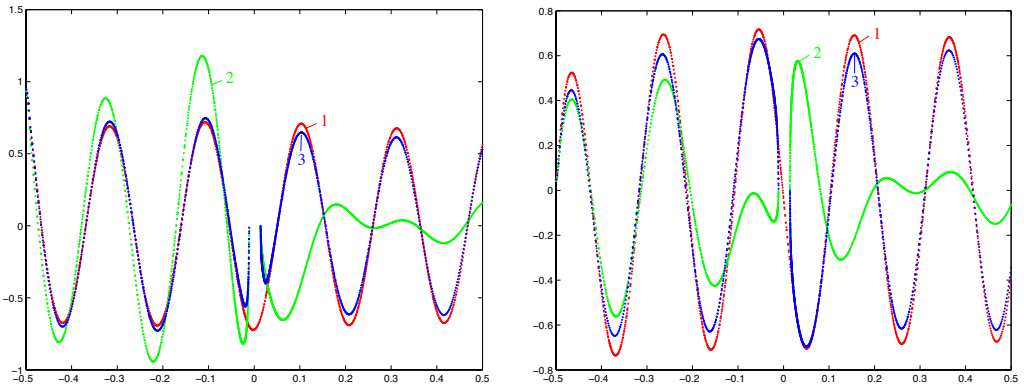

(a) (b)

Figure 2.13: Resulting total flexural amplitude plotted along the x_1-axis ((a) real, (b) imaginary) for plane wave propagation in a plate with no scatterer (corresponding to Fig. 2.12(a)) in red (numbered as 1), with an arbitrarily shaped scatterer (corresponding to Fig. 2.12(b)) in green (numbered as 2) and with the added active control sources (corresponding to Fig. 2.12(d)) in blue (numbered as 3).

2.13(b)) parts of the field in a plate with no scatterer, whilst data set 3 (in blue), shows that for an arbitrarily shaped cavity with the seven surrounding point sources discussed earlier. It is clear that data set 3 lies within close proximity to data set 1, indicating that the incident plane wave has been reconstructed in the plate, and no scattering is apparent from the cavity. Note that the small discontinuities in data sets 2 and 3 near the origin along the x_1-axis are due to the location of the scatterer.

2.7 Remarks and discussions

In this chapter we have demonstrated an efficient method of active cloaking for flexural waves scattered by rigid inclusions in Kirchhoff plates. The method has been developed for the fourth-order differential operator, where the Green's function is non-singular.

Leading multipole terms in the scattered field were cancelled by tuning the complex amplitudes of a finite number of point sources positioned around the inclusion. The results showed virtually complete suppression of the shadow region behind the clamped inclusion, which led to effective cloaking.

The method presented in the chapter is generic and was shown to extends to other types of boundary conditions as well as different types of incident wave. The engineering books by Nelson and Elliott [72] and Fuller *et al.* [28] discuss results for active cloaking systems in acoustics, which are relevant to the work described in this chapter. Frequently, coupled problems need to be treated, with the aim of controlling acoustic noise generated by a flexural vibration. The practical systems developed by Nelson and Elliott [72] and Fuller *et al.* [28] could indeed be modified to implement the active cloaking results presented in this chapter.

A natural extension from cloaking inclusions with clamped boundaries is to consider inclusions allowing for perfect transmission. The interesting problem to consider next is how the cloaking mechanism copes when the frequency of the incident wave coincides with resonant frequencies of the inclusion embedded within the plate.

Chapter 3

Active cloaking at resonant regimes

Resonant regimes result in strongly enhanced scattering amplitudes, which change rapidly with frequency, leaving our cloaking system vulnerable to frequency-swept probe beams. In these situations, the active sources of the cloaking device have to compensate for changes not only in the incident field, but also in scattering properties of the resonating inclusion. Often time lags in cloaking response inevitably increase with the sharpness (or Q factor) of the resonance. The effects of time lags caused by frequency-swept probe beams are discussed in the paper by Miller [61]. In the same paper, a cloaking algorithm involving active sources is presented in order to achieve a perfect cloak in a "limiting, classical case". Miller [61] also discusses the vulnerability of such a cloak to broad-band probing.

In this chapter, our objective is to ensure that active cloaking works well near resonant frequencies. We modify the configuration of the cloaked object, combining passive and active techniques to design a cloak for an inclusion in three frequency regimes: the low-frequency range, the intermediate range, and the higher frequency range in which scattering resonances occur.

A recent paper by Farhat *et al.* [23] advocated the mass compensation formula as stated by Voigt [102] in connection with the cloaking of an elastic circular inclusion in a Kirchhoff plate. The simple mass-compensation formula targets the monopole scatterer, and is only effective in low-frequency regimes. The authors of [23] introduced an inertial coating around the inclusion and stated that by a mass-compensation argument, the scattered field could be substantially reduced in the low-frequency regime. This argument is appealing, as it gives a simple formula for the mass density ρ_c of the ring-like coating around the inclusion

$$\rho_c = \frac{\rho_e - \rho_i (a_i/a_c)^2}{1 - (a_i/a_c)^2}. \tag{3.1}$$

Here ρ_i, ρ_e are mass densities of the inclusion and exterior matrix, respectively, and a_i, a_c are the interior and exterior radii of the coating. We soon show that, while this formula appears to be effective for a limited class of problems describing membrane waves governed by the Helmholtz equation, the formula does not apply to heterogeneous Kirchhoff plates containing inclusions whose elastic properties differ from the properties of the exterior matrix.

Instead, the configurational change that we propose, combines passive and active techniques; we introduce a coating around the inclusion that delivers a flat reflectance as a function of frequency, rather than cancelling the leading order behaviour of the scattered field. Note that passive techniques reducing the leading order behaviour of the scattered field are narrow-band at any but the quasi-static regime where they are designed to work. The cloaking method we develop in this chapter enables the active element of the cloak to operate effectively in the targeted frequency range. We illustrate that good quality cloaking is always possible in higher frequency resonance regimes.

It was highlighted by Norris and Vermula [84] that the approach of classical plate theory was suitable for "large plates with distant edges" as edge effects could be ignored in the first approximation. Poulton *et al.* [89] also discussed that the ratio of the plate thickness to wavelength must be small in order to accurately describe Bloch-Floquet waves in a structured elastic plate, and the paper by Rose and Wang [92] stated that classical plate theory is "known to be accurate for wavelengths greater than, say, $20h$", where h is the plate thickness. Throughout this thesis, we normalise plate thickness and consider an infinite plate, meaning that Kirchhoff plate theory is applicable at the frequencies we consider according to the arguments made by the aforementioned authors. We remark that in order to ensure applicability of classical plate theory in an experimental simulation, the condition on plate thickness as stated by Rose and Wang [92] must be observed when modelling a finite plate of a given material. As stated earlier in the thesis, one of the key assumptions in Kirchhoff plate theory is that deflections within the plate are assumed to be small. We note that one may observe large amplitudes when studying resonance regimes of inclusions, and these effects should be taken into consideration for practical applications.

We emphasise, on the importance of the high-order terms in the multipole representation of the overall solution. In particular, even in the long-wave approximation, the quadrupole coefficient (for the case of Kirchhoff plates) and the dipole coefficient (for the case of the Hemholtz equation) may be of the same order as the monopole coefficient.

In the paper by Farhat *et al.* [23], specific assumptions were made regarding the material parameters of the coated inclusion embedded in a Kirchhoff plate. In particular, mass densities differ from the exterior to the inclusion, but elastic properties (flexural rigidities and Poisson's ratio) of the three regions are the same. Under such assumptions, it can be shown that in the quasi-static regime, flexural waves in Kirchhoff plates can be approximated by flexural waves in a membrane, which was the setting used by Farhat *et al.* [23].

The ultimate aim of this chapter is to cloak an inclusion from flexural waves in a Kirchhoff plate at resonant frequencies by combining active and passive techniques. We study the case of membrane waves as a preliminary example and also show that as the frequency of the incident wave increases, the coupling between solutions of the Helmholtz and modified Helmholtz equations becomes essential through the interface conditions of perfect bonding.

In section 3.1, we study the case of membrane waves introducing the governing equations

in section 3.1.1. In order to write the scattered field, we find the scattering relation in section 3.1.2. In section 3.1.3, we locate regions of rapid variation in scattering properties of the inclusion, which serves as an indicator for the frequencies at which resonances occur. We show in section 3.1.4 how employing a coating satisfying the mass compensation formula is inadequate for cloaking at higher frequency regimes. Instead we design a coating that "tames" regions of rapid variation in scattering properties of the inclusion. We introduce active sources in section 3.1.5 and show that the combination of active and passive techniques we propose produces effective cloaking with twelve active sources.

An analogous analysis is carried out for Kirchhoff plates in section 3.2, where we show that active cloaking can be effective at resonance regimes due to the combination of passive and active techniques. In section 3.2.4 we also give a closed-form expression controlling the choice of inclusion and coating parameters, which delivers a zero monopole scattering coefficient. This generalises the classical result of Konenkov [46] to coated inclusions and active cloaking.

Note that throughout this chapter, we give special attention to the case of high-contrast scatterers, whose mass densities or elastic properties are very different from those of the exterior matrix. The high contrast changes the balance between the multipole coefficients and hence brings an interesting, and sometimes unexpected, results for scattering of the incident wave.

3.1 Scattering of membrane waves by a coated inclusion

Since we aim to cloak a resonating inclusion using both passive and active techniques, it is an instructive preliminary problem to study flexural waves in a membrane containing a coated inclusion. In this section, we give an illustrative example for active cloaking at resonant regimes in a membrane, and in what follows, we present a demonstative account of cloaking an inclusion at resonant regimes with the use of a specifically designed coating and active sources.

3.1.1 Governing equations

Since the ultimate aim of this chapter is to combine active and passive techniques, we state the governing equations for the problem of a coated inclusion embedded in a membrane. Membrane waves are governed by the Helmholtz equation and thus, assuming time-harmonic dependence, the wave amplitude $u^{(q)}(\mathbf{x})$ satisfies the following equations and transmission conditions in three regions:

$$\Delta u^{(q)}(\mathbf{x}) + \beta_q^2 u^{(q)}(\mathbf{x}) + f(\mathbf{x}) = 0, \quad \mathbf{x} \in \Omega_q, \tag{3.2}$$

where, q runs over e, c or i and denotes the exterior, coating and inclusion regions respectively, also $u^{(e)}(\mathbf{x})$, $u^{(c)}(\mathbf{x})$ and $u^{(i)}(\mathbf{x})$ denoting the displacements in the respective regions. Here β_q is the spectral parameter defined as $\beta_q = \omega\sqrt{\rho_q/\mu_q}$, μ_q are the shear moduli in the respective

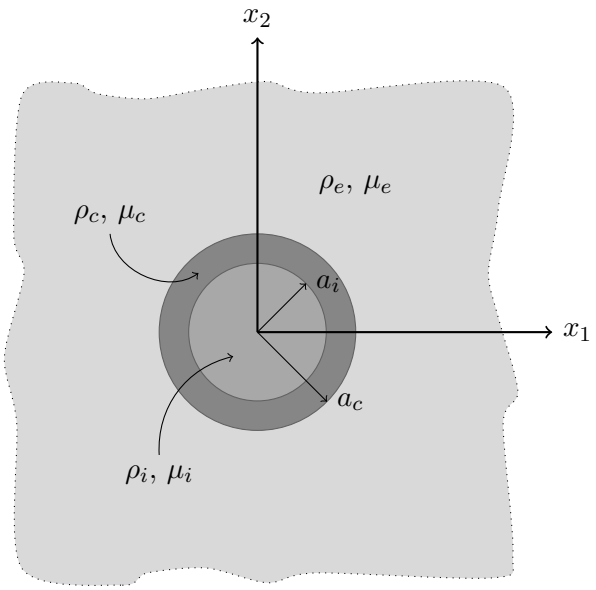

Figure 3.1: The geometry is shown for a coated inclusion embedded in a membrane. The material properties of the inclusion, its coating and the exterior medium are associated with the subscripts $i,\ c, e$, respectively. The respective interior and exterior radii of the coating are denoted by a_i, a_c.

regions, and $f(\mathbf{x})$ is the force term representing the active sources. In the case of a circular geometry, domains Ω_q representing the inclusion, coating and exterior are defined as follows:

$$\Omega_i = \{\mathbf{x} : x_1^2 + x_2^2 < a_i^2\}, \quad \Omega_c = \{\mathbf{x} : a_i^2 < x_1^2 + x_2^2 < a_c^2\}, \quad \Omega_e = \mathbb{R}^2 \setminus \overline{\Omega_i \cup \Omega_c}, \tag{3.3}$$

as shown in Fig. 3.1, where we denote, the radii of the inclusion and the exterior boundary of the coating by a_i and a_c, respectively. The interface conditions are written as

$$u^{(i)} = u^{(c)}, \quad \mu_i \frac{\partial u^{(i)}}{\partial r} = \mu_c \frac{\partial u^{(c)}}{\partial r} \quad \text{on} \quad r = a_i, \tag{3.4}$$

and

$$u^{(c)} = u^{(e)}, \quad \mu_c \frac{\partial u^{(c)}}{\partial r} = \mu_e \frac{\partial u^{(e)}}{\partial r} \quad \text{on} \quad r = a_c. \tag{3.5}$$

Excluding the positions of point sources, the associated solutions of equations (3.2) are

$$u^{(q)}(r,\theta) \quad = \quad \sum_{n=-\infty}^{\infty} \left[A_n^{(q)} J_n(\beta_q r) + E_n^{(q)} H_n^{(1)}(\beta_q r) \right] e^{in\theta}, \quad q = i, c, e, \tag{3.6}$$

where $E_n^{(i)}$ are identically zero to avoid singular displacements at the origin. Analogous to equation (1.6) in chapter 1, $A_n^{(q)}$ and $E_n^{(q)}$ are the respective coefficients for the incoming and outgoing fields, where $q = i, c, e$, denotes the inclusion, coating and exterior medium respectively.

3.1.2 Derivation of the scattering relation

In this section, we find the scattering relation for the problem of flexural waves scattered by a coated inclusion in a membrane. By substituting the appropriate field representations of equation (3.6) into the interface conditions (3.4) and (3.5), we can obtain the following

$$A_n^{(i)} J_n(\beta_i a_i) = A_n^{(c)} J_n(\beta_c a_i) + E_n^{(c)} H_n^{(1)}(\beta_c a_i), \tag{3.7}$$

$$A_n^{(c)} J_n(\beta_c a_c) + E_n^{(c)} H_n^{(1)}(\beta_c a_c) = A_n^{(e)} J_n(\beta_e a_c) + E_n^{(e)} H_n^{(1)}(\beta_e a_c), \tag{3.8}$$

and

$$\mu_i \beta_i A_n^{(i)} J_n{}'(\beta_i a_i) = \mu_c \beta_c \left[A_n^{(c)} J_n{}'(\beta_c a_i) + E_n^{(c)} H_n^{(1)'}(\beta_c a_i) \right], \tag{3.9}$$

$$\mu_c \beta_c \left[A_n^{(c)} J_n{}'(\beta_c a_c) + E_n^{(c)} H_n^{(1)'}(\beta_c a_c) \right] = \mu_e \beta_e \left[A_n^{(e)} J_n{}'(\beta_e a_c) + E_n^{(e)} H_n^{(1)'}(\beta_e a_c) \right]. \tag{3.10}$$

We eliminate $A_n^{(c)}$ from the above using (3.8) and (3.10), then solve the resulting equation for $E_n^{(c)}$ to obtain

$$\begin{aligned} E_n^{(c)} = & \frac{\mu_c \beta_c J_n(\beta_e a_c) J_n{}'(\beta_c a_c) - \mu_e \beta_e J_n{}'(\beta_e a_c) J_n(\beta_c a_c)}{\mu_c \beta_c \mathcal{W}[H_n^{(1)}(\beta_c a_c), J_n(\beta_c a_c)]} A_n^{(e)} \\ & + \frac{\mu_c \beta_c H_n^{(1)}(\beta_e a_c) J_n{}'(\beta_c a_c) - \mu_e \beta_e H_n^{(1)'}(\beta_e a_c) J_n(\beta_c a_c)}{\mu_c \beta_c \mathcal{W}[H_n^{(1)}(\beta_c a_c), J_n(\beta_c a_c)]} E_n^{(e)}. \end{aligned} \tag{3.11}$$

Substituting equation (3.11) into (3.8) gives

$$\begin{aligned} A_n^{(c)} = & \frac{\mu_e \beta_e H_n^{(1)}(\beta_c a_c) J_n{}'(\beta_e a_c) - \mu_c \beta_c H_n^{(1)'}(\beta_c a_c) J_n(\beta_e a_c)}{\mu_c \beta_c \mathcal{W}[H_n^{(1)}(\beta_c a_c), J_n(\beta_c a_c)]} A_n^{(e)} \\ & + \frac{\mu_e \beta_e H_n^{(1)}(\beta_c a_c) H_n^{(1)'}(\beta_e a_c) - \mu_c \beta_c H_n^{(1)'}(\beta_c a_c) H_n^{(1)}(\beta_e a_c)}{\mu_c \beta_c \mathcal{W}[H_n^{(1)}(\beta_c a_c), J_n(\beta_c a_c)]} E_n^{(e)}. \end{aligned} \tag{3.12}$$

Equations (3.11) and (3.12) invite us to construct the following matrix equation:

$$\begin{pmatrix} A_n^c \\ \\ E_n^c \end{pmatrix} = \begin{pmatrix} \mathcal{M}_n^{11} & \mathcal{M}_n^{12} \\ \\ \mathcal{M}_n^{21} & \mathcal{M}_n^{22} \end{pmatrix} \begin{pmatrix} A_n^e \\ \\ E_n^e \end{pmatrix}, \tag{3.13}$$

where

$$\mathcal{M}_n^{11} = \frac{\mu_c\beta_c J_n(\beta_e a_c)H_n^{(1)'}(\beta_c a_c) - \mu_e\beta_e J_n'(\beta_e a_c)H_n^{(1)}(\beta_c a_c)}{\mu_c\beta_c \mathcal{W}[J_n(\beta_c a_c), H_n^{(1)}(\beta_c a_c)]}, \tag{3.14}$$

$$\mathcal{M}_n^{12} = \frac{\mu_c\beta_c H_n^{(1)'}(\beta_c a_c)H_n^{(1)}(\beta_e a_c) - \mu_e\beta_e H_n^{(1)}(\beta_c a_c)H_n^{(1)'}(\beta_e a_c)}{\mu_c\beta_c \mathcal{W}[J_n(\beta_c a_c), H_n^{(1)}(\beta_c a_c)]}, \tag{3.15}$$

$$\mathcal{M}_n^{21} = \frac{-\mu_c\beta_c J_n(\beta_e a_c)J_n'(\beta_c a_c) + \mu_e\beta_e J_n'(\beta_e a_c)J_n(\beta_c a_c)}{\mu_c\beta_c \mathcal{W}[J_n(\beta_c a_c), H_n^{(1)}(\beta_c a_c)]}, \tag{3.16}$$

$$\mathcal{M}_n^{22} = \frac{-\mu_c\beta_c J_n'(\beta_c a_c)H_n^{(1)}(\beta_e a_c) + \mu_e\beta_e J_n(\beta_c a_c)H_n^{(1)'}(\beta_e a_c)}{\mu_c\beta_c \mathcal{W}[J_n(\beta_c a_c), H_n^{(1)}(\beta_c a_c)]}. \tag{3.17}$$

Eliminating $A_n^{(i)}$ using (3.7) and (3.9) yields

$$E_n^{(c)} = \mathcal{N}_n A_n^{(c)}, \tag{3.18}$$

where

$$\mathcal{N}_n = \frac{\mu_i\beta_i J_n(\beta_c a_i)J_n'(\beta_i a_i) - \mu_c\beta_c J_n'(\beta_c a_i)J_n(\beta_i a_i)}{\mu_c\beta_c J_n(\beta_i a_i)H_n^{(1)'}(\beta_c a_i) - \mu_i\beta_i J_n'(\beta_i a_i)H_n^{(1)}(\beta_c a_i)}. \tag{3.19}$$

We can write the following from equation (3.13)

$$E_n^{(c)} = \mathcal{M}_n^{21} A_n^{(e)} + \mathcal{M}_n^{22} E_n^{(e)}, \tag{3.20}$$

which is substituted into equation (3.18), to obtain

$$\mathcal{M}_n^{21} A_n^{(e)} + \mathcal{M}_n^{22} E_n^{(e)} = \mathcal{N}_n A_n^{(c)}. \tag{3.21}$$

Combining this with the fact that $A_n^{(c)} = \mathcal{M}_n^{11} A_n^{(e)} + \mathcal{M}_n^{12} E_n^{(e)}$ from equation (3.13), we eliminate the coefficient $A_n^{(c)}$and thus find the following

$$E_n^{(e)} = \mathcal{T}_n A_n^{(e)}, \tag{3.22}$$

where

$$\mathcal{T}_n = \frac{\mathcal{M}_n^{21} - \mathcal{N}_n\mathcal{M}_n^{11}}{\mathcal{N}_n\mathcal{M}_n^{12} - \mathcal{M}_n^{22}}. \tag{3.23}$$

Here $\mathcal{T}_n$ stands for the scattering coefficient, and the representations for $\mathcal{M}_n^{ab}$ $(a, b = 1, 2)$ and $\mathcal{N}_n$ are given by (3.14)-(3.17) and (3.19), respectively.

Having obtained the scattering relation (3.22), the coefficients $A_n^{(i)}$, $A_n^{(c)}$, and $E_n^{(c)}$ associated with the respective fields in the inclusion and coating can be found from equations (3.8), (3.11) and (3.12), respectively.

Once the relation (3.22) is established, the coefficients $A_n^{(c)}, E_n^{(c)}$ associated with the coating, as well as the coefficient $A_n^{(i)}$ associated with the inclusion can be readily found. For a

plane wave propagating along the x_1-axis, we use the Jacobi-Anger expansion given in equation (1.12) of chapter 1, which tells us that $A_n^{(e)} = i^n$. The scattered field in this particular case can therefore be represented as

$$u_{sc}(\mathbf{x}) \quad = \quad \mathcal{T}_0 H_0^{(1)}(\beta_e r) + \sum_{n=1}^{\infty} 2i^n \mathcal{T}_n H_n^{(1)}(\beta_e r)\, \cos(n\theta). \tag{3.24}$$

3.1.3 Resonant regimes for an uncoated inclusion

We aim to cloak a circular inclusion at resonant regimes, and in this section, we use an illustrative example to determine the frequencies at which such regimes occur. For the case of an inclusion with no coating, it can be shown that formula (3.22) reduces to

$$E_n^{(e)} = \frac{J_n(\beta_i a_i) J_n{}'(\beta_e a_i) - \sqrt{(\mu_i \rho_i)/(\mu_e \rho_e)}\, J_n{}'(\beta_i a_i) J_n(\beta_e a_i)}{\sqrt{(\mu_i \rho_i)/(\mu_e \rho_e)}\, H_n^{(1)}(\beta_e a_i) J_n{}'(\beta_i a_i) - H_n^{(1)\prime}(\beta_e a_i) J_n(\beta_i a_i)}\, A_n^{(e)}. \tag{3.25}$$

In particular, in the low-frequency regime ($|\beta_e a_i| \ll 1$), the monopole ($n = 0$) and dipole coefficients ($n = 1$) are of the same order, and can be expressed as

$$|E_0^{(e)}| \sim \frac{\pi}{4} \frac{|\rho_i - \rho_e|}{\rho_e} (\beta_e a_i)^2, \quad |E_1^{(e)}| \sim \frac{|\mu_i - \mu_e|}{\mu_i + \mu_e} (\beta_e a_i)^2. \tag{3.26}$$

To derive these simple asymptotics we used $A_0^{(e)} = 1$ and $A_1^{(e)} = i$. The monopole term for static problems corresponds to a net force produced by an elastic inclusion, and is consequently zero. In the dynamic case, the coefficient $E_0^{(e)}$ of the monopole term is defined by the formula (3.25), but, as shown in (3.26), in the low-frequency regime $E_0^{(e)}$ and $E_1^{(e)}$ have the same order of magnitude in $\beta_e a_i$. For the special case when the shear moduli of the inclusion and exterior matrix coincide, the monopole term becomes dominant.

When frequency increases, the contribution from higher-order multipole coefficients becomes significant. The active cloaking algorithm presented before is designed to annul multipole coefficients of the required order for the scattered field.

Recalling that our interest is in regimes where the coefficients change rapidly with the frequency, as an illustration, we consider $|E_0^{(e)}|$, which is shown in Fig. 3.2. Note that in Fig. 3.2, the densities of the inclusion and exterior matrix are comparable ($\rho_i = 1.5$, $\rho_e = 1.0$) and the shear modulus of the exterior is tenfold that of the inclusion ($\mu_i = 0.1$, $\mu_e = 1.0$).

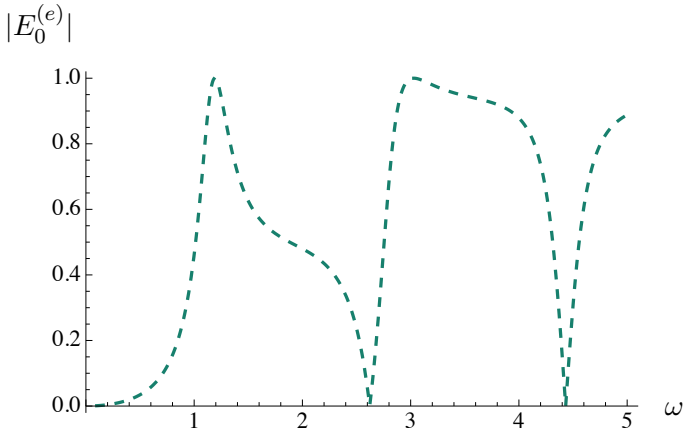

Figure 3.2: Membrane wave scattering by an uncoated inclusion with the parameters $\rho_i = 1.5$, $\rho_e = 1.0$, $\mu_i = 0.1$, $\mu_e = 1.0$, $a_i = 0.50$. The graph of $|E_0^{(e)}|$ as a function of ω displays spikes corresponding to some resonant regimes.

Sufficiently away from the low-frequency region, the major features of Fig. 3.2 include a strong peak near $\omega = 1.2$, a narrow zero near $\omega = 2.62$ and a rapid rise to a maximum near $\omega = 3.0$. The region of rapid variation of $|E_0^{(e)}|$ with ω between 2.62 and 3.0 would give rise to difficulties for active cloaking of a frequency-swept incident wave, and this is what we discuss in detail below.

For the case of a high-contrast inclusion, the scattered field is illustrated in Fig. 3.3. In Fig. 3.3(a), we present the total displacement for a small frequency value of $\omega = 0.3$, which clearly shows a low scattering pattern. Figs. 3.3(b) (with $\omega = 2.62$) and 3.3(c) (with $\omega = 3.0$) highlight the difference in the total displacement field patterns around the inclusion for the frequencies corresponding to the first non-trivial zero of $|E_0^{(e)}|$ and its subsequent maximum, repsectively. In Fig. 3.3(b) scattering is primarily due to terms of dipole order, but the wave fronts behind the inclusion are practically straight. In Fig. 3.3(c), both monopole and dipole terms are contributing to the distortion of the wavefronts behind the inclusion. The scattering patterns change dramatically even though the frequency difference is small.

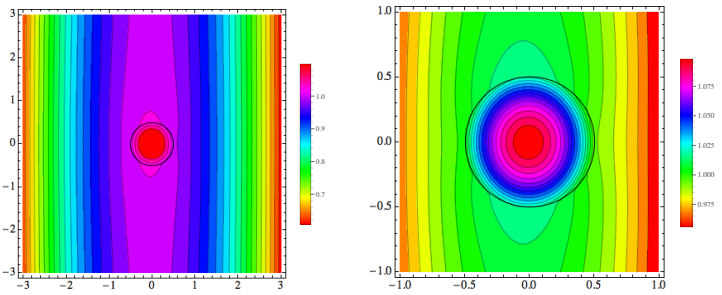

(a)

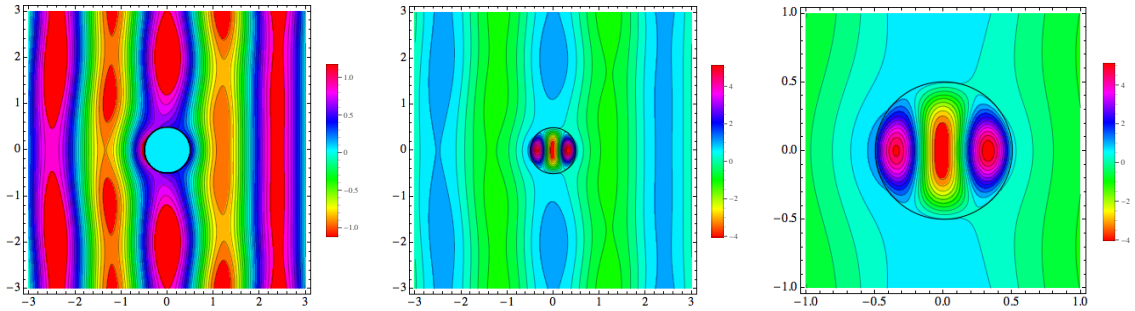

(b)

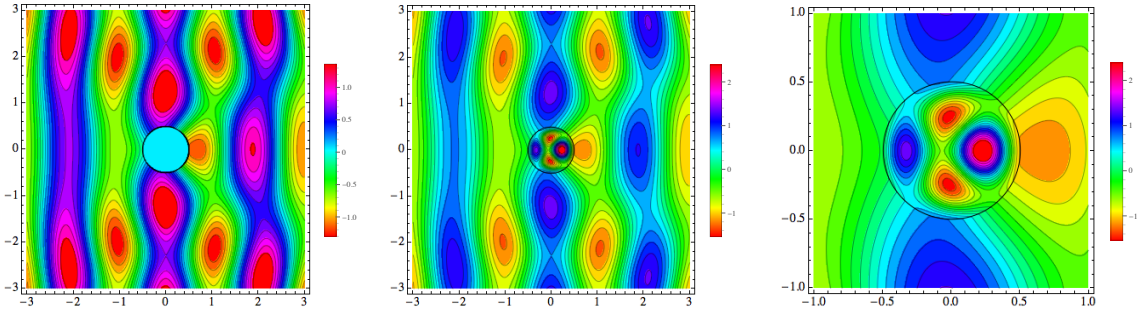

(c)

Figure 3.3: Membrane wave scattering by an uncoated inclusion for the parameters $\rho_i = 1.5$, $\rho_e = 1.0$, $\mu_i = 0.1$, $\mu_e = 1.0$, $a_i = 0.50$. (a) Total field for $\omega = 0.3$, (b) Total field for $\omega = 2.62$ where $E_0^{(e)}$ vanishes, (c) Total field for $\omega = 3.0$ where $|E_0^{(e)}|$ has nearly a maximum. In the last frame of each row, we present a zoomed-in version of the displacement inside and in the close vicinity of the inclusion. The first two frames in the inset (b) represent the same field outside the inclusion, but with different colour maps, where the first frame excludes the internal field, whereas the second frame includes it. The same comment applies to the first two frames of the inset (c).

3.1.4 Design of the coating targeting resonant frequencies

We now discuss two ways of controlling the scattering of membrane waves by a suitably designed coating placed around an inclusion. First, similar to Farhat *et al.* [23], we consider the low-frequency regime. In the setting of Farhat *et al.* [23], the scattered field was dominated by the monopole term, which led to the mass-compensation formula (3.1), fixing the choice of parameters for the coating around the inclusion. Here we extend the compensation procedure to higher orders, and analyse a higher frequency regime, which includes a resonance mode.

Mass-stiffness compensation formulae

In the long-wave (low-frequency) approximation, similar to (3.26), the monopole and dipole coefficients in the representation of the scattered field around a coated inclusion, are of the same order. Formula (3.22) together with (3.23) lead to

$$|E_0^{(e)}| \sim \frac{\pi}{4} \frac{\left|(\rho_i - \rho_c)(a_i/a_c)^2 + (\rho_c - \rho_e)\right|}{\rho_e} (\beta_e a_c)^2, \tag{3.27}$$

$$|E_1^{(e)}| \sim \frac{\pi}{4} \left| \frac{(\mu_i - \mu_c)(\mu_c + \mu_e)(a_i/a_c)^2 + (\mu_i + \mu_c)(\mu_c - \mu_e)}{(\mu_i - \mu_c)(\mu_c - \mu_e)(a_i/a_c)^2 + (\mu_i + \mu_c)(\mu_c + \mu_e)} \right| (\beta_e a_c)^2, \tag{3.28}$$

as $\beta_e a_c \to 0$. Equations (3.27) and (3.28) suggest the design (which differs from the one suggested by Farhat *et al.* in [23]) for a coating that compensates for differences in the mass density and stiffness between the inclusion and the exterior. Such a coating causes a reduction in the scattering cross-section at low frequencies, and the mass density and stiffness of the coating can be chosen as

$$\rho_c = \frac{\rho_e - \rho_i(a_i/a_c)^2}{1 - (a_i/a_c)^2}, \tag{3.29}$$

$$\mu_c = \frac{(\mu_e - \mu_i)(a_i^2 + a_c^2) + \sqrt{(\mu_e - \mu_i)^2(a_i^2 + a_c^2)^2 + 4\mu_i\mu_e(a_c^2 - a_i^2)^2}}{2(a_c^2 - a_i^2)}. \tag{3.30}$$

We note that in the example illustrated in Fig. 3.2, the inclusion is "soft" compared to the exterior, and the mass density of the inclusion is greater than that of the exterior. In this particular case, both monopole and dipole coefficients in the representation of the scattered field are of order $O(\omega^2)$. In the low-frequency regime, these coefficients can be reduced further by introducing a coating designed according to the mass-stiffness compensation formulae (3.29), (3.30). The graphs of $|E_0^{(e)}|$ and $|E_1^{(e)}|$ versus ω, when ρ_c, μ_c are chosen to satisfy (3.29), (3.30) respectively, are given in Fig. 3.4(a). It is also shown in Fig. 3.4(b) (see for example, the region enclosed by the red rectangle) that for higher frequencies we observe resonant scattering associated with rapid variation and increase of $|E_0^{(e)}|$. Consequently, a coating whose material parameters are chosen to satisfy the mass-stiffness balancing conditions (3.29), (3.30) is not effective at higher frequency resonant regimes.

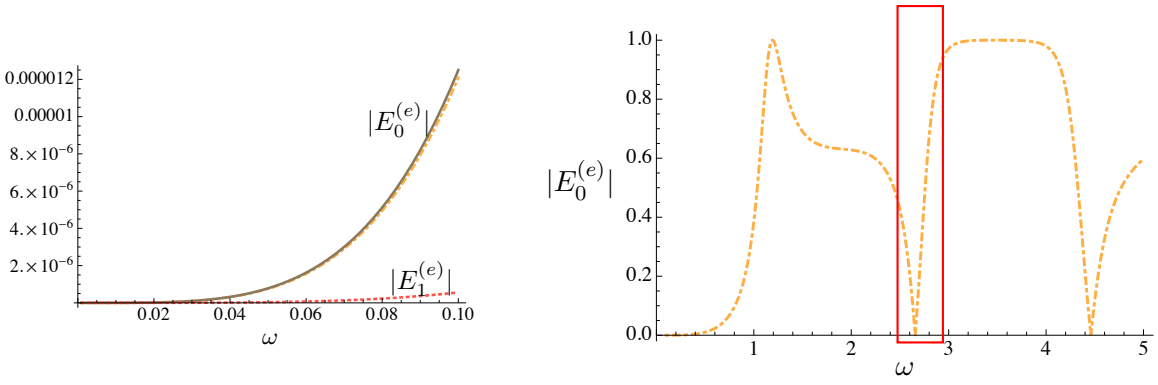

(a) (b)

Figure 3.4: (a) Monopole $|E_0^{(e)}|$ (dot-dashed/orange) and dipole $|E_1^{(e)}|$ (dotted/red) amplitudes for membrane wave scattering by a coated inclusion with parameter values $\rho_i = 1.5$, $\rho_e = 1.0$, $\rho_c \approx 0.635$ (see (3.29)), $\mu_i = 0.1$, $\mu_c \approx 2.257$ (see (3.30)), $\mu_e = 1.0$, $a_i = 0.50$, $a_c = 0.77$ as a function of ω. The empirical fit $0.15\omega^4$ (solid/grey) for the monopole term is also included. (b) Monopole amplitude over a wider range of frequencies.

Passive control of scattering by an appropriate coating

We show in this section that the method of active cloaking has the advantage of being efficient even at higher frequency regimes when combined with passive techniques. In what follows, we discuss here the applicability of a coating which has been specifically designed for scattering reduction in the quasi-static regime. At a frequency when the monopole coefficient $|E_0^{(e)}|$ is small but rapidly varying, active cloaking requires a rapid adjustment of the source amplitudes (see the red box enclosing $\omega \approx 2.62$ in Fig. 3.4(a)). In Fig. 3.5(a), we combine data from Figs 3.2, 3.4(b) together with $|E_0^{(e)}|$ resulting from the revised design. The revised choice of parameters gives a "flattened" curve near the resonant scattering frequency $\omega \approx 2.62$ (see the region enclosed by the red box). A magnified view is given in Fig. 3.5(b). We note that the mass compensation criterion for the coating clearly reduces the monopole coefficient from being $O(\omega^2)$ to $O(\omega^4)$. However, this is of little importance since the monopole amplitude is already very small even for an uncoated inclusion.

In Fig. 3.6, we present contour plots of the membrane wave amplitude for the low frequency value of $\omega = 0.3$; the inclusion has a coating whose density and stiffness are chosen according to the formulae (3.29) and (3.30). The other parameter values are chosen exactly as in Fig. 3.5(a). It is apparent that the scattering has been reduced compared with Fig. 3.3(a), however, the benefit of such a reduction is very low, as even without the coating there is no significant scattering.

3.1.5 Active cloaking of a coated inclusion

For the higher frequency near $\omega = 2.62$, we have chosen the coating that "flattens" the monopole coefficient $E_0^{(e)}$ over the targeted resonant range of ω. We then observe in Fig.

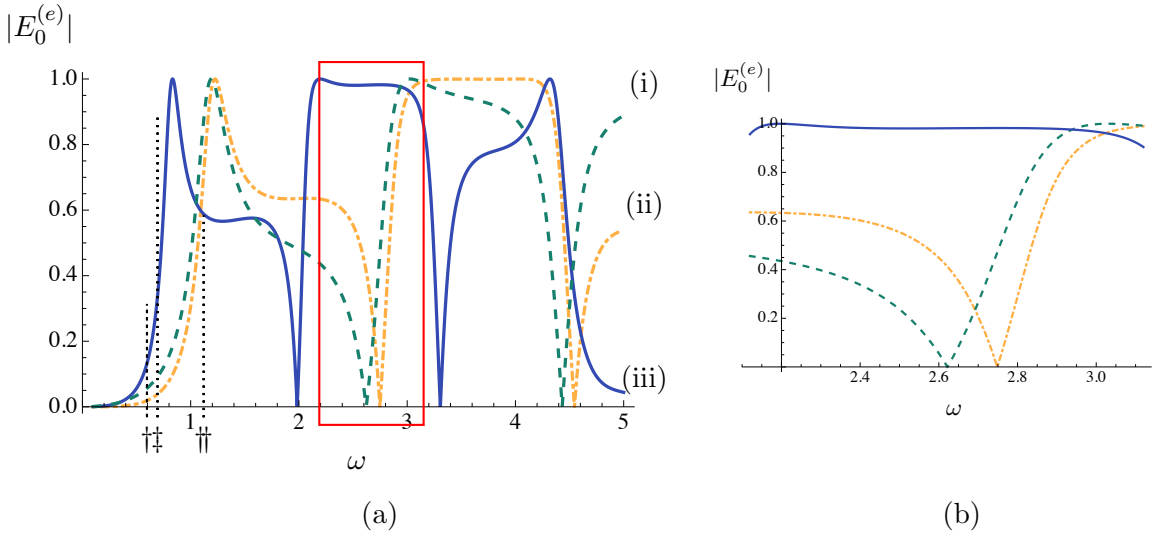

Figure 3.5: (a) Monopole amplitude for membrane wave scattering by (i) an uncoated inclusion (dashed/green) with parameter values $\rho_i = 1.5$, $\rho_e = 1.0$, $\mu_i = 0.1$, $\mu_e = 1.0$, $a_i = 0.50$, (ii) a coated inclusion (dot-dashed/orange) with parameter values as in (i) together with $\rho_c \approx 0.635$, $\mu_c \approx 2.257$ and $a_c = 0.77$, and (iii) a coated inclusion (solid/blue) with parameter values as in (i) together with $\rho_c = 0.81$, $\mu_c = 0.11$ and $a_c = 0.77$. Note, the red box highlights where the blue/solid curve flattens approximately for $\omega \in [2.4, 2.9]$. (b) Monopole amplitude for membrane wave scattering for the parameters of (i)-(iii) in (a), but for a range of ω highlighted by the red box in (a). We see strong variation in $|E_0^{(e)}|$ for an uncoated inclusion in this frequency range, but it is clear that with an appropriate choice of parameter values for the coating, we can create a region where $|E_0^{(e)}|$ remains fairly flat.

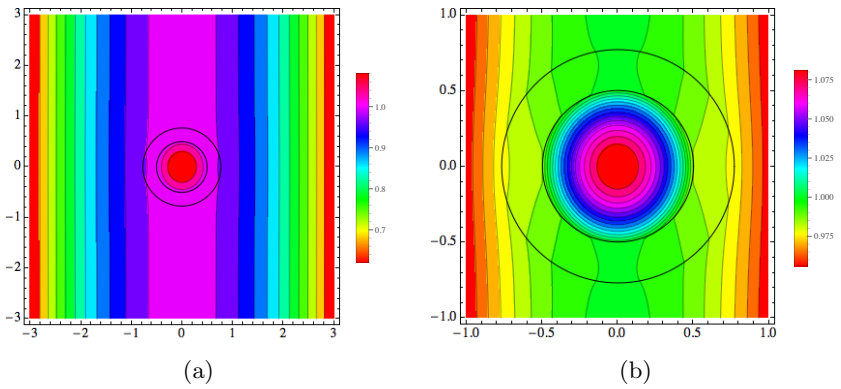

Figure 3.6: (a) Total field for membrane wave scattering by a coated inclusion with parameter values: $\rho_i = 1.5$, $\rho_e = 1.0$, $\rho_c \approx 0.635$, $\mu_i = 0.1$, $\mu_c \approx 2.257$, $\mu_e = 1.0$, $a_i = 0.50$, $a_c = 0.77$ and $\omega = 0.3$. (b) A zoomed in version of the total field inside the inclusion, coating and in close vicinity of the coating.

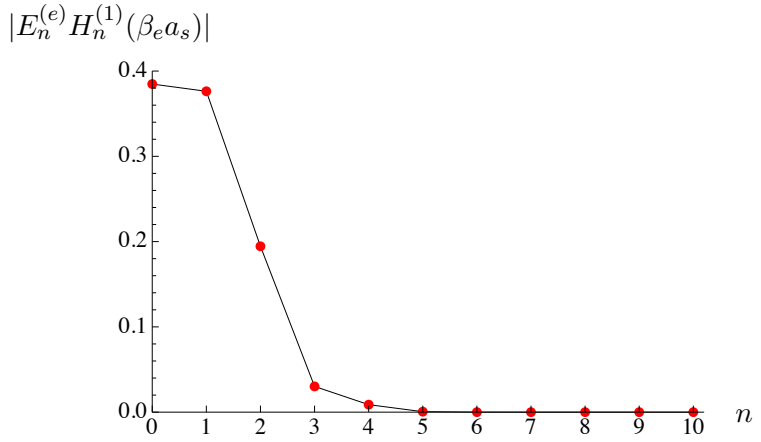

Figure 3.7: Membrane wave scattering: absolute value of the component n, $E_n^{(e)} H_n^{(1)}(\beta_e a_s)$, of the displacement field, where a_s is the radius of circle on which the control sources are placed, as a function of n for $\omega = 2.62$. Parameter values as for (blue/solid) curve in Fig. 3.5: $\rho_i = 1.5$, $\rho_c = 0.81$, $\rho_e = 1.0$, $\mu_i = 0.1$, $\mu_c = 0.11$, $\mu_e = 1.0$, $a_i = 0.5$, $a_c = 0.77$, $a_s = 1.57$.

3.7 that the multipole field components of higher order become significant, and hence a coating designed to achieve scattering reduction in the quasi-static regime would no longer be appropriate.

The main objective of this chapter is to combine passive and active techniques for cloaking an inclusion at resonant regimes. We have designed a coating such that the scattering properties of the resonating inclusion are controlled, which forms the passive contribution to our cloaking method. In what follows, we introduce active sources to cancel out the scattered wave from the coated inclusion, and demonstrate the active contribution of our cloaking method with four sources. The sources are symmetrically located on the x_1- and x_2-axes, all at a distance $a_s > a_c$ away from the origin. Note, the symmetry of the inclusion dictates that we set the amplitudes of the sources on the x_2-axis to be the same. Since the Green's function for the Helmholtz operator is given by

$$G\left(x_1 - x_1^{(s,l)}, x_2 - x_2^{(s,l)}\right) = \frac{1}{4i} H_0^{(1)}\left(\beta_e \sqrt{\left(x_1 - x_1^{(s,l)}\right)^2 + \left(x_2 - x_2^{(s,l)}\right)^2}\right), \tag{3.31}$$

where $\mathbf{x}^{(s,l)} = (x_1^{(s,l)}, x_2^{(s,l)})$ is the position of the point source, using Graf's addition theorem for the sources located at $\mathbf{x}^{(s,1)} = (a_s, 0)$, $\mathbf{x}^{(s,2)} = (-a_s, 0)$, $\mathbf{x}^{(s,3)} = (0, a_s)$ and $\mathbf{x}^{(s,4)} = (0, a_s)$, we obtain

$$\begin{aligned}
Q_1\, G(x_1 - a_s, x_2) &= \frac{Q_1}{4i} \sum_{k=-\infty}^{\infty} e^{ik\theta} H_k^{(1)}(\beta_e a_s) J_k(\beta_e r), \\
Q_2\, G(x_1 + a_s, x_2) &= \frac{Q_2}{4i} \sum_{k=-\infty}^{\infty} e^{ik(\theta-\pi)} H_k^{(1)}(\beta_e a_s) J_k(\beta_e r), \\
Q_3\, G(x_1, x_2 \mp a_s) &= \frac{Q_3}{4i} \sum_{k=-\infty}^{\infty} e^{ik(\theta\mp\pi/2)} H_k^{(1)}(\beta_e a_s) J_k(\beta_e r).
\end{aligned}$$

Here $Q_{1,2}$ are the amplitudes of the two sources located on the x_1-axis at $\mathbf{x}^{(s,1)} = (a_s, 0)$ and $\mathbf{x}^{(s,2)} = (-a_s, 0)$ respectively, whereas Q_3 is the amplitude of the sources located on the x_2-axis at $\mathbf{x}^{(s,3)} = (0, a_s)$ and $\mathbf{x}^{(s,4)} = (0, -a_s)$; note that these amplitudes are unknown, and to be found.

The n-th order coefficient for the total wave incident on the coated inclusion is thus

$$A_n^{(e)} = i^n + \frac{1}{4i} H_n^{(1)}(\beta_e a_s) \left[Q_1 + (-1)^n Q_2 + 2Q_3 \cos(n\pi/2) \right].$$

As in chapter 2, we set the n-th order coefficient of the $H_n^{(1)}$ term equal to zero when $r > a_s$ and obtain

$$\begin{aligned} 4i\mathcal{T}_0 &= -(Q_1 + Q_2 + 2Q_3)[\mathcal{T}_0 H_0^{(1)}(\beta_e a_s) + J_0(\beta_e a_s)], \\ 4\mathcal{T}_1 &= (Q_1 - Q_2)[\mathcal{T}_1 H_1^{(1)}(\beta_e a_s) + J_1(\beta_e a_s)], \\ 4i\mathcal{T}_2 &= (Q_1 + Q_2 + 2Q_3)[\mathcal{T}_2 H_2^{(1)}(\beta_e a_s) + J_2(\beta_e a_s)], \end{aligned}$$

which we solve for $Q_{1,2}$ and Q_3 for given β_e, a_s. Finally, we write the displacement outside the coated inclusion as

$$\begin{aligned} w(r,\theta) &\approx w_{inc}(x_1) + Q_1\, G(r\cos\theta - a_s, r\sin\theta) + Q_2\, G(r\cos\theta + a_s, r\sin\theta) \\ &+ Q_3 \Big\{ G(r\cos\theta, r\sin\theta - a_s) + G(r\cos\theta, r\sin\theta + a_s) \Big\} + \sum_{n=-N}^{N} E_n^{(e)} H_n^{(1)}(\beta_e r)\, e^{in\theta}, \end{aligned}$$

where N needs to be chosen sufficiently large to ensure the accuracy of the wave amplitude.

In Fig. 3.8(a), we present the membrane wave amplitude at the frequency $\omega = 2.62$ for the case of an inclusion with a coating specifically designed to give a "flattened" curve of $|E_0^{(e)}|$ in Fig. 3.5(b); this is the frequency value at which a small deviation creates large fluctuations in the monopole term for case of an uncoated inclusion. Comparing Fig. 3.8(a) with Fig. 3.3(b) (left) or even with Fig. 3.3(c) (left), it is clear that the increase in strength of the monopole term observable in Fig. 3.5(b), results in the higher scattering in the contour plot depicting the amplitude of the total field.

Equations for eight and twelve active sources

Applying Graf's addition theorem to equation (3.31), yields the following for sources located at $\mathbf{x}^{(s,l)} = (a_s \cos\psi, \pm a_s \sin\psi)$

$$Q_l\, G(x_1 - a_s\cos\psi, x_2 \pm a_s \sin\psi) = \frac{Q_l}{4i} \sum_{k=-\infty}^{\infty} e^{ik(\theta \mp \psi)} H_k^{(1)}(\beta_e a_s) J_k(\beta_e r).$$

Here Q_l is the complex amplitude of the l-th active source, and $\pm\psi$ is the polar angle of the source position. For a configuration involving twelve sources, the n-th order coefficient for the total wave incident on the coated inclusion reads

$$\begin{aligned} A_n^{(e)} = i^n + \frac{1}{4i} H_n^{(1)}(\beta_e a_s) \Big\{ & Q_1 + Q_2 \\ & + 2\big[Q_3 \cos(n\xi) + Q_4 \cos(n\zeta) + Q_5 \cos(n\eta) + Q_6 \cos(n\gamma) + Q_7 \cos(n\alpha) \big] \Big\}. \end{aligned}$$

The equations setting the n-th order coefficient of the $H_n^{(1)}$ term equal to zero when $r > a_s$ read

$$4i\mathcal{T}_0 = -\Big\{Q_1 + Q_2 + 2\big[Q_3 + Q_4 + Q_5 + Q_6 + Q_7\big]\Big\}\Big[\mathcal{T}_0 H_0^{(1)}(\beta_e a_s) + J_0(\beta_e a_s)\Big],$$

$$4\mathcal{T}_1 = \Big\{Q_1 - Q_2 + 2\big[Q_3\cos(\xi) + Q_4\cos(\zeta) + Q_5\cos(\eta) + Q_6\cos(\gamma) + Q_7\cos(\alpha)\big]\Big\}\Big[\mathcal{T}_1 H_1^{(1)}(\beta_e a_s) + J_1(\beta_e a_s)\Big],$$

$$4i\mathcal{T}_2 = \Big\{Q_1 + Q_2 + 2\big[Q_3\cos(2\xi) + Q_4\cos(2\zeta) + Q_5\cos(2\eta) + Q_6\cos(2\gamma) + Q_7\cos(2\alpha)\big]\Big\}\Big[\mathcal{T}_2 H_2^{(1)}(\beta_e a_s) + J_2(\beta_e a_s)\Big],$$

$$4\mathcal{T}_3 = -\Big\{Q_1 - Q_2 + 2\big[Q_3\cos(3\xi) + Q_4\cos(3\zeta) + Q_5\cos(3\eta) + Q_6\cos(3\gamma) + Q_7\cos(3\alpha)\big]\Big\}\Big[\mathcal{T}_3 H_3^{(1)}(\beta_e a_s) + J_3(\beta_e a_s)\Big],$$

$$4i\mathcal{T}_4 = -\Big\{Q_1 + Q_2 + 2\big[Q_3\cos(4\xi) + Q_4\cos(4\zeta) + Q_5\cos(4\eta) + Q_6\cos(4\gamma) + Q_7\cos(4\alpha)\big]\Big\}\Big[\mathcal{T}_4 H_4^{(1)}(\beta_e a_s) + J_4(\beta_e a_s)\Big],$$

$$4\mathcal{T}_5 = \Big\{Q_1 - Q_2 + 2\big[Q_3\cos(5\xi) + Q_4\cos(5\zeta) + Q_5\cos(5\eta) + Q_6\cos(5\gamma) + Q_7\cos(5\alpha)\big]\Big\}\Big[\mathcal{T}_5 H_5^{(1)}(\beta_e a_s) + J_5(\beta_e a_s)\Big],$$

$$4i\mathcal{T}_6 = \Big\{Q_1 + Q_2 + 2\big[Q_3\cos(6\xi) + Q_4\cos(6\zeta) + Q_5\cos(6\eta) + Q_6\cos(6\gamma) + Q_7\cos(6\alpha)\big]\Big\}\Big[\mathcal{T}_6 H_6^{(1)}(\beta_e a_s) + J_6(\beta_e a_s)\Big],$$

which we solve for Q_n, $n = 1, 2, \ldots, 5$, when β_e and a_s are known. Note that for eight sources, only the first five equations are considered in the above system, and $Q_6 = Q_7 = 0$. Figures 3.8(b) and 3.8(c) illustrate two attempts, with four and eight active sources located at 1.57 units away from the origin, to cloak the coated inclusion.

We also remark that employing four active sources is perfectly adequate for smaller frequencies. To illustrate this, we present cloaking attempts at the intermediate frequency values $\omega = 0.7, 0.8, 1.2$ denoted by $\dagger, \ddagger, \dagger\dagger$ in Fig. 3.5(a), respectively. These frequency values respectively correspond to small, large and intermediate values of the monopole term, as shown in the same figure using dotted lines. The contour plots for the membrane wave amplitudes when the coated inclusion is surrounded by four active control sources are presented in Fig. 3.10: Part (a) corresponds to $\omega = 0.7$, part (b) to $\omega = 0.8$ and part (c) to $\omega = 1.2$. In each of these plots, that on the left is with no sources, whereas the middle and that on the right have four sources, the last showing the membrane wave amplitude over a wider range of x_1, x_2 values. These computations confirm that the values of frequencies in the neighbourhood of

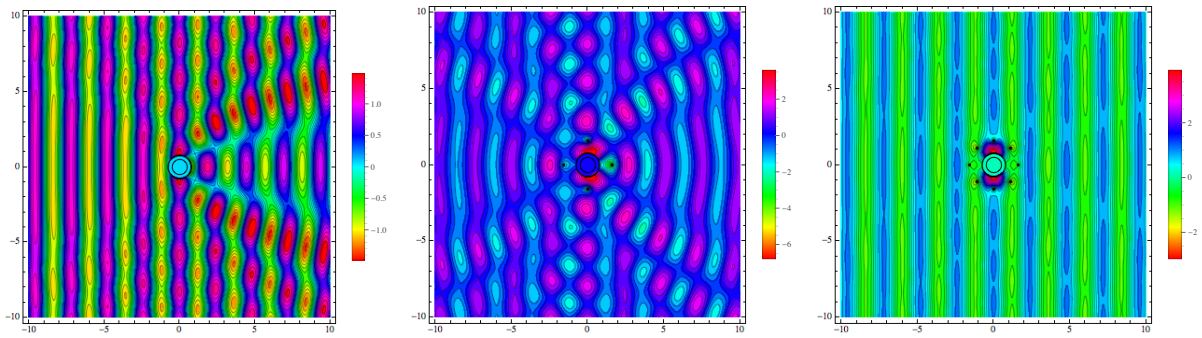

(a) (b) (c)

Figure 3.8: Membrane wave scattering: (a) Total displacement field exterior to a coated inclusion with parameter values $\omega = 2.62$, $\rho_i = 1.5$, $\rho_c = 0.81$, $\rho_e = 1.0$, $\mu_i = 0.1$, $\mu_c = 0.11$, $\mu_e = 1.0$, $a_c = 0.77$, $a_i = 0.5$ over a square region of side length 20. (b) Total displacement field exterior to a coated inclusion in the presence of 4 active sources located on the axes (black dots), all $a_s = 1.57$ units away from the origin. Parameter values as in (a). (c) Total displacement field exterior to a coated inclusion in the presence of 8 active sources (black dots), all $a_s = 1.57$ units away from the origin; sources off the x_1- and x_2-axes lie on $x_2 = \pm x_1$. Parameter values as in (a).

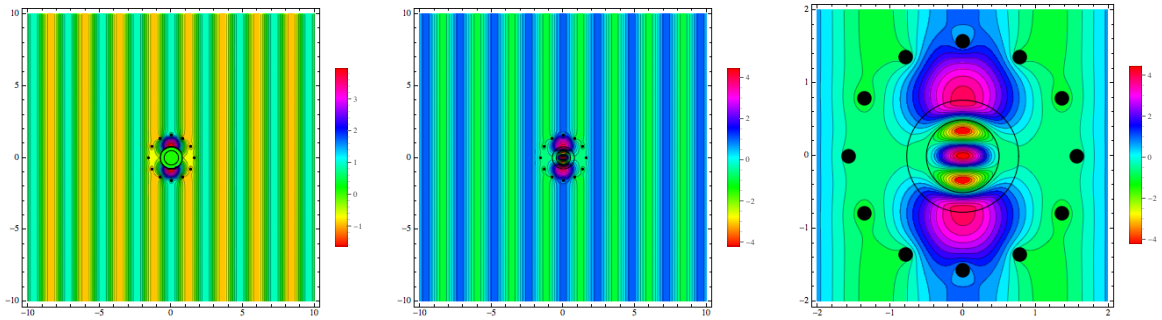

(a) (b) (c)

Figure 3.9: Total displacement field for membrane wave scattering in the presence of 12 active sources (small black dots surrounding the inclusion) all $a_s = 1.57$ units away from the origin: (a) exterior to the coated inclusion, (b) the entire plate including the inclusion and the coating, (c) as in (b) but a detailed view. The material properties and frequency value are the same as in Fig. 3.8.

the points of maximum for $|E_0^{(e)}|$, (which is clear in Fig. 3.5,) correspond to highly localised vibration modes, as seen in Fig. 3.10(b).

For the higher frequency value of Fig. 3.8, it is necessary to use far more than four sources to achieve good quality cloaking. This is demonstrated in Fig. 3.9, where cloaking of very good accuracy is achieved using twelve sources. This observation is in good accord with the plot given in Fig. 3.7 of the magnitudes of multipole field components. Bearing in mind that the number of active sources is twice the value of the order showing on the horizontal axis

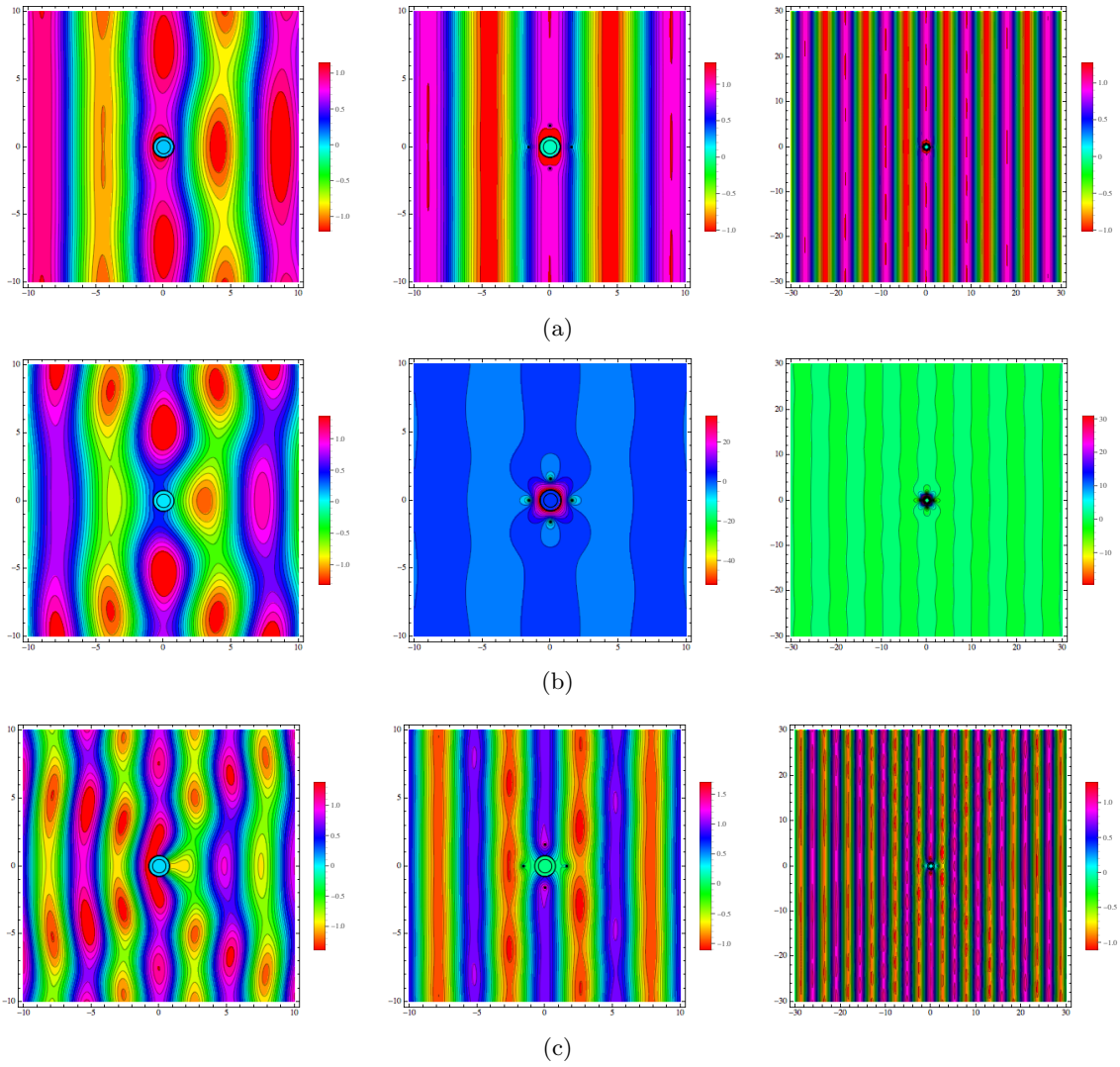

Figure 3.10: Membrane wave scattering: total displacement field exterior to a coated inclusion, where material properties are as in Fig. 3.8, for (a) $\omega = 0.7$, (b) $\omega = 0.8$, (c) $\omega = 1.2$. Left: uncloaked coated inclusion; centre: coated inclusion cloaked using four active control sources (small black dots surrounding the coated inclusion); right: same as the central images but over a wider range of x_1, x_2 values.

of Fig. 3.7, it is evident that good quality cloaking requires ten or more active sources.

Table 3.1 shows the total coefficient in front of the Hankel function term. For the case when there are no active sources, we see that there is a core set of multipole orders in $n \in [-2, 2]$ with magnitudes of order unity. When active sources are introduced, it is clear that the targeted coefficients are reduced to zero, which is highlighted by the shaded cells. We see an increase in magnitude for non-targeted coefficents which is generally significant for the two orders adjacent to the core. Noting for example, the magnitude 0.15 for $n = \pm 6$ with eight sources we see why the cloaking in Fig. 3.8(c) is still not adequate, but with twelve sources, we see from Table 3.1 that it is clearly adequate.

	n	**no sources**	4 sources	8 sources	12 sources
$\tilde{E}_n^{(e)}$	-8	$-1.34 \times 10^{-16} + 1.16 \times 10^{-8}\, i$	$4.14 \times 10^{-10} - 0.036\, i$	$4.14 \times 10^{-10} - 0.036\, i$	$3.01 \times 10^{-12} - 0.00026\, i$
	-7	$-6.25 \times 10^{-7} - 3.91 \times 10^{-13}\, i$	$0.043 + 2.67 \times 10^{-8}\, i$	$0.043 + 2.67 \times 10^{-8}\, i$	$-0.000092 - 5.72 \times 10^{-11}\, i$
	-6	$6.41 \times 10^{-10} - 0.000025\, i$	$-3.68 \times 10^{-6} + 0.15\, i$	$-3.68 \times 10^{-6} + 0.15\, i$	$-9.72 \times 10^{-17} + 3.52 \times 10^{-17} i$
	-5	$0.00074 + 5.50 \times 10^{-7}\, i$	$0.35 + 0.00026\, i$	$0.023 + 0.000017\, i$	$1.53 \times 10^{-17} + 3.13 \times 10^{-17}\, i$
	-4	$-0.00026 + 0.016\, i$	$0.036 - 2.21\, i$	$-8.45 \times 10^{-17} - 5.90 \times 10^{-17}\, i$	$-8.38 \times 10^{-17} + 1.08 \times 10^{-16}\, i$
	-3	$-0.066 - 0.0044\, i$	$0.99 + 0.065\, i$	$8.3 \times 10^{-17} - 4.94 \times 10^{-17}\, i$	$-1.11 \times 10^{-16} + 1.47 \times 10^{-16}\, i$
	-2	$0.218 - 0.413i$	0	$3.04 \times 10^{-16} + 3.33 \times 10^{-16}\, i$	1.25×10^{-16}
	-1	$0.305 + 0.896i$	-1.11×10^{-16}	$1.11 \times 10^{-16} - 3.47 \times 10^{-17}\, i$	$-2.22 \times 10^{-16} + 2.43 \times 10^{-17}\, i$
	0	$-0.963 - 0.188i$	$-5.55 \times 10^{-17} - 4.44 \times 10^{-16}\, i$	$-5.55 \times 10^{-17} + 4.44 \times 10^{-16}\, i$	$-1.67 \times 10^{-16} + 4.44 \times 10^{-16}\, i$
	1	$-0.305 - 0.896$	1.11×10^{-16}	$-1.11 \times 10^{-16} + 3.47 \times 10^{-17}\, i$	$2.22 \times 10^{-16} - 2.43 \times 10^{-17}\, i$
	2	$0.218 - 0.413i$	0	$3.04 \times 10^{-16} + 3.33 \times 10^{-16}\, i$	1.25×10^{-16}
	3	$0.066 + 0.0044\, i$	$-0.99 - 0.065\, i$	$-8.3 \times 10^{-17} + 4.94 \times 10^{-17}\, i$	$1.11 \times 10^{-16} - 1.47 \times 10^{-16}\, i$
	4	$-0.00026 + 0.016i$	$0.036 - 2.21\, i$	$-8.45 \times 10^{-17} - 5.90 \times 10^{-17}\, i$	$-8.38 \times 10^{-17} + 1.08 \times 10^{-16}\, i$
	5	$-0.00074 - 5.50 \times 10^{-7} i$	$-0.35 - 0.00026\, i$	$-0.023 - 0.000017\, i$	$-1.53 \times 10^{-17} - 3.13 \times 10^{-17}\, i$
	6	$6.41 \times 10^{-10} - 0.000025\, i$	$-3.68 \times 10^{-6} + 0.15\, i$	$-3.68 \times 10^{-6} + 0.15\, i$	$-9.72 \times 10^{-17} + 3.52 \times 10^{-17} i$
	7	$6.25 \times 10^{-7} + 3.91 \times 10^{-13}\, i$	$-0.043 - 2.67 \times 10^{-}8\, i$	$0.043 + 2.6 \times 10^{-8}\, i$	$0.000092 + 5.72 \times 10^{-11}\, i$
	8	$-1.34 \times 10^{-16} + 1.16 \times 10^{-8}\, i$	$4.14 \times 10^{-10} - 0.036\, i$	$4.14 \times 10^{-10} - 0.036\, i$	$3.01 \times 10^{-12} - 0.00026\, i$

Table 3.1: The coefficients $\tilde{E}_n^{(e)}$ of $H_n^{(1)}(\beta_e r)$ terms, for a configuration with zero, four, eight and twelve control sources positioned symmetrically on a circle of radius of 1.57 units from the origin. The frequency of the incident wave is $\omega = 2.62$.

3.2 Scattering of flexural waves by a coated inclusion in a Kirchhoff plate

We now study active cloaking of resonant inclusions in Kirchhoff plates, having dealt with, in section 3.1, the simpler case involving membrane waves for a system governed by the Helmholtz equation. The problem studied in this section is more involved, and we obtain useful results that are generic to thin elastic plates. The analysis in this section is analogous to that of the membrane waves case, and we show that effective cloaking can be achieved at resonant regimes by combining passive and active techniques as previously discussed in section 3.1. First, we consider the specific conditions under which flexural waves in membranes can be used to approximate those in Kirchhoff plates. Note that this relationship was exploited in the publication by Farhat *et al.* [23]. We show that a particular case in Kirchhoff plates allows for a similar treatment to scattering reduction as in the case of membrane waves. In general, the mass balance argument from section 3.1.4, does not apply to Kirchhoff plates. For the general case of flexural wave scattering in Kirchhoff plates, we observe additional features in scattering patterns, which are related to the interaction between solutions to the Helmholtz and modified Helmholtz equations.

In section 3.2.2, we state the governing equations for the problem of flexural wave scattering in Kirchhoff plates containing a coated inclusion, and in section 3.2.3, we derive the scattering matrix encapsulating the boundary conditions of perfect bonding between the exterior medium, coating and inclusion.

Later, in section 3.2.5, we derive the conditions necessary for annulling the leading order behaviour of the monopole term of the scattered field in the quasi-static regime, which generalises the results published by Farhat *et al.* [23]. However, we show in section 3.2.4, that in the quasi-static regime, for general scattering problems in Kirchhoff plates, both the monopole and quadrupole have the same order of magnitude in the leading order behaviour of the scattered field.

We know from studying the case of membrane waves, that at higher frequency regimes, a coating designed to shift a resonant mode is necessary for high-precision active cloaking. In what follows, we study the case of plates and introduce a coating following a similar approach to that described for membrane waves. In section 3.2.6, we provide illustrative examples demonstrating efficient cloaking in plates at intermediate frequencies as well as higher frequency resonant regimes.

3.2.1 Relationship between flexural waves in thin plates and membranes

As discussed in chapter 1, the solutions to the governing biharmonic plate equation can be represented as a sum of solutions to the Helmholtz and modified Helmholtz equations, respectively. We show that by making specific assumptions about the material parameters of a coated inclusion, the problem of flexural waves in plates can be approximated by considering

flexural waves in membranes. Note that this approximation is only valid in the quasi-static regime; for higher frequencies the coupling from the interface conditions becomes significant.

We assume that mass densities differ across the exterior medium, coating and inclusion (that is, $\rho_e \neq \rho_c \neq \rho_i$), but ensure that the elastic properties, flexural rigidities and Poisson's ratio are the same across the three regions (namely, $\nu_e = \nu_c = \nu_i$ and $D_e = D_c = D_i$). Under these specific assumptions, the four transmission conditions of perfect bonding as stated by equations (1.20)–(1.22) in chapter 1, reduce to conditions of continuity of the displacement $w^{(q)}(\mathbf{x})$, (where $q = i, c$ or e,) and its three derivatives with respect to r on each circular interface: $r = a_i$ and $r = a_c$. That is,

$$w^{(c)}(\mathbf{x}) = w^{(h)}(\mathbf{x}), \qquad \frac{\partial^k}{\partial r^k} w^{(c)}(\mathbf{x}) = \frac{\partial^k}{\partial r^k} w^{(h)}(\mathbf{x}), \text{ with } k = 1, 2, 3, \tag{3.32}$$

where $\mathbf{x}$ is a point on the circular interface, also $h = i$ and $h = e$ on $r = a_i$ and $r = a_c$, respectively. Under these assumptions, the displacements $w^{(q)}(\mathbf{x})$ for $q = i, c, e$, are dominated by solutions to the Helmholtz wave in the quasi-static regime. To show this, we consider a solution of the form

$$w^{(q)} = \sum_{-\infty}^{\infty} \left[A_n^{(q)} J_n(\beta_q r) + E_n^{(q)} H_n^{(1)}(\beta_q r) \right] e^{in\theta}, \tag{3.33}$$

where $q = i$, c, e (Note, that when $q = i$, $E_n^{(i)} = 0$ to avoid singular fields at the origin). In section 3.1.1, we stated that the equation given above is a solution to the governing equation for flexural waves in membranes. Under the specific assumptions on the material properties, the first two conditions in equation (3.32) are satisfied identically by the relevant solutions given in (3.33) on $r = a_i$, and $r = a_c$. Note that if we set $\mu_i = \mu_e = \mu_c$ in the interface conditions (3.4) and (3.5) given in section 3.1.1, then the resulting conditions for perfect bonding in membrane waves, coincide with the first two conditions for flexural waves in (3.32).

Next we show that on the interfaces $r = a_i$ and $r = a_c$, the discrepancy in the third and fourth conditions of (3.32) are small in the quasi-static regime. To do this, we calculate the wave coefficients $A_n^{(q)}$ and $E_n^{(q)}$, $q = i$, c, e, given in equation (3.33), using the method analogous to that outlined in section 3.1.2. We take the equations (3.22) and (3.23) from section 3.1.2, and write the following relation for the scattered wave coefficient in the exterior medium

$$E_n^{(e)} = \frac{\mathcal{P}_n^1}{\mathcal{P}_n^2} A_n^{(e)}, \tag{3.34}$$

where

$$\begin{aligned}\mathcal{P}_n^1 &= \beta_e\beta_c J_n'(\beta_e a_c)J_n(\beta_i a_i)\left[J_n(\beta_c a_c)H_n^{(1)\prime}(\beta_c a_i) - J_n'(\beta_c a_i)H_n^{(1)}(\beta_c a_c)\right]\\ &\quad -\beta_i\beta_e J_n'(\beta_e a_c)J_n'(\beta_i a_i)\left[J_n(\beta_c a_c)H_n^{(1)}(\beta_c a_i) - J_n(\beta_c a_i)H_n^{(1)}(\beta_c a_c)\right]\\ &\quad -\beta_c^2 J_n(\beta_e a_c)J_n(\beta_i a_i)\left[J_n'(\beta_c a_c)H_n^{(1)\prime}(\beta_c a_i) - J_n'(\beta_c a_i)H_n^{(1)\prime}(\beta_c a_c)\right]\\ &\quad +\beta_i\beta_c J_n(\beta_e a_c)J_n'(\beta_i a_i)\left[J_n'(\beta_c a_c)H_n^{(1)}(\beta_c a_i) - J_n(\beta_c a_i)H_n^{(1)\prime}(\beta_c a_c)\right], \quad (3.35)\end{aligned}$$

and

$$\begin{aligned}\mathcal{P}_n^2 &= \beta_i\beta_c J_n'(\beta_i a_i)H_n^{(1)}(\beta_e a_c)\left[J_n(\beta_c a_i)H_n^{(1)\prime}(\beta_c a_c) - J_n'(\beta_c a_c)H_n^{(1)}(\beta_c a_i)\right]\\ &\quad -\beta_i\beta_e J_n'(\beta_i a_i)H_n^{(1)\prime}(\beta_e a_c)\left[J_n(\beta_c a_i)H_n^{(1)}(\beta_c a_c) - J_n(\beta_c a_c)H_n^{(1)}(\beta_c a_i)\right]\\ &\quad -\beta_c^2 J_n(\beta_i a_i)H_n^{(1)}(\beta_e a_c)\left[J_n'(\beta_c a_i)H_n^{(1)\prime}(\beta_c a_c) - J_n'(\beta_c a_c)H_n^{(1)\prime}(\beta_c a_i)\right]\\ &\quad +\beta_c\beta_e J_n(\beta_i a_i)H_n^{(1)\prime}(\beta_e a_c)\left[J_n'(\beta_c a_i)H_n^{(1)}(\beta_c a_c) - J_n(\beta_c a_c)H_n^{(1)\prime}(\beta_c a_i)\right]. \quad (3.36)\end{aligned}$$

Note that $A_n^{(e)} = i^n$, from the plane wave expansion of equation (1.12) in chapter 1. Using the method outlined in section 3.1.2, we express the wave coefficients of the problem in terms of the incident wave coefficient in the exterior medium $A_n^{(e)}$. For the incoming wave coefficient in the coating, we obtain

$$A_n^{(c)} = \left(\mathcal{M}_n^{11} + \frac{\mathcal{P}_n^1}{\mathcal{P}_n^2}\mathcal{M}_n^{12}\right)A_n^{(e)},$$

which simplifies to

$$\begin{aligned}A_n^{(c)} &= \frac{\mathcal{W}[J_n(\beta_e a_c), H_n^{(1)}(\beta_e a_c)]\left[\beta_i\beta_e J_n'(\beta_i a_i)H_n^{(1)}(\beta_c a_i) - \beta_c\beta_e J_n(\beta_i a_i)H_n^{(1)\prime}(\beta_c a_i)\right]}{\mathcal{P}_n^2}A_n^{(e)},\\ &= \frac{2i}{\pi a_c}\frac{\beta_i J_n'(\beta_i a_i)H_n^{(1)}(\beta_c a_i) - \beta_c J_n(\beta_i a_i)H_n^{(1)\prime}(\beta_c a_i)}{\mathcal{P}_n^2}A_n^{(e)}, \quad (3.37)\end{aligned}$$

using the fact that

$$\mathcal{W}[J_n(\beta a), H_n^{(1)}(\beta a)] = \frac{2i}{\pi\beta a}. \quad (3.38)$$

From equations (3.13) and (3.34) we can write the following for $E_n^{(c)}$

$$E_n^{(c)} = \left(\mathcal{M}_n^{21} + \frac{\mathcal{P}_n^1}{\mathcal{P}_n^2}\mathcal{M}_n^{22}\right)A_n^{(e)} = \frac{2i}{\pi a_c}\frac{\beta_c J_n'(\beta_c a_i)J_n(\beta_i a_i) - \beta_i J_n(\beta_c a_i)J_n'(\beta_i a_i)}{\mathcal{P}_n^2}A_n^{(e)}. \quad (3.39)$$

From equations (3.7) and (3.37)-(3.39), we write $A_n^{(i)}$ as

$$A_n^{(i)} = \frac{4}{\pi^2 a_c a_i \mathcal{P}_n^2}A_n^{(e)}. \quad (3.40)$$

For $n = 0$, we substitute $E_0^{(e)}$, $A_0^{(c)}$, $E_0^{(c)}$ and $A_0^{(i)}$ from equations (3.34), (3.37), (3.39), and (3.40), respectively, into the corresponding field representations $w^{(q)}(\mathbf{x})$ for $q = i, c, e$, given in equation (3.33). The relevant field representations for $n = 0$, are then substituted

into the third and fourth interface conditions given in equation (3.32), when $k = 2, 3$. We find the leading order behaviour for the Bessel and modified Bessel functions appearing in these interface conditions, and find the respective discrepancies of order $O(\left|(\beta_c a_c)^2 - (\beta_e a_c)^2\right|)$ and $O(\left|(\beta_i a_i)^2 - (\beta_c a_i)^2\right|)$ left on the interfaces $r = a_c$ and $r = a_i$, for the case when $\beta_e a_c$, $\beta_c a_i$, $\beta_c a_c$, $\beta_i a_i \to 0$. Thus, solutions to the membrane waves problem governed by the Helmholtz equation, can approximate those of the plates problem in the quasi-static regime for very specific assumptions on the material parameters of the exterior medium, coating and inclusion. For this particular case, the mass balance formula (3.1), applied for membrane waves to annul the leading order contribution of the monopole term in the scattered field, can then be used as an approximation for the plates case. The theory given in the paper by Farhat. *et al.* [23], was for the particular set of material parameters stated at the beginning of this section. We note that this approximation is not applicable at frequencies in the intermediate regime when the coupling between Helmholtz and modified Helmholtz solutions becomes essential through the interface conditions on $r = a_i$ and $r = a_c$.

As shown in the previous section for membrane waves, we aim to control the monopole term at resonant regimes by introducing a specifically designed coating around the inclusion, noting that we do not necessarily annul the monopole term with the introduction of a passive element. Near resonant frequencies, we have shown in section 3.1.4 that for the case of membrane waves, scattering reduction cannot be achieved using a coating whose density is chosen according to the simple mass balance argument. The coating we employ instead, enables us to shift away from the resonance mode, and hence implement high-precision active cloaking using active sources.

3.2.2 Governing equations

We aim to combine passive and active techniques in our cloaking method for an inclusion in a Kirchhoff plate. Hence, we give the governing equation for flexural waves scattered by a coated inclusion surrounded by a finite number of active sources. The geometry of the problem is shown in Fig. 3.11. Assuming time-harmonic vibrations, the governing equation reads

$$\left(\Delta^2 - \frac{\rho_q h\, \omega^2}{D_q}\right) w^{(q)}(\mathbf{x}) = \left(\Delta + \beta_q^2\right)\left(\Delta - \beta_q^2\right) w^{(q)}(\mathbf{x}) = 0, \quad \mathbf{x} \in \Omega_q, \quad q = i, c, e. \tag{3.41}$$

Here $\beta_q^2 = \omega\sqrt{\rho_q h / D_q}$ is the spectral parameter with the super/sub-script q being either i, c, e denoting the inclusion, coating and exterior, respectively, and Ω_q denotes the region corresponding to the three regions. In the case of a circular geometry, the domains of the inclusion, coating and exterior matrix are defined as in equation (3.3).

We impose the conditions of perfect bonding to the interfaces $r = a_i$ and $r = a_c$, where the inclusion and coating meet, and the coating and exterior meet, respectively. Perfect bonding implies continuity of the displacement, its normal derivative, the moment and the transverse force, and are stated in chapter 1 in equations (1.20)-(1.22).

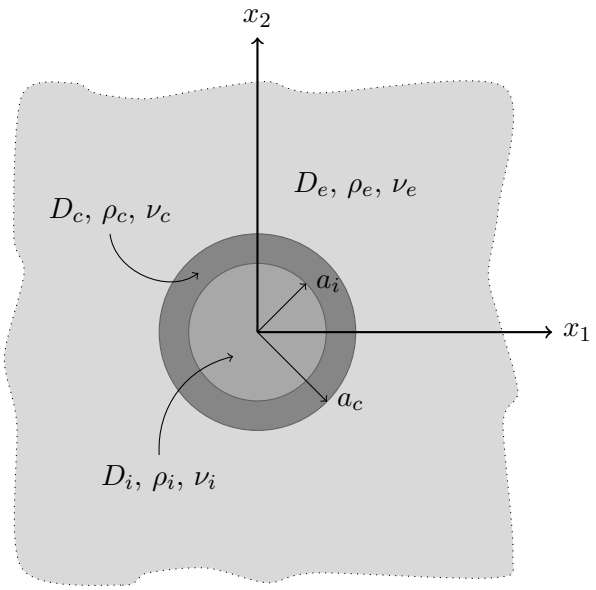

Figure 3.11: The geometry is shown for a coated inclusion embedded in a Kirchhoff plate. The material properties of the inclusion, its coating and the exterior medium are associated with the subscripts $i,\ c, e$, respectively. The respective interior and exterior radii of the coating are denoted by a_i, a_c.

3.2.3 Derivation of the scattering matrix

We write the multipole representation of the solution of equation (3.41) takes the form of equation (1.19) from chapter 1 but with $q = i, c, e$ to denote the inclusion, coating and exterior medium, respectively. We aim to obtain an analytical representation of the scattering matrix that encapsulates the interface conditions of perfect bonding. This is not a straight forward task, but we begin by following the theory outlined in section 1.2 of chapter 1, and write expressions for the fields $w^{(i)}, w^{(c)}$ and $w^{(e)}$, outside the active source locations as

$$w^{(q)}(r,\theta) = \sum_{n=-\infty}^{\infty} \left[A_n^{(q)} J_n(\beta_q r) + E_n^{(q)} H_n^{(1)}(\beta_q r) + B_n^{(q)} I_n(\beta_q r) + F_n^{(q)} K_n(\beta_q r) \right] e^{in\theta}, \quad (3.42)$$

where once again, q is either i, c or e, depending on the respective region. We note that when $q = i$, the coefficients $E_n^{(i)}$ and $F_n^{(i)}$ are identically zero to ensure displacements are finite at the origin. We substitute the appropriate representations of (3.42) into the corresponding interface conditions (1.20)-(1.22) on $r = a_i$ and $r = a_c$, to obtain two matrix equations relating the wave coefficients of the inclusion to the coating, and the coating to the exterior, respectively. The matrix relations are as follows

$$\mathcal{A}^{(ci)} \begin{pmatrix} A_n^{(c)} \\ E_n^{(c)} \\ B_n^{(c)} \\ F_n^{(c)} \end{pmatrix} = \mathcal{B}^{(ci)} \begin{pmatrix} A_n^{(i)} \\ B_n^{(i)} \end{pmatrix} \quad \text{on} \quad r = a_i, \quad (3.43)$$

where $\mathcal{A}^{(ci)}$ and $\mathcal{B}^{(ci)}$ are 4×4 and 4×2 matrices, respectively; and

$$\mathcal{A}^{(ec)} \begin{pmatrix} A_n^{(e)} \\ E_n^{(e)} \\ B_n^{(e)} \\ F_n^{(e)} \end{pmatrix} = \mathcal{B}^{(ec)} \begin{pmatrix} A_n^{(c)} \\ E_n^{(c)} \\ B_n^{(c)} \\ F_n^{(c)} \end{pmatrix} \quad \text{on} \quad r = a_c, \tag{3.44}$$

where $\mathcal{A}^{(ec)}$ and $\mathcal{B}^{(ec)}$ are both 4×4 matrices. The representations of these four matrices are lengthy, and likely to obscure the method of obtaining the scattering matrix, hence they are given in Appendix A.1. At this stage, it is important to emphasise that reducing the matrices $\mathcal{A}^{(ci)}$ and $\mathcal{A}^{(ec)}$ to block-diagonal structure is essential to pursue the derivation of an analytical formula for the scattering matrix. Hence, $\mathcal{A}^{(ci,*)}, \mathcal{A}^{(ec,*)}$ denote the required matrices in block-diagonal form and $\mathcal{B}^{(ci,*)}, \mathcal{B}^{(ec,*)}$ are matrices resulting from the row operations incurred when obtaining the block-diagonal matrices $\mathcal{A}^{(ci,*)}, \mathcal{A}^{(ec,*)}$. Note, that all entries of the matrices stated here have entries which are long and repetitive, hence are given in Appendix A.1.

We use the four matrices $\mathcal{A}^{(ci,*)}$, $\mathcal{B}^{(ci,*)}$, $\mathcal{A}^{(ec,*)}$ and $\mathcal{B}^{(ec,*)}$ to construct two further matrices $\mathcal{C}^{(ci,*)}$ and $\mathcal{C}^{(ec,*)}$, with the aim of obtaining a relation between the wave coefficients in the inclusion and exterior. The matrices $\mathcal{C}^{(ci,*)}$ and $\mathcal{C}^{(ec,*)}$ read

$$\mathcal{C}^{(ci,*)} = {\mathcal{A}^{(ci,*)}}^{-1} \mathcal{B}^{(ci,*)}, \quad \mathcal{C}^{(ec,*)} = {\mathcal{A}^{(ec,*)}}^{-1} \mathcal{B}^{(ec,*)}. \tag{3.45}$$

The final step in the construction of the scattering matrix is to represent via a matrix product, the progression from the interface between the inclusion and coating, to that of the coating and exterior medium. We obtain a transfer matrix $\mathcal{C}^{(ei,*)}$, which encapsulates the boundary conditions at both interfaces as follows

$$\mathcal{C}^{(ei,*)} = \mathcal{C}^{(ec,*)} \mathcal{C}^{(ci,*)}. \tag{3.46}$$

The transfer matrix $\mathcal{C}^{(ei,*)}$ can then be used to write the wave coefficients $A_n^{(e)}$, $B_n^{(e)}$, $E_n^{(e)}$ and $F_n^{(e)}$ in the exterior region in terms of the wave coefficients $A_n^{(i)}$, $B_n^{(i)}$ in the inclusion region:

$$\begin{pmatrix} A_n^{(e)} \\ E_n^{(e)} \\ B_n^{(e)} \\ F_n^{(e)} \end{pmatrix} = \mathcal{C}^{(ei,*)} \begin{pmatrix} A_n^{(i)} \\ B_n^{(i)} \end{pmatrix}. \tag{3.47}$$

We eliminate the wave coefficients in the inclusion region to determine the 2×2 scattering matrix $\mathcal{S}_n$ which relates the scattered wave coefficients in the exterior region to the incident wave coefficients in the exterior region. The relevant equations resulting from the procedure are described in Appendix A.2 and lead to the following matrix equation

$$\begin{pmatrix} E_n^{(e)} \\ F_n^{(e)} \end{pmatrix} = \mathcal{S}_n \begin{pmatrix} A_n^{(e)} \\ B_n^{(e)} \end{pmatrix}, \tag{3.48}$$

where the left- and right-hand sides correspond to scattered and incident wave coefficients, respectively. We consider the case of a normally incident plane wave, whose series representation is given by equation (1.12) in chapter 1.

The coefficients $A_n^{(i)}, B_n^{(i)}$ associated with the inclusion, $A_n^{(c)}, B_n^{(c)}, E_n^{(c)}, F_n^{(c)}$ associated with the coating and $E_n^{(e)}, F_n^{(e)}$ associated with the exterior, respectively, can be readily found from (3.47) (note, this analysis is lengthy and involved, so can be found in Appendix A.2). We note that in this particular case $A_n^{(e)} = i^n$ and $B_n^{(e)}$ is identically zero, as can be seen from equation (1.12).

Following the method outlined previously in section 1.1.2 of chapter 1, it can be shown that the general expression for the scattered field is

$$w_{inc}(r,\theta) = \mathcal{S}_0^{11} H_0^{(1)}(\beta_e r) + \mathcal{S}_0^{21} K_0(\beta_e r) + \sum_{n=1}^{\infty} 2i^n [\mathcal{S}_n^{11} H_n^{(1)}(\beta_e r) + \mathcal{S}_n^{21} K_n(\beta_e r)] \cos(n\theta), \quad (3.49)$$

where $\mathcal{S}_n^{ij}$, $i,j = 1,2$, denote the entries of the scattering matrix encapsulating the conditions of perfect bonding. At this point, we emphasise that the coefficient $\mathcal{S}_0^{11}$ in the right-hand side of the expression (3.49) is in fact equal to the scattering coefficient $E_0^{(e)}$ (using $A_0^{(e)} = 1$ and $B_0^{(e)} = 0$).

3.2.4 Resonant regimes for an uncoated inclusion

In this section, we locate the resonant regimes for an uncoated inclusion whose material parameters are chosen to be in high contrast to the surrounding medium. The scattering of a monochromatic plane flexural wave by a circular obstacle with various boundary conditions was intensively studied by Konenkov [46]. Analysis of the effective response of a cluster of obstacles, which also included explicit multipole representations for a single scatterer in the low-frequency regime, was published by Torrent *et al.* [101]. In particular Torrent *et al.* [101] acknowledged that the monopole and quadrupole coefficients have the same order of magnitude in the low-frequency regime.

In Section 4 of [46], the author gives a formula for the scattered field at a large distance away from the obstacle for small values of $\beta_e a_i$. This is also discussed in Section 3 of [101] (which is evident in equations (27), (28), (30) and (32) of [101]). The monopole and quadrupole coefficients are given by the formulae

$$\begin{aligned} |E_0^{(e)}| &\sim \frac{\pi}{4}\left[\frac{\rho_i}{2\rho_e} + \frac{D_e}{D_e(1-\nu_e) + D_i(1+\nu_i)} - 1\right](\beta_e a_i)^2, \\ |E_2^{(e)}| &\sim \frac{\pi}{4}\left[\frac{D_e(1-\nu_e) - D_i(1-\nu_i)}{2(D_e(3+\nu_e) + D_i(1-\nu_i))}\right](\beta_e a_i)^2, \end{aligned} \quad (3.50)$$

as $\beta_e a_i \to 0$. In the quasi-static regime, with the aim of removing the contribution of order $O((\beta_e a_i)^2)$ in the multipole coefficients, the following formulae can be used:

$$\frac{\rho_i}{2\rho_e} + \frac{D_e}{D_e(1-\nu_e) + D_i(1+\nu_i)} - 1 = 0, \qquad D_e(1-\nu_e) - D_i(1-\nu_i) = 0. \quad (3.51)$$

In particular, assuming that the plate has a uniform constant thickness, and the elastic materials of the inclusion and of the exterior matrix have the same shear moduli, the second equation in (3.51) is satisfied, and hence the quadrupole coefficient vanishes even if the mass densities are different. The monopole coefficient is due to a net force, produced by the dynamic inclusion of a different mass density and different stiffness. We note that in the static case of a plate containing an elastic inclusion, such net force is equal to zero.

Figure 3.12(a) shows $|E_0^{(e)}|$ and $|E_2^{(e)}|$ in the low-frequency regime for a specific choice of high-contrast material with properties $\rho_i = 0.05$, $\rho_e = 1.0$, $\nu_i = \nu_e = 0.3$, $D_i = 2.5 \times 10^{-4}$, $D_e = 1.0$ and $a_i = 0.50$. In Fig. 3.12(a) we observe the leading-order quadratic behaviour as stated in equation (3.50). For illustrative purposes we plot $|E_0^{(e)}|$ in Fig. 3.12(b) over a larger interval of frequencies which clearly shows the rapid variations it undergoes. Note that the spectral parameters β_q are related to the radian frequency ω via the formula $\beta_q^2 = \omega\sqrt{\rho_q h/D_q}$, where $q = i, c, e$.

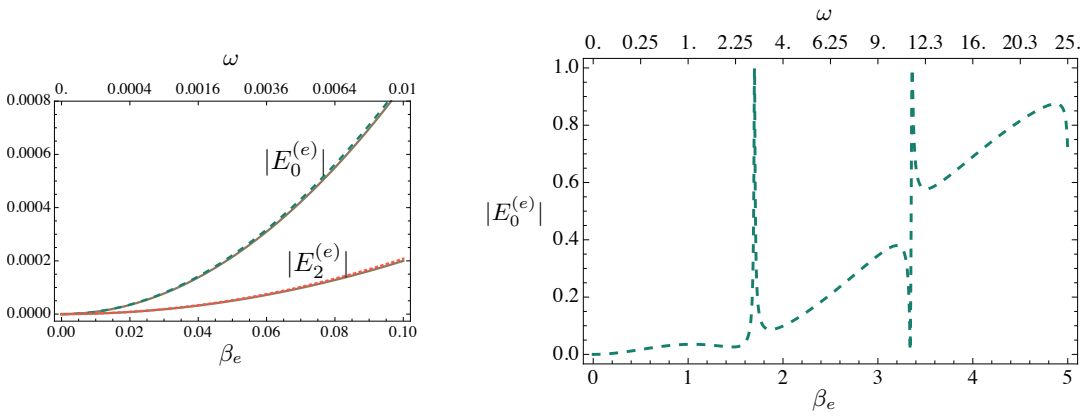

(a) (b)

Figure 3.12: Flexural wave scattering by an uncoated inclusion with the parameters $\rho_i = 0.05$, $\rho_e = 1.0$, $\nu_i = \nu_e = 0.3$, $D_i = 2.5 \times 10^{-4}$, $D_e = 1.0$, $a_i = 0.50$: (a) In the low-frequency regime, $|E_0^{(e)}|$ (dashed/green) and $|E_2^{(e)}|$ (dotted/red) are shown as functions of β_e (lower horizontal axis); for convenience ω is also shown (upper horizontal axis). The empirical fits are also presented: $|E_0^{(e)}| \approx 0.086\,\beta_e^2$, $|E_2^{(e)}| \approx 0.02\,\beta_e^2$ (both solid/grey), (b) the graph of $|E_0^{(e)}|$ as a function of β_e over a larger range.

In this chapter, we focus our attention to frequencies where resonances occur. Resonant regimes correspond to regions of rapid change of multipole coefficients as functions of frequency. To illustrate the challenging nature of resonant regimes, we present several computational examples in Fig. 3.13 for an uncoated inclusion. For three different frequencies, we give the total flexural wave spatial distributions for: (a) the low frequency of $\omega = 0.3$, where the scattering amplitudes are small; (b) the higher frequency of $\omega = 11.15$, where $E_0^{(e)} = 0$; and (c) a small increase in frequency from $\omega = 11.15$ to $\omega = 11.30$, where we see a

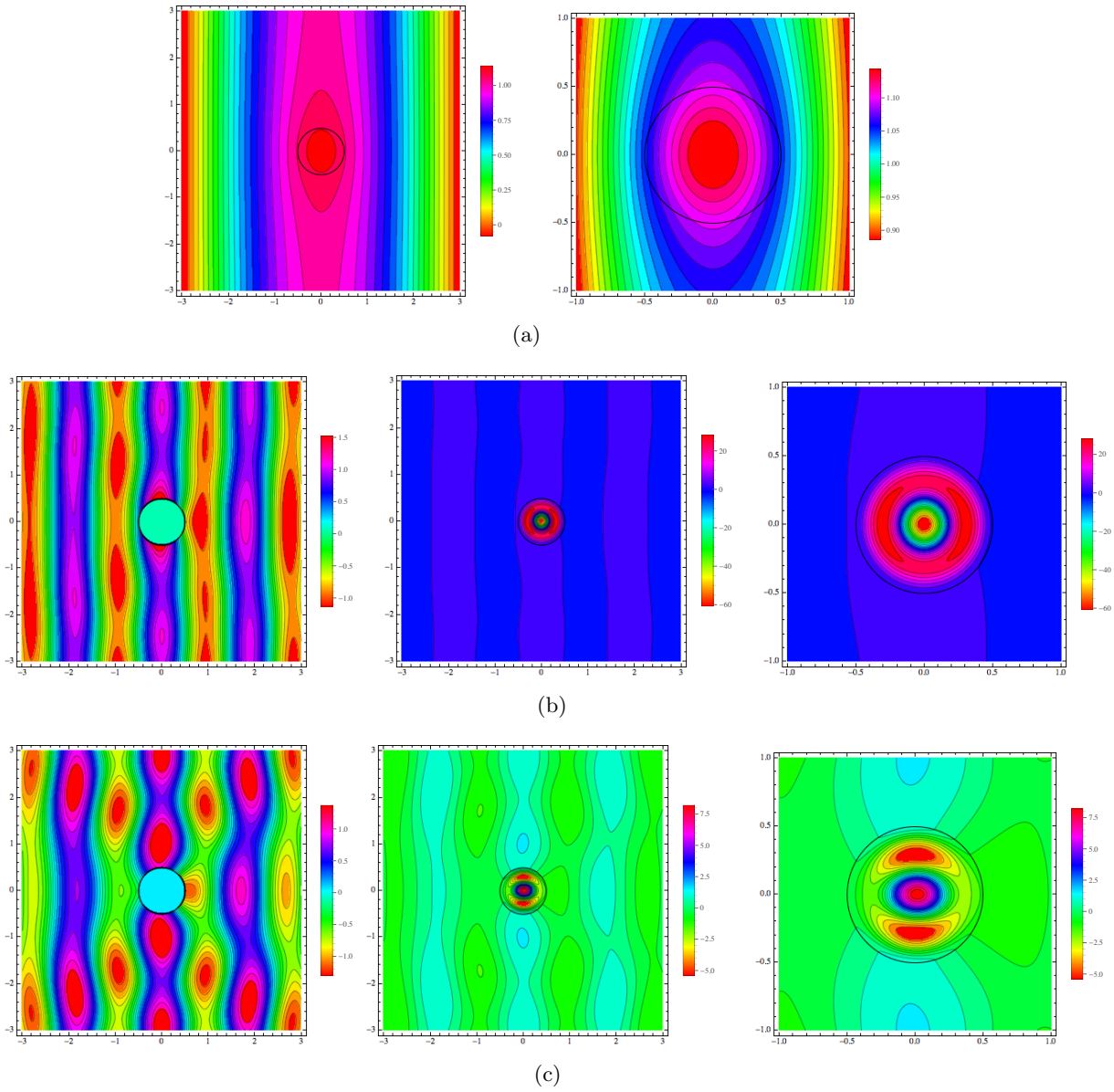

Figure 3.13: Flexural wave scattering by an uncoated inclusion for the parameters as in Fig. 3.12: (a) Total field for $\omega = 0.3$, (b) Total field for $\omega = 11.15$ where $E_0^{(e)}$ vanishes, (c) Total field for $\omega = 11.30$ where $|E_0^{(e)}|$ has a relatively large value. On the right, in each image we present a zoomed-in version of the displacement inside and in the close vicinity of the inclusion. The first two frames in the inset (b) and (c) represent the same field outside the inclusion, but with different colour maps, where the first frame excludes the internal field, whereas the second frame includes it. In all contour plots horizontal and vertical axes are the x_1- and x_2-axes, respectively.

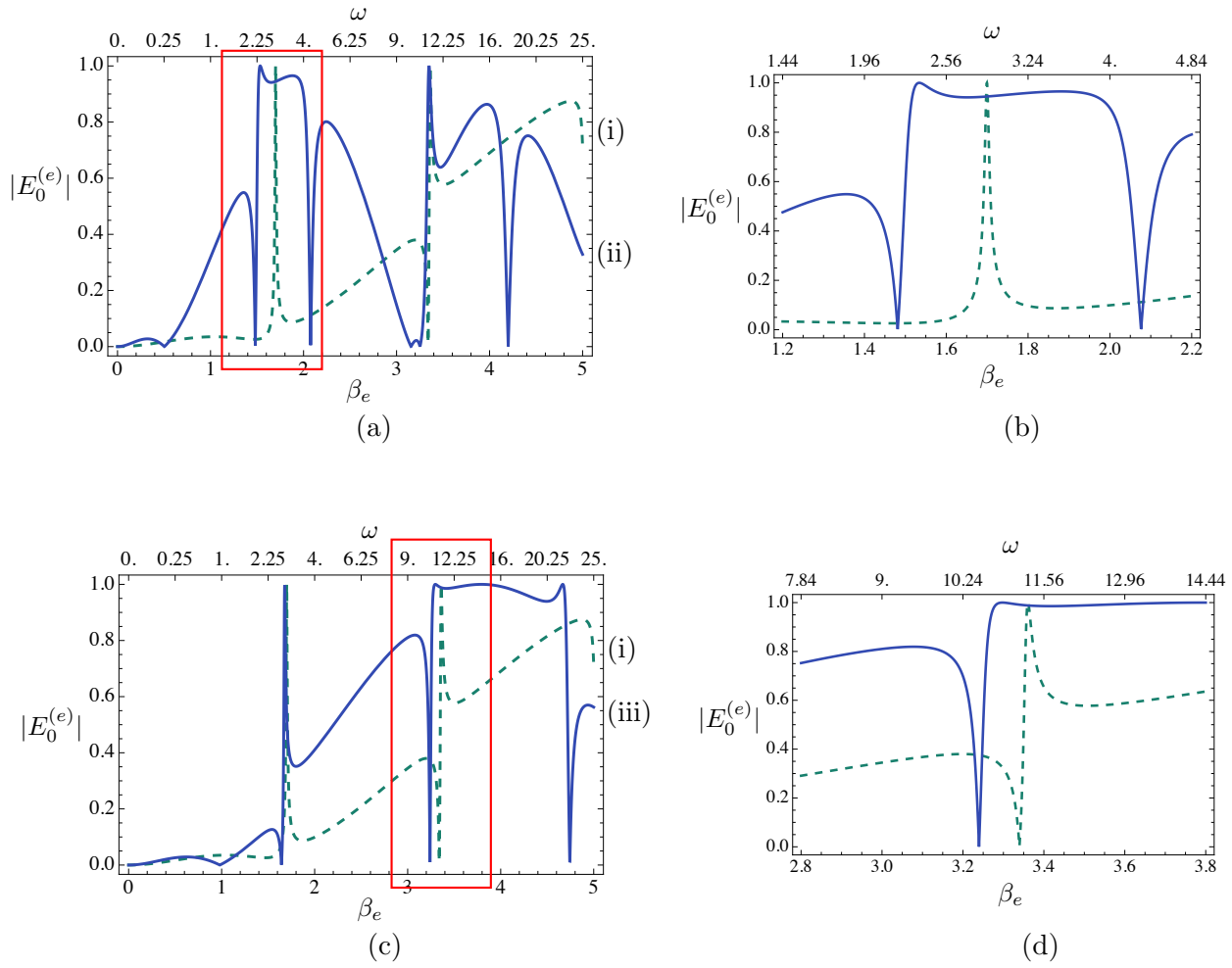

Figure 3.14: (a), (b) Flexural wave scattering by (i) an uncoated inclusion with parameter values $\rho_i = 0.05$, $\rho_e = 1.0$, $\nu_i = \nu_e = 0.3$, $D_i = 2.5 \times 10^{-4}$, $D_e = 1.0$, $a_i = 0.50$ (dashed/green); (a) (ii) a coated inclusion with parameter values as in (i) but with material properties of the coating reading $\rho_c = 0.005$, $\nu_c = 0.3$, $D_c = 2.5 \times 10^{-2}$ and $a_c = 0.77$ (solid/blue), (b) Flexural wave scattering for the parameters of (i) and (ii) in (a), but for a range of β_e highlighted by the (red) rectangular box in (a); (c) (iii) a coated inclusion with parameter values as in (i) but with material properties of the (heavier) coating reading $\rho_c = 0.05$, $\nu_c = 0.3$, $D_c = 3 \times 10^{-2}$ and $a_c = 1.5$ (solid/blue); (b) Flexural wave scattering for the parameters of (i) and (iii) in (a), but for a range of β_e highlighted by the (red) rectangular box in (c).

dramatic change in both the spatial distribution around the inclusion and in its amplitude variation. The notable change in scattering properties in such a small frequency interval can create difficulties in our active cloaking method if the incident field is swept in frequency at a resonant regime, as the active sources compensate for the rapid change in scattering properties from the inclusion.

3.2.5 Design of the coating targeting resonant frequencies

As mentioned previously, this chapter focuses on frequency regimes where multipole coefficients change rapidly. For illustrative purposes, we use the coefficient $E_0^{(e)}$, characterising a net force produced by the inclusion, to identify examples of such resonant regimes. Our primary objective is to use passive and active techniques to cloak at resonant regimes. The passive element of the cloak is a coating that surrounds the inclusion, that is designed to work at higher-frequencies rather than at the quasi-static regime. We illustrate the effect of such a coating in Fig. 3.14. In a targeted interval, the rapid change in the monopole coefficient (green/dashed curve) associated with a high-contrast inclusion (as in Fig. 3.12(b)) is shifted by the use of a suitably designed coating (solid/blue curve). The (red) rectangular boxes in Fig. 3.14(a), (c) (detail given in Fig. 3.14(b), (d)) highlight the difference in scattering properties between the uncoated and coated inclusions.

In exploration of the parameter space, we have used the principle of choosing a high contrast coating in order to "flatten" the profile of $|E_n^{(e)}|$ dependence on the frequency. The main parameters of the coating which we focus on, are the mass density and flexural rigidity. We also note that an appropriate choice of the shear modulus may simplify the analysis drastically, as mentioned in Sec. 3.2.4.

The above comparison shows that instead of the mass-compensation argument of equation (3.1), which is only applicable to a class of inclusions where the shear moduli of the inclusion and exterior matrix are equal, we employ the idea of shifting the resonance modes. The coating is designed to establish a smooth dependence on frequency in the function describing the selected multipole coefficient. Further illustrations show the efficiency of active cloaking in new regimes that include a high-contrast coating.

Before proceeding any further, we would like to emphasise once more that in the low-frequency regime the scattering is weak, and the scattered field is dominated by the monopole and quadrupole terms, whose coefficients are of order $O((\beta_e a_i)^2)$ as $\beta_e a_i \to 0$. Similar to Fig. 3.12(a), in Fig. 3.15 we illustrate this by plotting the graphs of $|E_0^{(e)}|$ and $|E_2^{(e)}|$ as functions of the spectral parameter β_e in the low-frequency regime, which correspond to quadratic asymptotics.

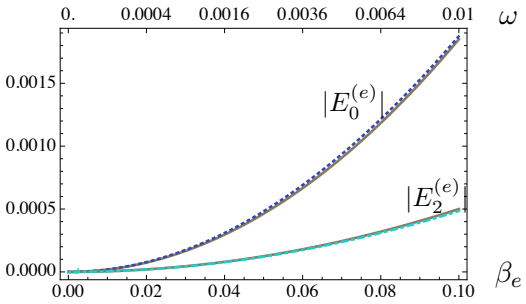

Figure 3.15: Flexural wave scattering in the low-frequency regime by a coated inclusion with parameter values $\rho_i = 0.05$, $\rho_c = 0.005$, $\rho_e = 1.0$, $\nu_i = \nu_c = \nu_e = 0.3$, $D_i = 2.5 \times 10^{-4}$, $D_c = 2.5 \times 10^{-2}$, $D_e = 1.0$, $a_i = 0.50$, $a_c = 0.77$. The absolute values of the monopole $|E_0^{(e)}|$ (dashed/dark blue) and the quadrupole $|E_2^{(e)}|$ (dot-dashed/light blue) coefficients are quadratic in spectral parameter β_e. The empirical fits are $|E_0^{(e)}| \approx 0.185{\beta_e}^2, |E_2^{(e)}| \approx 0.05{\beta_e}^2$ (both solid/grey).

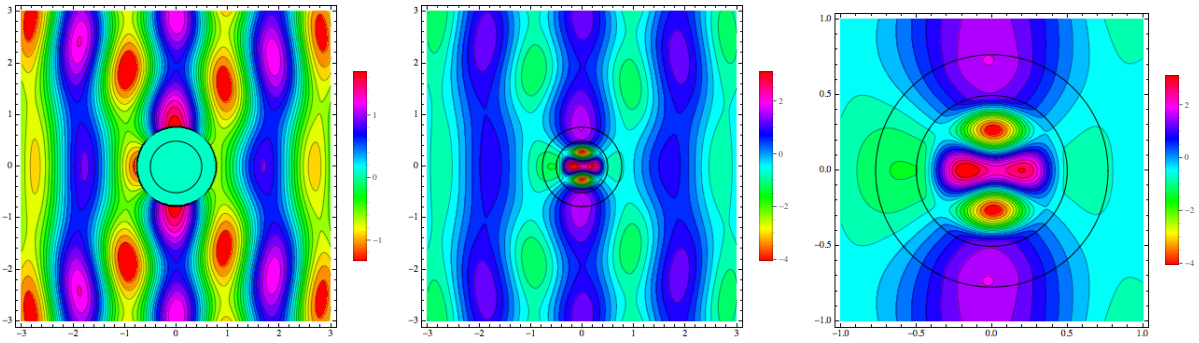

(a) (b) (c)

Figure 3.16: Flexural wave scattering: (a) Total displacement field exterior to a coated inclusion with parameter values as in Fig. 3.15 and $\omega = 11.15$. (b) Total displacement field of a coated inclusion with parameter values as in (a) plotted for the whole plate, including the coating and inclusion. Note that the displacements inside the coating and inclusion dominate in this case and thus the detail in the exterior is more difficult to observe. (c) A zoomed-in version of the displacement inside the inclusion, coating and in close vicinity of the coating.

Although we do not give explicit asymptotics for multipole coefficients, we note that when the shear moduli of the exterior matrix, coating and inclusion coincide, the quadrupole coefficient is of order $o((\beta_e a_i)^2)$. The monopole coefficient, and hence the net force produced by the dynamic inclusion, can be reduced to $o((\beta_e a_i)^2)$ by choosing parameters of the coating to satisfy the following equation:

$$\begin{aligned}&[2D_e\mathfrak{a}_1(\mathfrak{b}_1 + 2D_c - 2D_e)\beta_e^4 + \mathfrak{a}_1\mathfrak{b}_1\mathfrak{b}_2\beta_c^2\beta_e^2 - 2D_c\mathfrak{a}_1\mathfrak{b}_1\beta_c^4]\, a_c^4 + 2\mathfrak{a}_2\mathfrak{b}_2[D_c\beta_c^4 - D_i\beta_i^4]\, a_i^4 \\ &+ [4D_e\mathfrak{a}_2(\mathfrak{b}_2 + D_e)\beta_e^4 + \mathfrak{a}_2\mathfrak{b}_2^2\beta_c^2\beta_e^2 - 2D_i\mathfrak{a}_1\mathfrak{b}_1\beta_i^4 + 2D_c(\mathfrak{a}_1\mathfrak{b}_1 - \mathfrak{a}_2\mathfrak{b}_2)\beta_c^4]\, a_i^2 a_c^2 = 0,\end{aligned} \tag{3.52}$$

where

$$\begin{aligned}\mathfrak{a}_1 &= D_i(1+\nu_i)+D_c(1-\nu_c), \quad \mathfrak{a}_2 = D_i(1+\nu_i)-D_c(1+\nu_c),\\ \mathfrak{b}_1 &= D_c(1+\nu_c)+D_e(1-\nu_e), \quad \mathfrak{b}_2 = D_c(1-\nu_c)-D_e(1-\nu_e).\end{aligned}$$

We also note that in the very special case of $D_i = D_c = D_e$, $\nu_i = \nu_c = \nu_e$ and $\rho_i \neq \rho_c \neq \rho_e$, equation (3.52) reduces to (3.1).

In Fig. 3.16 we present the total flexural wave amplitude for the frequency $\omega = 11.15$ for an inclusion with a suitably designed coating chosen to give the "flattened" variation of $|E_0^{(e)}|$ (see solid/blue curve in Fig. 3.14(b)). Comparing Fig. 3.16 with Fig. 3.13(b), it is clear that the increase in strength of the monopole term results in high scattering.

3.2.6 Active cloaking of a coated inclusion

Now, we assume that a finite number of active sources are introduced in the exterior of the coated inclusion in order to reduce the scattering of an incident plane wave by the inclusion. Here we derive formally an algebraic system for the active source amplitudes, which are computed to make the required number of multipole coefficients vanish in the representation of the outgoing scattered field. This is achieved by employing a method of solution involving both passive and active techniques.

An algebraic system for active source amplitudes in the presence of an incident plane wave

In order to find the total wave scattered from the coated inclusion, we identify two model problems illustrated in Fig. 3.17. These problems deal with scattering from the coated circular inclusion, with the origin of coordinate axes positioned at the inclusion's centre. For the first model problem, the incident field is a plane wave of normal incidence (depicted in Fig. 3.17(a)), whereas in the second problem, the incident field is generated by a point source of unit amplitude placed externally to the coated inclusion (depicted in Fig. 3.17(b)).

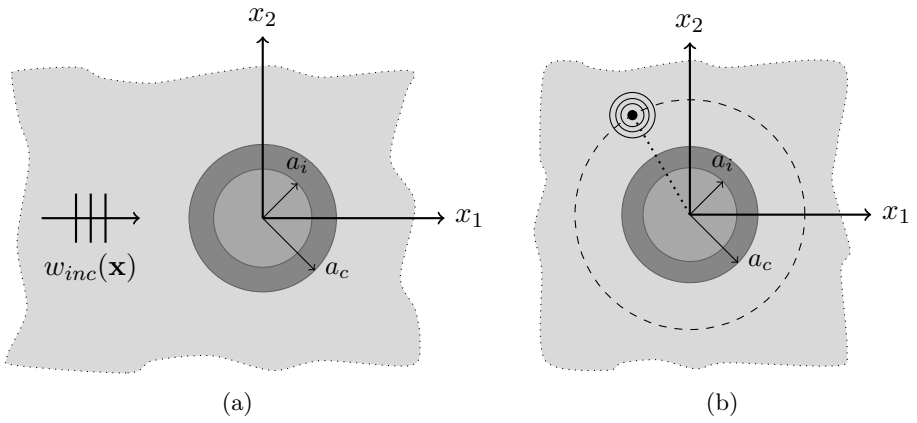

Figure 3.17: Model problems: (a) plane wave $w_{inc}(\mathbf{x})$ incident on a coated elastic inclusion; (b) a point source near the coated inclusion.

These model problems take the same form as in section 2.6 of chapter 2. Although the scatterer is a coated inclusion and not an arbitrarily shaped cavity, the analysis is analogous to that of section 2.6. By solving the model problems, we obtain the following far-field representations for the scattered field in the exterior matrix, from an incident plane wave

$$w_{sc}(\mathbf{x}) \sim \sum_{n=-\infty}^{\infty} E_n H_n^{(1)}(\beta_e r) e^{in\theta} \quad \text{for } \beta_e r \gg 1, \tag{3.53}$$

and the scattered field from a remote point source together with propagating contributions from the source itself

$$w^{(s,l)}(\mathbf{x}) \sim \sum_{n=-\infty}^{\infty} A_n^{(s,l)} H_n^{(1)}(\beta_e r) e^{in\theta}, \quad l = 1, \ldots, N, \quad \text{as } \beta_e r \to \infty, \tag{3.54}$$

note, exponentially small terms satisfying the modified Helmholtz equation, are not shown. The main idea of our cloaking method is to ensure that the total field everywhere outside the coated inclusion (and active sources) is approximately equal to the incident field of the unperturbed plane wave.

Assuming that the coefficients E_n and $A_n^{(s,l)}$ are given in the series representations (3.53) and (3.54), active cloaking is achieved by introducing a set of m control sources of complex amplitudes Q_l placed at the points $\mathbf{x}^{(s,l)}$ in the region exterior of the coated inclusion denoted by $\mathcal{D}$. After the truncation to order L in the expansions (3.53) and (3.54), we choose $m = 2L + 1$, so that the total displacement field $w_{(total)}(\mathbf{x})$ is approximately equal to the incident field w_{inc}, that is

$$w_{(total)} = w(\mathbf{x}) + \sum_{l=1}^{m} Q_l w^{(s,l)}(\mathbf{x}) \approx w_{inc}(\mathbf{x}). \tag{3.55}$$

To find Q_l, we substitute (3.53) and (3.54) into (3.55), and obtain the following system of linear algebraic equations

$$E_k + \sum_{l=1}^{2L+1} Q_l A_k^{(s,l)} = 0, \quad k = -L, \ldots, L. \tag{3.56}$$

It is assumed that the positions of active sources are chosen so that the system (3.56) is non-degenerate.

Introduction of active sources

Here we implement the algorithm outlined in section 3.2.6 for active cloaking of a coated inclusion, where the frequency does not necessarily lie in the quasi-static regime and thus multipole coefficients can vary rapidly as functions of frequency. In what follows, we give explicit analytical representations for amplitudes of active sources required for active cloaking.

When introducing active sources, we evenly distribute the control sources on a circle of radius a_s starting from the x_1-axis. Sources positioned off the x_1-axis are done so in pairs to maintain the symmetry of the problem (they will also have the same amplitude). For sources

positioned at $(a_s\cos\psi, \pm a_s\sin\psi)$, using Graf's addition theorem, we obtain the following representation of the Green's function for the biharmonic operator

$$Q_l G(x_1 - a_s\cos\psi, x_2 \pm a_s\sin\psi) = \\ -\frac{Q_l}{8\beta_e^2}\sum_{k=-\infty}^{\infty} e^{ik(\theta\mp\psi)}\left[iH_k^{(1)}(\beta_e a_s)J_k(\beta_e r) - \frac{2}{\pi}K_k(\beta_e a_s)I_k(\beta_e r)\right],$$

where Q_l is the complex amplitude of the l-th active source and $\pm\psi$ is the polar angle of the source position.

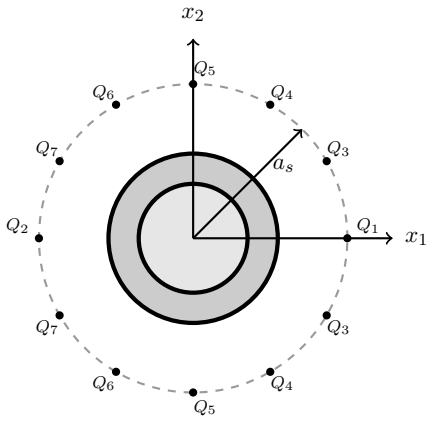

Figure 3.18: A configuration of twelve sources positioned symmetrically around the coated inclusion with complex amplitudes Q_1, $Q_2, \ldots, Q_7$.

For the twelve source configuration (see Fig. 3.18) the n-th order coefficient for the total wave incident on the coated inclusion is thus

$$A_n^{(e)} = i^n - \frac{i}{8\beta_e^2}H_n^{(1)}(\beta_e a_s)\Big\{Q_1 + (-1)^n Q_2 \\ + 2\big[Q_3\cos(n\xi) + Q_4\cos(n\zeta) + Q_5\cos(n\eta) + Q_6\cos(n\gamma) + Q_7\cos(n\alpha)\big]\Big\},$$

$$B_n^{(e)} = -\frac{i}{4\pi\beta_e^2}K_n(\beta_e a_s)\Big\{Q_1 + (-1)^n Q_2 \\ + 2\big[Q_3\cos(n\xi) + Q_4\cos(n\zeta) + Q_5\cos(n\eta) + Q_6\cos(n\gamma) + Q_7\cos(n\alpha)\big]\Big\},$$

where Q_n, $n = 3, 4, \ldots, 7$, are the amplitudes of the sources positioned off the x_1-axis.

The coefficients of the total wave scattered from the coated inclusion read as follows,

$$E_n^{(e)} = \mathcal{S}_{11}^{(n)}A_n^{(e)} + \mathcal{S}_{12}^{(n)}B_n^{(e)}, \qquad F_n^{(e)} = \mathcal{S}_{21}^{(n)}A_n^{(e)} + \mathcal{S}_{22}^{(n)}B_n^{(e)}.$$

Thus, to eliminate the total wave propagating away from the coated inclusion, we set

$$\mathcal{S}_{11}^{(n)}A_n^{(e)} + \mathcal{S}_{12}^{(n)}B_n^{(e)} - \frac{i}{8\beta_e^2}J_n(\beta_e a_s)\Big\{Q_1 + (-1)^n Q_2 \\ + 2\big[Q_3\cos(n\xi) + Q_4\cos(n\zeta) + Q_5\cos(n\eta) + Q_6\cos(n\gamma) + Q_7\cos(n\alpha)\big]\Big\} = 0.$$

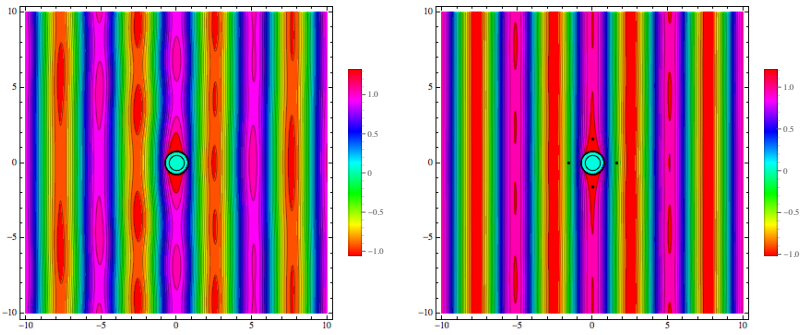

(a) (b)

Figure 3.19: Flexural wave scattering: (a) Total displacement field exterior to a coated inclusion with material properties as in Fig. 3.15 but at the smaller frequency of $\omega = 1.50$. (b) Total displacement field for the parameter values as in (a) but in the presence of 4 active sources located on the axes (black dots), all $a_s = 1.57$ units away from the centre of the inclusion.

Cloaking of weak scattering in a non-resonant regime

As noted in section 3.2.5, the scattering produced by the elastic inclusion is very weak in the limit when the wavelength of the incident plane wave tends to infinity compared to the size of the inclusion. In such a regime, the scattering pattern is also dominated by the Helmholtz type waves. However, as the frequency of the incident wave increases, the role played by the modified Helmholtz waves in the transmission conditions becomes important, and we show in this section that a finite number of active sources are capable of producing a substantial reduction of the scattered field. We note that our study in chapter 2 confirmed that, in a low-frequency regime, at least four sources were required for cloaking a rigid circular inclusion.

In Fig. 3.19(a), we present the field plot where $\omega = 1.50$ (and hence $\beta_e = 1.2247$); the wavelength of the incident plane wave is evidently comparable with the diameter of the elastic inclusion. The geometrical and elastic parameters of the inclusion and coating are the same as in Fig. 3.14. Figure 3.19(a) shows a perturbation of the incident wave by the inclusion. As described in Section 3.2.6, four active sources can be introduced to compensate for the scattering of the incident plane wave produced by the coated inclusion. The symmetric configuration of sources, shown in Fig. 3.19(b), is used in the simulation, and the amplitudes of the active sources are derived in an explicit closed form according to the above discussion. The cloaking with four sources is quite successful in compensating for the scattering by the coated inclusion for $\omega = 1.50$; we will shortly show that beyond this frequency four sources are no longer adequate. In the following subsection, we introduce more sources and demonstrate how the higher-order multipole terms can be suppressed.

Higher-frequency regime

The multipole representation (3.42) for the total field is used to produce the numerical illustrations below. The sources are placed on a circle of radius $a_s = 1.57$, outside the coated inclusion, whose external radius is $a_c = 0.77$. The simulations are presented for the cases of 4, 8 and 12 sources, together with tabular data on the values of high-order multipole coefficients.

In fact, the required number of sources can be easily deduced by plotting the n-th order multipole term $|E_n^{(e)} H_n^{(1)}(\beta_e a_s)|$ against the multipole order n. We note that the symmetry of the inclusion forces us to use two sources for each order. Thus it is clear from Fig. 3.20 that we require twelve sources to annul all significant multipole coefficients.

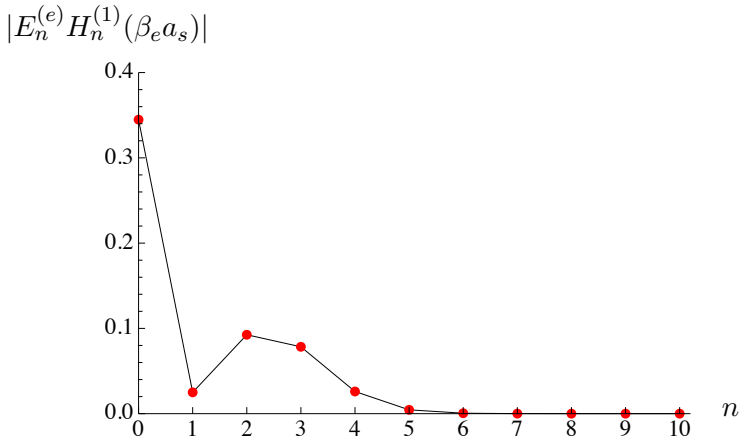

Figure 3.20: Flexural wave scattering: absolute value of the normalised outgoing wave components $E_n^{(e)} H_n^{(1)}(\beta_e a_s)$ against the multipole order n for $\omega = 11.15$. Parameter values as in Fig. 3.15 with $a_s = 1.57$.

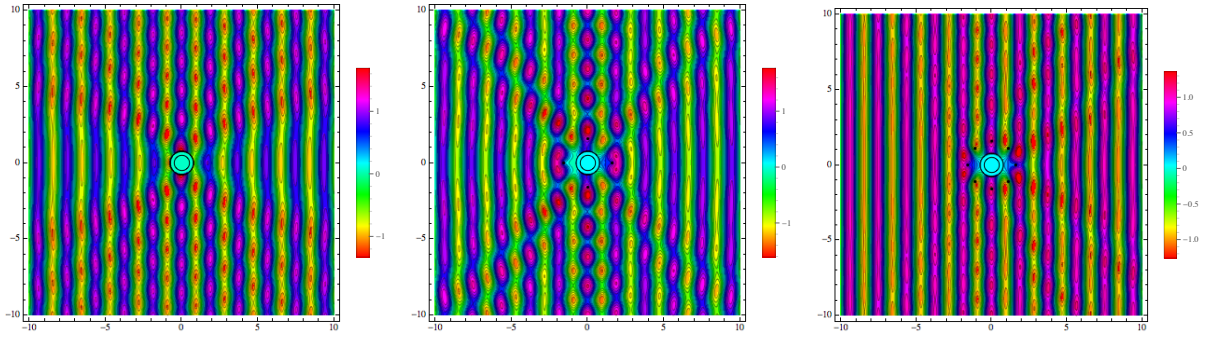

(a) (b) (c)

Figure 3.21: Flexural wave scattering: (a) Total displacement field exterior to a coated inclusion with parameter values as in Fig. 3.15 and $\omega = 11.15$. (b), (c) Total displacement field in the presence of 4 and 8, respectively active sources located on the axes (black dots), $a_s = 1.57$ units away from the origin.

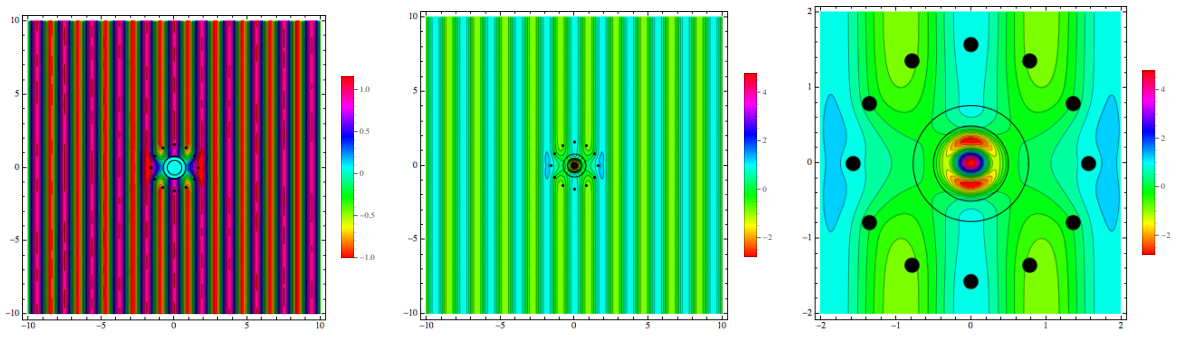

(a) (b) (c)

Figure 3.22: Flexural wave scattering: (a) Total displacement field exterior to a coated inclusion with parameter values as in Fig. 3.15 and $\omega = 11.15$ in the presence of 12 active sources positioned $a_s = 1.57$ units away from the origin. (b) Same as (a) but the total displacement field plotted in all three regions. (c) Same as (b) but over a smaller range of the plate detailing localised fields in the inclusion.

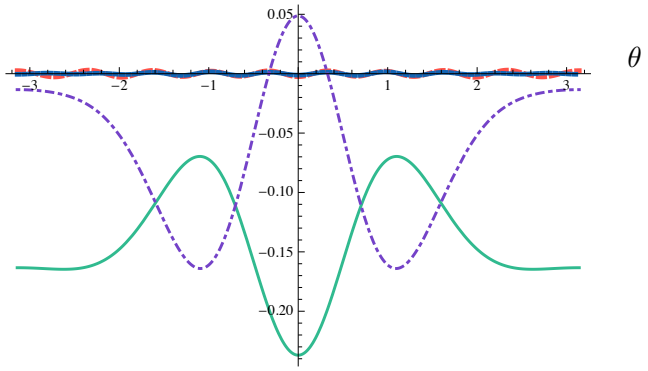

Figure 3.23: Angular plot of the scattered field along the circular contour of radius 7.85 (five times the radius of the circle on which the active sources are located) centred at the origin, for the simulations in Fig. 3.21(a) with no sources present and in Fig. 3.22 with 12 sources present. No active sources present: Solid/green curve represents the real and dot-dashed/purple curve the imaginary part of the scattered field; active cloaking with 12 sources present: Dashed/red curve represents the real and dotted/blue curve the imaginary part of the scattered field, which show a significant reduction in the amplitude of the scattered field.

In Fig. 3.21, we present three cases corresponding to an incident plane wave scattered by a coated inclusion. The parameters of the coating are chosen to be the same as in the simulation depicted in Fig. 3.15. The case when active sources are absent (Fig. 3.21(a)) is compared with the two cases incorporating four (Fig. 3.21(b)) and eight (Fig. 3.21(c)) active sources, respectively. Although the scattering pattern has been reduced, in this higher-frequency regime, we need to have twelve sources for efficient cloaking. The combination of twelve sources, with the amplitudes computed according to (3.56), is given in Fig. 3.22, which shows efficient cloaking, with a notable suppression of the scattered field. Fig. 3.22(a) and Fig. 3.22(b) use a different colour code scheme; in (a) we present the field in the exterior on-

	n	**no sources**	4 sources	8 sources	12 sources
$\tilde{E}_n^{(e)}$	-8	$-3.98 \times 10^{-12} + 2.00 \times 10^{-6}\, i$	$1.50 \times 10^{-7} - 0.075\, i$	$1.49 \times 10^{-7} - 0.075\, i$	$7.66 \times 10^{-9} - 0.0038\, i$
	-7	$-0.000048 - 2.31 \times 10^{-9}\, i$	$-0.015 - 7.16 \times 10^{-7}\, i$	$-0.015 - 7.16 \times 10^{-7}\, i$	$-0.0022 - 1.05 \times 10^{-7}\, i$
	-6	$6.70 \times 10^{-7} - 0.00082\, i$	$0.00027 - 0.33\, i$	$0.00027 - 0.33\, i$	$-3.43 \times 10^{-17} + 5.55 \times 10^{-17}\, i$
	-5	$0.0092 + 0.000085\, i$	$-0.055 - 0.00051\, i$	$0.24 + 0.0022\, i$	$-1.39 \times 10^{-17} - 8.02 \times 10^{-17}\, i$
	-4	$-0.0039 + 0.0629\, i$	$0.072 - 1.15\, i$	$-1.96 \times 10^{-17} + 1.11 \times 10^{-16}\, i$	$-4.84 \times 10^{-18} - 1.11 \times 10^{-16}\, i$
	-3	$-0.20 - 0.043\, i$	$-0.26 - 0.055\, i$	$-6.94 \times 10^{-17} + 1.08 \times 10^{-16}\, i$	$1.39 \times 10^{-17} - 1.71 \times 10^{-18}\, i$
	-2	$0.066 - 0.25\, i$	$-9.26 \times 10^{-18} + 8.33 \times 10^{-17}\, i$	$-4.87 \times 10^{-17} + 1.53 \times 10^{-16}\, i$	$4.49 \times 10^{-18} + 1.25 \times 10^{-16}\, i$
	-1	$-0.071 + 0.0051\, i$	$-1.39 \times 10^{-17} + 4.50 \times 10^{-18}\, i$	$-4.16 \times 10^{-17} + 8.71 \times 10^{-17}\, i$	$-4.16 \times 10^{-17} + 6.31 \times 10^{-17}\, i$
	0	$-0.98 - 0.13i$	$1.58 \times 10^{-16} - 5.55 \times 10^{-17}\, i$	-7.88×10^{-17}	$-9.27 \times 10^{-17} - 2.78 \times 10^{-17}\, i$
	1	$0.071 - 0.0051\, i$	$1.39 \times 10^{-17} - 4.50 \times 10^{-18}$	$4.16 \times 10^{-17} - 8.71 \times 10^{-17}\, i$	$4.16 \times 10^{-17} - 6.31 \times 10^{-17}\, i$
	2	$0.066 - 0.25\, i$	$-9.26 \times 10^{-18} + 8.33 \times 10^{-17}$	$-4.87 \times 10^{-17} + 1.53 \times 10^{-16}\, i$	$4.49 \times 10^{-18} + 1.25 \times 10^{-16}\, i$
	3	$0.20 + 0.043\, i$	$0.26 + 0.055\, i$	$6.94 \times 10^{-17} - 1.08 \times 10^{-16}\, i$	$-1.39 \times 10^{-17} + 1.71 \times 10^{-18}\, i$
	4	$-0.0039 + 0.0629\, i$	$0.072 - 1.15\, i$	$-1.96 \times 10^{-17} + 1.11 \times 10^{-16}\, i$	$-4.84 \times 10^{-18} - 1.11 \times 10^{-16}\, i$
	5	$-0.0092 - 0.000085\, i$	$0.055 + 0.00051\, i$	$-0.24 - 0.0022\, i$	$1.39 \times 10^{-17} + 8.02 \times 10^{-17}\, i$
	6	$6.70 \times 10^{-7} - 0.00082\, i$	$0.00027 - 0.33\, i$	$0.00027 - 0.33\, i$	$-3.43 \times 10^{-17} + 5.55 \times 10^{-17}\, i$
	7	$0.000048 + 2.31 \times 10^{-9}\, i$	$0.015 + 7.16 \times 10^{-7}\, i$	$0.015 + 7.16 \times 10^{-7}\, i$	$0.0022 + 1.05 \times 10^{-7}\, i$
	8	$-3.98 \times 10^{-12} + 2.00 \times 10^{-6}\, i$	$1.50 \times 10^{-7} - 0.075\, i$	$1.49 \times 10^{-7} - 0.075\, i$	$7.66 \times 10^{-9} - 0.0038\, i$

Table 3.2: The coefficients $\tilde{E}_n^{(e)}$ of $H_n^{(1)}(\beta_e r)$ terms for a configuration with zero, four, eight and twelve control sources positioned symmetrically on a circle of radius of 1.57 units from the origin. The frequency of the incident plane wave is $\omega = 11.15$.

ly, while in (b) and (c) we show the field in the inclusion, which also indicates the field localisation.

In Fig. 3.23 we show the angular plot of the scattered field from the coated inclusion with no active sources present compared to the scattered field when twelve active sources are introduced. The geometry, frequency and material parameters are the same as in Figs. 3.21(a) and 3.22. Successful cloaking is produced by twelve active sources, resulting in a significant reduction of the scattered wave due to cancelling the required number terms in the scattered field representation.

The data in Table 3.2 for multipole coefficients demonstrates that the core region of multipole orders runs from $n = -3$ to $n = 3$. Our procedure reduces all the amplitudes of targeted orders to zero, while increasing the moduli of adjacent orders. By inspecting the amplitudes of orders $n = \pm 4$ for four sources and $n = \pm 5$ for eight sources, we can see that in both cases we have an insufficient number of sources for successful cloaking. For twelve sources, both the entries in Table 3.2 and the displacement field components shown in Fig. 3.22 confirm good quality cloaking.

3.3 Remarks and discussions

In this chapter we consider active cloaking for an inclusion in a Kirchhoff plate at resonant regimes. The cloak involves a combination of passive and active techniques, and we consider different frequency regimes ranging from the quasi-static up to higher frequencies, where multipole terms in the outgoing scattered field may be rapidly varying functions of frequency. We considered higher frequency regimes in order to investigate the interesting effects on scattering that occur at frequencies such that the propagating and evanescent solutions to the governing equation play an important role in scattering cross section.

We have highlighted that reduction of scattering in quasi-static regimes may be achieved by an appropriate choice of coating around an elastic inclusion, however, this becomes a challenge for higher frequencies. Nevertheless, the use of a coating can be extended in conjunction with active cloaking, with the aim to cancel the required number of multipole coefficients in the representation of the scattered field. In particular, for frequencies close to resonance values, the technique involves choosing the coating surrounding the inclusion to diminish the frequency sensitivity of the scattered field, and then applying active control sources.

A comparison between the flexural waves in Kirchhoff plates and membrane waves has revealed interesting connections for low frequencies. In particular, we have identified the cases when the flexural wave scattering is driven by the Helmholtz waves. On the other hand, we have also identified important differences where the evanescent waves, which are present in the expressions for the solutions to the fourth-order problem contribute significantly.

The proposed algorithm is highly useful, as amplitudes for active sources are given in the explicit analytical form, and accuracy of the cloaking of coated inclusions in resonant regimes has been well demonstrated. In the following chapter we aim to use ideas explored chapter

2, to cloak a finite cluster of pins, which also produces interesting effects on wave scattering.

Chapter 4

Active cloaking of finite clusters of pins

Having cloaked single continuous structure embedded in a thin elastic plate, we now focus our attention to cloaking a discrete set of scatterers. We recall that cloaking should be taken to mean that scattered fields are cancelled in such a way that an observer exterior to the cloak, receives no information about the object's presence. This is a slightly different approach to that of shielding problems, for which a quiet region is created around an object.

In this chapter we consider cloaking flexural waves for the simplest case of multiple scatterer - a finite cluster of rigid pins. There exists a rich resource of literature in the field of platonics, that involve wave propagation through pinned plate systems. For Kirchhoff plates subjected to incident flexural waves, the finite cluster produces interesting scattered fields due to evanescent solutions of the governing equation interacting between the pins.

To the best of our knowledge, this is the first time that a finite cluster is cloaked using active sources. However, there are examples in the literature for which the cloak itself is a discrete structure. In the paper by Colquitt *et al.* [18], a system of rods and point masses was used to approximate a regularised square-shaped continuum cloak, leading to effective transformational cloaking of waves governed by the Helmholtz equation, in the low frequency regime.

Passive techniques were also employed by Nicorovici *et al.* [76] in the field of optics. Plasmonic metamaterials were used to cloak a finite cluster of cylinders in the quasi-static regime. This was done by calculating the relative local density of states which was used to describe how a source interacts with the finite system of N coated cylinders. The coating was designed to be a medium attaining plasmonic resonance at the targeted frequencies.

We do not employ passive techniques in the cloaking method described in this chapter. Instead, we adapt the method of cloaking previously described in sections 2.2 and 2.3 in chapter 2, which employs a finite number of active sources positioned exterior to the scatterer, whose complex amplitudes are chosen to cancel selected propagating orders of the scattered field. In a finite cluster, each pin is assumed to act a point source with an unknown amplitude. The pins are modelled using a multiple of Green's function for the biharmonic operator

centred at the pin's position. Unknown amplitudes for each pin are found by applying the condition of zero displacement at every pin position and solving the resulting matrix equation for the total field. A detailed discussion on the broadband nature of our cloaking method, with the emphasis on choosing specific values of the spectral parameter from relevant band diagrams and dispersion surfaces for a thin plate pinned in a doubly periodic fashion, is in section 4.1.3.

Finally, in section 4.2, we present illustrative examples of effective cloaking for various spectral parameter values; for higher frequencies, where the cluster generates a more complicated scattering pattern, we clarify the transition from locating the active control sources on the grid of the cluster to a circle surrounding the cluster, and demonstrate the advantages of this latter configuration.

4.1 Formulation of the problem and governing equations

In this section, we first present the governing equations for flexural wave propagation in a Kirchhoff plate pinned at points forming a finite cluster surrounded by active control sources. The amplitudes of these sources are then found by solving a system of linear algebraic equations. The broadband nature of this cloaking method is also discussed in detail, with the aid of band diagrams and dispersion surfaces associated with a doubly periodic pinned plate.

4.1.1 Problem setting

Let a two-dimensional cluster of $N \times N$ pins, denoted by Π, be surrounded by m active control sources (a particular example is shown in Fig. 4.1). We define a pin as the limiting case of a circular void with a clamped boundary, that is, we require the displacement and its normal derivative to vanish, as the radius of the void tends to zero. The origin of the axes coincides with the centre of the cluster, and a plane time-harmonic wave $W_{inc}(\mathbf{x};t) = W_{inc}(x_1,x_2;t) = w_{inc}(\mathbf{x})\exp\{-i\omega t\}$, with ω being the angular frequency, is incident at an angle θ_{inc} to the x_1-axis. We consider a square array, such that the spacing between the pins in the x_1- and x_2-directions is denoted by d. The spacings between the sources and the pins forming the boundary of the cluster, in the x_1- and x_2-directions, are denoted by S.

Let the locations of the pins be denoted by $\mathbf{x}^{\mathbf{p}} = (x_1^{\mathbf{p}}, x_2^{\mathbf{p}})$, where $\mathbf{p} = (p_1, p_2)$ is a multi-index with integer components that describes the square array Π, and the position of the l-th active source by $\mathbf{x}^{(s,l)} = (x_1^{(s,l)}, x_2^{(s,l)})$. Assuming time-harmonic vibrations, the amplitude $w(\mathbf{x})$, of out-of-plane displacement satisfies the following equation

$$\left(\Delta^2 - \beta^4\right) w(\mathbf{x}) + \sum_{\mathbf{p}\in\Pi} \mathcal{A}_{\mathbf{p}}\delta(\mathbf{x}-\mathbf{x}^{\mathbf{p}}) + \sum_{l=1}^{m} \mathcal{B}_l\delta(\mathbf{x}-\mathbf{x}^{(s,l)}) = 0, \quad \mathbf{x}\in\Omega, \tag{4.1}$$

where Δ^2 is the biharmonic operator and β is the spectral parameter with $\beta^2 = \omega\sqrt{\rho h/D}$. Here ρ, h and D are the mass density, thickness and flexural rigidity of the plate $D =$

$Eh^3/[12(1-\nu^2)]$, with E being Young's modulus and ν, Poisson's ratio of the elastic material. The region Ω is exterior to the pins and sources, $\mathcal{A}_{\mathbf{p}}$ represent the normalised transverse forces acting at the points $\mathbf{x}^{\mathbf{p}}$, $\mathcal{B}_l$ represent the unknown complex amplitudes of the active sources and $\delta(\mathbf{x}-\mathbf{x}')$ is the Dirac delta function centred at $\mathbf{x}'$. The solution to equation (4.1) has the form

$$w(\mathbf{x}) = \sum_{\mathbf{p}\in\Pi} \mathcal{A}_{\mathbf{p}} G(\mathbf{x};\mathbf{x}^{\mathbf{p}}) + \sum_{l=1}^{m} \mathcal{B}_l G(\mathbf{x};\mathbf{x}^{(s,l)}). \tag{4.2}$$

Here $G(\mathbf{x};\mathbf{x}')$ the Green's function for the biharmonic operator which is non-singular at $\mathbf{x}=\mathbf{x}'$ and is written as a sum of two Bessel functions

$$G(\mathbf{x};\mathbf{x}') = -\frac{1}{8\beta^2}\left(iH_0^{(1)}(\beta|\mathbf{x}-\mathbf{x}'|) - \frac{2}{\pi}K_0(\beta|\mathbf{x}-\mathbf{x}'|)\right). \tag{4.3}$$

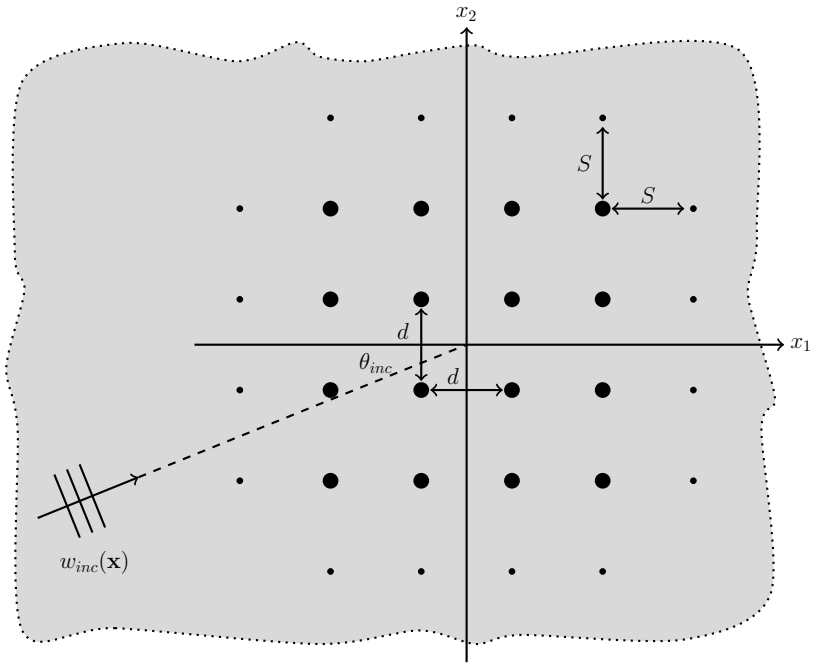

Figure 4.1: Grid for a 4×4 ($N=4$) cluster of pins (larger black discs) surrounded by $m=4N=16$ active sources (smaller grey discs). A plane wave at an angle θ_{inc} to the x_1-axis, $w_{inc}(\mathbf{x})$, is incident upon the array. The spacings between the pins in the x_1 and x_2-directions are denoted by d. The spacings between the sources and the pins in the x_1 and x_2-directions are denoted by S.

4.1.2 Calculating active source amplitudes $\mathcal{B}_m$

Given an incoming plane wave, $w_{inc}(\mathbf{x})$, incident on a finite cluster of rigid pins, we obtain the following system of equations at the pin-position $\mathbf{x}^{\mathbf{q}}$, for $\mathbf{q}\in\Pi$

$$w_{inc}(\mathbf{x}^{\mathbf{q}}) + \sum_{\mathbf{p}\in\Pi} \mathcal{A}_{\mathbf{p}} G(\mathbf{x}^{\mathbf{q}};\mathbf{x}^{\mathbf{p}}) + \sum_{l=1}^{m} \mathcal{B}_l G(\mathbf{x}^{\mathbf{q}};\mathbf{x}^{(s,l)}) = 0, \tag{4.4}$$

where $\mathbf{p}$ and $\mathbf{q}$ are multi-indices in Π, the cluster of pins. Equation (4.4) in matrix form is

$$\mathbf{w}_{inc}(\mathbf{x^q}) + \mathbf{G}(\mathbf{x^q};\mathbf{x^p})\mathbf{A} + \mathbf{G}(\mathbf{x^q};\mathbf{x}^{(s,l)})\mathbf{B} = \mathbf{0}, \quad l = 1, 2, \ldots, m, \tag{4.5}$$

where $\mathbf{w}_{inc}(\mathbf{x^q})$ represents a column vector whose entries are the amplitudes $w_{inc}(\mathbf{x^q})$ at the pin-position $\mathbf{x^q}$, for $\mathbf{q} \in \Pi$, and $\mathbf{G}(\mathbf{x^q};\mathbf{x^p})$ and $\mathbf{G}(\mathbf{x^q};\mathbf{x}^{(s,l)})$ are $N^2 \times N^2$ and $N^2 \times m$ matrices comprised of Green's functions for the biharmonic operator whose arguments depend on the distance between pin positions in the array Π, and the distance between pin positions and active source locations, respectively. $\mathbf{A}$ and $\mathbf{B}$ are $N^2 \times 1$ and $m \times 1$ column vectors, respectively.

Using equation (4.5), we write the matrix $\mathbf{A}$ of the coefficients $\mathcal{A}_\mathbf{p}$ in terms of the unknown source amplitudes $\mathcal{B}_l$ of the matrix $\mathbf{B}$

$$\mathbf{A} = -\mathbf{G}^{-1}(\mathbf{x^q};\mathbf{x^p})\mathbf{w}_{inc}(\mathbf{x^q}) - \mathbf{G}^{-1}(\mathbf{x^q};\mathbf{x^p})\mathbf{G}(\mathbf{x^q};\mathbf{x}^{(s,l)})\mathbf{B}. \tag{4.6}$$

The amplitude of the total displacement $w_{(tot)}(\mathbf{x})$, at a point $\mathbf{x}$, exterior to the sources and array of pins, is given by

$$w_{(tot)}(\mathbf{x}) = w_{inc}(\mathbf{x}) + \mathbf{A}^\top\overline{\mathbf{G}}(\mathbf{x};\mathbf{x^p}) + \mathbf{B}^\top\overline{\mathbf{G}}(\mathbf{x};\mathbf{x}^{(s,l)}), \quad m = 1, 2, \ldots, m. \tag{4.7}$$

In equation (4.7), the entries of the $N^2 \times 1$ column vector $\overline{\mathbf{G}}(\mathbf{x};\mathbf{x^p})$ are Green's functions whose arguments depend on the distance between the general point $\mathbf{x}$ and the position of the $\mathbf{p}$-th pin in the cluster. Similarly, the entries of the $m \times 1$ column vector $\overline{\mathbf{G}}(\mathbf{x};\mathbf{x}^{(s,l)})$ are Green's functions whose arguments depend on the distance between the general point $\mathbf{x}$ and the position of the l-th active source external to the cluster. For effective cloaking, we require the total field outside the region occupied by the pins and active sources to be approximately equal to the incident plane wave

$$w_{(tot)}(\mathbf{x}) \approx w_{inc}(\mathbf{x}). \tag{4.8}$$

The active source amplitudes $\mathcal{B}_l$ are to be found by cancelling out leading order multipole terms of the scattered field and thereby ensuring that condition (4.8) is satisfied. Eliminating the scattered field guarantees that an observer exterior to the active sources surrounding the finite array does not perceive the cluster's presence. Using condition (4.8) together with equations (4.6) and (4.7) we obtain

$$\begin{aligned}\mathbf{w}_{inc}^\top(\mathbf{x^q})\mathbf{G}^{-1}(\mathbf{x^q};\mathbf{x^p})\overline{\mathbf{G}}(\mathbf{x};\mathbf{x^p}) \\ + \mathbf{B}^\top\left[\mathbf{G}^\top(\mathbf{x^q};\mathbf{x}^{(s,l)})\mathbf{G}^{-1}(\mathbf{x^q};\mathbf{x^p})\overline{\mathbf{G}}(\mathbf{x};\mathbf{x^p}) - \overline{\mathbf{G}}(\mathbf{x};\mathbf{x}^{(s,l)})\right] \approx 0,\end{aligned} \tag{4.9}$$

where we used the symmetry of the matrix $\mathbf{G}(\mathbf{x^q};\mathbf{x^p})$.

We use Graf's addition theorem to re-expand entries of the vectors $\overline{\mathbf{G}}(\mathbf{x};\mathbf{x}^{(s,l)})$ and $\overline{\mathbf{G}}(\mathbf{x};\mathbf{x^p})$ about a general point $\mathbf{x} = R\exp(i\theta)$, $R > 0$ in polar form. For entries $G(\mathbf{x};\mathbf{x}^{(s,l)})$ of the vector $\overline{\mathbf{G}}(\mathbf{x};\mathbf{x}^{(s,l)})$, we write the multipole representation

$$G(\mathbf{x};\mathbf{x}^{(s,l)}) = -\frac{1}{8\beta^2}\sum_{k=-\infty}^{\infty}\left[iH_k^{(1)}(\beta R)J_k(\beta|\mathbf{x}^{(s,l)}|) - \frac{2}{\pi}K_k(\beta R)I_k(\beta|\mathbf{x}^{(s,l)}|)\right]e^{ik(\theta - \arg(\mathbf{x}^{(s,l)}))}, \tag{4.10}$$

where $\mathbf{x}^{(s,l)} = |\mathbf{x}^{(s,l)}|\exp\{i\arg(\mathbf{x}^{(s,l)})\}$ and $R > |\mathbf{x}^{(s,l)}|$. Similarly, entries of $\overline{\mathbf{G}}(\mathbf{x};\mathbf{x}^{\mathbf{p}})$ can be written as equation (4.10) but with $\mathbf{x}^{(s,l)}$ replaced with $\mathbf{x}^{\mathbf{p}}$.

Substitution of the propagating terms of equations (4.10) and their analogues for $G(\mathbf{x};\mathbf{x}^{\mathbf{p}})$ into equation (4.9) yields a system of linear algebraic equations for the unknown source amplitudes $\mathcal{B}_l$, $l = 1, 2, \ldots, m$, which eliminate the scattered field to a specific multipole order. This order is connected with the number of active sources in the configuration set-up. Thus, for the index k running over the appropriate range, we obtain the following equations

$$\mathbf{w}_{inc}^{\top}(\mathbf{x}^{\mathbf{q}})\mathbf{G}^{-1}(\mathbf{x}^{\mathbf{q}};\mathbf{x}^{\mathbf{p}})\mathbf{J}_k(\mathbf{x}^{\mathbf{p}}) + \mathbf{B}^{\top}\left[\mathbf{G}^{\top}(\mathbf{x}^{\mathbf{q}};\mathbf{x}^{(s,l)})\mathbf{G}^{-1}(\mathbf{x}^{\mathbf{q}};\mathbf{x}^{\mathbf{p}})\mathbf{J}_k(\mathbf{x}^{\mathbf{p}}) - \mathbf{J}_k(\mathbf{x}^{(s,l)})\right] = \mathbf{0}, \tag{4.11}$$

where $\mathbf{J}_k(\mathbf{x}^{\mathbf{p}})$ represents a matrix with entries $J_k(\beta|\mathbf{x}^{\mathbf{p}}|)\exp\{-ik\arg(\mathbf{x}^{\mathbf{p}})\}$ for all $\mathbf{p} \in \Pi$ and $\mathbf{J}_k(\mathbf{x}^{(s,l)})$ represents a matrix with entries $J_k(\beta|\mathbf{x}^{(s,l)}|)\exp\{-ik\arg(\mathbf{x}^{(s,l)})\}$ for all $l = 1, 2, \ldots, m$. Note that $\mathbf{J}_k(\mathbf{x}^{\mathbf{p}})$ and $\mathbf{J}_k(\mathbf{x}^{(s,l)})$ are matrices of size $N^2 \times 1$ and $m \times 1$, respectively, their entries are propagating terms from equation (4.10) and the corresponding analogue for entries of $\overline{\mathbf{G}}(\mathbf{x};\mathbf{x}^{\mathbf{p}})$.

4.1.3 Selecting the spectral parameter to demonstrate broadband cloaking

The method of cloaking employed here is a natural extension of that presented in the previous chapters 2 and 3, where a single clamped void and a coated inclusion were cloaked using active sources, the former for non-resonant and the latter case for resonant regimes. As in these chapters, the cloaking method implemented in what follows, is broadband for discrete structures, in the sense that we can produce efficient cloaking over a wide range of frequencies. We select illustrative frequencies from the band diagram (see Fig. 4.2) and the dispersion surfaces (see Fig. 4.3) for a thin plate pinned in a doubly periodic fashion. We also consider frequencies for examples of trapped flexural waves in finite arrays of gratings. Three typical regimes are identified from the dispersion surfaces: Zero frequency stop band and its edge, flat bands with standing wave frequencies and Dirac-like points.

In chapter 1, we showed that the dispersion curves plot the solutions of the dispersion relation for Bloch-Floquet waves in the infinite platonic crystal,

$$\frac{i}{8\beta^2}\left(S_0^H(\beta,\mathbf{k_0}) + 1 + \frac{2i}{\pi}S_0^K(\beta,\mathbf{k_0})\right) = 0, \tag{4.12}$$

expressed here in terms of lattice sums S_0^H and S_0^K stated in the work by Movchan *et al.* [67] and McPhedran *et al.* [57]:

$$S_0^H = \sum_{\mathbf{q}\neq(0,0)} H_0^{(1)}(\beta R_{\mathbf{q}})e^{i\mathbf{k_0}\cdot\mathbf{R_q}}\,; \qquad S_0^K = \sum_{\mathbf{q}\neq(0,0)} K_0(\beta R_{\mathbf{q}})e^{i\mathbf{k_0}\cdot\mathbf{R_q}}\,, \tag{4.13}$$

where $\mathbf{k_0} = (k_x, k_y)$ denotes the Bloch wave vector and $\mathbf{R_q} = R_{\mathbf{q}}\exp(i\theta_{\mathbf{q}})$ denotes the real-space array vector corresponding to the position of the pins in polar coordinates. We gave the dispersion diagram for the first five dispersion curves for an infinite square array of rigid pins with $d = 1$ in chapter 1, which we repeat for convenience in Fig. 4.2. In chapter 1,

we discussed frequencies at which interesting scattering properties occurred in the infinite structure. We plot the dispersion diagram of the infinite array of pins and highlight the frequencies at which we apply our active cloaking method, in Fig. 4.3.

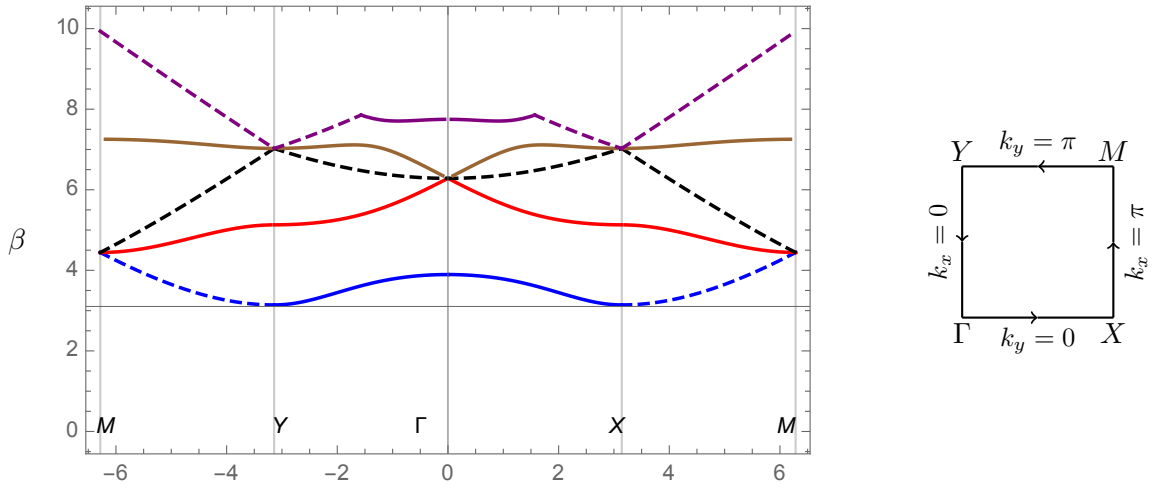

Figure 4.2: Band diagram for square array of rigid pins with $d = 1$, using square Brillouin zone $(k_x, k_y) = [0, \pi] \times [0, \pi]$. The solid lines represent solutions of the dispersion relation (4.12), (4.13), and the dashed lines represent both dispersion curves and segments of the singularity lines (1.51) from chapter 1.

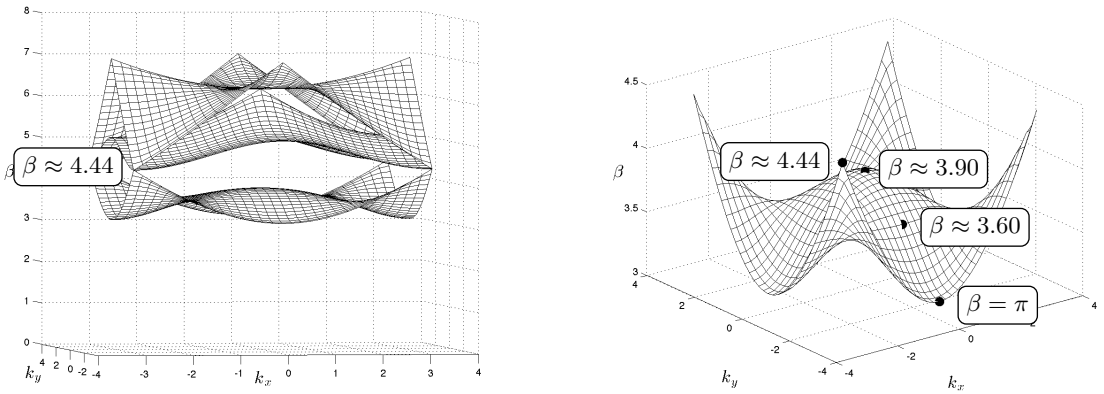

(a) (b)

Figure 4.3: (a) The first three dispersion surfaces shown together with the Dirac-like point highlighted. In (b) we display the first dispersion surface with the β-values of interest.

We note that we also select some β-values from known scattering and eigenvalue problems for subsets of the infinite doubly periodic array, namely gratings. A finite number of semi-infinite gratings, can act like Fabry-Pérot plates where repeated reflections lead to constructive interference and localisation by simply tuning the frequency of the system. The associated eigenvalue problem yields the Bloch modes linked with such resonance regimes for specified angles of incident plane waves. In the work of Haslinger *et al.* [40] a table was

given noting optimised frequencies for a range of incident angles $0 \leq \theta_{inc} \leq \pi/3$, which was relevant both to finite numbers of gratings, and to finite clusters like those studied here. The Green's function approach applied in the work of Haslinger *et al.* [40] (also employed by Evans & Porter [22], Linton & Martin [50], and Foldy [27]) leads to rapidly converging numerical solutions, determining propagating frequencies for pinned clusters, which we seek to cloak in this chapter.

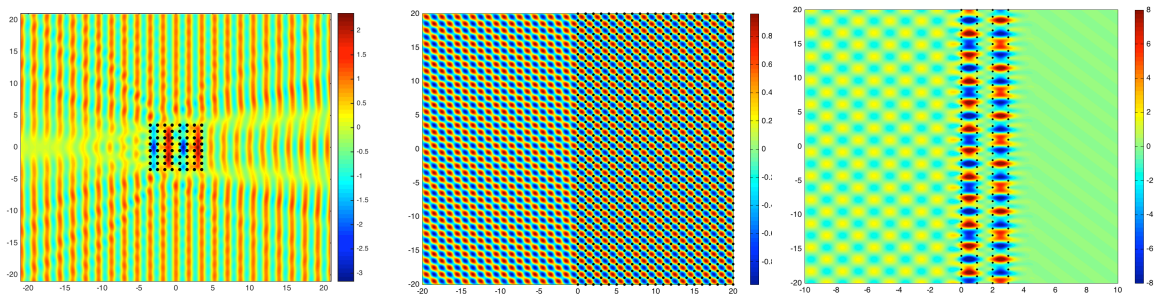

(a) (b) (c)

Figure 4.4: In all figures here and in what follows, the real part of the amplitude of flexural displacement for the total field is shown, with its range, indicated by the colourbar, determined by the degree of localisation within the system. In addition, the pins are depicted by black discs and the horizontal and vertical axes are the x_1 and x_2-axes, respectively. (a) Plane wave normally incident on an uncloaked 8×8 ($N = 8$) cluster of pins. (b) Plane wave incident at $\theta_{inc} = \pi/4$ on 2000 gratings with $d = 1$ for $\beta = 4.44$, $\kappa_y = 3.1396$ corresponding to M in the reciprocal lattice. (c) Localisation of flexural waves in a stack of 4 gratings with $d = 1$ for a plane wave incident at $\theta_{inc} = \pi/6$ for $\beta = 3.60$.

Here we show an example for a stack of four gratings in Fig. 4.4(c); the choice of $\theta_{inc} = \pi/6$ and $\beta = 3.60$, with the spacings $d = 1$, are the optimised parameter settings for localisation (note that these values were taken from Table 1 in the paper by Haslinger *et al.* [40]). We observe high amplitudes of waves trapped within the gratings, which illustrate the Fabry-Pérot wave trapping capabilities of clusters of pins. In section 4.2.2, we demonstrate active cloaking at the angle of incidence and frequency for Fig. 4.4(c) for a finite cluster of pins (the corresponding square subset of the finite stack of infinite gratings), where localisation effects are also observed.

4.2 Active cloaking results

With our focus on achieving efficient cloaking, we begin by positioning the active control sources on the grid's rows and columns adjacent to the cluster of pins (see Fig. 4.1 with $S = d = 1$) and first set m, the number of sources, to be $4N$. Fig. 4.1 shows the general set up for a $4 \times 4\,(N = 4)$ cluster of pins surrounded by 16 sources. Naturally, we also consider the case of a $5 \times 5\,(N = 5)$ cluster of pins, hence distinguishing between even and odd cases. For higher frequency regimes, we then move on to position the active sources on

a circle surrounding the finite cluster of pins, introducing flexibility in locating and choosing the number of these sources.

4.2.1 Cloaking in the zero-frequency stop band

The first β-value we select is from the zero-frequency stop band of the doubly periodic square array. We first consider positioning $m = 4N$ sources exterior to the cluster, aligned with the rows and columns of the pins (see Fig. 4.1 for a schematic view of the configuration for the case when $N = 4$). Secondly, we place four additional sources at the corners, creating a square array of sources that lies on the grid surrounding the cluster (hence $m = 4(N+1)$). We plot the flexural displacement amplitudes of the total field for each configuration of sources, comparing them with the uncloaked cases.

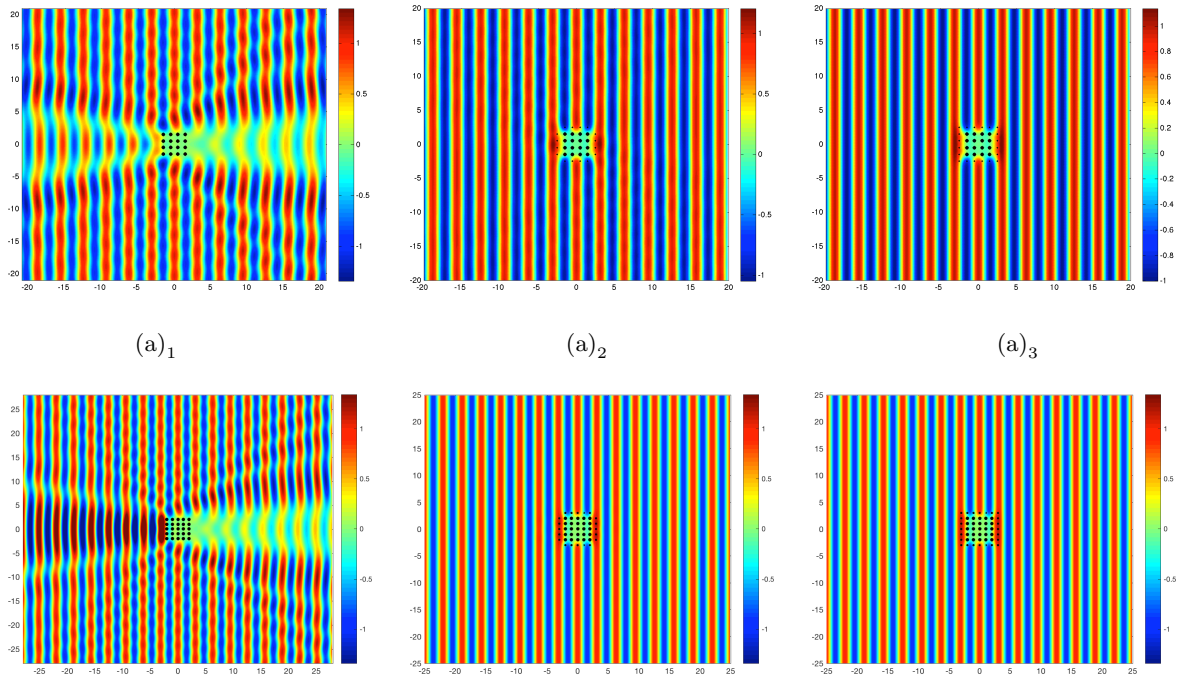

$(a)_1$ $(a)_2$ $(a)_3$

$(b)_1$ $(b)_2$ $(b)_3$

Figure 4.5: Flexural wave scattering by (a) a 4×4 ($N = 4$) and (b) a 5×5 ($N = 5$) cluster of pins, depicted by large black discs. Plane wave is incident at $\theta_{inc} = 0$ with $\beta = 2.0$. Left: scattering with no active sources; middle: cloaking with $m = 4N$ active sources; right: cloaking with $m = 4(N+1)$ active sources. We note here and in what follows that the active source are illustrated by small black discs surrounding the cluster.

Figure 4.5 shows the results of cloaking for $N = 4$ (Fig. 4.5(a)) and $N = 5$ (Fig. 4.5(b)) at $\beta = 2.0$. In both cases, when no sources are present, waves do not penetrate the cluster and a large shadow region is created behind (see Figs. $4.5(a)_1$ and $4.5(b)_1$). Even for the small number of pins, the effect of the zero frequency stop band is seen in Fig. $4.5(a)_1$ since virtually no waves pass through the cluster and there is strong reflection. It should be noted here that clusters of 4 ($N = 2$), or 9 ($N = 3$), pins are too small to inherit such features from

the infinite array and so are not considered in this chapter. The choices of $N = 4$ and 5 were made to represent the smallest finite arrays that inherit behaviour from the infinite array. Similarly small finite structures such as the clusters considered by Antonakakis *et al.* [6], and triplets of gratings by Haslinger *et al.*[40], have previously been shown to exhibit properties of the corresponding infinite systems.

In Figs. $4.5(a)_2$ and $4.5(b)_2$, we see the reconstruction of the incident wave in the total field displacement amplitudes. There is no evidence of the shadow region and the field remains quiet inside the cluster. When sources are added along the diagonal at the corners, (see Figs. $4.5(a)_3$ and $4.5(b)_3$) we see further improvement in cloaking for $N = 4$, with wave fronts straightened compared to the no-corners case of Fig. $4.5(a)_2$. For $N = 5$, sources on the grid without corners is sufficient to produce near-perfect cloaking.

4.2.2 Cloaking at higher spectral values in the pass band

We now extend our method to higher values of the spectral parameter β. Referring to Fig. 4.3(b), we focus our attention to β-values of interest on the first dispersion surface, starting with $\beta = \pi$, the edge of the zero frequency stop band. We remark that the dispersion surfaces are obtained for an infinite plate pinned at a doubly periodic set of points and so they serve as a rough estimate for the β-values for which interesting features are observed for the finite cluster.

Figures 4.6(a) and 4.6(b) show amplitudes for a plane wave incident at $\theta_{inc} = 0$ with $\beta = \pi$ for the cases of $N = 4$ and $N = 5$, respectively. Although $\beta = \pi$ lies on the boundary of the pass band for an infinite array, we see in Figs. $4.6(a)_1$ and $4.6(b)_1$ that a large shadow region remains behind the finite cluster. It appears that the cluster is too small to inherit the exact frequency at which the pass band begins for the infinite structure. However, when active sources are introduced, the wave clearly penetrates through the finite cluster (see Figs. $4.6(a)_{2,3}$ and $4.6(b)_{2,3}$). We observe that adding sources at the corners of the diagonals of the cluster, illustrated in Figs. $4.6(a)_3$ and $4.6(b)_3$, improves the cloaking further, and the incident plane wave is successfully reconstructed in the total field exterior to the finite cluster and sources.

We note that localised fields are encountered when cloaking the $N = 5$ cluster, with amplitudes significantly greater than for the corresponding $N = 4$ case. Throughout this chapter, when necessary, we restrict the amplitude values to provide better comparison between corresponding cases and to improve the information gained about the cloaked fields outside the localised regions within the clusters.

The next β-value we choose from the first dispersion surface in Fig. 4.3(b) is $\beta \approx 3.60$, where the surface is locally flat at an inflexion. As flat sections of dispersion curves are associated with wave trapping and localisation, it is interesting to see how this affects the cloaking procedure. Since we are now attempting to cloak at a higher spectral parameter value, we note that efficient cloaking with sources restricted to the grid ($m = 4N$ or $m =$

$4(N+1)$) may prove difficult, which is illustrated in Fig. 4.7.

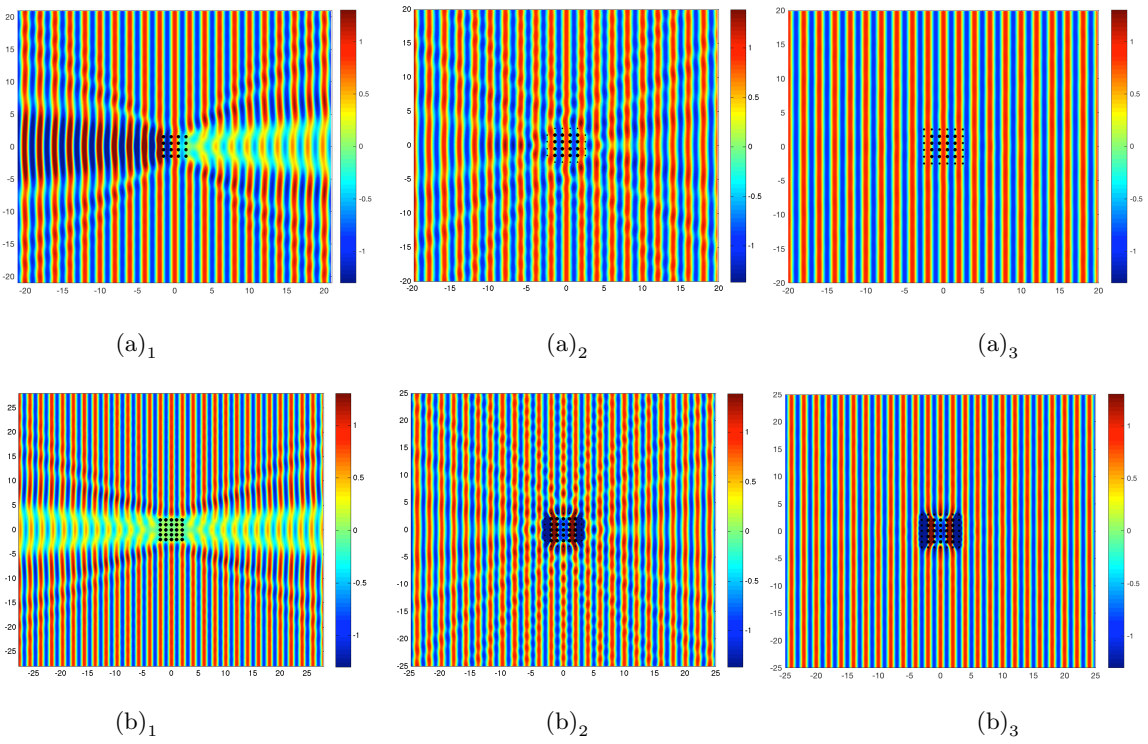

Figure 4.6: Flexural wave scattering by a (a) 4×4 ($N = 4$) and (b) 5×5 ($N = 5$) cluster of pins with an incident plane wave at an angle of $\theta_{inc} = 0$. From left to right: (left) no active sources, (middle) $m = 4N$ active sources, (right) $m = 4N + 4$ active sources, all for $\beta = \pi$.

Cloaking of the 4×4 cluster when $\beta = 3.60$ indicates strong localisation effects, which is demonstrated in Fig. 4.7(a). For the 5×5 cluster, we see strong localisation effects at a slightly lower value of $\beta = 3.565$, as shown in Fig. 4.7(b). We emphasise that the dispersion surface in Fig. 4.3(b) highlights key β-values for the infinite array and serves as a rough guide for us to pick spectral values of interest associated with the finite cluster. We also note that the variation in β for which we see localisation is due to internal resonances of the finite cluster.

In Figs. $4.7(\text{a})_1$ and $4.7(\text{b})_1$, localisation dominates the field inside the cluster. Figures $4.7(\text{a})_{2,3}$ and $4.7(\text{b})_{2,3}$ display two unsuccessful cloaking attempts for each configuration. It is apparent that the cloaking efficacy is beginning to deteriorate at higher frequencies if the sources are restricted to the grid, with or without additional sources located at the corners of the diagonals.

As a consequence of the above results, it is clear that more active sources are needed for efficient cloaking at higher frequencies. If we restrict the sources to the grid, this can be done either by moving the sources further away from the cluster or by adding more sources between those which are already present, there are many different variations in configuration that could be implemented. We instead follow the configuration of sources presented in

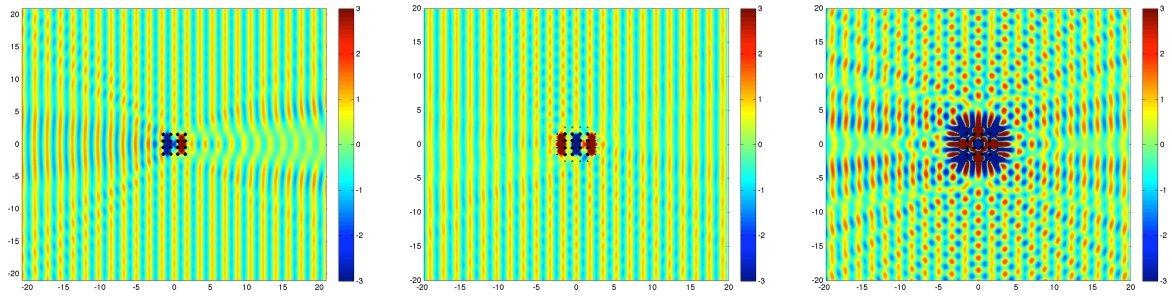

(a)$_1$ (a)$_2$ (a)$_3$

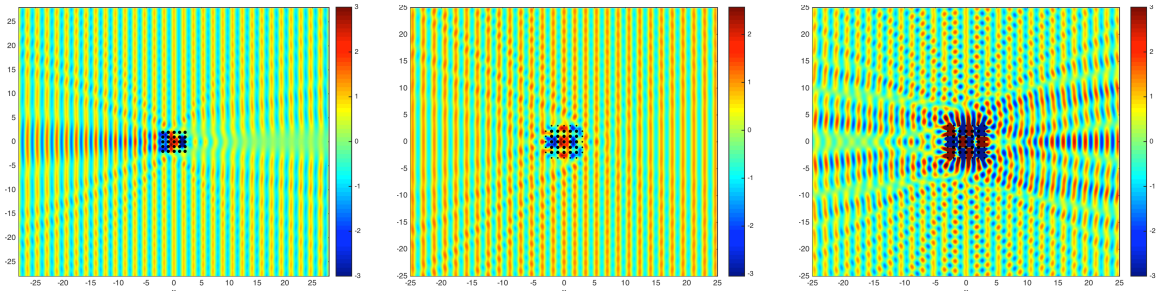

(b)$_1$ (b)$_2$ (b)$_3$

Figure 4.7: Same as in Fig. 4.6 but (a) shows the case of $N = 4$ for $\beta = 3.60$ and (b) shows the case of $N = 5$ for $\beta = 3.565$.

chapters 2 and 3, and examine the effect of cloaking with active sources positioned on a circle surrounding the cluster, of radius a_s centred at the origin. We ensure that two sources always lie on the x_1-axis, one in front and one behind the cluster, and the remaining sources are distributed evenly, obeying up-down symmetry.

Retaining the maximum number of sources $m = 20$ (see Fig. 4.7(a)$_3$) used for a 4×4 cluster, but now locating them on a circle of radius $a_s = (3\sqrt{2} + 2)/2$ (corresponding to a distance along the diagonal of 1 unit away from the corners of the cluster), we illustrate the resulting wave amplitudes in Fig. 4.8(a). This configuration brings an improvement in cloaking but the number of sources appears to be insufficient.

It is natural to consider how to estimate the number of sources required for effective cloaking. We address this by plotting the absolute value of the coefficient premultiplying the Hankel function term in the total field $w^{(p)}$ on the circle at which the sources are located, i.e.

$$|w^{(p)}| = \left| \sum_{\mathbf{p} \in \Pi} H_n^{(1)}(\beta a_s) J_n(\beta |\mathbf{x^p}|) \exp\{in \arg(\mathbf{x^p})\} \right|, \tag{4.14}$$

versus the multipole order n. This is shown in Fig. 4.8 (b), where it can be deduced, that the minimum number of sources required for efficient cloaking is $m = 26$. This is done by determining the multipole order after which the contribution to the total field due to scattering is exponentially small. Finally, we plot amplitudes of the cloaked cluster using 26 sources in Fig. 4.8 (c).

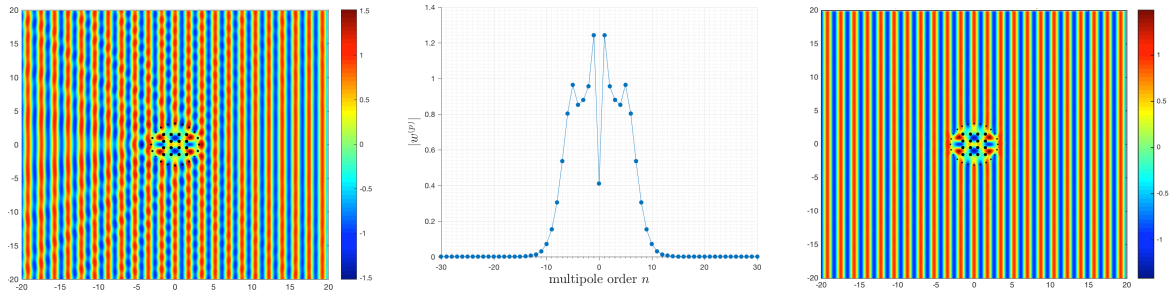

(a) (b) (c)

Figure 4.8: For a 4×4 ($N = 4$) cluster of pins with an incident plane wave at an angle of $\theta_{inc} = 0$: (a) Flexural wave amplitudes for a cloaked cluster with $m = 20$ evenly spaced sources on a circle of radius $a_s = (3\sqrt{2}+2)/2$, (b) absolute value of the coefficient premultiplying the Hankel function in the total field $|w^{(p)}|$ on the circle a_s versus multipole order n, (c) flexural displacement amplitudes for a cloaked cluster with $m = 26$, all for $\beta = 3.60$.

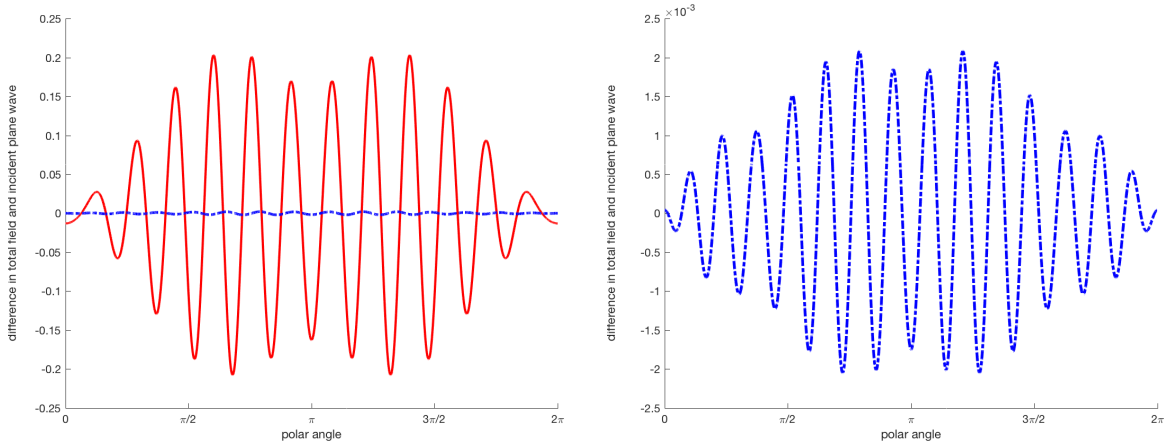

(a) (b)

Figure 4.9: Difference in total wave amplitude and the incident plane wave evaluated on a circle of radius 15 versus the polar angle. 4×4 cluster of pins for $\theta_{inc} = 0$ and $\beta = 3.60$. (a) $m = 20$ (solid curve), $m = 26$ (dashed curve) which is magnified in part (b) to clearly display its order.

To further establish the efficiency of cloaking, we plot the difference between the total wave amplitude and the incoming plane wave evaluated at a circle of radius 15 (sufficiently far away from the cluster and active sources) versus the polar angle. Fig. 4.9(a) shows the comparison between 20 (solid curve) and 26 (dashed curve) sources located on a circle surrounding a 4×4 cluster for $\beta = 3.60$. It is clear that for the case of 26 sources, we see a significantly reduced difference between the two fields; the difference is of order 10^{-1} for $m = 20$, but is of order 10^{-3} for $m = 26$ (see Fig. 4.9(b)). In this chapter, we regard a cloaking to be satisfactorily efficient if the difference between the total wave amplitude and the incoming plane wave (absolute error) is of order 10^{-3} or less. We remark that the main body of the text from now on will include only the $N = 4$ case and the analogous analysis

for $N = 5$ is placed in Appendix B.

The method of cloaking outlined in section 4.1.2 works equally well for oblique incidence. We illustrate this for $\theta_{inc} = \pi/6$ and $\beta = 3.60$ in Fig. 4.10, recalling that for a set of four gratings illustrated in Fig. 4.4(c), localisation was observed between the gratings. As expected, we see this localisation manifest itself as trapped waves in Fig. 4.10(a). Cloaking at localised fields within the cluster is possible provided that we select the appropriate number of sources, as shown by Fig. 4.10(b). Using 4.10(c), the minimum number of sources required for efficient cloaking of absolute error 10^{-3} is $m = 26$. Note that this is the same number of sources required for the case of normal incidence presented in Fig. 4.8(b).

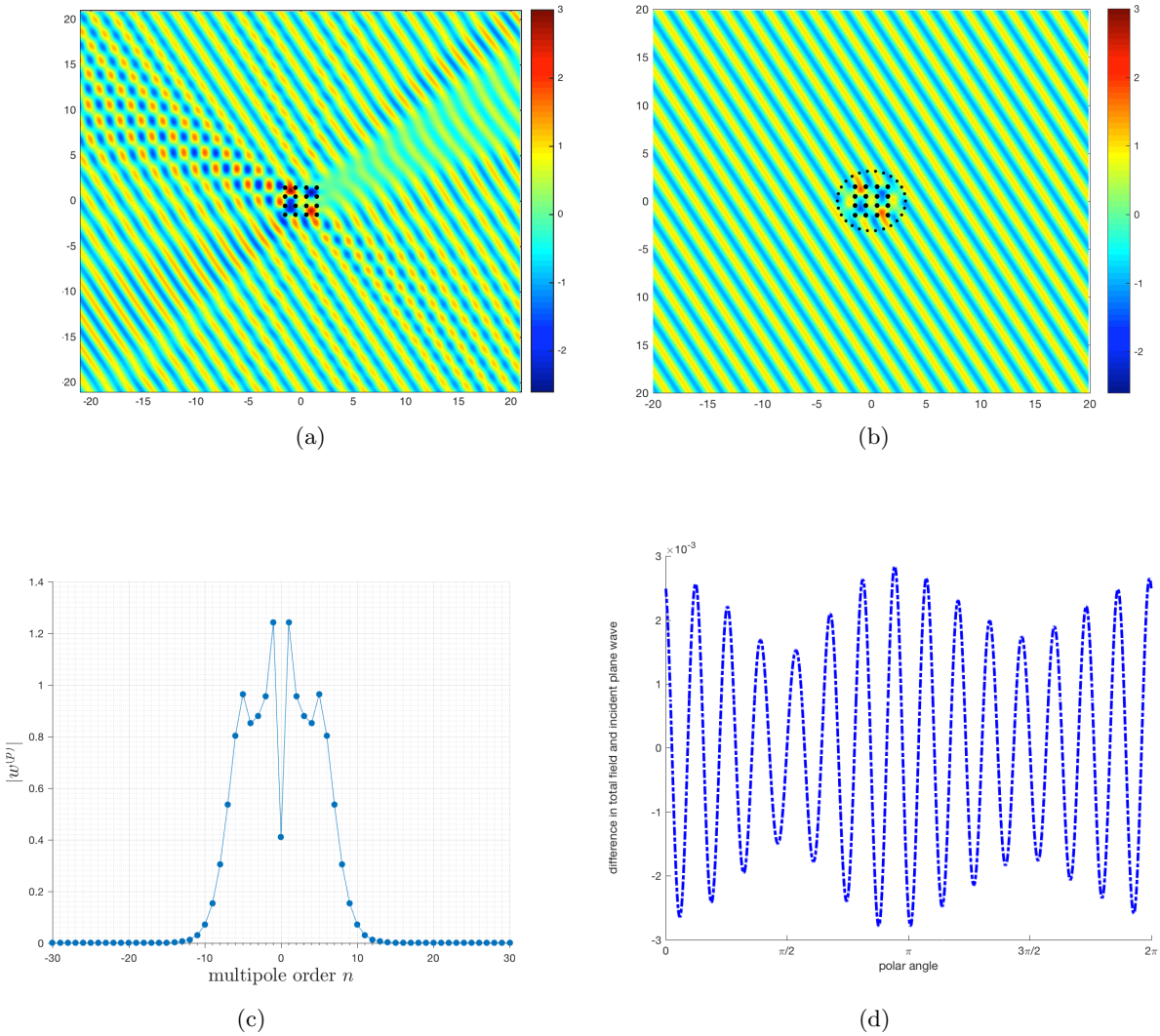

Figure 4.10: 4×4 ($N = 4$) cluster of pins with a plane wave incident at $\theta_{inc} = \pi/6$ for $\beta = 3.60$. Flexural wave amplitudes for (a) an uncloaked, (b) a cloaked cluster with $m = 26$, (c) absolute value of the coefficient premultiplying the Hankel function in the total field $|w^{(p)}|$ on the circle, of radius $a_s = (3\sqrt{2} + 2)/2$, versus multipole order n, (d) absolute error evaluated on a circle of radius 15 versus the polar angle.

Next, we turn our attention to cloaking at $\beta = 3.90$, which is a local maximum and

a standing wave frequency of the dispersion surface Fig. 4.3(b). In Figs. 4.11 and 4.12, we demonstrate the results of our cloaking method for a plane wave incident at angles of $\theta_{inc} = 0$ and $\theta_{inc} = \pi/4$, respectively. In both cases, it is shown that 26 sources were required for effective cloaking. We clearly reconstruct the incident plane wave, which is evident in both plots of the total flexural displacement amplitudes (see Figs. 4.11(b) and 4.12(b)). In parts (c) and (d) of Fig. 4.11 and part (d) of 4.12, the choice of the number of sources for effective cloaking is illustrated graphically for the desired accuracy. We note that $|w^{(p)}|$ (4.14), plotted in Fig. 4.11(c) versus multipole order for $\beta = 3.90$, is independent of θ_{inc} and therefore we omit the equivalent plot for $\theta_{inc} = \pi/4$ from Fig. 4.12.

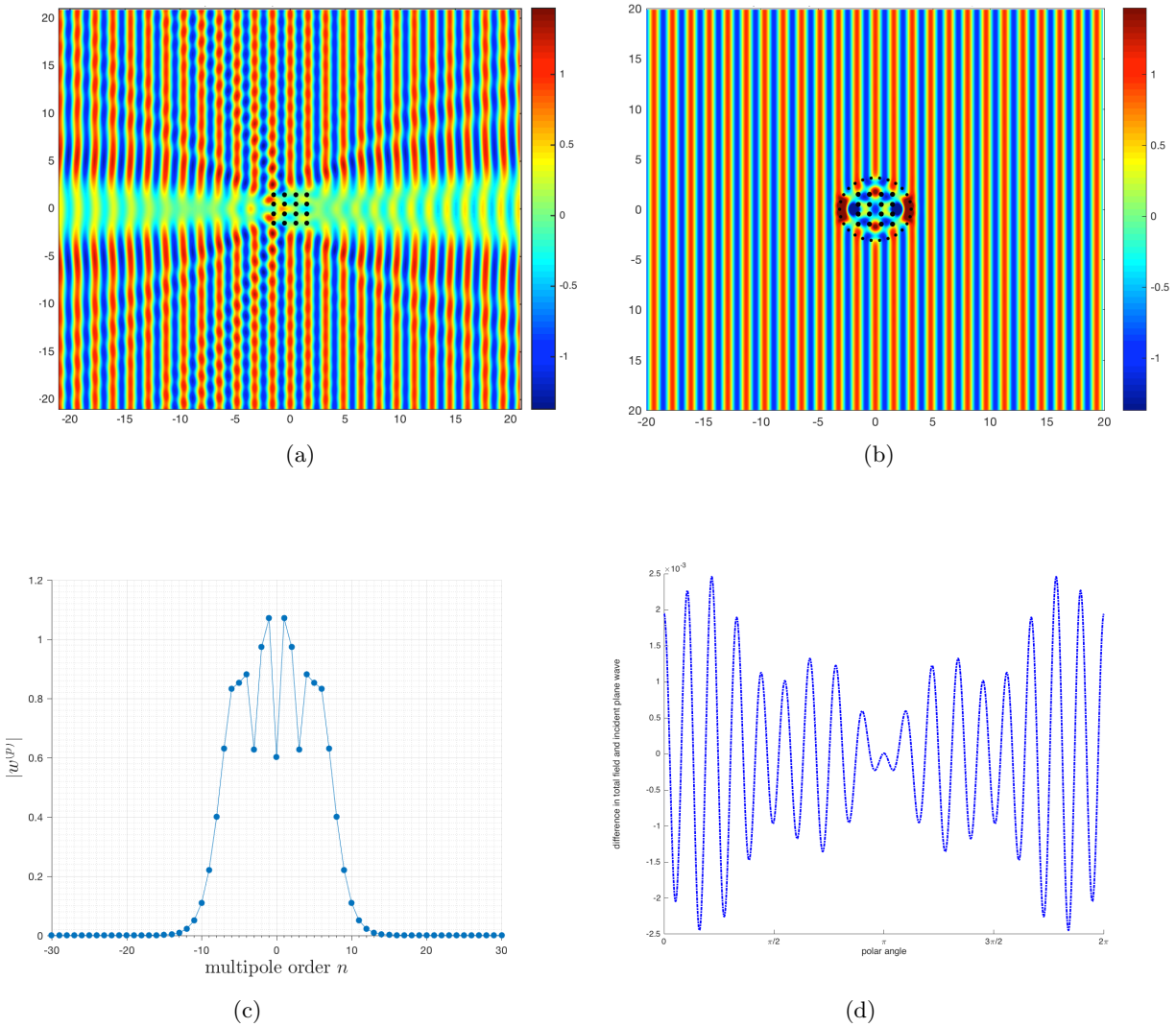

Figure 4.11: 4×4 ($N = 4$) cluster of pins with a plane wave incident at $\theta_{inc} = 0$ for $\beta = 3.90$. Flexural wave amplitudes for (a) an uncloaked , (b) a cloaked cluster with $m = 26$, (c) $|w^{(p)}|$ versus multipole order n for a circle of radius $a_s = (3\sqrt{2}+2)/2$, (d) absolute error evaluated on a circle of radius 15 versus the polar angle.

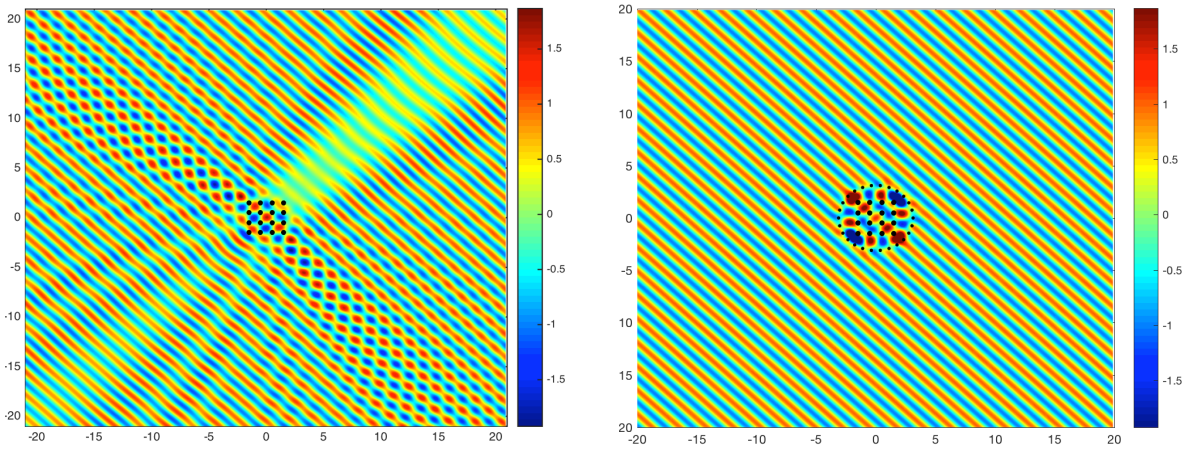

(a) (b)

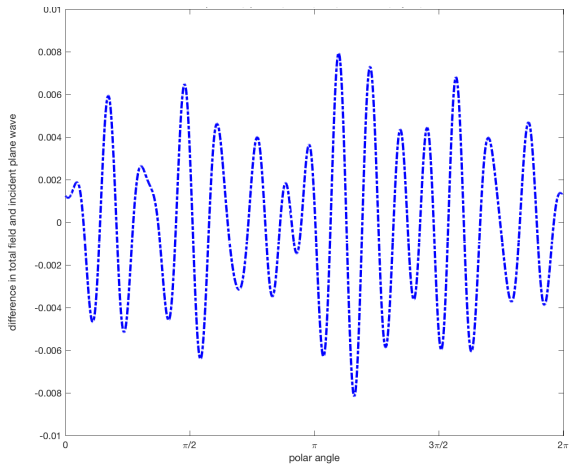

(c)

Figure 4.12: 4×4 ($N = 4$) cluster of pins with a plane wave incident at $\theta_{inc} = \pi/4$ for $\beta = 3.90$. Flexural wave amplitudes for (a) an uncloaked, (b) a cloaked cluster with $m = 26$, (c) absolute error evaluated on a circle of radius 15 versus the polar angle.

We finally consider $\beta = 4.44$ for an angle of incidence $\theta_{inc} = \pi/4$. In Figs. 4.2 and 4.3(a) this value of the spectral parameter is in the vicinity of a Dirac-like point, where we expect to see some effects of dynamic neutrality within the finite cluster that shares the same periodicity as the infinite array in Figs. 4.2, 4.3. This is apparent in Fig. 4.13(a) where we see a similar pattern to that of Fig. 4.4(b). It is clear from Fig. 4.13(b) that we can once again achieve effective cloaking, and absolute error of the desired order is obtained for 30 sources using Fig. 4.13(c).

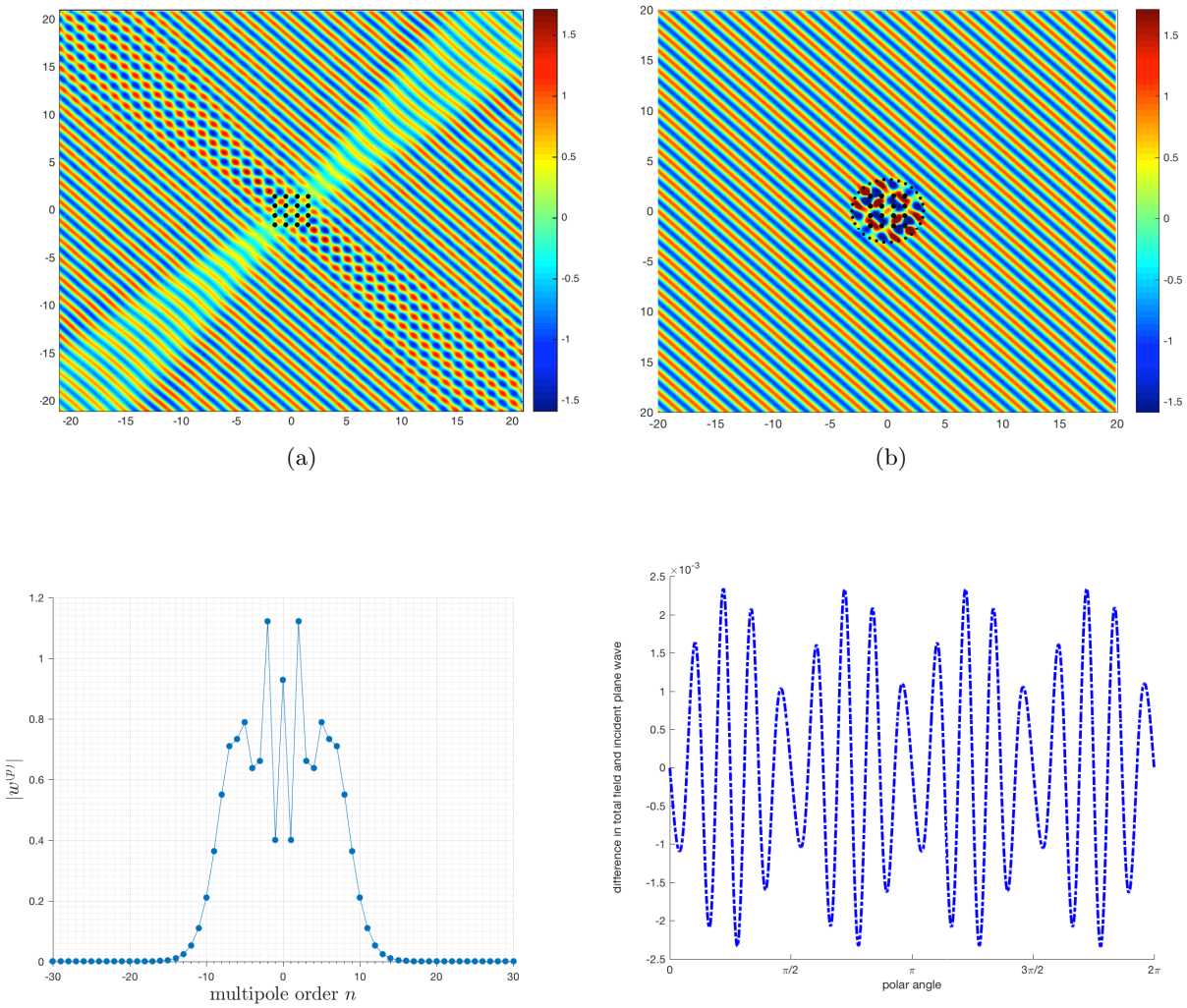

(a) (b)

(c) (d)

Figure 4.13: 4×4 ($N = 4$) cluster of pins with a plane wave incident at $\theta_{inc} = \pi/4$ for $\beta = 4.44$. Flexural wave amplitudes for (a) an uncloaked, (b) a cloaked cluster with $m = 30$, (c) $|w^{(p)}|$ versus multipole order n for a circle of radius $a_s = (3\sqrt{2}+2)/2$, (d) absolute error evaluated on a circle of radius 15 versus the polar angle.

4.3 Remarks and discussions

In this chapter, we have presented a powerful mathematical method for cloaking finite clusters of pins from flexural waves in a Kirchhoff plate. The approach adapted from chapter 2, uses multipole methods to cancel wave scattering up to a specific order, through the use of active sources located exterior to the cluster. As in chapter 2, a system of algebraic equations was derived determining the active source amplitudes required for effective cloaking.

We have demonstrated, through several illustrative examples, the capability of the cloaking method for key values of the spectral parameter β, for which interesting features arise in the corresponding infinite array. Two types of configuration of active sources were considered: positioning the active control sources on the grid's rows and columns adjacent to the

cluster of pins, and sources located on a circle surrounding the cluster. The latter approach was adopted for higher frequencies at which the former approach became insufficient.

Locating the active sources on the circle provides greater flexibility in terms of their quantity and also enabled us to identify precisely the order of multipoles to be annulled. This was accomplished by plotting the absolute value of the coefficient premultiplying the Hankel function in the total field on the circle describing the source positions, versus multipole order. (Note that analogous plots were presented in sections 3.2.6 and 3.1.5 of chapter 3.) Thus, given a frequency and a finite array, we can predict how many sources are required to achieve a specified level of efficient cloaking. The results obtained for point scatterers, such as the rigid pins investigated here, may be readily extended to the case of finite-sized inclusions for which they act as a starting point.

Chapter 5

Conclusions and future work

We have presented a method for the approximate active cloaking of finite defects embedded into Kirchhoff plates subject to flexural waves. The cloaking method involved positioning several active sources exterior to the scatterer, and choosing their amplitudes to cancel a specific number of terms from the scattered field. The amplitudes necessary for cloaking were found analytically, using a linear system of algebraic equations. In this thesis, we have demonstrated through a number of examples, that our cloaking method is generic and applicable to different types boundary conditions and incident waves.

Our cloaking method consisted of cancelling the scattered wave with an appropriate choice of active source amplitudes. The active sources were represented by the non-singular Green's function, and the configuration of sources was chosen in the problem formulation. This formed a well-posed problem that led to closed-form analytical expressions for the unknown complex amplitudes for effective cloaking.

In chapter 2, it was shown that active cloaking was achievable for a circular clamped cavity with as little as six active sources. We considered flexural waves described by an incident plane wave and a remote point source. In considering cloaking for a remote point source, it was highlighted that we had in fact, obtained the fundamental solution to the cloaking problem. Using the fundamental solution, we can solve the cloaking problem of scattering from a circular clamped boundary for any arbitrary forcing term, provided we know its Fourier expansion.

We highlighted the method's generality by cloaking a clamped cavity of arbitrary shape. For the illustrative example considered, it was shown that only seven sources were required to cloak the scatterer. The method employed numerical techniques to find Fourier coefficients, which were used in the algebraic system of equations for the unknown active source amplitudes. This system of equations was based on those derived for the case of circular scatterers.

One possible extension of our cloaking method is to optimise the configuration of sources since we are free to choose the source position. For example, when cloaking a rigid circular inclusion, it was discussed that the radius of the circle on which the sources were placed

affected the amplitudes necessary for cloaking. It was shown that amplitudes of sources located closer to the rigid inclusion were larger than those positioned on a circle farther away.

By employing active techniques as our primary method of scattering cancellation, we achieve broadband cloaking, which can be adapted to a number of different frequency regimes. This cannot be said for passive techniques, where invisibility is often only achievable for a narrow frequency range or particular type of incident wave.

In chapter 3, we showed that cloaking was possible for an inclusion at resonant regimes. It was discussed that scattering properties of the inclusion change rapidly at resonant regimes, which could cause potential difficulties for high precision active cloaking. We modified our cloaking configuration to include a passive element in the form of a coating. This coating was specifically designed to control scattering properties of the inclusion, ensuring that broadband cloaking was possible for the coated inclusion. We provided several illustrative examples, demonstrating that effective cloaking was possible in both the intermediate and higher frequency regimes. Note that in low frequency regimes, the inclusion produces very little scattering and cloaking is not necessary. The coating that was introduced is passive in the sense that its properties do not change with frequency or type of incident field. To the best of our knowledge, this was the first instance for which a combination of active and passive techniques was used to cloak scatterers at resonant regimes in Kirchhoff plates.

In the context of cloaking in Kirchhoff plates, Farhat *et al.* [23] published a paper employing passive techniques. A coating was designed to annul the leading order behaviour of the monopole term of the scattered field for frequencies limited to the quasi-static regime. The authors advocated the mass-balance argument as stated by Voigt [102], which led to a simple formula for the mass density of the coating. In chapter 3, we showed that the method of cloaking presented by Farhat *et al.* [23] was only applicable to a limited class of problems, and did not apply to the general case in Kirchhoff plates when the elastic properties of the inclusion differ from those of the exterior medium. For low frequencies, the general conditions necessary for annulling the leading order behaviour of the monopole term in the scattered field were derived in chapter 3 of this thesis.

In chapter 4, we applied our method of active cloaking to finite clusters of pins, cloaking scattering of flexural waves in Kirchhoff plates. We showed that effective cloaking could be achieved using a square or circular configuration of active sources for low or higher frequency regimes, respectively. Efficient cloaking was illustrated at frequencies selected from band diagrams and dispersion surfaces for the corresponding infinite array where interesting effects could be observed. These effects included no transmission at the zero-frequency stop band, wave-trapping and localisation within the cluster corresponding to flat bands at standing wave frequencies, and dynamic neutrality inside the cluster, which was observed at Dirac-like points.

The papers on high frequency homogenisation in photonic and phononic crystals by An-

tonakakis *et al.* [4], [5], discussed a "cloaking" effect observable near Dirac-like cones for an object with a Dirichlet boundary surrounded by a periodic structure. There often remained some perturbation in the field outside the periodic structure, but transmission and reflection were greatly reduced compared to scattering produced by the object itself. The paper by McPhedran *et al.* [57], discusses the ability to "steer" Dirac cones in rectangular lattices. These are interesting phenomena which could be exploited in the design of cloaks involving active and passive techniques. In this thesis, we studied only the square array but the method is equally applicable to other Bravais lattices, such as hexagonal and rectangular. For example, the paper by Smith *et al.* [95] discusses double Dirac cones in a hexagonal lattice highlighting that there is a wide range of interesting periodic structures for which the cloaking method could be implemented.

The promising field of active cloaking receives much attention with the aim of building cloaking systems experimentally. An experimental set-up of active cloaking in electromagnetism, analogous to the ideas presented in Miller [61], was presented by Selvanayagam and Eleftheriades in [94]. Other experimental works often involve passive techniques, including that of Misseroni *et al.* [64] for Kirchhoff plates, as well as notable works from the Wegener group, [99]-[11].

Finally, it is known that cloaking methods can be particularly vulnerable to pulses, where sources have to adapt to a changing frequency of the incident field. Active cloaking in transient regimes was not discussed in this thesis and would be an exciting and insightful problem to study.

Bibliography

[1] M. Abramowitz and I.A. Stegun, Handbook of mathematical functions with formulas, graphs, and mathematical tables, Dover Publications, (1965).

[2] A. Alú and N. Engheta, Achieving transparency with plasmonic and metamaterial coatings, *Phys. Rev. E*, **72**(1), (2005), 016623.

[3] T. Antonakakis and R.V. Craster, High-frequency asymptotics for microstructured thin elastic plates and platonics, *Proc. R. Soc. A*, **468** (2141), (2012), 1408.

[4] T. Antonakakis, R.V. Craster and S. Guenneau, High-frequency homogenization of zero-frequency stop band photonic and phononic crystals, *New J. Phys.*, **15**, (2013), 103014.

[5] T. Antonakakis, R.V. Craster and S. Guenneau, Asymptotics for metamaterials and photonic crystals, *Proc. R. Soc. A*, **469** (2152), (2013), 20120533.

[6] T. Antonakakis, R.V. Craster and S. Guenneau, Moulding and shielding flexural waves in elastic plates, *EPL*, **105**, (2014), 54004.

[7] M. Born and E. Wolf, *Principles of Optics*, (1975), 5^{th} Ed., Pergamon Press, Oxford.

[8] L. C. Botten, Electromagnetic theory and applications for photonic crystals (Optical Engineering), pp. 47-122, (2005), Boca Raton, FL: CRC Press, Inc.

[9] L. Brillouin, Wave propagation in periodic structures: electric filters and crystal lattices, (1953), Dover, New York.

[10] M. Brun, S. Guenneau and A.B. Movchan, Achieving control of in-plane elastic waves, *Appl. Phys. Lett.*, **94**, (2009), 061903.

[11] T. Bückmann, M. Kadic, R. Schittny, and M. Wegener, Mechanical cloak design by direct lattice transformation, *PNAS* **112**, (2015), 4930.

[12] T. Bückmann, M. Thiel, M. Kadic, R. Schittny, and M. Wegener, An elasto-mechanical unfeelability cloak made of pentamode metamaterials, *Nat. Commun.* **5**, (2014), 4130.

[13] A.H. Castro Neto, F. Guinea, N.M.R. Peres, K.S. Novoselov, and A.K. Geim, The electronic properties of graphene, *Rev. Mod. Phys.*, **81**, (2009), 109.

[14] P-Y. Chen, C. Argyropoulos and A. Alù, Broadening the cloaking bandwidth with non-Foster metasurfaces, *Phys. Rev. Lett.*, **111**, (2013), 233001.

[15] P. Y. Chen, M. A. Byrne, A. A. Asatryan, L. C. Botten, K. B. Dossou, A. Tuniz, R. C. McPhedran, C. M. de Sterke, C. G. Poulton and M. J. Steel, Plane wave scattering by a photonic crystal slab: multipole modal formulation and accuracy, *Wave Random Complex*, **22**(4), (2012), 531-570.

[16] H. Chen and C.T. Chen, Acoustic cloaking in three dimensions using acoustic metamaterials, *Appl. Phys. Lett.*, **91**, (2007), 183518.

[17] S. K. Chin, N. A. Nicorovici and R. C. McPhedran, Green's function and lattice sums for electromagnetic scattering by a square array of cylinders, *Phys. Rev. E*, **49**, (1994), 4590-4602.

[18] D. J. Colquitt, I. S. Jones, N. V. Movchan, A. B. Movchan, M. Brun and R. C. McPhedran, Making waves round a structured cloak: lattices, negative refraction and fringes, *Proc. R. Soc. A*, **469**, (2013), 20130218.

[19] R. V. Craster, J. Kaplunov and A. V. Pichugin, High-frequency homogenization for periodic media, *Proc. Roy. Soc. A* **466**, (2010), 2341-2362.

[20] R. V. Craster, J. Kaplunov and J. Postnova, High-frequency asymptotics, homogenisation and localisation for lattices, *Q. J. Mech. Appl. Math.* **63**, (4), (2010), 497-519.

[21] L. S. Dolin, To the possibility of comparison of three-dimensional electromagnetic systems with non-uniform anisotropic filling, *Izv. Vyssh. Uchebn. Zaved. Radiofizika*, **4**(4), (1961), 964-967.

[22] D.V. Evans and R. Porter, Penetration of flexural waves through a periodically constrained thin elastic plate floating on water, *J. Eng. Math.*, **58**, (2007) , 317-337.

[23] M. Farhat, P.-Y. Chen, H. Bağcı, S. Enoch, S. Guenneau and A. Alù, Platonic scattering cancellation for bending waves in a thin plate, *Nature, Scientific Reports*, **4**, (2014), 4644.

[24] M. Farhat, S. Enoch, S. Guenneau and A.B. Movchan, Broadband cylindrical acoustic cloak for linear surface waves in a fluid, *Phys. Rev. Lett.*, **101**, (2008), 134501.

[25] M. Farhat, S. Guenneau, A.B. Movchan and S. Enoch, Achieving invisibility over a finite range of frequencies, *Opt. Express*, **16**, (2008), 5656-61.

[26] J. E. Ffowcs Williams, Review Lecture: Anti-Sound, *Proceedings of the Royal Society London A*, **395**, (1984), 63.

[27] L.L. Foldy, The multiple scattering of waves, *Phys. Rev*, **67**, (1945), 107-119.

[28] C.R. Fuller, S.J Elliott and P.A. Nelson, Active control of vibration, Academic Press, London, (1996).

[29] G. Futhazar, W. J. Parnell and A. N. Norris, Active cloaking of flexural waves in thin plates, *Journal of Sound and Vibration*, **356**, (2015), 1.

[30] K.F. Graff, *Wave motion in elastic solids*, (1975), Oxford, UK: Clarendon Press.

[31] A. Greenleaf, M. Lassas and G. Uhlmann, Anisotropic conductivities that cannot be detected by EIT, *Physiol. Meas.*, **24**, (2003),413-419.

[32] S. Guenneau, R.C. McPhedran, S. Enoch, A.B. Movchan, M. Farhat and N-A. P. Nicorovici, The colours of cloaks, *J. Opt.*, **13**, (2011), 024014.

[33] F. Guevara Vasquez, G.W. Milton and D. Onofrei, Active exterior cloaking for the 2D Laplace and Helmholtz equations, *Phys. Rev. Lett.*, **103**, (2009), 073901.

[34] F. Guevara Vasquez, G.W. Milton, and D. Onofrei, Broadband exterior cloaking, *Optics Express*, **17**, (2009), 14800-14805.

[35] F. Guevara Vasquez, G.W. Milton and D. Onofrei, Exterior cloaking with active sources in two dimensional acoustics, *Wave Motion*, **48**, (2011), 515-524.

[36] F. Guevara Vasquez, G.W. Milton, and D. Onofrei, Mathematical analysis of the two dimensional active exterior cloaking in the quasi static regime, *arxiv.org/abs/1109.3526v1* (2011).

[37] F. Guevara Vasquez, G.W. Milton, D. Onofrei and P. Seppecher, Transformation elastodynamics and active exterior acoustic cloaking, *Acoustic Metamaterials*, Springer Series in Materials Science 166, (2013), R.V. Craster, S. Guenneau, (eds.)

[38] S.G. Haslinger, R.V. Craster, A.B. Movchan, N.V. Movchan and I.S. Jones, Dynamic interfacial trapping of flexural waves in structured plates, . *Proc. Roy. Soc. A* **472**, (2015), 20150658.

[39] S. G. Haslinger, N. V. Movchan, A. B. Movchan and R. C. McPhedran, Transmission, trapping and filtering of waves in periodically constrained elastic plates, *Proc. R. Soc. A*, **468**, (2012), 76.

[40] S. G. Haslinger, N. V. Movchan, A. B. Movchan and R. C. McPhedran, Symmetry and resonant modes in platonic grating stacks, *Wave Random Complex*, **24** (2), (2014)126.

[41] I. S. Jones, M. Brun, N. V. Movchan and A. B. Movchan, Singular perturbations and cloaking illusions for elastic waves in membranes and Kirchhoff plates, *International Journal of Solids and Structures*, **69-70**, (2015), 498.

[42] M. Kadic, S. Guenneau and S. Enoch, Transformational plasmonics: cloak, concentrator and rotator for SPPs, *Optics Express*, **18** (11), (2010), 12027-12032.

[43] D. J. Kan, A. A. Asatryan, C. G. Poulton, and L. C. Botten, Multipole method for modelling linear defects in photonic woodpiles, *J. Opt. Soc. Am. B*,**27**(2), (2010), 246-248.

[44] M. Kerker, Invisible bodies, *J. Opt. Soc. Am*, **65**(4), (1975), 376-379.

[45] G. Kirchhoff, Über das Gleichgewicht und die Bewegung einer elastischen Scheibe, *Journal für die reine und angewandte Mathematik*, **40**, (1850), 51-88.

[46] Yu. K. Konenkov, Diffraction of a flexural wave by a circular obstacle in a plate, *Soviet Physics-Acoustics*, **10** (2), (1964), 153-156.

[47] Y. Lai, H. Chen, Z.Q. Zhang and C.T. Chan, Complementary media invisibility cloak that cloaks objects at a distance outside the cloaking shell, *Phys. Rev. Lett.*, **102**, (2009), 093901.

[48] A.W. Leissa, *Vibration of Plates*, (1969), NASA. SP-160.

[49] U. Leonhardt, Optical conformal mapping, *Science*, **312**, (2006), 1777-1780.

[50] C.M. Linton and P.A. Martin, Semi-infinite arrays of isotropic point scatterers. A unified approach, *SIAM J. Appl. Math.*, **64**(3), (2004), 1035-1056.

[51] L. Lu, J.D. Joannopoulos and M. Soljaĉić, Topological photonics, *Nat. Photonics*, **8**, (2014), 821.

[52] B. R. Mace, The vibration of plates on two-dimensionally periodic point supports, *J. Sound Vibration*, **192** (3), (1996), 629.

[53] P.A. Martin, *Multiple scattering: interaction of time-harmonic waves with N obstacles*, (2006), Cambridge, Cambridge University Press.

[54] R. C. McPhedran and D. H. Dawes, Lattice sums for an electromagnetic scattering problem, *J. Electromagnet. Wave*, **6**, (1992), 1327-1340.

[55] R. C. McPhedran and A. B. Movchan, The Rayleigh multipole method for linear elasticity, *J. Mech. Phys. Solids*, **42**, (1994), 711-727.

[56] R.C. McPhedran, A.B. Movchan and N.V. Movchan, Platonic crystals: Bloch bands, neutrality and defects, *Mech. Mater.*, **41**, (2009), 356-363.

[57] R. C. McPhedran, A. B. Movchan, N. V. Movchan, M. Brun and M. J. A. Smith, 'Parabolic' trapped modes and steered Dirac cones in platonic crystals, *Proc. R. Soc. A*, **471**, (2015), 20140746.

[58] R. C. McPhedran, N. A. Nicorovici, L. C. Botten, and Ke-Da Bao. Green's function, lattice sum and Rayleigh's identity for a dynamic scattering problem in *IMA Volumes in Mathematics and its Applications*, (1997), Vol. 96, Springer-Verlag, New York,

[59] D. J. Mead, Wave propagation in continuous periodic structures: Research contributions from Southampton, 1964-1995, *J. Sound Vibration*, **190** (3), (1996), 495.

[60] J. Mei, Y. Wu, C.T. Chan and Z-Q. Zhang, First-principles study of Dirac and Dirac-like cones in phononic and photonic crystals, *Phys. Rev. B*, **86**, (2012), 035141.

[61] D.A.B. Miller, On perfect cloaking, *Opt. Express*, **14**, (2006), 12457-12466.

[62] G.W. Milton, M. Briane and J.R. Willis, On cloaking for elasticity and physical equations with a transformation invariant form, *New J. Phys.*, **8**, (2006), 248.

[63] G.W. Milton and N-A.P. Nicorovici, On the cloaking effects associated with anomalous localised resonance, *Proc. R. Soc. A*, **462**, (2006), 3027-3059.

[64] D. Misseroni, D. J. Colquitt, A. B. Movchan, N. V. Movchan, and I. S. Jones, Cymatics for the cloaking of flexural vibrations in a structured plate, *Nature, Scientific Reports*, **6**, (2016).

[65] F. Monticone and A. Alú, Do Cloaked Objects Really Scatter Less? *Phys. Rev. X*, **3**, (2013), 041005.

[66] A.B. Movchan and N.V. Movchan, *Mathematical modelling of solids with non-regular boundaries*, (c1995), Boca Raton: CRC Press.

[67] A.B. Movchan, N.V. Movchan and R.C. McPhedran, Bloch-Floquet bending waves in perforated thin plates, *Proc. R. Soc. A*, **463**, (2007), 2505-2518.

[68] A. B. Movchan, N. V. Movchan and C. G. Poulton, Asymptotic models of fields in dilute and densely packed composites, (2002), London, Imperial College Press.

[69] A. B. Movchan, N. A. Nicorovici, and R. C. McPhedran, Green's tensors and lattice sums for elastostatics and elastodynamics, *Proc. R. Soc. Lond. A*, **453** (1997), 643-662.

[70] N.V. Movchan, R.C. McPhedran and A.B. Movchan, Flexural waves in structured elastic plates: Mindlin versus bi-harmonic models, *Proc. R. Soc. A*, **467**, (2011), 869-880.

[71] N.V. Movchan, R.C. McPhedran, A.B. Movchan and C.G. Poulton, Wave scattering by platonic grating stacks, *Proc. R. Soc. A*, **465**, (2009), 3383-3400.

[72] P.A. Nelson and S.J. Elliott, Active control of sound, Academic Press, London, (1992).

[73] N. A. Nicorovici and R. C. McPhedran, Lattice sums for off-axis electromagnetic scattering by gratings, *Phys. Rev. E*, **50**, (1994), 3143-3160.

[74] N. A. Nicorovici, R. C. McPhedran, and L. C. Botten, Photonic band gaps for arrays of perfectly conducting cylinders, *Phys. Rev. E*, **52**, (1995), 1135-1145.

[75] N. A. Nicorovici, R. C. McPhedran, and L. C. Botten, Photonic band gaps: Non-commuting limits and the 'acoustic band', *Phys. Rev. Lett.*, **75** (1995), 1507-1510.

[76] N.-A.P. Nicorovici, R.C. McPhedran and L.C. Botten, Relative local density of states and cloaking of finite clusters of coated cylinders, *Wave Random Complex*, **21**(2), (2011), 248-277.

[77] N. A. Nicorovici, R. C. McPhedran, and Ke-Da Bao, Propagation of electromagnetic waves in periodic lattices of spheres: Green's function and lattice sums, *Phys. Rev. E*, **51**, (1995), 690-702.

[78] N.-A.P. Nicorovici, R. C. McPhedran and G. W. Milton, Transport properties of a three-phase composite material: the square array of coated cylinders, *Proc. R. Soc. Lond. A*, **442**, (1993), 599-620.

[79] N.-A.P. Nicorovici, R. C. McPhedran and G. W. Milton, Optical and dielectric properties of partially resonant composites, *Phys. Rev. B*, **49**(12), (1994).

[80] N. A. Nicorovici, R. C. McPhedran, and R. Petit, Efficient calculation of the Green's function for electromagnetic scattering by gratings, *Phys. Rev. E*, **49**, (1994), 4563-4577.

[81] N-A.P. Nicorovici, G.W. Milton, R.C. McPhedran and L.C. Botten, Quasistatic cloaking of two-dimensional polarizable discrete systems by anomalous resonance, *Opt. Express*, **15**, (2007), 6314-6323.

[82] A.N. Norris, F.A. Amirkulova and W.J. Parnell, Source amplitudes for active exterior cloaking, *Inverse Problems*, **28**, (2012), 105002.

[83] A.N. Norris, F.A. Amirkulova and W.J. Parnell, Active elastodynamic cloaking, *Math. Mech. Solids*, **19** (6), (2014), 603-625.

[84] A.N. Norris and C. Vemula, Scattering of flexural waves on thin plates, *J. Sound Vib.*, **181**(1), (1995), 115-125.

[85] J. O'Neill, Ö. Selsil, S. G. Haslinger, N.V. Movchan and R. V. Craster, Active cloaking for finite clusters of pins in thin plates, *http://arxiv.org/pdf/1608.08512.pdf*, (2016), (submitted to *SIAM J. Appl. Math.*).

[86] J. O'Neill, Ö. Selsil, R.C. McPhedran, A.B. Movchan and N.V. Movchan, Active cloaking of inclusions for flexural waves in thin elastic plates, *Quart. J. Mech. Appl. Math.*, **68** (3), (2015), 263.

[87] J. O'Neill, Ö. Selsil, R.C. McPhedran, A.B. Movchan, N.V. Movchan and C. Henderson Moggach, Active cloaking of resonant coated inclusions for waves in membranes and Kirchhoff plates, *Quart. J. Mech. Appl. Math.*, **69** (2), (2016), 115.

[88] J. B. Pendry, D. Schurig and D. R. Smith, Controlling electromagnetic fields, *Science*, **312**, (2006), 1780-1782.

[89] C. G. Poulton, R. C. McPhedran, N. V. Movchan and A. B. Movchan, Convergence properties and flat bands in platonic crystal band structures using the multipole formulation, *Wave Random Complex*, **20** (4), (2010), 702.

[90] C. G. Poulton, A. B. Movchan, N. V. Movchan and R. C. McPhedran Analytic theory of defects in periodically structured elastic plates, *Proc. R. Soc. Lond. A*, **468** (2140), (2012), 1196-1216.

[91] Lord Rayleigh, On the influence of obstacles arranged in rectangular order upon the properties of a medium, *Phil. Mag*, Series 5, **34**, (1892), 481-502.

[92] L. R. F. Rose and C. H. Wang, Mindlin plate theory for damage detection: Source solutions, *J. Acoust. Soc. Am.*, **116**, (2004), 154-171.

[93] M. Selvanayagam, and G. V. Eleftheriades, Discontinuous electromagnetic fields using orthogonal electric and magnetic currents for wavefront manipulation, *Opt. Express*, **21**, 12, (2013), 14409.

[94] M. Selvanayagam and G. V. Eleftheriades, Experimental demonstration of active electromagnetic cloaking, *Phys. Rev. X*, **3**, (2013), 041011.

[95] M. J. A. Smith, R. C. McPhedran and M. H. Meylan, Double Dirac cones at $\kappa = 0$ in pinned platonic crystals, *Wave Random Complex*, **24**(1), (2014), 35-54.

[96] M. J. A. Smith, R. C. McPhedran, C. G. Poulton and M. H. Meylan, Negative refraction and dispersion phenomena in platonic clusters, *Wave Random Complex*, **22**(4), (2012), 435-458.

[97] M. J. A. Smith, M. H. Meylan, and R. C. McPhedran, Scattering by cavities of arbitrary shape in an infinite plate and associated vibration problems, *J. Sound Vib.*, **330**, (2011), 4029-4046.

[98] M. J. A. Smith, M. H. Meylan, R. C. McPhedran and C. G. Poulton, A short remark on the band structure of free-edge platonic crystals, *Wave Random Complex*, **24**(4), (2014), 421-430.

[99] N. Stenger, M. Wilhelm and M. Wegener, Experiments on elastic cloaking in thin plates, *Phys. Rev. Lett.*, **108**, (2012), 014301.

[100] S.P. Timoshenko and S. Woinowsky-Krieger, *Theory of plates and shells*, (1959), New York, McGraw-Hill.

[101] D. Torrent, Y. Pennec and B. Djafari-Rouhani, Effective medium theory for elastic metamaterials in thin elastic plates, *Phys. Rev. B*, **90**, (2014), 104110.

[102] W. Voigt, Ueber die Beziehung zwischen den beiden Elasticitätsconstanten isotroper Körper, *Annalen der Physik*, **274** (12), (1889), 573-587.

[103] W. Wijngaard, Guided normal modes of two parallel circular dielectric rods, *J. Opt. Soc. Am.*, **63**(8), (1973), 944-950.

[104] H.H. Zheng, J.J. Xiao, Y. Lai and C.T. Chan, Exterior optical cloaking and illusions by using active sources: A boundary element perspective, *Phys, Rev. B*, **81**, (2010), 195116.

Appendix A

A.1 Kirchhoff plates: The representations for the matrices $\mathcal{A}^{(ci)}$, $\mathcal{B}^{(ci)}$, $\mathcal{A}^{(ec)}$, $\mathcal{B}^{(ec)}$ and their reduced forms $\mathcal{A}^{(ci,*)}$, $\mathcal{B}^{(ci,*)}$, $\mathcal{A}^{(ec,*)}$, $\mathcal{B}^{(ec,*)}$

Here we give a detailed description of how to obtain the entries of the matrices $\mathcal{A}_{kl}^{(ci)}$, $k,l = 1,2,3,4$; $\mathcal{B}_{kl}^{(ci)}$, $k = 1,2,3,4$; $l = 1,2$ and their reduced forms $\mathcal{A}_{kl}^{(ci,*)}$, $k,l = 1,2,3,4$; $\mathcal{B}_{kl}^{(ci,*)}$, $k = 1,2,3,4; l = 1,2$.

A.1.1 Transmission conditions at the interior interface of the coating

We first consider the interface between the inclusion and coating positioned at $r = a_i$. Substitution of the relevant field representations (3.42) into the first two conditions (1.20) of perfect bonding (corresponding to the continuity of the displacement and its normal derivative across the interface), for each multipole order n, gives

$$\begin{aligned} A_n^{(c)} J_n(\beta_c a_i) + E_n^{(c)} H_n^{(1)}(\beta_c a_i) + B_n^{(c)} I_n(\beta_c a_i) + F_n^{(c)} K_n(\beta_c a_i) \\ = A_n^{(i)} J_n(\beta_i a_i) + B_n^{(i)} I_n(\beta_i a_i), \end{aligned} \tag{A.1}$$

$$\begin{aligned} \beta_c a_i \left[A_n^{(c)} J_n{}'(\beta_c a_i) + E_n^{(c)} H_n^{(1)'}(\beta_c a_i) + B_n^{(c)} I_n{}'(\beta_c a_i) + F_n^{(c)} K_n{}'(\beta_c a_i) \right] \\ = \beta_i a_i \left[A_n^{(i)} J_n{}'(\beta_i a_i) + B_n^{(i)} I_n{}'(\beta_i a_i) \right], \end{aligned} \tag{A.2}$$

where above, and in what follows, the prime denotes the derivative with respect to the argument. With the help of equations (A.1), (A.2), we can write condition (1.21), which corresponds to the continuity of the moment across the interface, as

$$\begin{aligned} \beta_c^2 a_i^2 \left[A_n^{(c)} J_n{}''(\beta_c a_i) + E_n^{(c)} H_n^{(1)''}(\beta_c a_i) + B_n^{(c)} I_n{}''(\beta_c a_i) + F_n^{(c)} K_n{}''(\beta_c a_i) \right] \\ = \frac{D_i}{D_c} \beta_i^2 a_i^2 \left[A_n^{(i)} J_n{}''(\beta_i a_i) + B_n^{(i)} I_n{}''(\beta_i a_i) \right] \\ + \left(\frac{D_i}{D_c} \nu_i - \nu_c \right) \beta_i a_i \left[A_n^{(i)} J_n{}'(\beta_i a_i) + B_n^{(i)} I_n{}'(\beta_i a_i) \right] \\ - \left(\frac{D_i}{D_c} \nu_i - \nu_c \right) n^2 \left[A_n^{(i)} J_n(\beta_i a_i) + B_n^{(i)} I_n(\beta_i a_i) \right]. \end{aligned} \tag{A.3}$$

Next, we deal with condition (1.22), which enforces the continuity of the transverse force across the interface. We first note that

$$\frac{\partial}{\partial r}\Delta_{r\theta}w+\frac{1-\nu_k}{r^2}\frac{\partial^2}{\partial\theta^2}\left(\frac{\partial w}{\partial r}-\frac{w}{r}\right)=\frac{\partial^3 w}{\partial r^3}-\frac{1}{r^2}\frac{\partial w}{\partial r}+\frac{1}{r}\frac{\partial^2 w}{\partial r^2}+\frac{2-\nu_c}{r^2}\frac{\partial^3 w}{\partial r\partial\theta^2}-\frac{3-\nu_c}{r^3}\frac{\partial^2 w}{\partial\theta^2}. \quad \text{(A.4)}$$

Hence (1.22) can be written as

$$\begin{aligned}
&\beta_c^3 a_i^3\left[A_n^{(c)}J_n'''(\beta_c a_i)+E_n^{(c)}H_n^{(1)'''}(\beta_c a_i)+B_n^{(c)}I_n'''(\beta_c a_i)+F_n^{(c)}K_n'''(\beta_c a_i)\right]\\
&-\beta_c a_i\left[A_n^{(c)}J_n'(\beta_c a_i)+E_n^{(c)}H_n^{(1)'}(\beta_c a_i)+B_n^{(c)}I_n'(\beta_c a_i)+F_n^{(c)}K_n'(\beta_c a_i)\right]\\
&+\beta_c^2 a_i^2\left[A_n^{(c)}J_n''(\beta_c a_i)+E_n^{(c)}H_n^{(1)''}(\beta_c a_i)+B_n^{(c)}I_n''(\beta_c a_i)+F_n^{(c)}K_n''(\beta_c a_i)\right]\\
&-(2-\nu_c)\beta_c n^2 a_i\left[A_n^{(c)}J_n'(\beta_c a_i)+E_n^{(c)}H_n^{(1)'}(\beta_c a_i)+B_n^{(c)}I_n'(\beta_c a_i)+F_n^{(c)}K_n'(\beta_c a_i)\right]\\
&-(3-\nu_c)n^2\left[A_n^{(c)}J_n(\beta_c a_i)+E_n^{(c)}H_n^{(1)}(\beta_c a_i)+B_n^{(c)}I_n(\beta_c a_i)+F_n^{(c)}K_n(\beta_c a_i)\right]\\
&\quad=\frac{D_i}{D_c}\Big\{\beta_i^3 a_i^3\left[A_n^{(i)}J_n'''(\beta_i a_i)+B_n^{(i)}I_n'''(\beta_i a_i)\right]-\beta_i a_i\left[A_n^{(i)}J_n'(\beta_i a_i)+B_n^{(i)}I_n'(\beta_i a_i)\right]\\
&\qquad\qquad+\beta_i^2 a_i^2\left[A_n^{(i)}J_n''(\beta_i a_i)+B_n^{(i)}I_n''(\beta_i a_i)\right]\\
&\qquad\qquad-(2-\nu_i)\beta_i n^2 a_i\left[A_n^{(i)}J_n'(\beta_i a_i)+B_n^{(i)}I_n'(\beta_i a_i)\right]\\
&\qquad\qquad+(3-\nu_i)n^2\left[A_n^{(i)}J_n(\beta_i a_i)+B_n^{(i)}I_n(\beta_i a_i)\right]\Big\}.
\end{aligned} \quad \text{(A.5)}$$

Now, using (A.1), (A.2) and (A.3), equality (A.5) can be reduced to

$$\begin{aligned}
&\beta_c^3 a_i^3\left[A_n^{(c)}J_n'''(\beta_c a_i)+E_n^{(c)}H_n^{(1)'''}(\beta_c a_i)+B_n^{(c)}I_n'''(\beta_c a_i)+F_n^{(c)}K_n'''(\beta_c a_i)\right]\\
&=\frac{D_i}{D_c}\beta_i^3 a_i^3\left[A_n^{(i)}J_n'''(\beta_i a_i)+B_n^{(i)}I_n'''(\beta_i a_i)\right]+3n^2\left(\frac{D_i}{D_c}-1\right)\left[A_n^{(i)}J_n(\beta_i a_i)+B_n^{(i)}I_n(\beta_i a_i)\right]\\
&-\left\{\frac{D_i}{D_c}\nu_i-\nu_c+\frac{D_i}{D_c}\left[1+(2-\nu_i)n^2\right]-\left[1+(2+\nu_c)n^2\right]\right\}\beta_i a_i\left[A_n^{(i)}J_n'(\beta_i a_i)+B_n^{(i)}I_n'(\beta_i a_i)\right].
\end{aligned} \quad \text{(A.6)}$$

A.1.2 Reduction of the system of transmission conditions on $r = a_i$ to block diagonal form

To deal with the second and third-order derivatives in (A.3) and (A.6) respectively, we consider the Bessel equations

$$z^2\mathcal{W}_\pm''(z)+z\mathcal{W}_\pm'(z)\pm(z^2\mp n^2)\mathcal{W}_\pm(z)=0,$$

and their derivatives with respect to z, rearrange and obtain

$$\beta_c^2 a_i^2\mathcal{W}_\pm''(\beta_c a_i)=-\beta_c a_i\mathcal{W}_\pm'(\beta_c a_i)\pm(\beta_c^2 a_i^2\mp n^2)\mathcal{W}_\pm(\beta_c a_i), \quad \text{(A.7)}$$

$$\beta_c^3 a_i^3\mathcal{W}_\pm'''(\beta_c a_i)=\left(2\mp\beta_c^2 a_i^2+n^2\right)\beta_c a_i\mathcal{W}_\pm'(\beta_c a_i)\pm\left(\beta_c^2 a_i^2\mp 3n^2\right)\mathcal{W}_\pm(\beta_c a_i), \quad \text{(A.8)}$$

where we replaced z by $\beta_c a_i$. Here $\mathcal{W}_+$ corresponds to $J_n, H_n^{(1)}$ and $\mathcal{W}_-$ to I_n, K_n, respectively. Using (A.7) and (A.8), we re-write the equality (A.3) as

$$\begin{aligned}
&A_n^{(c)}\left[-\beta_c a_i {J_n}'(\beta_c a_i) - \left(\beta_c^2 a_i^2 - n^2\right) J_n(\beta_c a_i)\right] \\
&\quad + E_n^{(c)}\left[-\beta_c a_i {H_n^{(1)}}'(\beta_c a_i) - \left(\beta_c^2 a_i^2 - n^2\right) H_n^{(1)}(\beta_c a_i)\right] \\
&\quad + B_n^{(c)}\left[-\beta_c a_i {I_n}'(\beta_c a_i) + \left(\beta_c^2 a_i^2 + n^2\right) I_n(\beta_c a_i)\right] \\
&\quad + F_n^{(c)}\left[-\beta_c a_i {K_n}'(\beta_c a_i) + \left(\beta_c^2 a_i^2 + n^2\right) K_n(\beta_c a_i)\right] \\
&= A_n^{(i)}\Bigg\{ - \left[\frac{D_i}{D_c}(1-\nu_i) + \nu_c\right]\beta_i a_i {J_n}'(\beta_i a_i) + \left[-\frac{D_i}{D_c}\beta_i^2 a_i^2 + n^2\left[\frac{D_i}{D_c}(1-\nu_i) + \nu_c\right]\right] J_n(\beta_i a_i) \\
&\quad + B_n^{(i)}\Bigg\{ - \left[\frac{D_i}{D_c}(1-\nu_i) + \nu_c\right]\beta_i a_i {I_n}'(\beta_i a_i) + \left[\frac{D_i}{D_c}\beta_i^2 a_i^2 + n^2\left[\frac{D_i}{D_c}(1-\nu_i) + \nu_c\right]\right] I_n(\beta_i a_i).
\end{aligned} \tag{A.9}$$

and (A.6) as

$$\begin{aligned}
&A_n^{(c)}\left[\left(2 - \beta_c^2 a_i^2 + n^2\right)\beta_c a_i {J_n}'(\beta_c a_i) + \left(\beta_c^2 a_i^2 - 3n^2\right) J_n(\beta_c a_i)\right] \\
&\quad + E_n^{(c)}\left[\left(2 - \beta_c^2 a_i^2 + n^2\right)\beta_c a_i {H_n^{(1)}}'(\beta_c a_i) + \left(\beta_c^2 a_i^2 - 3n^2\right) H_n^{(1)}(\beta_c a_i)\right] \\
&\quad + B_n^{(c)}\left[\left(2 + \beta_c^2 a_i^2 + n^2\right)\beta_c a_i {I_n}'(\beta_c a_i) - \left(\beta_c^2 a_i^2 + 3n^2\right) I_n(\beta_c a_i)\right] \\
&\quad + F_n^{(c)}\left[\left(2 + \beta_c^2 a_i^2 + n^2\right)\beta_c a_i {K_n}'(\beta_c a_i) - \left(\beta_c^2 a_i^2 + 3n^2\right) K_n(\beta_c a_i)\right] \\
&= A_n^{(i)}\Bigg\{ \left[\frac{D_i}{D_c}\left[(1-\nu_i)(1-n^2) - \beta_i^2 a_i^2\right] + 1 + \nu_c + (2-\nu_c)n^2\right]\beta_i a_i {J_n}'(\beta_i a_i) \\
&\qquad\qquad + \left(\frac{D_i}{D_c}\beta_i^2 a_i^2 - 3n^2\right) J_n(\beta_i a_i)\Bigg\} \\
&\quad + B_n^{(i)}\Bigg\{ \left[\frac{D_i}{D_c}\left[(1-\nu_i)(1-n^2) + \beta_i^2 a_i^2\right] + 1 + \nu_c + (2-\nu_c)n^2\right]\beta_i a_i {I_n}'(\beta_i a_i) \\
&\qquad\qquad + \left(-\frac{D_i}{D_c}\beta_i^2 a_i^2 - 3n^2\right) I_n(\beta_i a_i)\Bigg\}.
\end{aligned} \tag{A.10}$$

Equations (A.1), (A.2), (A.9) and (A.10) finally lead us to the matrix equation (3.43) with the left hand sides and right hand sides forming the rows of $\mathcal{A}_{kl}^{(ci)}$ and $\mathcal{B}_{kl}^{(ci)}$ respectively. The

components of the matrices $\mathcal{A}_{kl}^{(ci)}$, $k,l=1,2,3,4$; $\mathcal{B}_{kl}^{(ci)}$, $k=1,2; l=1,2,3,4$ are given below:

$$
\begin{aligned}
&\mathcal{A}_{11}^{(ci)} = J_n(\beta_c a_i), \quad \mathcal{A}_{12}^{(ci)} = H_n^{(1)}(\beta_c a_i), \quad \mathcal{A}_{13}^{(ci)} = I_n(\beta_c a_i), \quad \mathcal{A}_{14}^{(ci)} = K_n(\beta_c a_i),\\
&\mathcal{A}_{21}^{(ci)} = \beta_c a_i J_n{}'(\beta_c a_i), \quad \mathcal{A}_{22}^{(ci)} = \beta_c a_i H_n^{(1)}{}'(\beta_c a_i),\\
&\mathcal{A}_{23}^{(ci)} = \beta_c a_i I_n{}'(\beta_c a_i), \quad \mathcal{A}_{24}^{(ci)} = \beta_c a_i K_n{}'(\beta_c a_i),\\
&\mathcal{A}_{31}^{(ci)} = -(\beta_c^2 a_i^2 - n^2) J_n(\beta_c a_i) - \beta_c a_i J_n{}'(\beta_c a_i),\\
&\mathcal{A}_{32}^{(ci)} = -(\beta_c^2 a_i^2 - n^2) H_n^{(1)}(\beta_c a_i) - \beta_c a_i H_n^{(1)}{}'(\beta_c a_i),\\
&\mathcal{A}_{33}^{(ci)} = (\beta_c^2 a_i^2 + n^2) I_n(\beta_c a_i) - \beta_c a_i I_n{}'(\beta_c a_i),\\
&\mathcal{A}_{34}^{(ci)} = (\beta_c^2 a_i^2 + n^2) K_n(\beta_c a_i) - \beta_c a_i K_n{}'(\beta_c a_i),\\
&\mathcal{A}_{41}^{(ci)} = (\beta_c^2 a_i^2 - 3n^2) J_n(\beta_c a_i) + (-\beta_c^2 a_i^2 + n^2 + 2)\beta_c a_i J_n{}'(\beta_c a_i),\\
&\mathcal{A}_{42}^{(ci)} = (\beta_c^2 a_i^2 - 3n^2) H_n^{(1)}(\beta_c a_i) + (-\beta_c^2 a_i^2 + n^2 + 2)\beta_c a_i H_n^{(1)}{}'(\beta_c a_i),\\
&\mathcal{A}_{43}^{(ci)} = -(\beta_c^2 a_i^2 + 3n^2) I_n(\beta_c a_i) + (\beta_c^2 a_i^2 + n^2 + 2)\beta_c a_i I_n{}'(\beta_c a_i),\\
&\mathcal{A}_{44}^{(ci)} = -(\beta_c^2 a_i^2 + 3n^2) K_n(\beta_c a_i) + (\beta_c^2 a_i^2 + n^2 + 2)\beta_c a_i K_n{}'(\beta_c a_i);
\end{aligned}
$$

$$
\begin{aligned}
&\mathcal{B}_{11}^{(ci)} = J_n(\beta_i a_i), \quad \mathcal{B}_{12}^{(ci)} = I_n(\beta_i a_i), \quad \mathcal{B}_{21}^{(ci)} = \beta_i a_i J_n{}'(\beta_i a_i), \quad \mathcal{B}_{22}^{(ci)} = \beta_i a_i I_n{}'(\beta_i a_i),\\
&\mathcal{B}_{31}^{(ci)} = \left\{ -\frac{D_i}{D_c}\beta_i^2 a_i^2 + n^2 \left[(1-\nu_i)\frac{D_i}{D_c} + \nu_c \right] \right\} J_n(\beta_i a_i) - \left[(1-\nu_i)\frac{D_i}{D_c} + \nu_c \right] \beta_i a_i J_n{}'(\beta_i a_i),\\
&\mathcal{B}_{32}^{(ci)} = \left\{ \frac{D_i}{D_c}\beta_i^2 a_i^2 + n^2 \left[(1-\nu_i)\frac{D_i}{D_c} + \nu_c \right] \right\} I_n(\beta_i a_i) - \left[(1-\nu_i)\frac{D_i}{D_c} + \nu_c \right] \beta_i a_i I_n{}'(\beta_i a_i),\\
&\mathcal{B}_{41}^{(ci)} = \left(\frac{D_i}{D_c}\beta_i^2 a_i^2 - 3n^2 \right) J_n(\beta_i a_i)\\
&\qquad\qquad + \left\{ \frac{D_i}{D_c} \left[(1-\nu_i)(1-n^2) - \beta_i^2 a_i^2 \right] + 1 + \nu_c + (2-\nu_c)n^2 \right\} \beta_i a_i J_n{}'(\beta_i a_i),\\
&\mathcal{B}_{42}^{(ci)} = -\left(\frac{D_i}{D_c}\beta_i^2 a_i^2 + 3n^2 \right) I_n(\beta_i a_i)\\
&\qquad\qquad + \left\{ \frac{D_i}{D_c} \left[(1-\nu_i)(1-n^2) + \beta_i^2 a_i^2 \right] + 1 + \nu_c + (2-\nu_c)n^2 \right\} \beta_i a_i I_n{}'(\beta_i a_i).
\end{aligned}
$$

In order to obtain the matrices $\mathcal{A}_{kl}^{(ci,*)}$, $k,l=1,2,3,4$; $\mathcal{B}_{kl}^{(ci,*)}$, $k=1,2,3,4; l=1,2$, where $\mathcal{A}_{kl}^{(ci,*)}$ is a block diagonal matrix, we perform the following row operations on the matrix $\mathcal{A}^{(ci)}$

$$
\begin{aligned}
-(\beta_c^2 a_i^2 + n^2)R_1 + R_2 + R_3 &\longrightarrow R_1^*,\\
2n^2 R_1 - (\beta_c^2 a_i^2 + n^2 + 1)R_2 + R_3 + R_4 &\longrightarrow R_2^*,\\
(\beta_c^2 a_i^2 - n^2)R_1 + R_2 + R_3 &\longrightarrow R_3^*,\\
2n^2 R_1 + (\beta_c^2 a_i^2 - n^2 - 1)R_2 + R_3 + R_4 &\longrightarrow R_4^*,
\end{aligned}
$$

where R_i, R_i^*, $i=1,2,3,4$, denote the rows and the reduced rows of the matrix $\mathcal{A}^{(ci)}$, respec-

tively. Hence the reduced form matrix $\mathcal{A}_{kl}^{(ci,*)}$, $k,l=1,2,3,4$, can be obtained as

$$\begin{aligned}
&\mathcal{A}_{11}^{(ci,*)}=-2\beta_c^2a_i^2J_n(\beta_ca_i),\quad \mathcal{A}_{12}^{(ci,*)}=-2\beta_c^2a_i^2H_n^{(1)}(\beta_ca_i),\quad \mathcal{A}_{13}^{(ci,*)}=\mathcal{A}_{14}^{(ci,*)}=0,\\
&\mathcal{A}_{21}^{(ci,*)}=-2\beta_c^3a_i^3J_n{}'(\beta_ca_i),\quad \mathcal{A}_{22}^{(ci,*)}=-2\beta_c^3a_i^3H_n^{(1)\prime}(\beta_ca_i),\quad \mathcal{A}_{23}^{(ci,*)}=\mathcal{A}_{24}^{(ci,*)}=0,\\
&\mathcal{A}_{31}^{(ci,*)}=\mathcal{A}_{32}^{(ci,*)}=0,\quad \mathcal{A}_{33}^{(ci,*)}=2\beta_c^2a_i^2I_n(\beta_ca_i),\quad \mathcal{A}_{34}^{(ci,*)}=2\beta_c^2a_i^2K_n(\beta_ca_i),\\
&\mathcal{A}_{41}^{(ci,*)}=\mathcal{A}_{42}^{(ci,*)}=0,\quad \mathcal{A}_{43}^{(ci,*)}=2\beta_c^3a_i^3I_n{}'(\beta_ca_i),\quad \mathcal{A}_{44}^{(ci,*)}=2\beta_c^3a_i^3K_n{}'(\beta_ca_i).
\end{aligned}$$

Referring to the matrix equation (3.43), we use the same row operations on matrix $\mathcal{B}_{kl}^{(ci)}$, $k=1,2,3,4;l=1,2$. It is clear that its reduced form reads as follows

$$\begin{aligned}
\mathcal{B}_{1k}^{(ci,*)}&=-(\beta_c^2a_i^2+n^2)\mathcal{B}_{1k}^{(ci)}+\mathcal{B}_{2k}^{(ci)}+\mathcal{B}_{3k}^{(ci)},\\
\mathcal{B}_{2k}^{(ci,*)}&=2n^2\mathcal{B}_{1k}^{(ci)}-(\beta_c^2a_i^2+n^2+1)\mathcal{B}_{2k}^{(ci)}+\mathcal{B}_{3k}^{(ci)}+\mathcal{B}_{4k}^{(ci)},\\
\mathcal{B}_{3k}^{(ci,*)}&=(\beta_c^2a_i^2-n^2)\mathcal{B}_{1k}^{(ci)}+\mathcal{B}_{2k}^{(ci)}+\mathcal{B}_{3k}^{(ci)},\\
\mathcal{B}_{4k}^{(ci,*)}&=2n^2\mathcal{B}_{1k}^{(ci)}+(\beta_c^2a_i^2-n^2-1)\mathcal{B}_{2k}^{(ci)}+\mathcal{B}_{3k}^{(ci)}+\mathcal{B}_{4k}^{(ci)},k=1,2.
\end{aligned}$$

A.1.3 Transmission conditions at the exterior interface of the coating

To obtain the entries of the matrices $\mathcal{A}_{kl}^{(ec)}$; $\mathcal{B}_{kl}^{(ec)}$, $k,l=1,2,3,4$, and their reduced forms $\mathcal{A}_{kl}^{(ec,*)}$; $\mathcal{B}_{kl}^{(ec,*)}$, $k,l=1,2,3,4$, we use a similar method to that described above, however, at the interface between the coating and exterior medium, the conditions for perfect bonding are equated on the radius $r=a_c$. By substituting the corresponding field representations into the first two equations of (1.20), we write the following

$$\begin{aligned}
&A_n^{(e)}J_n(\beta_ea_c)+E_n^{(e)}H_n^{(1)}(\beta_ea_c)+B_n^{(e)}I_n(\beta_ea_c)+F_n^{(e)}K_n(\beta_ea_c)\\
&\qquad=A_n^{(c)}J_n(\beta_ca_c)+E_n^{(c)}H_n^{(1)}(\beta_ca_c)+B_n^{(c)}I_n(\beta_ca_c)+F_n^{(c)}K_n(\beta_ca_c)
\end{aligned}\tag{A.11}$$

$$\begin{aligned}
&\beta_ea_c\left[A_n^{(e)}J_n{}'(\beta_ea_c)+E_n^{(e)}H_n^{(1)\prime}(\beta_ea_c)+B_n^{(e)}I_n{}'(\beta_ea_c)+F_n^{(e)}K_n{}'(\beta_ea_c)\right]\\
&\quad=\beta_ca_c\left[A_n^{(c)}J_n{}'(\beta_ca_c)+E_n^{(c)}H_n^{(1)\prime}(\beta_ca_c)+B_n^{(c)}I_n{}'(\beta_ca_c)+F_n^{(c)}K_n{}'(\beta_ca_c)\right].
\end{aligned}\tag{A.12}$$

We can now use (A.11) and (A.12) to write condition (1.21) on $r=a_c$ as

$$\begin{aligned}
&\beta_e^2a_c^2\left[A_n^{(e)}J_n{}''(\beta_ea_c)+E_n^{(e)}H_n^{(1)\prime\prime}(\beta_ea_c)+B_n^{(e)}I_n{}''(\beta_ea_c)+F_n^{(e)}K_n{}''(\beta_ea_c)\right]\\
&=\frac{D_c}{D_e}\beta_c^2a_c^2\left[A_n^{(c)}J_n{}''(\beta_ca_c)+E_n^{(c)}H_n^{(1)\prime\prime}(\beta_ca_c)+B_n^{(c)}I_n{}''(\beta_ca_c)+F_n^{(c)}K_n{}''(\beta_ca_c)\right]\\
&+\left(\frac{D_c}{D_e}\nu_c-\nu_e\right)\beta_ca_c\left[A_n^{(c)}J_n{}'(\beta_ca_c)+E_n^{(c)}H_n^{(1)\prime}(\beta_ca_c)+B_n^{(c)}I_n{}'(\beta_ca_c)+F_n^{(c)}K_n{}'(\beta_ca_c)\right]\\
&-\left(\frac{D_c}{D_e}\nu_c-\nu_e\right)n^2\left[A_n^{(c)}J_n(\beta_ca_c)+E_n^{(c)}H_n^{(1)}(\beta_ca_c)+B_n^{(c)}I_n(\beta_ca_c)+F_n^{(c)}K_n(\beta_ca_c)\right].
\end{aligned}\tag{A.13}$$

In order to write the interface condition (1.22) on $r=a_c$, we use equation (A.4) as well as equations (A.11), (A.12) and (A.13) to group together zeroth and first order deriviatives

on the left hand side, which gives

$$\begin{aligned}
&\beta_e^3 a_c^3 \left[A_n^{(e)} {J_n}'''(\beta_e a_c) + E_n^{(e)} {H_n^{(1)}}'''(\beta_e a_c) + B_n^{(e)} {I_n}'''(\beta_e a_c) + F_n^{(e)} {K_n}'''(\beta_e a_c)\right] \\
&= \frac{D_c}{D_e}\beta_c^3 a_c^3 \left[A_n^{(c)} {J_n}'''(\beta_c a_c) + E_n^{(c)} {H_n^{(1)}}'''(\beta_c a_c) + B_n^{(c)} {I_n}'''(\beta_c a_c) + F_n^{(c)} {K_n}'''(\beta_c a_c)\right] \\
&+ 3n^2\left(\frac{D_i}{D_c} - 1\right)\left[A_n^{(c)} J_n(\beta_c a_c) + E_n^{(c)} H_n^{(1)}(\beta_c a_c) + B_n^{(c)} I_n(\beta_c a_c) + F_n^{(c)} K_n(\beta_c a_c)\right] \\
&-\Bigg\{\frac{D_c}{D_e}\nu_c - \nu_e + \frac{D_c}{D_e}\left[1 + (2-\nu_c)n^2\right] \\
&\quad -\left[1 + (2-\nu_e)n^2\right]\Bigg\}\beta_c a_c\Big[A_n^{(c)} {J_n}'(\beta_c a_c) + E_n^{(c)} {H_n^{(1)}}'(\beta_c a_c) + B_n^{(c)} {I_n}'(\beta_c a_c) + F_n^{(c)} {K_n}'(\beta_c a_c)\Big].
\end{aligned} \tag{A.14}$$

A.1.4 Reduction of the system of transmission conditions on $r = a_c$ to block diagonal form

We use the relevant form of equations (A.7) and (A.8) to replace the second and third order derivatives in equations (A.13) and (A.14). Equation (A.13) simplifies to

$$\begin{aligned}
&A_n^{(e)}\left[-\beta_e a_c {J_n}'(\beta_e a_c) - \left(\beta_e^2 a_c^2 - n^2\right) J_n(\beta_e a_c)\right] + E_n^{(e)}\left[-\beta_e a_c {H_n^{(1)}}'(\beta_e a_c) - \left(\beta_e^2 a_c^2 - n^2\right) H_n^{(1)}(\beta_e a_c)\right] \\
&+B_n^{(e)}\left[-\beta_e a_c {I_n}'(\beta_e a_c) + \left(\beta_e^2 a_c^2 + n^2\right) I_n(\beta_e a_c)\right] + F_n^{(e)}\left[-\beta_e a_c {K_n}'(\beta_e a_c) + \left(\beta_e^2 a_c^2 + n^2\right) K_n(\beta_e a_c)\right] \\
&= A_n^{(c)}\Bigg\{ -\left[\frac{D_c}{D_e}(1-\nu_c) + \nu_e\right]\beta_c a_c {J_n}'(\beta_c a_c) + \left[-\frac{D_c}{D_e}\beta_c^2 a_c^2 + n^2\left[\frac{D_c}{D_e}(1-\nu_c) + \nu_m\right]\right] J_n(\beta_c a_c) \\
&\quad +E_n^{(c)}\Bigg\{ -\left[\frac{D_c}{D_e}(1-\nu_c) + \nu_e\right]\beta_c a_c {H_n^{(1)}}'(\beta_c a_c) + \left[-\frac{D_c}{D_e}\beta_c^2 a_c^2 + n^2\left[\frac{D_c}{D_e}(1-\nu_c) + \nu_m\right]\right] H_n^{(1)}(\beta_c a_c) \\
&\quad +B_n^{(c)}\Bigg\{ -\left[\frac{D_c}{D_e}(1-\nu_c) + \nu_e\right]\beta_c a_c {I_n}'(\beta_c a_c) + \left[\frac{D_c}{D_e}\beta_c^2 a_c^2 + n^2\left[\frac{D_c}{D_e}(1-\nu_c) + \nu_e\right]\right] I_n(\beta_c a_c) \\
&\quad +F_n^{(c)}\Bigg\{ -\left[\frac{D_c}{D_e}(1-\nu_c) + \nu_e\right]\beta_c a_c {K_n}'(\beta_c a_c) + \left[\frac{D_c}{D_e}\beta_c^2 a_c^2 + n^2\left[\frac{D_c}{D_e}(1-\nu_c) + \nu_e\right]\right] K_n(\beta_c a_c),
\end{aligned} \tag{A.15}$$

and (A.14) becomes

$$
\begin{aligned}
&A_n^{(e)}\left[\left(2-\beta_e^2a_c^2+n^2\right)\beta_ea_cJ_n{}'(\beta_ea_c)+\left(\beta_e^2a_c^2-3n^2\right)J_n(\beta_ea_c)\right]\\
&+E_n^{(e)}\left[\left(2-\beta_e^2a_c^2+n^2\right)\beta_ea_cH_n^{(1)\prime}(\beta_ea_c)+\left(\beta_e^2a_c^2-3n^2\right)H_n^{(1)}(\beta_ea_c)\right]\\
&+B_n^{(c)}\left[\left(2+\beta_e^2a_c^2+n^2\right)\beta_ea_cI_n{}'(\beta_ea_c)-\left(\beta_e^2a_c^2+3n^2\right)I_n(\beta_ea_c)\right]\\
&+F_n^{(e)}\left[\left(2+\beta_e^2a_c^2+n^2\right)\beta_ea_cK_n{}'(\beta_ea_c)-\left(\beta_e^2a_c^2+3n^2\right)K_n(\beta_ea_c)\right]\\
&\qquad=A_n^{(c)}\Bigg\{\left[\frac{D_c}{D_e}\left[(1-\nu_c)(1-n^2)-\beta_c^2a_c^2\right]+1+\nu_e+(2-\nu_e)n^2\right]\beta_ca_cJ_n{}'(\beta_ca_c)\\
&\qquad\quad+\left(\frac{D_c}{D_e}\beta_c^2a_c^2-3n^2\right)J_n(\beta_ca_c)\Bigg\}\\
&\qquad+E_n^{(c)}\Bigg\{\left[\frac{D_c}{D_e}\left[(1-\nu_c)(1-n^2)-\beta_c^2a_c^2\right]+1+\nu_e+(2-\nu_e)n^2\right]\beta_ca_cH_n^{(1)\prime}(\beta_ca_c)\\
&\qquad\quad+\left(\frac{D_c}{D_e}\beta_c^2a_c^2-3n^2\right)H_n^{(1)}(\beta_ca_c)\Bigg\}\\
&\qquad+B_n^{(c)}\Bigg\{\left[\frac{D_c}{D_e}\left[(1-\nu_c)(1-n^2)+\beta_c^2a_c^2\right]+1+\nu_e+(2-\nu_e)n^2\right]\beta_ca_cI_n{}'(\beta_ca_c)\\
&\qquad\quad-\left(\frac{D_c}{D_e}\beta_c^2a_c^2+3n^2\right)I_n(\beta_ca_c)\Bigg\}\\
&\qquad+F_n^{(c)}\Bigg\{\left[\frac{D_c}{D_e}\left[(1-\nu_c)(1-n^2)+\beta_c^2a_c^2\right]+1+\nu_e+(2-\nu_e)n^2\right]\beta_ca_cK_n{}'(\beta_ca_c)\\
&\qquad\quad-\left(\frac{D_c}{D_e}\beta_c^2a_c^2+3n^2\right)K_n(\beta_ca_c)\Bigg\}. \qquad\text{(A.16)}
\end{aligned}
$$

The matrices $\mathcal{A}^{(ec)}$ and $\mathcal{B}^{(ec)}$ in equation (3.44) can be written explicitly, and their elements are given below:

$$
\begin{aligned}
&\mathcal{A}_{11}^{(ec)}=J_n(\beta_ea_c),\quad \mathcal{A}_{12}^{(ec)}=H_n^{(1)}(\beta_ea_c),\quad \mathcal{A}_{13}^{(ec)}=I_n(\beta_ea_c),\quad \mathcal{A}_{14}^{(ec)}=K_n(\beta_ea_c),\\
&\mathcal{A}_{21}^{(ec)}=\beta_ea_cJ_n{}'(\beta_ea_c),\quad \mathcal{A}_{22}^{(ec)}=\beta_ea_cH_n^{(1)\prime}(\beta_ea_c),\quad \mathcal{A}_{23}^{(ec)}=\beta_ea_cI_n{}'(\beta_ea_c),\\
&\mathcal{A}_{24}^{(ec)}=\beta_ea_cK_n{}'(\beta_ea_c),\quad \mathcal{A}_{31}^{(ec)}=-(\beta_e^2a_c^2-n^2)J_n(\beta_ea_c)-\beta_ea_cJ_n{}'(\beta_ea_c),\\
&\mathcal{A}_{32}^{(ec)}=-(\beta_e^2a_c^2-n^2)H_n^{(1)}(\beta_ea_c)-\beta_ea_cH_n^{(1)\prime}(\beta_ea_c),\\
&\mathcal{A}_{33}^{(ec)}=(\beta_e^2a_c^2+n^2)I_n(\beta_ea_c)-\beta_ea_cI_n{}'(\beta_ea_c),\\
&\mathcal{A}_{34}^{(ec)}=(\beta_e^2a_c^2+n^2)K_n(\beta_ea_c)-\beta_ea_cK_n{}'(\beta_ea_c),\\
&\mathcal{A}_{41}^{(ec)}=(\beta_e^2a_c^2-3n^2)J_n(\beta_ea_c)+(-\beta_e^2a_c^2+n^2+2)\beta_ea_cJ_n{}'(\beta_ea_c),\\
&\mathcal{A}_{42}^{(ec)}=(\beta_e^2a_c^2-3n^2)H_n^{(1)}(\beta_ea_c)+(-\beta_e^2a_c^2+n^2+2)\beta_ea_cH_n^{(1)\prime}(\beta_ea_c),\\
&\mathcal{A}_{43}^{(ci)}=-(\beta_e^2a_c^2+3n^2)I_n(\beta_ea_c)+(\beta_e^2a_c^2+n^2+2)\beta_ea_cI_n{}'(\beta_ea_c),\\
&\mathcal{A}_{44}^{(ci)}=-(\beta_e^2a_c^2+3n^2)K_n(\beta_ea_c)+(\beta_e^2a_c^2+n^2+2)\beta_ea_cK_n{}'(\beta_ea_c);
\end{aligned}
$$

$$\mathcal{B}_{11}^{(ec)} = J_n(\beta_c a_c), \quad \mathcal{B}_{12}^{(ec,*)} = H_n^{(1)}(\beta_c a_c), \quad \mathcal{B}_{13}^{(ec)} = I_n(\beta_c a_c), \quad \mathcal{B}_{14}^{(ec,*)} = K_n(\beta_c a_c),$$
$$\mathcal{B}_{21}^{(ec)} = \beta_c a_c J_n{}'(\beta_c a_c), \quad \mathcal{B}_{22}^{(ec)} = \beta_c a_c H_n^{(1)'}(\beta_c a_c),$$
$$\mathcal{B}_{23}^{(ec)} = \beta_c a_c I_n{}'(\beta_c a_c), \quad \mathcal{B}_{24}^{(ec)} = \beta_c a_c K_n{}'(\beta_c a_c),$$
$$\mathcal{B}_{31}^{(ec)} = \left\{ n^2 \left[\frac{D_c}{D_e}(1-\nu_c) + \nu_e \right] - \frac{D_c}{D_e}\beta_c^2 a_c^2 \right\} J_n(\beta_c a_c) - \beta_c a_c \left[\frac{D_c}{D_e}(1-\nu_c) + \nu_e \right] J_n{}'(\beta_c a_c),$$
$$\mathcal{B}_{32}^{(ec)} = \left\{ n^2 \left[\frac{D_c}{D_e}(1-\nu_c) + \nu_e \right] - \frac{D_c}{D_e}\beta_c^2 a_c^2 \right\} H_n^{(1)}(\beta_c a_c) - \beta_c a_c \left[\frac{D_c}{D_e}(1-\nu_c) + \nu_e \right] H_n^{(1)'}(\beta_c a_c),$$
$$\mathcal{B}_{33}^{(ec)} = \left\{ n^2 \left[\frac{D_c}{D_e}(1-\nu_c) + \nu_e \right] + \frac{D_c}{D_e}\beta_c^2 a_c^2 \right\} I_n(\beta_c a_c) - \beta_c a_c \left[\frac{D_c}{D_e}(1-\nu_c) + \nu_e \right] I_n{}'(\beta_c a_c),$$
$$\mathcal{B}_{34}^{(ec)} = \left\{ n^2 \left[\frac{D_c}{D_e}(1-\nu_c) + \nu_e \right] + \frac{D_c}{D_e}\beta_c^2 a_c^2 \right\} K_n(\beta_c a_c) - \beta_c a_c \left[\frac{D_c}{D_e}(1-\nu_c) + \nu_e \right] K_n{}'(\beta_c a_c),$$
$$\mathcal{B}_{41}^{(ec)} = \left(\frac{D_c}{D_e}\beta_c^2 a_c^2 - 3n^2 \right) J_n(\beta_c a_c) + \beta_c a_c \left\{ \frac{D_c}{D_e}\left[1 - \beta_c^2 a_c^2 + n^2(\nu_c - 1) - \nu_c \right] + \nu_e + 1 + n^2(2-\nu_e) \right\} J_n{}'(\beta_c a_c),$$
$$\mathcal{B}_{42}^{(ec)} = \left(\frac{D_c}{D_e}\beta_c^2 a_c^2 - 3n^2 \right) H_n^{(1)}(\beta_c a_c) + \beta_c a_c \left\{ \frac{D_c}{D_e}\left[1 - \beta_c^2 a_c^2 + n^2(\nu_c - 1) - \nu_c \right] + \nu_e + 1 + n^2(2-\nu_e) \right\} H_n^{(1)'}(\beta_c a_c),$$
$$\mathcal{B}_{43}^{(ec)} = \left(-\frac{D_c}{D_e}\beta_c^2 a_c^2 - 3n^2 \right) I_n(\beta_c a_c) + \beta_c a_c \left\{ \frac{D_c}{D_e}\left[1 + \beta_c^2 a_c^2 + n^2(\nu_c - 1) - \nu_c \right] + \nu_e + 1 + n^2(2-\nu_e) \right\} I_n{}'(\beta_c a_c),$$
$$\mathcal{B}_{44}^{(ec)} = \left(-\frac{D_c}{D_e}\beta_c^2 a_c^2 - 3n^2 \right) K_n(\beta_c a_c) + \beta_c a_c \left\{ \frac{D_c}{D_e}\left[1 + \beta_c^2 a_c^2 + n^2(\nu_c - 1) - \nu_c \right] + \nu_e + 1 + n^2(2-\nu_e) \right\} K_n{}'(\beta_c a_c).$$

A.1.5 Further algebraic simplification

In order to obtain the matrices $\mathcal{A}_{kl}^{(ec,*)}$; $\mathcal{B}_{kl}^{(ec,*)}$, $k,l = 1,2,3,4$, (where $\mathcal{A}_{kl}^{(ec,*)}$ is block diagonal), we initially perform the following row operations on the matrix $\mathcal{A}^{(ec)}$ which gives

$$\begin{aligned}
(\beta_e^2 a_c^2 + n^2)R_1 - R_2 - R_3 &\longrightarrow R_1^*, \\
-2n^2 R_1 + (\beta_e^2 a_c^2 + n^2 + 1)R_2 - R_3 - R_4 &\longrightarrow R_2^*, \\
(\beta_e^2 a_c^2 - n^2)R_1 + R_2 + R_3 &\longrightarrow R_3^*, \\
2n^2 R_1 + (\beta_e^2 a_c^2 - n^2 - 1)R_2 + R_3 + R_4 &\longrightarrow R_4^*.
\end{aligned}$$

The reduced form matrix $\mathcal{A}_{kl}^{(ec,*)}$, $k,l = 1,2,3,4$, can be obtained as

$$\mathcal{A}_{11}^{(ec,*)} = 2\beta_e^2 a_c^2 J_n(\beta_e a_c), \quad \mathcal{A}_{12}^{(ec,*)} = 2\beta_e^2 a_c^2 H_n^{(1)}(\beta_e a_c), \quad \mathcal{A}_{13}^{(ec,*)} = \mathcal{A}_{14}^{(ec,*)} = 0,$$
$$\mathcal{A}_{21}^{(ec,*)} = 2\beta_e^3 a_c^3 J_n{}'(\beta_e a_c), \quad \mathcal{A}_{22}^{(ec,*)} = 2\beta_e^3 a_c^3 H_n^{(1)}{}'(\beta_e a_c), \quad \mathcal{A}_{23}^{(ec,*)} = \mathcal{A}_{24}^{(ec,*)} = 0,$$
$$\mathcal{A}_{31}^{(ec,*)} = \mathcal{A}_{32}^{(ec,*)} = 0, \quad \mathcal{A}_{33}^{(ec,*)} = 2\beta_e^2 a_c^2 I_n(\beta_e a_c), \quad \mathcal{A}_{34}^{(ec,*)} = 2\beta_e^2 a_c^2 K_n(\beta_e a_c),$$
$$\mathcal{A}_{41}^{(ec,*)} = \mathcal{A}_{42}^{(ec,*)} = 0, \quad \mathcal{A}_{43}^{(ec,*)} = 2\beta_e^3 a_c^3 I_n{}'(\beta_e a_c), \quad \mathcal{A}_{44}^{(ec,*)} = 2\beta_e^3 a_c^3 K_n{}'(\beta_e a_c).$$

We perform the same row operations on matrix $\mathcal{B}_{kl}^{(ec)}$, $k,l = 1,2,3,4$. It is clear that its reduced form reads as follows

$$\begin{aligned}
\mathcal{B}_{1k}^{(ec,*)} &= (\beta_e^2 a_c^2 + n^2)\mathcal{B}_{1k}^{(ec)} - \mathcal{B}_{2k}^{(ec)} - \mathcal{B}_{3k}^{(ec)},\\
\mathcal{B}_{2k}^{(ec,*)} &= -2n^2\mathcal{B}_{1k}^{(ec)} + (\beta_e^2 a_c^2 + n^2 + 1)\mathcal{B}_{2k}^{(ec)} - \mathcal{B}_{3k}^{(ec)} - \mathcal{B}_{4k}^{(ec)},\\
\mathcal{B}_{3k}^{(ec,*)} &= (\beta_e^2 a_c^2 - n^2)\mathcal{B}_{1k}^{(ec)} + \mathcal{B}_{2k}^{(ec)} + \mathcal{B}_{3k}^{(ec)},\\
\mathcal{B}_{4k}^{(ec,*)} &= 2n^2\mathcal{B}_{1k}^{(ec)} + (\beta_e^2 a_c^2 - n^2 - 1)\mathcal{B}_{2k}^{(ec)} + \mathcal{B}_{3k}^{(ec)} + \mathcal{B}_{4k}^{(ec)},
\end{aligned}$$

$k = 1,2,3,4$.

A.2 Kirchhoff plate: explicit representations for the entries of the scattering matrix $\mathcal{S}$ and the coefficients $A_n^{(i)}$, $B_n^{(i)}$, $A_n^{(c)}$, $E_n^{(c)}$, $B_n^{(c)}$, $F_n^{(c)}$, $E_n^{(e)}$ and $F_n^{(e)}$

Splitting the matrix $\mathcal{C}^{(ei,*)}$ into two parts we can write

$$\begin{pmatrix} A_n^{(e)} \\ B_n^{(e)} \end{pmatrix} = \begin{pmatrix} \mathcal{C}_{11}^{(ei,*)} & \mathcal{C}_{12}^{(ei,*)} \\ \mathcal{C}_{31}^{(ei,*)} & \mathcal{C}_{32}^{(ei,*)} \end{pmatrix} \begin{pmatrix} A_n^{(i)} \\ B_n^{(i)} \end{pmatrix}, \quad \begin{pmatrix} E_n^{(e)} \\ F_n^{(e)} \end{pmatrix} = \begin{pmatrix} \mathcal{C}_{21}^{(ei,*)} & \mathcal{C}_{22}^{(ei,*)} \\ \mathcal{C}_{41}^{(ei,*)} & \mathcal{C}_{42}^{(ei,*)} \end{pmatrix} \begin{pmatrix} A_n^{(i)} \\ B_n^{(i)} \end{pmatrix}.$$

Now eliminating $A_n^{(i)}, B_n^{(i)}$ from these two equations, we obtain

$$\begin{pmatrix} E_n^{(e)} \\ F_n^{(e)} \end{pmatrix} = \mathcal{S}_n \begin{pmatrix} A_n^{(e)} \\ B_n^{(e)} \end{pmatrix},$$

where $\mathcal{S}_n$ is the scattering matrix with the elements

$$\begin{aligned}
\mathcal{S}_n^{11} &= \frac{\mathcal{C}_{21}^{(ei,*)}\mathcal{C}_{32}^{(ei,*)} - \mathcal{C}_{22}^{(ei,*)}\mathcal{C}_{31}^{(ei,*)}}{\mathcal{C}_{11}^{(ei,*)}\mathcal{C}_{32}^{(ei,*)} - \mathcal{C}_{12}^{(ei,*)}\mathcal{C}_{31}^{(ei,*)}}, \quad \mathcal{S}_n^{12} = \frac{\mathcal{C}_{11}^{(ei,*)}\mathcal{C}_{22}^{(ei,*)} - \mathcal{C}_{12}^{(ei,*)}\mathcal{C}_{21}^{(ei,*)}}{\mathcal{C}_{11}^{(ei,*)}\mathcal{C}_{32}^{(ei,*)} - \mathcal{C}_{12}^{(ei,*)}\mathcal{C}_{31}^{(ei,*)}},\\
\mathcal{S}_n^{21} &= \frac{\mathcal{C}_{32}^{(ei,*)}\mathcal{C}_{41}^{(ei,*)} - \mathcal{C}_{31}^{(ei,*)}\mathcal{C}_{42}^{(ei,*)}}{\mathcal{C}_{11}^{(ei,*)}\mathcal{C}_{32}^{(ei,*)} - \mathcal{C}_{12}^{(ei,*)}\mathcal{C}_{31}^{(ei,*)}}, \quad \mathcal{S}_n^{22} = \frac{\mathcal{C}_{11}^{(ei,*)}\mathcal{C}_{42}^{(ei,*)} - \mathcal{C}_{12}^{(ei,*)}\mathcal{C}_{41}^{(ei,*)}}{\mathcal{C}_{11}^{(ei,*)}\mathcal{C}_{32}^{(ei,*)} - \mathcal{C}_{12}^{(ei,*)}\mathcal{C}_{31}^{(ei,*)}}.
\end{aligned}$$

We note that using the relation (3.47), all coefficients appearing in the representation

(3.42) can be obtained as follows:

$$A_n^{(i)} = \frac{\mathcal{C}_{32}^{(ei,*)}}{\mathcal{C}_{11}^{(ei,*)}\mathcal{C}_{32}^{(ei,*)} - \mathcal{C}_{12}^{(ei,*)}\mathcal{C}_{31}^{(ei,*)}} A_n^{(e)}, \quad B_n^{(i)} = -\frac{\mathcal{C}_{31}^{(ei,*)}}{\mathcal{C}_{11}^{(ei,*)}\mathcal{C}_{32}^{(ei,*)} - \mathcal{C}_{12}^{(ei,*)}\mathcal{C}_{31}^{(ei,*)}} A_n^{(e)}; \quad \text{(A.17)}$$

$$A_n^{(c)} = \frac{\mathcal{C}_{11}^{(ci,*)}\mathcal{C}_{32}^{(ei,*)} - \mathcal{C}_{12}^{(ci,*)}\mathcal{C}_{31}^{(ei,*)}}{\mathcal{C}_{11}^{(ei,*)}\mathcal{C}_{32}^{(ei,*)} - \mathcal{C}_{12}^{(ei,*)}\mathcal{C}_{31}^{(ei,*)}} A_n^{(e)}, \quad B_n^{(c)} = \frac{\mathcal{C}_{31}^{(ci,*)}\mathcal{C}_{32}^{(ei,*)} - \mathcal{C}_{32}^{(ci,*)}\mathcal{C}_{31}^{(ei,*)}}{\mathcal{C}_{11}^{(ei,*)}\mathcal{C}_{32}^{(ei,*)} - \mathcal{C}_{12}^{(ei,*)}\mathcal{C}_{31}^{(ei,*)}} A_n^{(e)}, \quad \text{(A.18)}$$

$$E_n^{(c)} = \frac{\mathcal{C}_{21}^{(ci,*)}\mathcal{C}_{32}^{(ei,*)} - \mathcal{C}_{22}^{(ci,*)}\mathcal{C}_{31}^{(ei,*)}}{\mathcal{C}_{11}^{(ei,*)}\mathcal{C}_{32}^{(ei,*)} - \mathcal{C}_{12}^{(ei,*)}\mathcal{C}_{31}^{(ei,*)}} A_n^{(e)}, \quad F_n^{(c)} = \frac{\mathcal{C}_{41}^{(ci,*)}\mathcal{C}_{32}^{(ei,*)} - \mathcal{C}_{42}^{(ci,*)}\mathcal{C}_{31}^{(ei,*)}}{\mathcal{C}_{11}^{(ei,*)}\mathcal{C}_{32}^{(ei,*)} - \mathcal{C}_{12}^{(ei,*)}\mathcal{C}_{31}^{(ei,*)}} A_n^{(e)}; \quad \text{(A.19)}$$

$$E_n^{(e)} = \frac{\mathcal{C}_{21}^{(ei,*)}\mathcal{C}_{32}^{(ei,*)} - \mathcal{C}_{22}^{(ei,*)}\mathcal{C}_{31}^{(ei,*)}}{\mathcal{C}_{11}^{(ei,*)}\mathcal{C}_{32}^{(ei,*)} - \mathcal{C}_{12}^{(ei,*)}\mathcal{C}_{31}^{(ei,*)}} A_n^{(e)}, \quad F_n^{(e)} = \frac{\mathcal{C}_{41}^{(ei,*)}\mathcal{C}_{32}^{(ei,*)} - \mathcal{C}_{42}^{(ei,*)}\mathcal{C}_{31}^{(ei,*)}}{\mathcal{C}_{11}^{(ei,*)}\mathcal{C}_{32}^{(ei,*)} - \mathcal{C}_{12}^{(ei,*)}\mathcal{C}_{31}^{(ei,*)}} A_n^{(e)}. \quad \text{(A.20)}$$

Appendix B

B.1 Supplementary cloaking results for a 5×5 cluster

In this appendix, we present illustrative examples for a 5×5 cluster of pins. We choose values of the spectral parameter β consistent with those presented for $N = 4$ in the main text of chapter 4.

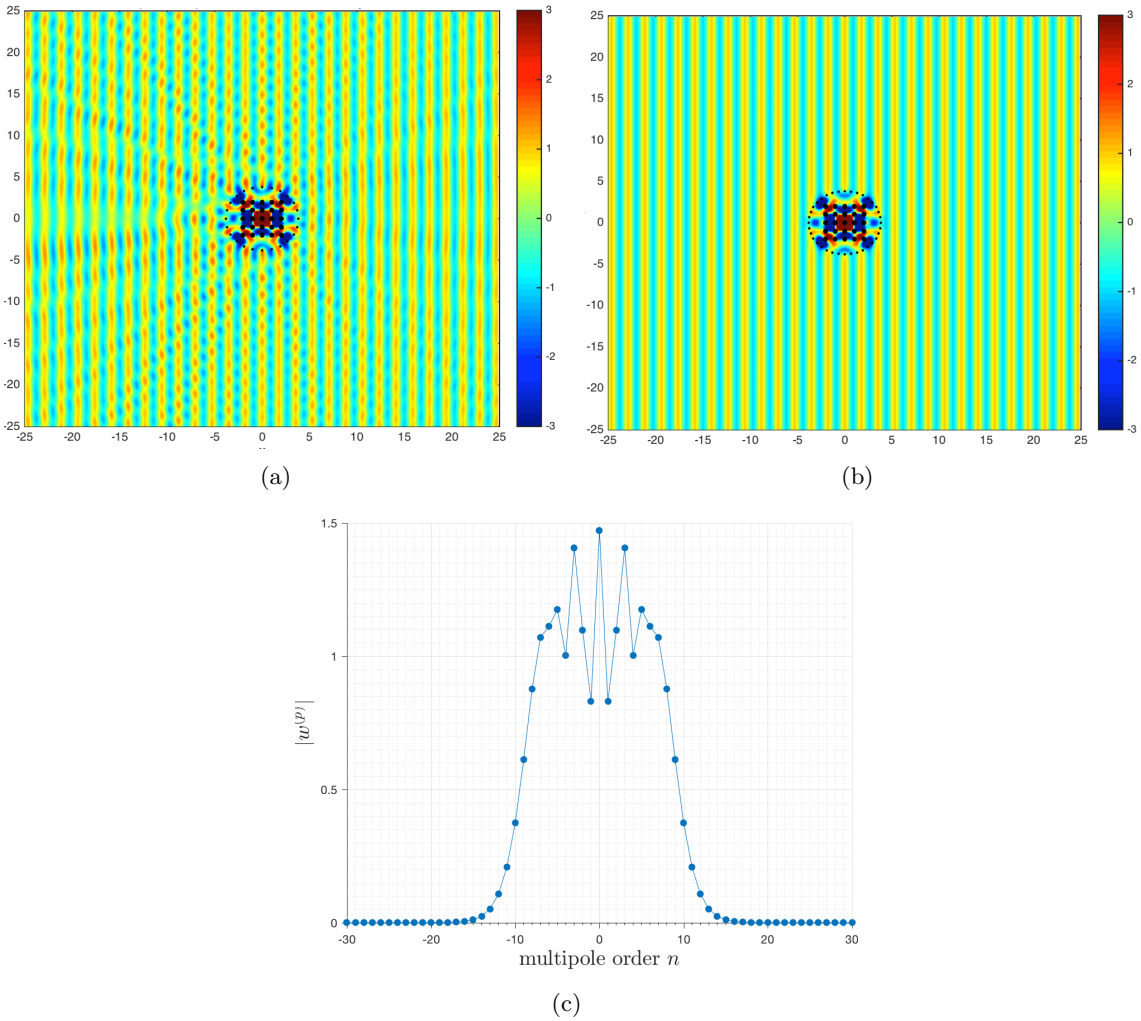

Figure B.1: Cloaking results for a 5×5 cluster for comparison with the corresponding Figure 4.8 for the 4×4 cluster. Here, $\theta_{inc} = 0$, $\beta = 3.565$ and in (a) $m = 24$ and in (b) $m = 36$.

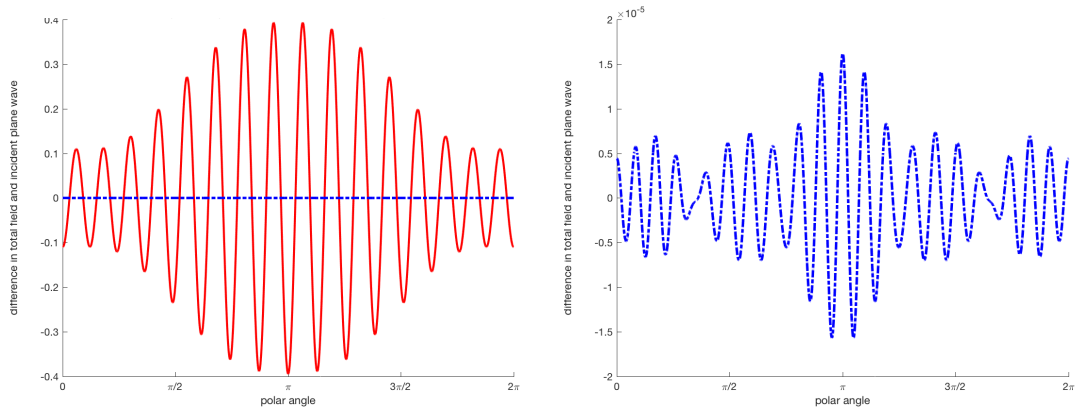

(a) (b)

Figure B.2: Absolute error evaluated on a circle of radius 15 versus the polar angle. 5×5 cluster of pins for $\theta_{inc} = 0$ and $inc = 3.565$. (a) $m = 24$ (solid curve), $m = 36$ (dashed curve) which is magnified in part (b).

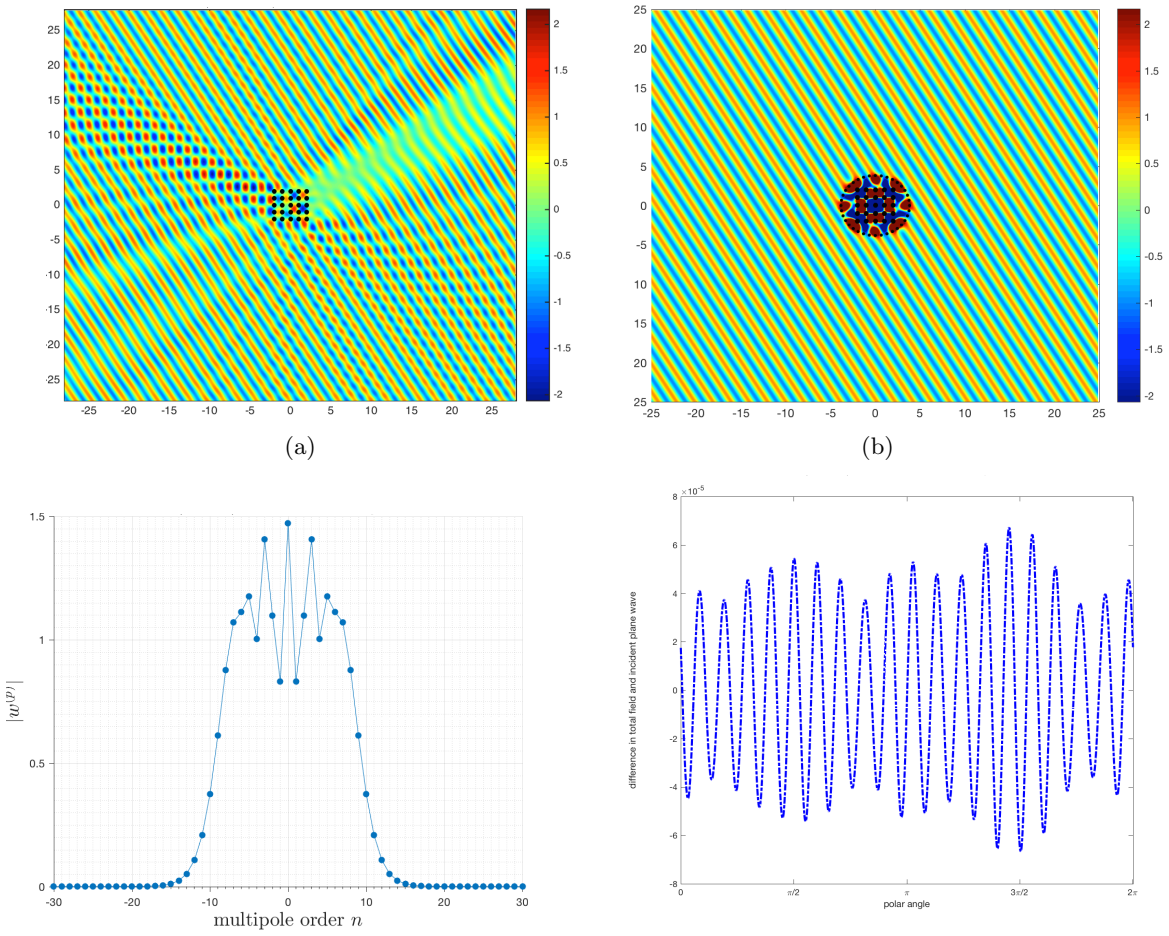

(a) (b)

(c) (d)

Figure B.3: Cloaking results for a 5×5 cluster for comparison with the corresponding Figure 4.10 for the 4×4 cluster. Here, $\theta_{inc} = \pi/6$, $\beta = 3.565$ and $m = 36$.

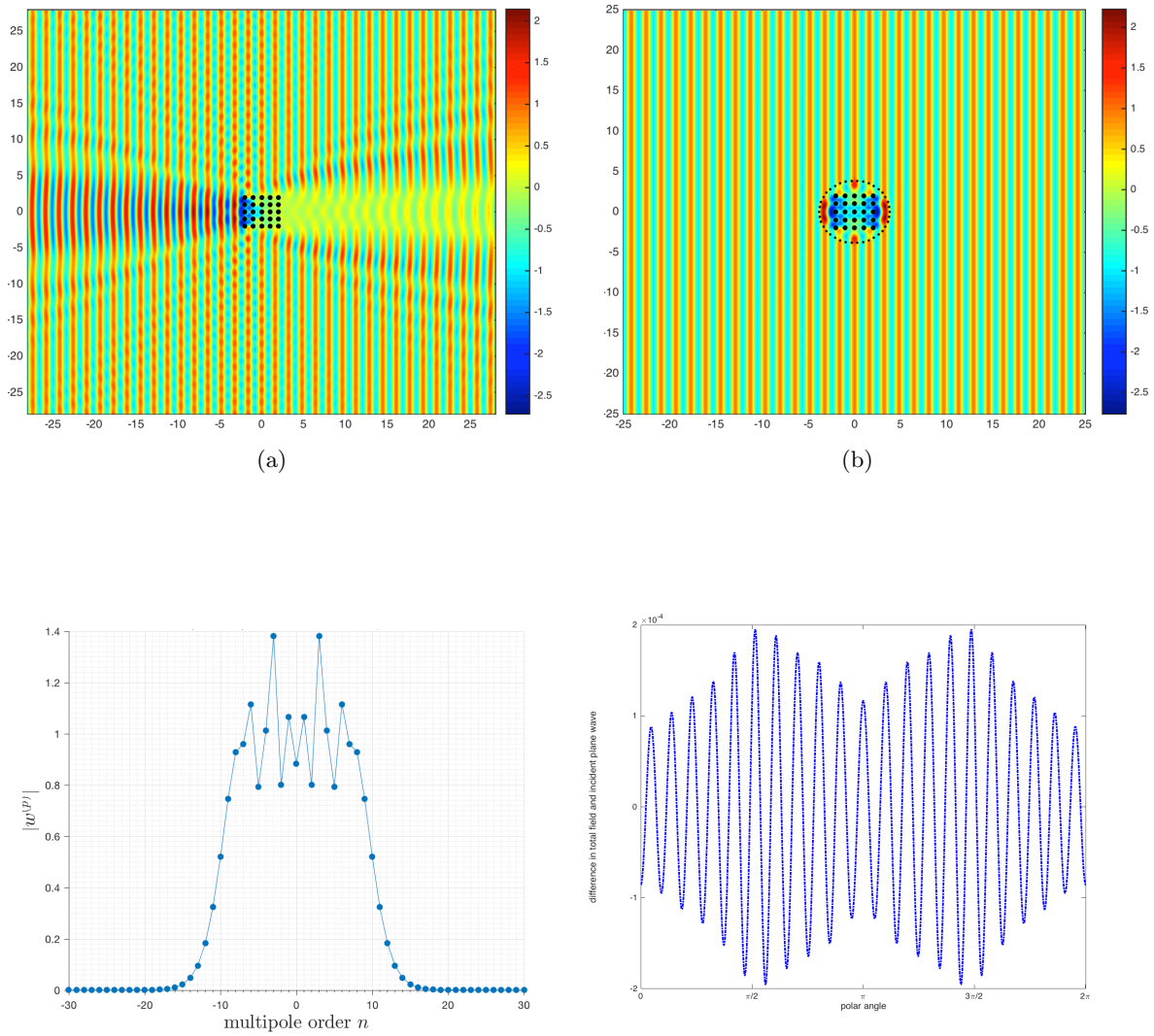

Figure B.4: Cloaking results for a 5×5 cluster for comparison with the corresponding Figure 4.11 for the 4×4 cluster. Here, $\theta_{inc} = 0$, $\beta = 3.90$ and $m = 38$.

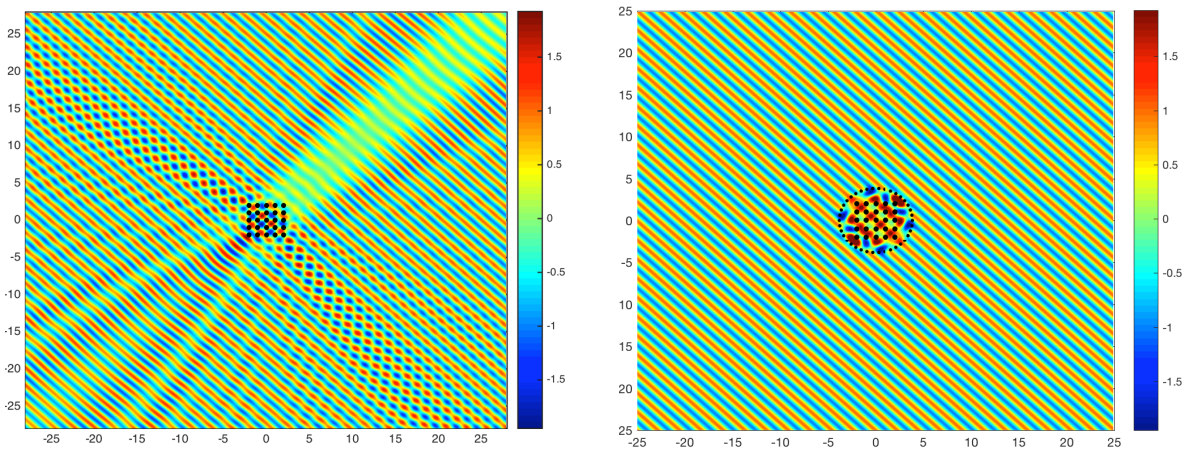

(a) (b)

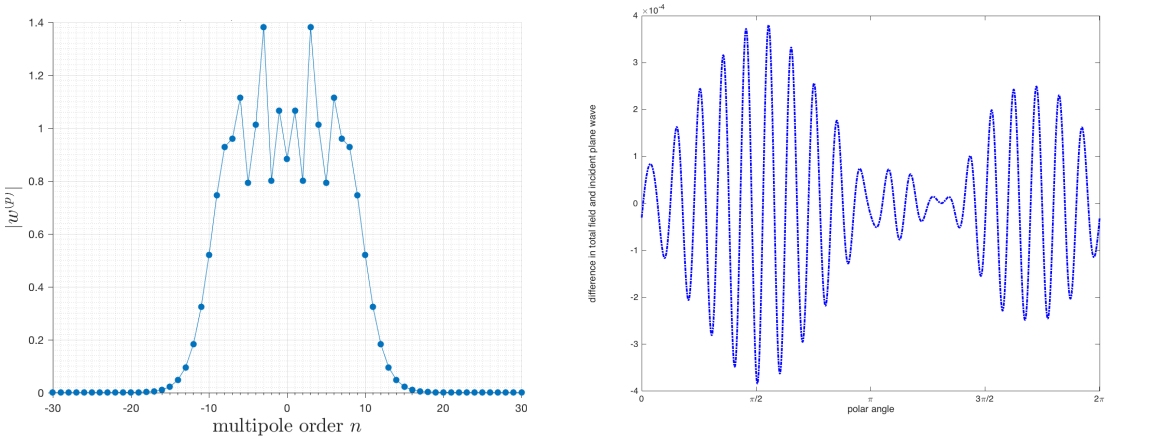

(c) (d)

Figure B.5: Cloaking results for a 5×5 cluster for comparison with the corresponding Figure 4.12 for the 4×4 cluster. Here, $\theta_{inc} = \pi/4$, $\beta = 3.90$ and $m = 38$.

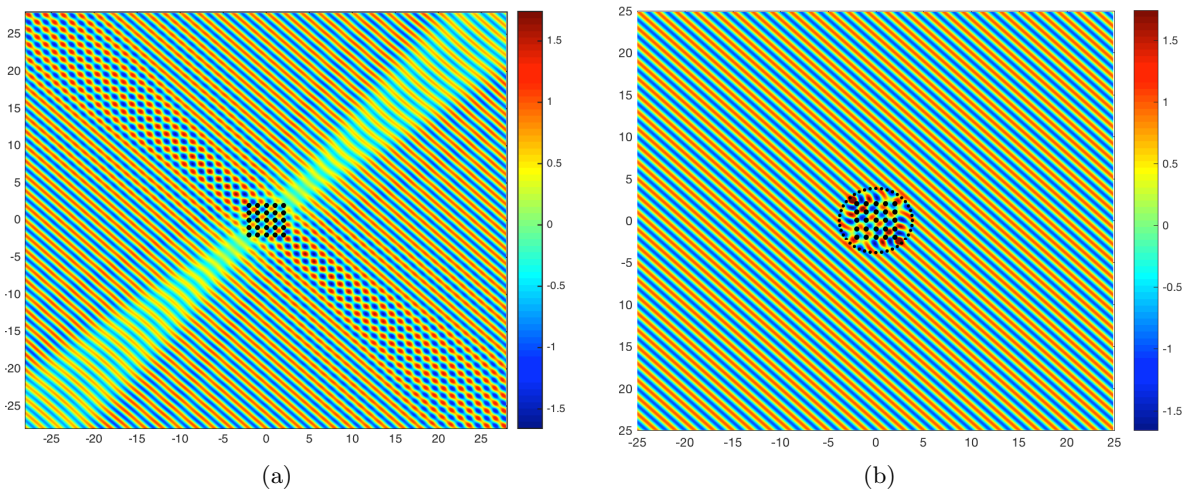

(a) (b)

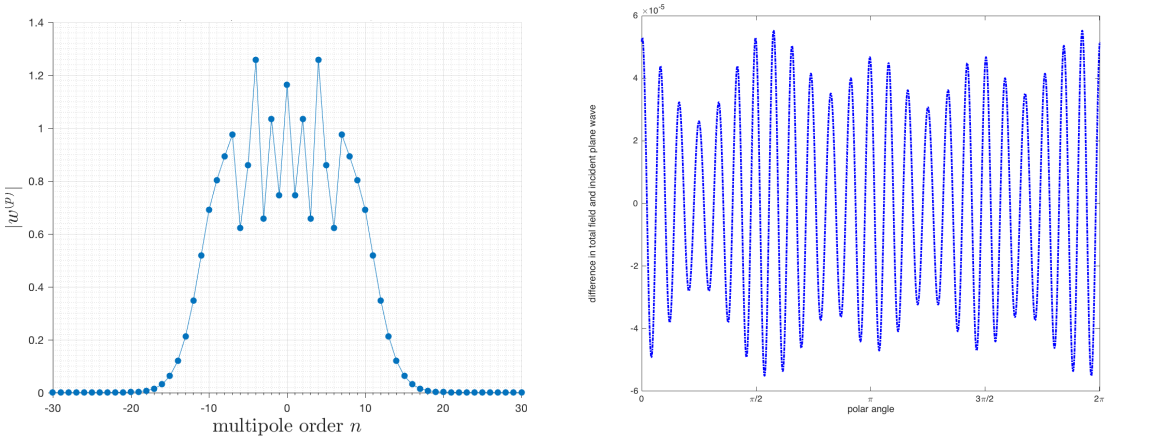

(c) (d)

Figure B.6: Cloaking results for a 5×5 cluster for comparison with the corresponding Figure 4.13 for the 4×4 cluster. Here, $\theta_{inc} = \pi/4$, $\beta = 4.44$ and $m = 40$.